HIGH PRECISION GRAVITY MEASUREMENTS
USING ATOM INTERFEROMETRY

By

Achim Peters

May 1998

I certify that I have read this dissertation and that in my opinion it is fully adequate, in scope and quality, as a dissertation for the degree of Doctor of Philosophy.

_____
Steven Chu
(Principal Adviser)

I certify that I have read this dissertation and that in my opinion it is fully adequate, in scope and quality, as a dissertation for the degree of Doctor of Philosophy.

_____
Steven E. Harris

I certify that I have read this dissertation and that in my opinion it is fully adequate, in scope and quality, as a dissertation for the degree of Doctor of Philosophy.

_____
Yoshihisa Yamamoto

Approved for the University Committee on Graduate Studies:

_____

Abstract

Using atom interferometry, we have measured g, the local acceleration due to gravity, with a resolution of $\Delta g/g = 2 \times 10^{-8}$ after a single $1.3\,\text{s}$ measurement cycle, 2×10^{-9} after 1 minute and 1×10^{-10} after 2 days of integration time. The difference between our value for g and one obtained by a "falling corner–cube" optical interferometer is $(7 \pm 7) \times 10^{-9}$. The beam splitters and mirrors of the atom interferometer are implemented using velocity sensitive stimulated Raman transitions and laser cooled cesium atoms in an atomic fountain are used as a well defined source of atoms.

We present experimental results, including the observation of tidal effects and a comparison with the "falling corner–cube" absolute gravimeter. We extend previous methods of analyzing the interferometer to include the effects of a gravitational gradient and finite length Raman pulses. We also present a detailed experimental and theoretical study of potential systematic errors and noise sources.
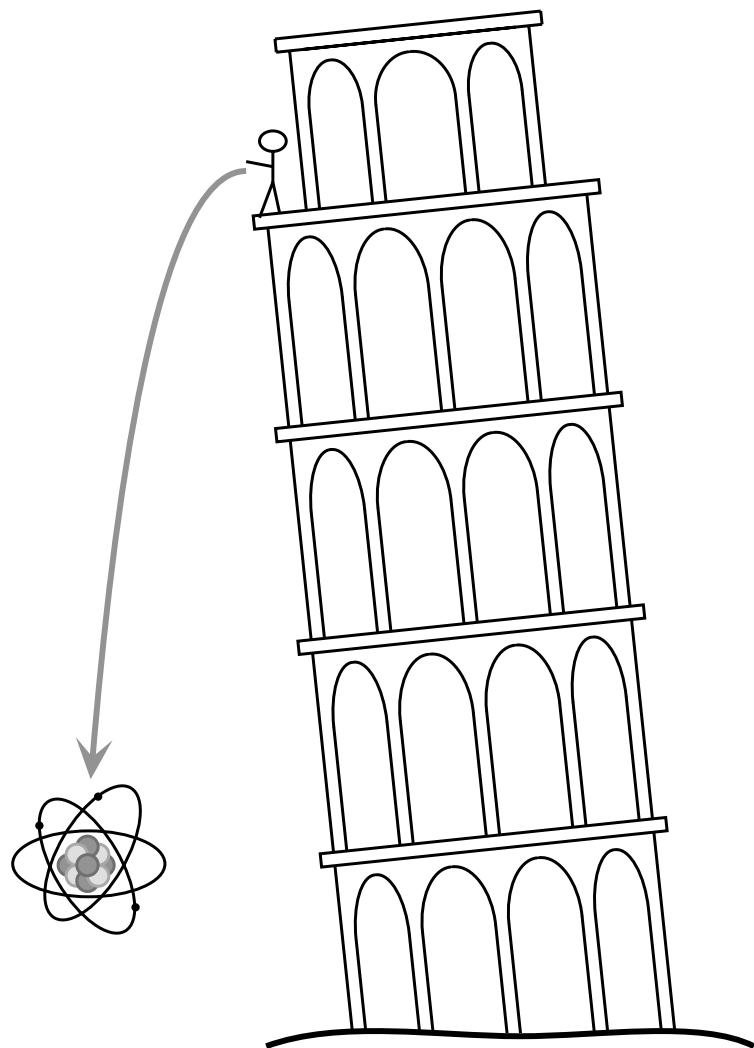
Figure 1: A very old idea . . .

Für meine Eltern,

und für Opa.

Acknowledgements

I would like to thank ...

my advisor Steven Chu for giving me the opportunity to work on this interesting experiment and in an environment that has been both stimulating and challenging. I hope that I have acquired some of his good taste in scientific experiments, his mastery of experimental details and his skill in presenting science.

Mark Kasevich for the training he gave me early in my graduate student career and for the many helpful discussions we had over the years. It has always been impressive to see him work in the lab and observe how he gets things done by focusing on the issues that are really important.

Keng Yeow Chung for working with me in the lab for countless hours and making many valuable contributions.

Kurt Gibble and David Weiss for the skills they have taught me and for many fruitful discussions.

All the members of the Chu lab for many interesting conversations and in particular Heun Jin Lee, Brenton Young, and Joel Hensley.

Marcia Keating for always being kind and helpful. She has made my stay at Stanford even more enjoyable.

Ken Sherwin for all his technical assistance and his help in acquiring and fixing equipment.

Wolfgang Jung for teaching me how not to kill myself in the machine shop.

Contents

List of Tables

List of Figures

Chapter 1

Introduction

1.1 Gravity measurements

The acceleration due to gravity*, commonly denoted as g, is a site dependent quantity which also varies with time. Its value is important for many scientific fields, including geophysics and metrology [1]. Precise measurements of g also have profound practical applications in prospecting for oil, water and other natural resources.

In metrologie, g is important because most force measurements use the weight of a known mass as a reference, which is only possible if the value of g is accurately known. Force measurements in turn are used to realize many other quantities — including pressure, temperature and current — which therefore depend on the value of g as well.

Geophysical applications, as well as prospecting, mostly involve mapping spatial variations in gravity to gather information about Earth's spin, shape and composition. The required measurement accuracy for these purposes may be anywhere between 10^{-6} and 10^{-8}. Other applications require monitoring the small, time dependent changes in gravity caused by tides or crustal deformations. In fact, these measurements are usually the ones that require the highest measurement accuracies, typically a few parts in 10^9 or better. Table 1.1 lists many gravitational effects and their typical magnitudes.

Instruments which measure gravity come in many different forms, several of which are listed in Table 1.2, together with their typical performance parameters. The main distinction is between relative and absolute gravimeters.

---

*Although gravity is by far the most important contribution to g, it also includes centrifugal terms due to Earth's rotation.

Type	Magnitude
Geographical gravity variations	
• global scale	$\sim 10^{-3}$ g
• regional scale	$\sim 10^{-6}$ g
Free air gravity gradient	$\sim 3 \times 10^{-7}$ g/m
Tidal effects	
• basic tides	$\sim 10^{-7}$ g
• elastic response	$\sim 10^{-8}$ g
• ocean loading	$\sim 10^{-8}$ g
• polar motion	$\sim 10^{-8}$ g
Environmental effects	
• atmospheric pressure	$\sim 3 \times 10^{-10}$ g/mbar
• water table	
Man–made environmental changes	
• trains, trucks, elevators, people, ...	$\sim 10^{-9}$ g
• major construction work	$\sim 10^{-8}$ g
Geological and geophysical effects	
• postglacial rebound	$\sim 10^{-9}$ g/year
• tectonic plate movements	$\sim 10^{-9}$ g/year
• change in ocean levels	
• core/mantle boundary effects	
• inner/outer core boundary effects	$\sim 10^{-12}$ g

Table 1.1: Important gravitational effects and their typical magnitude.

Relative gravimeters are usually spring–type instruments which employ a very stable and well characterized spring to support a test mass against gravity. Even slight variations in gravity manifest themselves as measurable changes in the spring's extensions. The resolution of these instruments can approach 10^{-9} and they can be made very compact and transportable, which makes them useful for geophysical prospecting applications. Their main shortcoming is that their readings are only relative and need to be calibrated against known gravity differences. They also show very substantial drifts which require frequent re–calibration and make it very hard to compare measurements taken at different times.

Type of gravimeter	Noise ($g/\sqrt{Hz}$)	Drift (g/day)	Accuracy (g)
Spring/mass systems	1×10^{-10}	3×10^{-8}	N/A
Levitated superconducting spheres	$< 10^{-12}$	2×10^{-10}	N/A
Falling corner–cubes	5×10^{-8}	-	2×10^{-9}
Atom interferometer	2×10^{-8}	-	$< 1 \times 10^{-8}$

Table 1.2: Different types of gravimeters and their typical performance. The noise levels for the falling corner–cube gravimeter and the atom interferometer are for measurements in our lab (see Sec. 4.4). Under ideal conditions the noise of the falling corner–cube gravimeter can be 10 times lower.

Cryogenic gravimeters [2, 3] offer the best noise performance of all instruments. In many respects they are an improved version of spring–type gravimeter. They employ a superconducting sphere which is levitated in a magnetic field and use force feedback techniques to counter–balance variations in gravity. While the observed drift rate is substantially smaller and better predictable compared with other spring-type gravimeters, it is still present and complicates long term measurements. Vibration induced flux–jumps in the superconductor can cause offsets in the gravity readings. Since they are essentially unavoidable when transporting the instrument, this type of gravimeter is unsuitable for comparing gravity values between different sites.

Absolute gravimeters are required for several applications that go beyond the capabilities of relative instruments. In addition to metrology applications, which obviously require an absolute gravity value, this includes comparing gravity measurements taken far apart in space and time. Pendulum measurements are the classical method for obtaining absolute gravity values, but they are very tedious and their accuracy is limited to about 10^{-7}. Modern

instruments instead use a laser interferometer to monitor the motion of a freely falling object, usually a corner–cube retro–reflector. Many such absolute gravimeters [1, 4, 5] have been developed since 1950, and after many improvements they have now reached accuracies of $\sim 2\,\mu\mathrm{Gal}$ [†].

Even the performance of the latest falling corner–cube gravimeters leaves room for improvement. Their noise levels are higher than those of relative gravimeters, mostly because the measurement is not continuous but uses discrete drops at a maximum rate of 1 Hz. In practice, the drop rates are often reduced further to increase the lifetime of the instrument and to provide sufficient settling time for drop related vibrations. The measurement accuracy is currently limited by a number of systematic effects, not all of he fully understood [5].

Our approach to absolute gravity measurements is in many respects resembles the falling corner–cube method. However, instead of observing a corner–cube we monitor the acceleration of laser cooled cesium atoms in an atomic fountain. This method is interesting in its own right, since for the first time it allows one to measure the effect of gravity on microscopic particles with an accuracy similar to that achievable for macroscopic objects. Furthermore, it has the potential of achieving better measurement resolutions, since it allows higher repetition rates. Finally, it could offer better measurement accuracies, since it is not subject to some of the systematic effects affecting falling corner–cube instruments.

While the idea of observing atoms while they accelerate in a gravitational field is very straightforward, the actual implementation is substantially more difficult. The most intuitive method would be to monitor the Doppler shift of a suitable atomic transition while the atom accelerates, but there are several problems with this approach. Most importantly, reaching a resolution of 10^{-9} requires measuring Doppler shifts to within few milli–Hertz, which is much to small compared with the transition linewidth, the laser linewidth or even the Doppler broadening due to the velocity distribution of the laser cooled atoms. One also has to consider that the atomic momentum is disturbed whenever a photon is absorbed or emitted.

Despite these objections it is still possible to make the idea work. The solution is to employ a more sophisticated approach using atom interferometry. By choosing an appropriate interferometer configuration one can then circumvent all the problems mentioned above

---

[†]The μGal is the most common unit for precision gravity measurements and we will use it extensively in this work. 1 μGal $= 10^{-6}$ cm/s$^2 = 10^{-8}$ m/s$^2 \approx 10^{-9}$ g.

and indeed measure the acceleration induced Doppler shift with the envisioned very high levels of accuracy and resolution.

1.2   Atom Interferometry

The idea of making an matter–wave interferometer using neutral atoms [6, 7] has been around for a long time. It was finally realized in 1991, when four very different atom interferometers were demonstrated by research groups in the United States and Germany. Two of the experiments used diffraction by micro–fabricated slits (Konstanz [8]) or gratings (MIT [9]) to implement beam splitters and mirrors. The other two utilized the momentum recoil associated with the absorption or stimulated emission of optical photons during one–photon (PTB [10]) or two–photon transitions (Stanford [11]). Subsequent experiments [12] have also shown the feasibility of using diffraction by periodic light fields.

Since 1991 the performance of atom interferometers has improved substantially. By now they reached a stage of development where they are not just mere demonstrations of quantum mechanics anymore. Instead, one can now us them as tools to perform a variety of useful measurements with a precision and accuracy that challenges, if not exceeds, the performance of any competing instrument. The method pioneered by Kasevich and Chu here at Stanford in 1991 has been proven especially successful in this respect. It uses stimulated Raman transitions between atomic hyperfine groundstates to implement the optical elements of the interferometer and has already been used to measure gravity [11], rotations [13] and fundamental constants [14, 15, 16]. It is also the method of choice for our measurement of g.

Stimulated Raman transitions have been discussed elsewhere in great detail [14, 17]. The basic process is illustrated in Fig. 1.1 and can be summarized as follows:

(a) The atom is illuminated by two counter-propagating laser beams whose frequency difference equals the splitting between two hyperfine ground states of the atom. We can assign them an effective wave number $\mathbf{k}_{\mathrm{eff}} = \mathbf{k}_1 - \mathbf{k}_2$ ($k_{\mathrm{eff}} = |\mathbf{k}_2| + |\mathbf{k}_1|$ for counter propagating beams) and an effective frequency $\omega_{\mathrm{eff}} = \omega_1 - \omega_2$, where $\mathbf{k}_i$ and ω_i are the equivalent quantities for the individual laser beams.

(b) Absorption and stimulated emission of photons during a Raman pulse can simultaneously change the internal state of the atom and its momentum by $m\mathbf{v}_{\mathrm{rec}}$, where $\mathbf{v}_{\mathrm{rec}} = \hbar \mathbf{k}_{\mathrm{eff}}/m$ is the recoil velocity. The transition probability depends on the pulse area

Initial:

$\hbar k_1$ $|a\rangle, p = 0$ $\hbar k_2$

Final:

$2\,\hbar k_2$ $|b\rangle, p = \hbar\,(k_1\text{-}k_2) = \hbar\,k_{\text{eff}}$

$|i\rangle$

Δ

ω_1 ω_2

$|b\rangle$

ω_{hfs}

$|a\rangle$
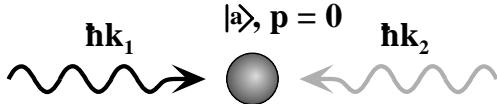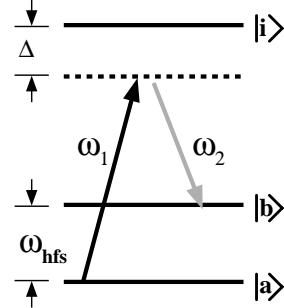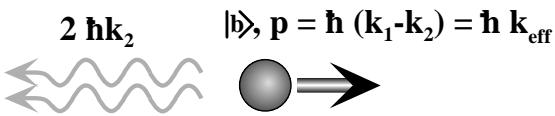
Figure 1.1: An atom undergoes a stimulated Raman transition. It absorbs a photon of frequency ω_1 and emits another one (via a stimulated emission) of frequency ω_2. Since both photons carry momentum, and because momentum has to be conserved in the process, the atom receives a recoil momentum kick.

and can be adjusted to create either beam splitters or mirrors.

(c) The quantum mechanical phase the resulting superposition state depends on the local Raman phase $\phi_i = k_{\text{eff}} z_i - \omega_{\text{eff}} t_i$.

Figure 1.2 shows how a sequence of three such Raman pulses is used to split, reflect and recombine an atom while simultaneously changing its internal state. At the end of this sequence the fraction of the atoms in one of the states is detected[‡]. The result is an oscillatory function of the interferometer path difference, which, among other things, depends on the gravitational acceleration.

The total phase difference between paths A and B can be divided into two parts. The first contribution describes the periods of free evolution between laser pulses and is given by

$$\Delta\phi_{\text{path}} \quad = \quad \frac{1}{\hbar}\left(S^B_{\text{cl}} - S^A_{\text{cl}}\right) \tag{1.1}$$

in the limit where the classical action

$$S_{\text{cl}} \quad = \quad \int_0^{2T} \mathcal{L}\left[z(t), \dot{z}(t)\right]\,dt \tag{1.2}$$

along each path is much greater than $\hbar$ [18].

[‡]There is a one–to–one correspondence between atomic momentum and internal state. In principle one could therefore also determine the final state using a momentum measurement, but this is much harder to implement experimentally.
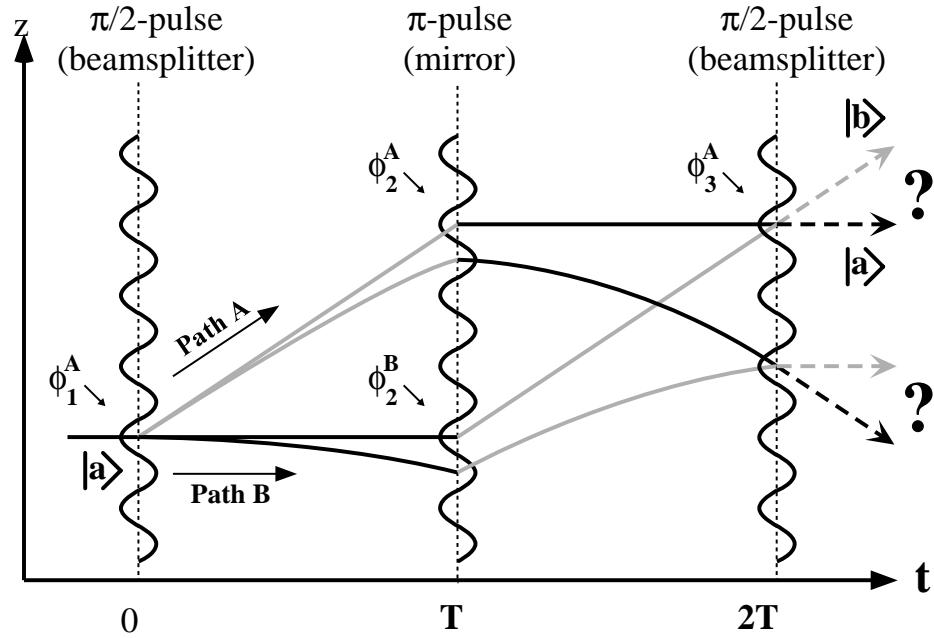
Figure 1.2: Basic Mach-Zehnder type atom interferometer with (curved lines) and without (straight lines) gravity. The atom can either be in the internal state $|a\rangle$ (dark) or $|b\rangle$ (light). The lines represent the classical trajectories originating from one of the space–time points comprising the initial wave packet.

The second contribution is due to the interaction with the Raman beams. Whenever the state of the atom changes during such an interaction, it acquires an additional phase shift that is determined by the local Raman phase ϕ_i and has a sign that depends on the initial state of the atom (see chapter 2). Tracing all the state changes we find that this causes a phase difference of

$$\Delta\phi_{\text{light}} \quad = \quad (\phi_1^A - \phi_2^A) - (\phi_2^B - \phi_3^A). \tag{1.3}$$

For uniform gravitational fields ($\mathcal{L} = \frac{m}{2}v^2 - mgz$) the free evolution contribution vanishes. The second contribution is calculated using the local Raman phases $\phi_i = k_{\text{eff}}z_i - \omega_{\text{eff}}t_i$ and the known atomic trajectories $z(t)$. Without a gravitational field the trajectories are straight lines and the inherent symmetry of the situation (Fig. 1.2) leads to $\Delta\phi = 0$. The introduction of a gravitational field breaks the symmetry. The atom now falls three times as far during the second half of the interferometer as during the first half and we find a phase shift proportional to the gravitational acceleration:

$$\Delta\phi \quad = \quad k_{\text{eff}}gT^2 \quad = \quad \frac{m}{\hbar}v_{\text{rec}}gT^2. \tag{1.4}$$

This simple equation describes the interferometer extremely well and has to be modified only slightly to account for gravity gradients and finite length Raman pulses (Sec. 2). The equation also indicates that it is highly desirable to make the time T between the interferometer pulses as long as possible since the measurements sensitivity scales quadratically with this parameter. Indeed, one of the biggest improvements made since the first measurements in 1991 has been the implementation of an active vibration isolation system that allowed us to increase T to at least 160 ms without loss of interferometer phase contrast.

Our interferometer uses laser cooled cesium atoms in an atomic fountain and Raman lasers that operate close to the D_2–line at 852 nm. For a typical time $T = 160$ ms between Raman pulses an interferometer phase shift of 1 radian corresponds to $\sim 2.6 \times 10^{-7}$ g. Accordingly, the standard gravitational acceleration of 9.81 m/s causes a phase shift of approximately 3.8×10^6 rad!

1.3   Overview of this thesis

Chapter 2 presents a more detailed theoretical analysis of the interferometer, including the effects of gravitational gradients and finite length Raman pulses. Chapter 3 describes the experimental setup. Chapter 4 gives a overview of the experimental results, including long term gravity measurements and a direct comparison with one of the best classical gravimeters. The next two chapters are then devoted to an extensive discussion of the instrument's performance: Chapter 5 deals with issues related to measurement noise and fringe contrast, while Chapter 6 contains a extensive analysis of potential systematic errors and how they affect the accuracy of the measurement. Finally, chapter 7 summarizes the results, puts them in context and considers the prospects for future improvements and applications.

Chapter 2

Theory

In this chapter we use several different methods to analyze our light pulse interferometer, with a special emphasis an aspects that are often neglected but become important for high accuracy measurements. First, we present various forms of a path integral treatment that includes the effect of a linear gravity gradient. Then, we use a modified Bloch–vector formalism to study the effect of finite length interferometer pulses.

2.1   Gravity gradients

There are many different ways to describe an atom interferometer's sensitivity to gravitational forces. For the early interferometer experiments [11] Kasevich and Chu used a method that describes the experiment in a freely falling frame where the gravitational force vanishes and the atomic momentum between light pulses becomes a conserved quantity. Under these conditions the interferometer can be analyzed in the momentum picture as a sequence of stimulated Raman pulses acting on a stationary atom and one can easily calculate the interferometer phase shift from the phases of the transformed light fields.

   As elegant as this method is, it relies on an equivalence principle argument and therefore only works if the gravitational field in the measurement region can be considered constant. At our targeted measurement accuracy of $1\,\mu$Gal and for a typical gravity gradient of $300\,\mu$Gal/m this is definitely not the case anymore. Over the standard free fall distance of $15\,$cm gravity changes by $45\,\mu$Gal, and even the $1\,$mm maximum splitting between the two interferometer arms (for ^{133}Cs atoms, lighter atoms would give an even bigger splitting) corresponds to a worrisome gravity difference of $0.3\,\mu$Gal. We therefore need a more general

description which takes into account spatially inhomogeneous forces.

Since we have to deal with *spatially* varying forces it seems advisable to analyze the experiment in the position picture. In principle, it would be possible to analyze the whole process by solving the time dependent Schrödinger equation for the atomic wave packet propagating through the system and calculating the expectation value for the appropriate quantum mechanical observable. Several authors have indeed followed this approach [19, 20], but there are difficulties caused by the very different nature of the atomic evolution during interactions with the light fields compared to the periods of free propagation. The obvious solution is to treat these two cases separately and then combine the results.

Between pulses the atomic wave packets propagate over macroscopic distances while being subjected only to smoothly varying fields and forces. This suggests using the path integral description of quantum mechanics [18] as a natural framework for analyzing the atom interferometer. The effects of infinitesimally short beam splitter and mirror pulses can be integrated into the formalism using a simple set of rules, which have been worked out by Bordé and others [21, 22] for the case of single photon transitions. With small modifications, they can also be used to treat stimulated Raman transitions.

These rules are summarized in Table 2.1 and illustrated in Fig. 2.1. Each interaction with the light field forms a potential beam splitter because the internal state of the atom can either change or stay the same, with a relative probability that depends on the details of the process. Whenever the internal state changes there is a corresponding change of the atomic momentum and future trajectory. Since there are two possible input states there are four possible processes and each is associated with a phase factor. This phase factor, which depends on the phase of the light field, has to be added to the quantum mechanical phase of each path which involves that particular process.

While this path integral approach has been used successfully to analyze a wide variety of interferometry experiments, it has never been applied to one with the same accuracy requirements as ours. Therefore, in order to properly understand the formalism and to make sure that it is up to the task, we perform our own analysis starting from more basic principles and paying special attention to all the approximations which are usually made. We present three different methods, compare their relative merits and obtain an error estimate for making approximations in two of them.
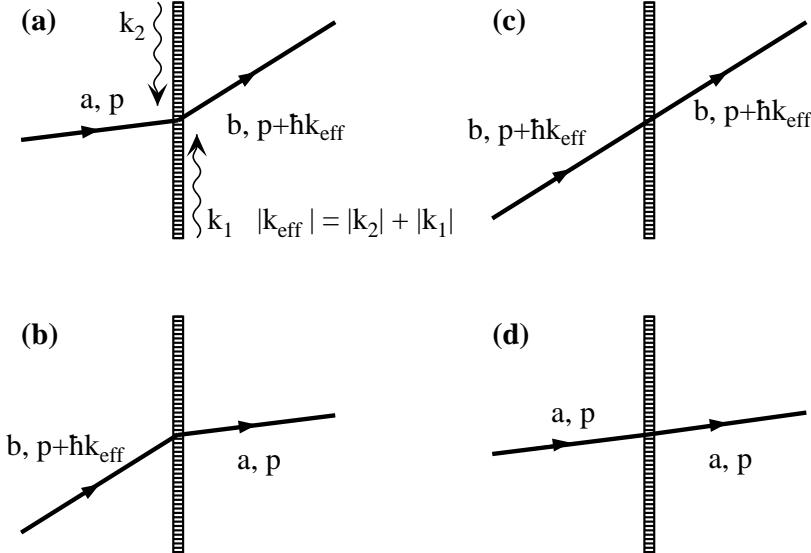
Figure 2.1: **Basic processes during atom/light interaction.** (a) When changing from internal state $|a\rangle$ to $|b\rangle$ the atom absorbs one photon from Raman beam 1 and emits another one co–propagating with Raman beam 2. Its momentum changes by $+\hbar k_{\mathrm{eff}}$. (b) When changing from internal state $|b\rangle$ to $|a\rangle$ the atom absorbs one photon from Raman beam 2 and emits another one co–propagating with Raman beam 1. Its momentum changes by $-\hbar k_{\mathrm{eff}}$. (c)(d) The atom may also stay in its original state.

	int. state	momentum	phase factor ϕ_i
Single photon transitions	$a \rightarrow b$	$p \rightarrow p + \hbar k$	$+(k_i z - \omega t_i - \phi + \frac{\pi}{2})$
	$b \rightarrow a$	$p + \hbar k \rightarrow p$	$-(k_i z - \omega t_i - \phi + \frac{\pi}{2})$
	$a \rightarrow a$	$p \rightarrow p$	0
	$b \rightarrow b$	$p + \hbar k \rightarrow p + \hbar k$	0
Raman transitions	$a \rightarrow b$	$p \rightarrow p + \hbar k_{\mathrm{eff}}$	$\phi^{\mathrm{AC}}_{\mathrm{avg}} + (k_{\mathrm{eff}} z_i - \omega_{\mathrm{eff}} t_i - \phi_{\mathrm{eff}} + \frac{\pi}{2})$
	$b \rightarrow a$	$p + \hbar k_{\mathrm{eff}} \rightarrow p$	$\phi^{\mathrm{AC}}_{\mathrm{avg}} - (k_{\mathrm{eff}} z_i - \omega_{\mathrm{eff}} t_i - \phi_{\mathrm{eff}} + \frac{\pi}{2})$
	$a \rightarrow a$	$p \rightarrow p$	$(\phi^{\mathrm{AC}}_{\mathrm{avg}} - \frac{1}{2}\phi^{\mathrm{AC}}_{\mathrm{diff}})$
	$b \rightarrow b$	$p + \hbar k_{\mathrm{eff}} \rightarrow p + \hbar k_{\mathrm{eff}}$	$(\phi^{\mathrm{AC}}_{\mathrm{avg}} + \frac{1}{2}\phi^{\mathrm{AC}}_{\mathrm{diff}})$

Table 2.1: bf Rules for atom/light interaction. (z_i, t_i) is the spacetime point of the interaction. The quantities k, ω and ϕ denote the wave vector, frequency and phase of the light field. Note that the only change for stimulated Raman transitions — besides using the effective quantities k_{eff}, ω_{eff} and ϕ_{eff} — is the appearance of additional phase factors $\phi^{\mathrm{AC}}_{\mathrm{avg}}$ and $\phi^{\mathrm{AC}}_{\mathrm{diff}}$ due to AC–Stark shifts. See Sec. 2.2 for related definitions.

2.1.1   "Exact" path integral treatment

Kasevich and Chu used the path integral formalism as one method to analyze their interferometer in 1991 [11]. We now extend their treatment to include the effect of a linear gravity gradient, closely following the steps outlined in the tutorial paper by Storey and Cohen-Tannoudji [23].

We will assume a two level system with wavefunctions Ψ_a and Ψ_b, and an initial plane wave state with momentum p_0:

$$\Psi_a(z_0, t_0) = \frac{1}{\sqrt{2\pi\hbar}} \exp\left[\frac{i(p_0 z_0 - E_0 t_0)}{\hbar}\right] \qquad \text{and} \qquad \Psi_b(z_0, t_0) = 0 \tag{2.1}$$

For a two–path interferometer, knowing the phase difference between the different paths leading a spacetime point (z_d, t_d) is sufficient to predict the phase, though not the contrast, of the observed interferometer fringe as a function of g. It can be calculated using the following algorithm:

- Find the two classical paths Γ_A and Γ_B (taking into account the momentum changes due to the interactions with the light field.) which (a) go through point z_d at time t_d, (b) have initial momentum p_0 at time t_0 and (c) lead to a specified internal state. Notice that the different paths originate from points z_0^A and z_0^B which generally are *not* identical (see figure 2.2).

- Calculate the classical action

$$S_{\text{cl}} \quad = \quad \int_{t_0}^{t_f} \mathcal{L}\left[z(t), \dot{z}(t)\right] dt \tag{2.2}$$

  along each path and find the phase difference

$$\Delta\phi_{\text{path}} \quad = \quad \frac{1}{\hbar}\left(S_{\text{cl}}^B - S_{\text{cl}}^A\right) . \tag{2.3}$$

- For each path add up the additional phase shifts due to the interactions with the light fields (see Table 2.1) and find the phase difference

$$\Delta\phi_{\text{light}} \quad = \quad \sum_{\text{PathB}} \phi_j^B \; - \; \sum_{\text{PathA}} \phi_i^A . \tag{2.4}$$

- Account for the different initial points by defining the quantity

$$\Delta\phi_{\text{splitting}} \quad = \quad \frac{p_0(z_0^B - z_0^A)}{\hbar} . \tag{2.5}$$

- Calculate the total phase difference as

$$\Delta\phi_{\text{total}} \quad = \quad \Delta\phi_{\text{path}} \quad + \quad \Delta\phi_{\text{light}} \quad + \quad \Delta\phi_{\text{splitting}} \, . \tag{2.6}$$

For a gravitational field with a linear gradient, the Lagrangian is given by

$$\mathcal{L} = \tfrac{m}{2}\dot{z}^2 - mg_0 z + \tfrac{m}{2}\gamma z^2 \, , \tag{2.7}$$

where z denotes altitude and the signs for acceleration g_0 and gradient γ are chosen to be positive for normal conditions (objects accelerate downwards, magnitude of acceleration decreases with increasing z).

Solving the Euler–Lagrange equation we find the exact classical path for initial position z_0 and velocity v_0:

$$z(t) \quad = \quad \frac{g_0}{\gamma} + \left(z_0 - \frac{g_0}{\gamma}\right)\cosh\left(t\sqrt{\gamma}\right) + \frac{v_0}{\sqrt{\gamma}}\sinh\left(t\sqrt{\gamma}\right)$$

$$\dot{z}(t) \quad = \quad \sqrt{\gamma}\left(z_0 - \frac{g_0}{\gamma}\right)\sinh\left(t\sqrt{\gamma}\right) + v_0\cosh\left(t\sqrt{\gamma}\right) \tag{2.8}$$

When expanding to second order in the gradient γ we regain the well known parabolic motion for constant acceleration plus some corrections for the gradient:

$$z(t) \quad = \quad \left(z_0 + v_0 t - \tfrac{1}{2}g_0 t^2\right) + \gamma t^2\left(\tfrac{1}{2}z_0 + \tfrac{1}{6}v_0 t - \tfrac{1}{24}g_0 t^2\right) + \cdots \tag{2.9}$$

$$\dot{z}(t) \quad = \quad (v_0 - g_0 t) + \gamma t\left(z_0 + \tfrac{1}{2}v_0 t - \tfrac{1}{6}g_0 t^2\right) + \cdots \, . \tag{2.10}$$
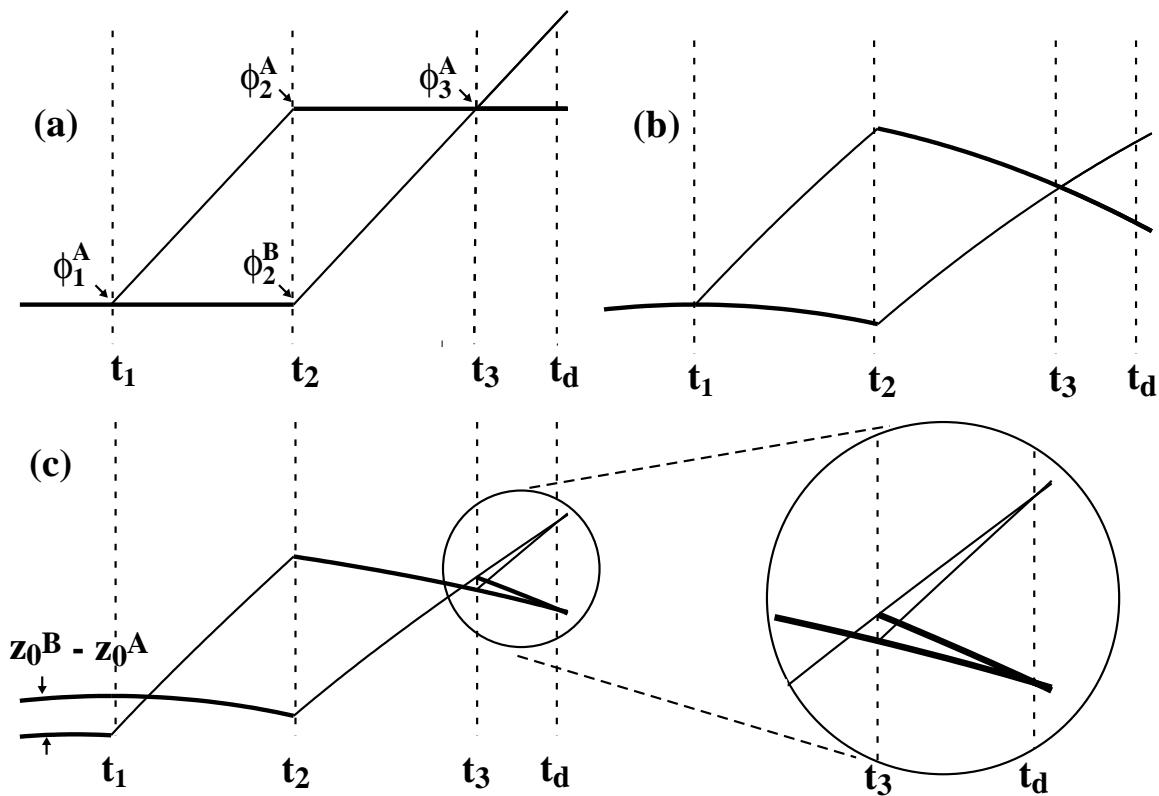
Figure 2.2: Classical interferometer paths. (a) No gravitational field, linear trajectories. (b) Uniform gravitational field, parabolic trajectories. After the final beam splitter pulse at time t_3 both paths overlap exactly, for both possible outcomes. (c) Gravitational field with linear gravity gradient, hyperbolic trajectories. Interference at time t_d demands different initial positions at time t_1.

Following the above algorithm outlined in equations 2.2–2.6 we have obtained an exact analytical solution using computer algebra. Here we present only the first few terms of its power series expansion in the gradient γ:

$$
\begin{aligned}
\Delta\phi_{\text{total}} \;=\;& \left(mv_{\text{rec}}T^2/\hbar\right)g_0 \\
+\;& \gamma\left(mv_{\text{rec}}T^2/\hbar\right)\left(\tfrac{7}{12}\,g_0T^2 - \bar{v}_0T - z_0\right) \\
+\;& \gamma^2 T^2\left(mv_{\text{rec}}T^2/\hbar\right)\left(\tfrac{31}{360}\,g_0T^2 - \tfrac{1}{4}\,\bar{v}_0T - \tfrac{7}{12}\,z_0 - \tfrac{1}{2}\,v_{\text{rec}}T - \tfrac{1}{2}\,v_{\text{rec}}T_{det}\right) \\
+\;& \cdots .
\end{aligned}
\tag{2.11}
$$

We may rewrite this as

$$
\begin{aligned}
g_{\text{meas}} \;=\;& g_0 \\
+\;& \gamma\quad\left\{\tfrac{7}{12}\,g_0T^2 - \bar{v}_0T - z_0\right\} \\
+\;& \gamma^2 T^2\left\{\tfrac{31}{360}\,g_0T^2 - \tfrac{1}{4}\,\bar{v}_0T - \tfrac{7}{12}\,z_0 - \tfrac{1}{2}\,v_{\text{rec}}T - \tfrac{1}{2}\,v_{\text{rec}}T_{det}\right\} \;+\; \cdots
\end{aligned}
\tag{2.12}
$$

if we define the measured gravity value $g_{\text{meas}} = \Delta\phi/(mv_{\text{rec}}T^2/\hbar)$ which equals the actual gravity value g_0 when there is no gravity gradient.

In these equations T is the time interval separating the interferometer pulses, T_{det} is time delay between the final pulse and the actual detection of the atomic state and t_0 denotes the time of the first pulse. The quantities z_0 and v_0 are the initial position[*] and velocity of the classical paths, g_0 is the local gravity value at z_0. The recoil velocity $v_{\text{rec}} = \hbar k_{\text{eff}}/m$ is directly proportional to the effective wave vector of the Raman beams and also determines the maximum separation of the two interferometer paths. To simplify the equations slightly, and for additional reasons that will become clear later, we also introduce the average velocity $\bar{v}_0 = v_0 + \tfrac{1}{2}v_{\text{rec}}$ of the two different paths just after the first Raman pulse.

An interesting feature of this result is that the phase shift depends on the detection delay $T_{det} = t_d - t_3$. This comes about because the separation of the two path's initial points z_0^A and z_0^B (see algorithm and Fig. 2.2) is a function of T_{det}. However, for typical experimental parameters (see Sec. 2.1.4) the separation is only 1.7 Å and the effect is extremely small ($< 10^{-16}$ g).

---

[*]The two paths may have slightly different initial positions. In that case we use z_0^B.

2.1.2   Perturbative treatment

The above treatment is fairly involved mathematically and is therefore rarely used. Instead, one generally uses a much simpler perturbative path integral approach to calculate the interferometer phase shift.

Let us assume that we already know the interferometer phase difference for a certain field configuration and just want to calculate the change due to an additional field. As long as this additional field is sufficiently small, it should be possible to use the following method:

- We already know the interferometer phase difference $\Delta\phi^{(0)}_{\text{total}}$ and classical paths $\Gamma^{(0)}$ for a system with Lagrangian $\mathcal{L}_0$.

- Introduce the additional field as a perturbation to the Lagrangian ($\epsilon \ll 1$):

$$\mathcal{L} \quad = \quad \mathcal{L}_0 + \epsilon\mathcal{L}_1 \tag{2.13}$$

- Integrate the perturbing Lagrangian along the *unperturbed* paths $\Gamma^{(0)}$ to calculate the first order phase correction:

$$\Delta\phi^{(1)}_{\text{total}} \quad = \quad \frac{\epsilon}{\hbar}\left(\int_{\Gamma^{(0)}_B}\mathcal{L}_1\,dt \;-\; \int_{\Gamma^{(0)}_A}\mathcal{L}_1\,dt\right) \tag{2.14}$$

- The new interferometer phase difference is approximately

$$\Delta\phi_{\text{total}} \quad = \quad \Delta\phi^{(0)}_{\text{total}} + \Delta\phi^{(1)}_{\text{total}} \tag{2.15}$$

There are actually two different ways to perform the perturbative calculation. One might first treat both the gradient *and* the constant field as perturbations. In this case the perturbation Lagrangian $\mathcal{L}_1 = -mg_0 z + \frac{m}{2}\gamma z^2$ is integrated along straight paths to obtain the complete phase shift. But the result,

$$g_{\text{meas}} \quad = \quad g_0 \quad - \quad \gamma\{\bar{v}_0 T + z_0\} \quad, \tag{2.16}$$

does not agree with the previous one, not even to first order. It is actually wrong if $g_0 T$ is bigger or comparable to $\bar{v}_0$. This is not totally unexpected, since the gravity induced changes in the trajectories of slow atoms are dramatic and large compared to other relevant size scales, like the path separation. Considering gravity a "small" perturbation is therefore

quite implausible and it is rather surprising that this method gives the correct result for constant gravitational fields [23].

A better approach is to treat only the gravitational gradient as a perturbation on top of a constant gravitational field. This means that we integrate the perturbation Lagrangian $\mathcal{L}_1 = \frac{m}{2}\gamma z^2$ along "unperturbed" paths which are the parabolic free fall trajectories in a constant gravitational field. The resulting phase shift is then combined with the known contribution for the constant gravitational field. This way we find

$$g_{\text{meas}} \quad = \quad g_0 \quad + \quad \gamma\Big\{\tfrac{7}{12}\,g_0 T^2 - \bar{v}_0 T - z_0\Big\} \quad , \tag{2.17}$$

which replicates the exact path integral result from above up to first order.

2.1.3 Classical description

The terms up to first order in equations 2.12 and 2.11 do not depend on the recoil velocity (i.e., the separation of the two interferometer arms), the mass of the atom or Planck's constant. One might argue that the phase shift $\Delta\phi_{\text{tot}}$, given by equation 2.12, is the relevant quantity and that it *does* depend on all these parameters through the scale factor $mv_{\text{rec}}T^2/\hbar$. However, this is merely an illusion, since we can use the definition $v_{\text{rec}} = \hbar k_{\text{eff}}/m$ of the recoil velocity to rewrite this scale factor in terms of the parameters we control experimentally, i.e., Raman wave vector and pulse timing. It then takes the form $k_{\text{eff}}T^2$.

This is very interesting, since it suggests that this type of measurement is not intrinsically "quantum mechanical" [†]. Consider the limit of infinite mass m: The separation between the interferometer arms goes to zero, the deBroglie wavelength gets arbitrarily short and the particle essentially behaves in a totally classical manner — but the measured phase shift remains unaffected.

All this means that for most practical purposes there is a much simpler way of predicting the measured phase shift. We can simply ignore the quantum nature of the atom and model it as a classical point particle that carries an internal clock and can measure the local phase of the light field. Then we can calculate the phase shift using the following algorithm:

[†]The same is true for gravity measurements performed by single crystal neutron interferometers. Although in this case the phase shift is usually expressed as $\Delta\phi = g\frac{m}{\hbar}A_{\text{phasespace}}$, it can be rewritten as $\Delta\phi = gk_{\text{lat}}\left(\frac{\Delta x}{v_0}\right)^2$ in terms of the experimentally controlled parameters lattice wave vector k_{lat}, distance Δx between the three portions of the silicon crystal acting as beam splitters, and initial neutron velocity.

- Calculate the classical path $z(t)$ of the particle for initial position z_0 and initial velocity v_0 (not affected by light pulses).

- At times t_1, t_2 and t_3, separated by intervals T, calculate the local phase ϕ_i of the light field at the position of the atom. If the Raman laser frequencies are constant we have $\phi_i = k_{\text{eff}} z(t_i) - \omega_{\text{eff}} t_i - \phi_0$

- Obtain the interferometer phase shift as $\Delta\phi = \phi_3 - 2\phi_2 + \phi_1$.

- Define measured gravity as $g_{\text{meas}} = \Delta\phi / k_{\text{eff}} T^2$

If we think of light field as a ruler with graduations spaced λ_{eff} apart, then it becomes clear that this essentially mimics the procedure one would follow to determine gravity with just three position measurements:

- Calculate the classical path $z(t)$ of the particle for initial position z_0 and initial velocity v_0.

- At times t_1, t_2 and t_3, separated by intervals T, measure the position $z_i = z(t_i)$ of the atom.

- Define measured gravity as $g_{\text{meas}} = (z_3 - 2z_2 + z_1)/T^2$

In the case of a linear gravity gradient (using equation 2.8 for $z(t)$) both methods give us [‡]

$$g_{\text{meas}} \quad = \quad \frac{4}{T^2\gamma} \left[(g_0 - z_0\gamma)\cosh\left(T\sqrt{\gamma}\right) - v_0\sqrt{\gamma}\sinh\left(T\sqrt{\gamma}\right) \right] \sinh^2\left(\frac{T\sqrt{\gamma}}{2}\right). \quad (2.18)$$

The resulting power series expansion,

$$g_{\text{meas}} \quad = \quad g_0 \quad + \quad \gamma \quad \left\{ \tfrac{7}{12}g_0 T^2 - v_0 T - z_0 \right\} \\ \qquad\qquad + \quad \gamma^2 T^2 \left\{ \tfrac{31}{360}g_0 T^2 - \tfrac{1}{4}v_0 T - \tfrac{7}{12}z_0 \right\} \quad + \quad \cdots \; , \qquad (2.19)$$

is identical to the one (Eq. 2.11) obtained using the exact path integral method if we substitute v_0 for $\bar{v}_0$ and neglect the v_{rec} term (or, in other words, take the limit of infinite mass m).

[‡]For the symmetrical case, where t_0 coincides with the middle pulse instead of the first one, this simplifies to $g_{\text{meas}} = \frac{4}{T^2\gamma}(g_0 - z_0\gamma)\sinh^2\left(\frac{T\sqrt{\gamma}}{2}\right)$.

2.1.4 Comparison

We have presented three methods which all agree up to first order. This poses the obvious question whether the higher order terms are at all relevant for our experiment. To answer it, we evaluate Eq. 2.12 for the typical experimental parameters

$$g_0 \simeq 9.8 \,\text{m/s}^2, \quad \gamma \simeq 2.9 \times 10^{-6} \,1/\text{s}^2, \quad v_{\text{rec}} \simeq 7.0 \times 10^{-3} \,\text{m/s},$$

$$\bar{v}_0 \simeq 1.57 \,\text{m/s}, \quad x_0 \simeq 0 \,\text{m}, \quad T \simeq 0.16 \,\text{s}, \quad T_{det} \simeq 0.16 \,\text{s}$$

and find

$$g^{(1)} = 3.1 \times 10^{-8} \, g_0, \quad g^{(2)} = 9.2 \times 10^{-16} \, g_0, \quad g^{(3)} = 1.9 \times 10^{-24} \, g_0,$$

where $g^{(n)}$ denotes the n–th order term in γ. At our targeted accuracy of $10^{-9}\,$g we can therefore safely neglect terms of second order and higher.

Given this result, are there any circumstances under which one of the three methods should be prefered? The "exact" path integral method seems to be safest approach, but is obviously relatively complicated and also not well suited to deal with finite length light pulses.

The classical method, on the other hand, is especially easy to adapt for such finite length pulses (see below). However, one can expect trouble for more complicated field distributions which lead to forces that are substantially different for the two interferometer paths. Such problems would become even worse for interferometers with bigger separations between paths, and the method would be particularly unsuited for situations where material objects are placed between the two paths. Obviously, the method would also fail to describe any topological phases, for example due to Aharanov–Bohm or Aharanov–Cashier effects.

The perturbation method also has problems in incorporating finite length pulses. Otherwise, it seems to be applicable even under all the problematic circumstances mentioned above, as long as the fields involved are not to big. However, while Storey and Cohen-Tannoudji give very good arguments for the validity of this method under most circumstances, they do not *explicitly* justify its use when combined with the rules for light field interaction. It is certainly not *a priori* clear how integrating over the perturbation Lagrangian compensates for ignoring any changes in the atomic position during the laser pulses. As long as these points are not addressed, some caution remains necessary when applying this method to high precision measurements.

2.2   Finite length Raman pulses

In the previous section we have shown that we can get excellent phase shift predictions using a purely classical method. We do this by effectively assuming an infinite particle mass, allowing us to treat the external degrees of freedom classically. Furthermore, we ignore all the quantum mechanical details related to the internal degrees of freedom by simply summarizing their effect as the ability to measure time, make phase measurements and combine them into a final phase shift.

It is actually not necessary to make both simplifications at the same time. In fact, treating just the internal degrees of freedom quantum mechanically will give us a lot of additional insight into how the interferometer works under less idealized conditions: Presence of AC–Stark shifts as well as finite duration light pulses of variable length, intensity, detuning and chirp rate.

2.2.1   Bloch equations

To analyze the effect of using finite length Raman pulses we use a modified Bloch vector method. We start by modeling the stimulated Raman process as an effective transition between the two atomic ground states, $|a\rangle$ and $|b\rangle$. The justification for this approach, which involves adiabatic elimination of the intermediate states, can be found elsewhere [17, 14, 24]. We now summarize the most important definitions from the paper by Weiss *et.al.* [14] for use in our own analysis and elsewhere in this thesis.

To analyze this situation we could in principle work directly with the internal atomic states and try to solve the appropriate time dependent Schrödinger equation. However, we find it slightly more convenient to work with the optical Bloch equations. We furthermore ignore the exited states of the atom, skip the explicit treatment of the Raman process (see for example Weiss et. al., [14]) and model it simply as an effective transition between the two atomic ground states, $|a\rangle$ and $|b\rangle$.

The effective 2–photon Rabi frequency and detuning,

$$\Omega_0 = \sum_i \frac{\Omega_{1ai}^* \Omega_{2bi}}{2\Delta_{1ai}}, \tag{2.20}$$

$$\delta = (\omega_1 - \omega_2) - \left(\omega_{ab} + \frac{\mathbf{p} \cdot \mathbf{k_{eff}}}{m} + \frac{\hbar k_{eff}^2}{2m}\right) \tag{2.21}$$
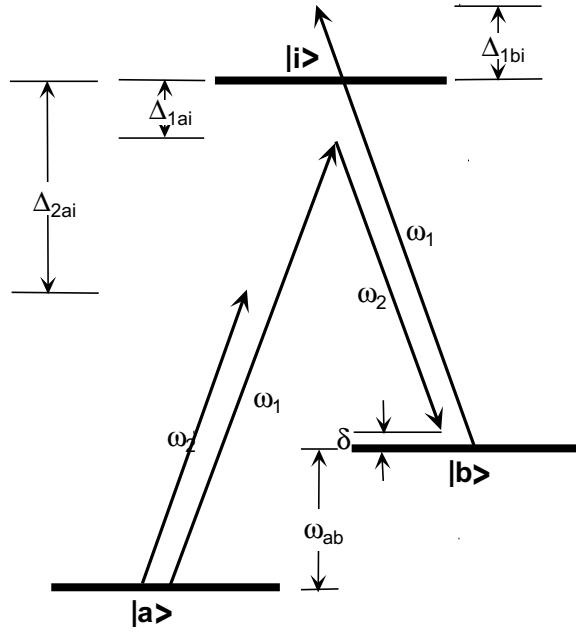
Figure 2.3: Level scheme for stimulated Raman transitions.

can be defined in terms of the 1–photon Rabi frequencies and detunings,

$$\Omega_{kji} \;=\; \frac{\langle j|\hat{\mathbf{d}}\cdot\mathbf{E}_k|i\rangle}{\hbar}\;, \tag{2.22}$$

$$\Delta_{kji} \;=\; \omega_k - (\omega_i - \omega_j) + \frac{\mathbf{p}_j^2}{2m\hbar} - \frac{|\mathbf{p}_j + \mathbf{k}_k|^2}{2m\hbar}\;. \tag{2.23}$$

In all these equations k is index for the light field, i for the excited states, and j for the two ground states. Fig. 2.3 illustrates the level scheme. The effective frequency, phase and wave vector are defined as

$$\omega_{\text{eff}} \;=\; \omega_2 - \omega_1, \qquad \phi_{\text{eff}} \;=\; \phi_2 - \phi_1, \qquad \mathbf{k}_{\text{eff}} \;=\; \mathbf{k}_2 - \mathbf{k}_1 \tag{2.24}$$

$$(\; |\mathbf{k}_{\text{eff}}| \;=\; |\mathbf{k}_2| + |\mathbf{k}_1| \quad \text{for counterpropagating beams }\;)$$

and the average and differential AC–Stark shifts are

$$\delta_{\text{avg}}^{\text{AC}} \;=\; (\Omega_b^{\text{AC}} + \Omega_a^{\text{AC}})/2\,, \qquad \delta_{\text{diff}}^{\text{AC}} \;=\; \Omega_b^{\text{AC}} - \Omega_a^{\text{AC}}\,, \tag{2.25}$$

with

$$\Omega_j^{\text{AC}} \;=\; \sum_{k,i} \frac{|\Omega_{kji}|^2}{4\Delta_{kji}}\;. \tag{2.26}$$

As a convenient way to describe the state of the effective 2–level system we use the interaction picture density matrix ρ, defined by

$$|\psi\rangle\langle\psi| \;=\; \rho_{\mathrm{aa}}|a\rangle\langle a| \;+\; \rho_{\mathrm{bb}}|b\rangle\langle b| \;+\; \rho_{\mathrm{ab}}|a\rangle\langle b| \;+\; \rho_{\mathrm{ba}}|b\rangle\langle a| \,. \tag{2.27}$$

The density matrix evolves according to

$$i\hbar\dot\rho \;=\; \mathcal{H}^I\rho - \rho\mathcal{H}^I \,, \tag{2.28}$$

where the interaction picture Hamiltonian for the effective 2–level system is given by

$$\mathcal{H}^I \;=\; -\tfrac{1}{2}\hbar\Omega_0\left(e^{-i\omega_{\mathrm{eff}}t}\,|a\rangle\langle b| \;+\; e^{i\omega_{\mathrm{eff}}t}\,|b\rangle\langle a|\right)\,. \tag{2.29}$$

We introduce the Bloch vector

$$\tilde{\mathbf{X}} \;=\; \begin{pmatrix} \tilde{U} \\ \tilde{V} \\ \tilde{W} \end{pmatrix} \;=\; \begin{pmatrix} \rho_{\mathrm{ab}} + \rho_{\mathrm{ba}} \\ i\rho_{\mathrm{ba}} - i\rho_{\mathrm{ab}} \\ \rho_{\mathrm{aa}} - \rho_{\mathrm{bb}} \end{pmatrix} \;=\; \begin{pmatrix} 2\,\mathrm{Re}[\rho_{\mathrm{ab}}] \\ 2\,\mathrm{Im}[\rho_{\mathrm{ab}}] \\ \rho_{\mathrm{aa}} - \rho_{\mathrm{bb}} \end{pmatrix}\,. \tag{2.30}$$

For situations where the atom is subjected to external fields of known frequencies it is usually convenient to go into the "rotating frame" by making the transformation

$$\mathbf{X} \;=\; \begin{pmatrix} \cos\varphi(t) & \sin\varphi(t) & 0 \\ -\sin\varphi(t) & \cos\varphi(t) & 0 \\ 0 & 0 & 1 \end{pmatrix}\tilde{\mathbf{X}}\,. \tag{2.31}$$

Usually this is done for a fixed frequency ω_{eff}, in which case the Raman phase is simply given by $\varphi(t) = \omega_{\mathrm{eff}}t$ and the rotating frame is rotating at a fixed rate.

For our experiment, however, the Raman phase in the rest frame of the freely falling atom is affected by the time dependent Doppler shift and is given by

$$\varphi(t) \;=\; \phi_{\mathrm{eff}} \;+\; \int_0^t \left[\omega_{\mathrm{eff}} \;+\; \mathbf{v}(t')\cdot\mathbf{k}_{\mathrm{eff}}\right]dt' \tag{2.32}$$

and the rotating frame therefore has a variable rotation rate.

The evolution of the Bloch vector in the rotating frame is governed by the equation

$$\frac{\partial}{\partial t}\begin{pmatrix} U \\ V \\ W \end{pmatrix} \;=\; \begin{pmatrix} 0 & -\delta(t) & 0 \\ \delta(t) & 0 & \Omega_0 \\ 0 & -\Omega_0 & 0 \end{pmatrix}\begin{pmatrix} U \\ V \\ W \end{pmatrix}\,, \tag{2.33}$$

which follows from Eq. 2.29. Note that this equation is valid for arbitrary time dependence of the effective detuning $\delta(t)$. However, we are specifically interested in the case of a linear "chirp" introduced by the Doppler shift of the accelerating atom. We then have $\delta(t) = \delta_0 + \alpha t$, where α is the "chirp rate".

2.2.2   Time dependent perturbation theory

For constant detuning it is straight forward to solve equation 2.33 exactly [25, 26]. For a constant chirp it is also possible to find an exact solution in terms of parabolic cylinder functions [19]. However, since in our experiment detuning and chirp are both small, we treat them using time dependent perturbation theory. We first rewrite equation 2.33 in matrix form:

$$\frac{\partial}{\partial t}\mathbf{X} \;=\; \mathbf{MX}+\mathbf{VX}, \quad \mathbf{M} = \begin{pmatrix} 0 & 0 & 0 \\ 0 & 0 & \Omega_0 \\ 0 & -\Omega_0 & 0 \end{pmatrix}, \quad \mathbf{V} = \begin{pmatrix} 0 & -\delta(t) & 0 \\ \delta(t) & 0 & 0 \\ 0 & 0 & 0 \end{pmatrix}. \tag{2.34}$$

We then use the unperturbed solution

$$\mathbf{X}(t) \;=\; e^{\mathbf{M}t}\,\mathbf{X}(0) \qquad \text{with} \qquad e^{\mathbf{M}t} \;=\; \begin{pmatrix} 1 & 0 & 0 \\ 0 & \cos\Omega_0 t & \sin\Omega_0 t \\ 0 & -\sin\Omega_0 t & \cos\Omega_0 t \end{pmatrix} \tag{2.35}$$

to go into a new interaction picture by making the transformations

$$\mathbf{X}^I \;=\; e^{-\mathbf{M}t}\,\mathbf{X} \qquad \text{and} \qquad \mathbf{V}^I \;=\; e^{-\mathbf{M}t}\,\mathbf{V}\,e^{\mathbf{M}t}\,. \tag{2.36}$$

Finally, we can write down the perturbation expansion

$$\mathbf{X}^I(t) \;=\; \mathbf{X}^I(0) \;+\; \int_0^t\! dt'\,\mathbf{V}^I(t')\mathbf{X}^I(0) \;+\; \int_0^t\! dt'\!\int_0^{t'}\! dt''\,\mathbf{V}^I(t')\mathbf{V}^I(t'')\mathbf{X}^I(0) \;+\cdots. \tag{2.37}$$

We can use this formalism to describe a finite length, chirped Raman pulse with $\delta(t) = \delta_0 + \alpha t$. The Bloch vector (in the original rotating frame) is then given by

$$\mathbf{X}(\tau) \;=\; \mathbf{X}^{(0)}(\tau) \;+\; \mathbf{X}^{(1)}(\tau) \;+\; \mathbf{X}^{(2)}(\tau) \;+\;\cdots \tag{2.38}$$

with the zero order terms

$$\begin{aligned} U^{(0)}(\tau) &= U(0) \\ V^{(0)}(\tau) &= \cos\Omega_0\tau\,V(0) \;+\; \sin\Omega_0\tau\,W(0) \\ W^{(0)}(\tau) &= -\sin\Omega_0\tau\,V(0) \;+\; \cos\Omega_0\tau\,W(0) \end{aligned} \tag{2.39}$$

and the first order terms

$$
\begin{aligned}
U^{(1)}(\tau) &= \left\{ \frac{\alpha}{\Omega_0^2}\left(1 - \cos\Omega_0\tau\right) - \frac{\alpha\tau}{\Omega_0}\sin\Omega_0\tau - \frac{\delta_0}{\Omega_0}\sin\Omega_0\tau \right\} V(0) \\
&+ \left\{ -\frac{\alpha}{\Omega_0^2}\sin\Omega_0\tau + \frac{\alpha\tau}{\Omega_0}\cos\Omega_0\tau - \frac{\delta_0}{\Omega_0}\left(1 - \cos\Omega_0\tau\right) \right\} W(0) \\
V^{(1)}(\tau) &= \left\{ \frac{\alpha}{\Omega_0^2}\left(1 - \cos\Omega_0\tau\right) + \frac{\delta_0}{\Omega_0}\sin\Omega_0\tau \right\} U(0) \\
W^{(1)}(\tau) &= \left\{ \frac{\alpha}{\Omega_0^2}\sin\Omega_0\tau - \frac{\alpha\tau}{\Omega_0} - \frac{\delta_0}{\Omega_0}\left(1 - \cos\Omega_0\tau\right) \right\} U(0)
\end{aligned}
\tag{2.40}
$$

We can combine these terms and describe the special cases of a $\frac{\pi}{2}$-pulse $(\Omega_0\tau = \pi/2)$

$$
\begin{aligned}
U_{\frac{\pi}{2}} &= U(0) \;+\; \left\{ \frac{\alpha}{\Omega_0^2} - \frac{\delta(\tau)}{\Omega_0} \right\} V(0) \;-\; \left\{ \frac{\alpha}{\Omega_0^2} + \frac{\delta(0)}{\Omega_0} \right\} W(0) \\
V_{\frac{\pi}{2}} &= \left\{ \frac{\alpha}{\Omega_0^2} + \frac{\delta(0)}{\Omega_0} \right\} U(0) \;+\; W(0) \\
W_{\frac{\pi}{2}} &= \left\{ \frac{\alpha}{\Omega_0^2} - \frac{\delta(\tau)}{\Omega_0} \right\} U(0) \;-\; V(0)
\end{aligned}
\tag{2.41}
$$

or a π-pulse $(\Omega_0\tau' = \pi)$

$$
\begin{aligned}
U_\pi &= U(0) \;+\; \left\{ \frac{2\alpha}{\Omega_0^2} \right\} V(0) \;-\; \left\{ \frac{\delta(0)}{\Omega_0} + \frac{\delta(\tau')}{\Omega_0} \right\} W(0) \\
V_\pi &= \left\{ \frac{2\alpha}{\Omega_0^2} \right\} U(0) \;-\; V(0) \\
W_\pi &= \left\{ \frac{\delta(0)}{\Omega_0^2} + \frac{\delta(\tau')}{\Omega_0} \right\} U(0) \;-\; W(0)
\end{aligned}
\tag{2.42}
$$

In the periods of free evolution between pulses the atomic state evolves according to

$$
\begin{aligned}
U(T) &= \cos\bar{\delta}T \; U(0) \;+\; \sin\bar{\delta}T \; V(0) \\
V(T) &= -\sin\bar{\delta}T \; U(0) \;+\; \cos\bar{\delta}T \; V(0) \\
W(T) &= W(0)
\end{aligned}
\tag{2.43}
$$

where T is the length of the time interval and

$$
\bar{\delta} = \frac{1}{T}\int_{t_0}^{t_0+T} \delta(t)\,dt \qquad \left(\bar{\delta} = \delta(t_0) + \frac{\alpha T}{2} \quad \text{for a linear chirp} \right)
\tag{2.44}
$$

the average detuning during the free evolution.

A Ramsey sequence consists of two $\frac{\pi}{2}$–pulses of length τ, separated by a time interval T. We can calculate its effect on the atomic state by first applying Eq. 2.41, then Eq. 2.43 and finally Eq. 2.41 a second time. The result is

$$
\begin{aligned}
U_{\text{Ramsey}} \;=\; & U(0)\left[\cos\bar{\delta}T - \frac{2\bar{\delta}}{\Omega_0}\sin\bar{\delta}T\right] \\
+ \;& V(0)\left[\left\{\frac{\alpha}{\Omega_0^2} - \frac{\delta(\tau)}{\Omega_0}\right\}\cos\bar{\delta}T + \left\{\frac{\alpha}{\Omega_0^2} + \frac{\delta(T+\tau)}{\Omega_0}\right\}\right] \\
+ \;& W(0)\left[-\frac{2\bar{\delta}}{\Omega_0}\cos\bar{\delta}T - \sin\bar{\delta}T\right] \\[1em]
V_{\text{Ramsey}} \;=\; & U(0)\left[\left\{\frac{\alpha}{\Omega_0^2} + \frac{\delta(T+\tau)}{\Omega_0}\right\}\cos\bar{\delta}T + \left\{\frac{\alpha}{\Omega_0^2} - \frac{\delta(\tau)}{\Omega_0}\right\}\right] \\
- \;& V(0) \\
- \;& W(0)\left[\left\{\frac{\alpha}{\Omega_0^2} + \frac{\delta(T+\tau)}{\Omega_0}\right\}\sin\bar{\delta}T\right] \\[1em]
W_{\text{Ramsey}} \;=\; & U(0)\left[-\frac{2\bar{\delta}}{\Omega_0}\cos\bar{\delta}T - \sin\bar{\delta}T\right] \\
- \;& V(0)\left[\left\{\frac{\alpha}{\Omega_0^2} - \frac{\delta(\tau)}{\Omega_0}\right\}\sin\bar{\delta}T\right] \\
- \;& W(0)\left[\cos\bar{\delta}T - \frac{2\bar{\delta}}{\Omega_0}\sin\bar{\delta}T\right]
\end{aligned}
\tag{2.45}
$$

2.2.3 Interferometer sequence

We can now calculate the atomic state after the $\frac{\pi}{2}$–π–$\frac{\pi}{2}$ atom interferometer sequence. We model it as two back–to–back Ramsey sequences to reflect the inherent symmetry of the situation (modeling it as three individual pulses gives the same result).
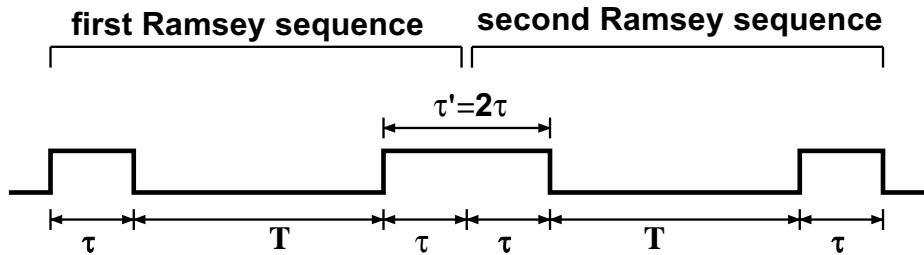
Figure 2.4: Interferometer pulse sequence.

Assume $W_0 = 1$, $U_0 = V_0 = 0$ at $t = 0$. Using Eq. 2.45 twice we then find the final atomic inversion

$$
\begin{aligned}
W_{\frac{\pi}{2}-\pi-\frac{\pi}{2}} &= \cos{(\bar{\delta}_b - \bar{\delta}_a)T} - \frac{2(\bar{\delta}_b - \bar{\delta}_a)}{\Omega_0} \sin{(\bar{\delta}_b - \bar{\delta}_a)T} && (2.46) \\
&= \cos{[\alpha(T + 2\tau)T]} - \frac{2\alpha(T + 2\tau)}{\Omega_0} \sin{[\alpha(T + 2\tau)T]} \\
&\approx \cos{\left[(\bar{\delta}_b - \bar{\delta}_a)\left(1 + \frac{2\tau}{\pi T}\right)T\right]} \quad \approx \quad \cos{\left[\alpha T^2 \left(1 + \frac{2\tau}{T} + \frac{2\tau}{\pi T}\right)\right]}
\end{aligned}
$$

where $\bar{\delta}_a$ and $\bar{\delta}_b$ are the average detunings during the first and second interval of free evolution (see Eq. 2.44).

In the case of infinitely short pulses ($\tau \to 0$, $\Omega_0 \to \infty$, $\Omega_0 \tau = $ const.) and for a constant gravitational field ($\alpha = k_{\mathrm{eff}} g$) this simplifies to

$$
W_{\frac{\pi}{2}-\pi-\frac{\pi}{2}} \quad = \quad \cos{[\alpha t^2]} \quad = \quad \cos{[k_{\mathrm{eff}} g T^2]}, \tag{2.47}
$$

and we recover the previously known result. For finite length pulses equation 2.46 indicates that the periodicity of the interferometer signal is now generally given by $(T+2\tau)T$ instead of T^2 and that there are further modifications because of the sine term in Eq. 2.46.

These changes would normally complicate the interpretation of the interferometer signal. In the actual experiment, however, this problem is significantly reduced because we compensate for most of the acceleration induced Doppler shift by changing the frequency ω_{eff} (see Sec. 3.4.2).

Chapter 3

Experimental Apparatus

The overall experimental apparatus (Fig. 3.1) can be divided in three subsystems:

(a) The atomic fountain apparatus, which provides a well defined source of laser cooled atoms for the interferometer. It also allows the detection of the final state of the atoms at the output of the interferometer.

(b) The system for implementing the actual light pulse interferometer, including the phase-locked diode lasers and the equipment for controlling the frequency and timing of the Raman pulses. Other components are the Raman beam optics and the magnetic shielding of the measurement region.

(c) The vibration isolation system, which allows the large interferometer pulse separations essential for obtaining our current measurement accuracy and precision. Another part of this system controls the tilt of optical table to guarantee the proper vertical alignment of the measurement axis.

3.1 Vacuum system

3.1.1 Main chamber

The experiment is performed inside vacuum chamber (manufactured by Nor-Cal products) made from type 304 stainless steel (Fig. 3.2). At its core is a 6-way cross with 6 inch diameter Conflat viewports, which has been mounted with the axis of 3-fold symmetry (1,1,1 - axis) in the vertical direction. Twelve additional Conflat ports (two 6 inch ports along the vertical axis, six 4–1/2 inch ports along the remaining 1,1,1-axes, four 2–3/4 inch
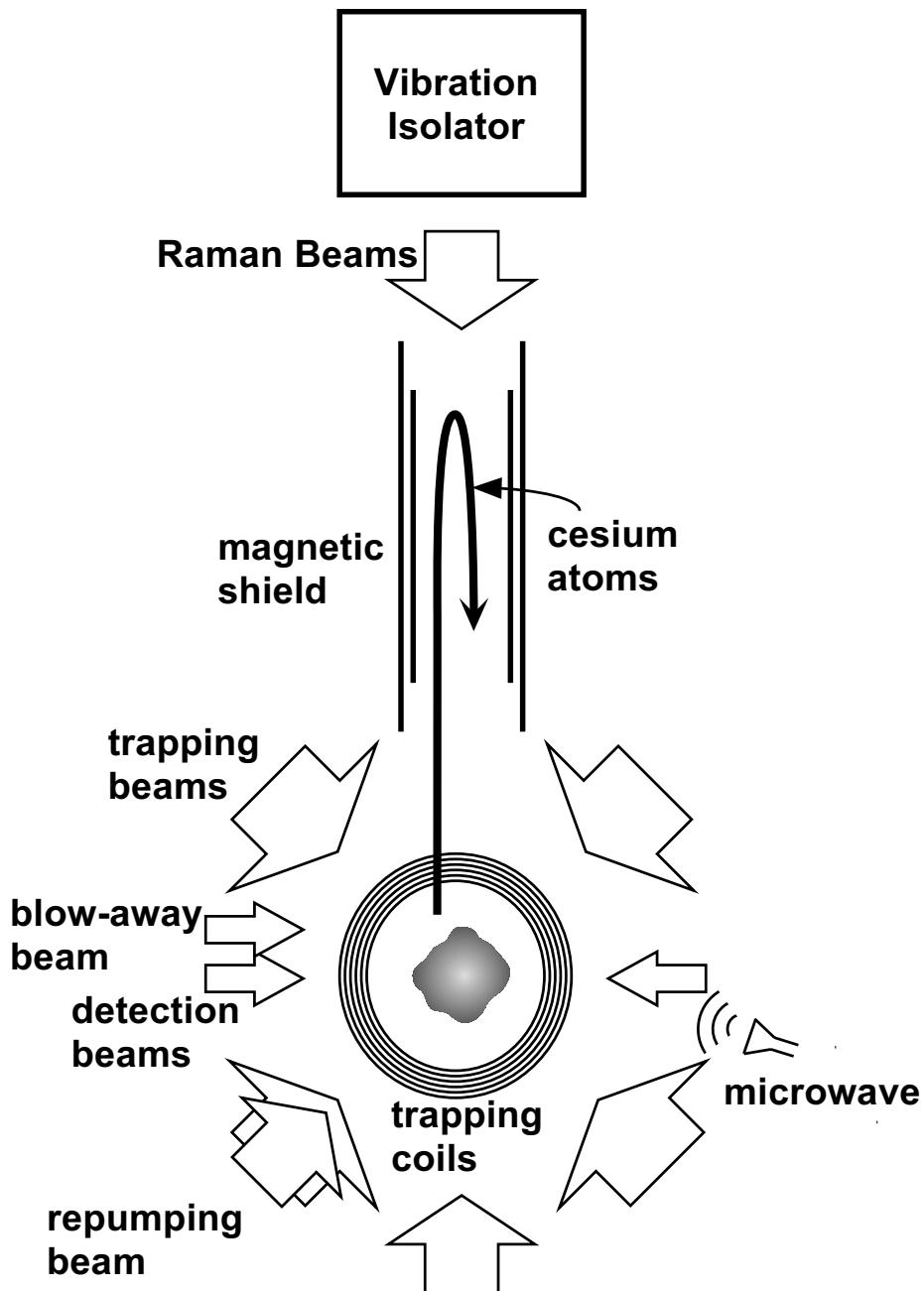
Figure 3.1: Overview of experimental setup.

ports in same plane as four of the original ports) have been added to this cross and mostly fitted with viewports to provide better optical access. Two of the 4–1/2 inch ports are used to attach a nude UHV ion-gauge and the vacuum pump, originally a high compression turbo molecular drag pump (56 l/s, Balzers TMU 065), backed by a rotary vane pump (Edwards RV3).

The upper 6 inch port is extended by a 15 inch long tube to make room for the atomic fountain. This tube also contains a four layer magnetic shielding assembly made from Hipernom, which has vacuum properties very similar to stainless steel. Inside this shield is a 11.5 inch long bias field solenoid, wound on an aluminum core and made from ~ 60 m of 1 mm diameter, Kapton coated wire. The whole assembly mounted using several aluminum spacers. The top and the bottom flanges of the vacuum chamber are both fitted with self made, high quality, indium sealed viewports.

3.1.2 Cesium source chamber

One of the main chambers horizontal 2–3/4 inch ports connects, through a gate-valve (MDC GV-1500M), to smaller chamber containing the cesium supply. During normal operation cesium is kept at the flat bottom of a cold finger made from thin wall (0.01 inch) stainless steel. The lower part of the cold finger is surrounded by a copper clamp, which can be cooled to temperatures as low as $-35°$C using a two stage thermo electric cooler ($2 \times$ Melcor CP 1.4-71-045L) and a water cooled heat sink. The cesium source chamber can also be connected to an additional ion pump (8 l/s, Varian RVA-8) and pumped down through a second valve (MDC MAV-150-V). A third valve leads to a thin wall stainless steel tube containing a cesium ampule.

At some point the cesium needs to be transfered from the ampule to the cold finger. First the ampule is crushed by using pliers to deform the thin wall tube containing it. Then the valve to the cold finger is opened and the cesium ampule heated to $\sim 150°$C. After 24 hours a substantial amount of cesium will have deposited at the bottom of the maximally cooled cold finger. There are a few very important precautions to take for a successful transfer: (a) In order to prevent cesium deposition every part of the system, except the cold finger, should be at a temperature higher than that of the oven. This includes the ion pump, since it has many internal surfaces that are not actively pumping! (b) Only the bottom plate of the cold finger should be cooled during transfer and not, as during normal operation, the walls as well. This is necessary because otherwise cesium is deposited in

Figure 3.2: Vacuum system.

regions which will not be sufficiently cold during later operation (this problem is less severe for a material with lower heat conductivity, glass for example). (c) It is advisable to use a standard UHV valve between oven and cold finger. While a less expensive, UHV compatible needle valve (Nupro H series) might work as well, there is a substantial danger of clogging.

3.1.3   Bake out

Because of possible out gassing problems — caused by the Kapton coated wire, graphite coatings and the magnetic shielding assembly — the initial bake out was performed 150° Celsius, with all the indium coated windows replaced by blanks. This resulted in a final pressure of 2.5×10^{-10} torr after 3 weeks of baking. Subsequently, the indium sealed windows were put back in place and a 1 week bake out at 80° proved sufficient to attain the same pressure level.

At some later point the turbo pump was replaced by an ion pump (30 l/s, Varian) because of concerns about vibrations. The lower pumping speed of this pump should have resulted in a base pressure approximately two times higher. This was hard to verify, because at that time cesium had already been introduced to the system and dominated the vapor pressure* Still, measurements of the MOT loading time constant indicate that the base pressure indeed went up by this factor.

3.2   Atomic Fountain

3.2.1   Overview

The atomic fountain provides a pulsed source of cold cesium atoms for the interferometer. The atoms are initially extracted from a low pressure background vapor and loaded into a magneto-optic trap [27, 28]. After 600 ms the trap contains $\sim 5 \times 10^8$ atoms in a ~ 5 mm diameter cloud. They are then launched vertically using moving optical molasses [29], with an initial velocity of ~ 3.0 m/s and on trajectories that will peak ~ 46 cm above the trap. The temperature of the atoms after the launch is ~ 1.5 μK, well below the usual steady state minimum temperature of ~ 2.5 μK [30]. This is achieved by using far detuned, low

---

*Cesium vapor also seems to cause problems with the ion gauge. Not only is the measured cesium pressure a factor 4 to high (according to Varian), but over time the ion gauge performance degrades because of leakage currents, supposedly caused by the formation of a conductive cesium coating.

intensity optical molasses during the last stage of the launch and by ramping down the laser intensity slowly instead of shutting it off instantaneously.

While moving upwards, the atoms are placed in a magnetic bias field and subjected to a sequence of microwave, velocity selective Raman and state selective blow-away pulses. The remaining $\sim 5 \times 10^6$ cesium atoms are in the $6s_{1/2}$, $F = 3$, $m_F = 0$ state and have an substantially reduced vertical velocity spread, corresponding to a 1D-temperature of only ~ 10 nK. This very well defined sample of atoms then enters a magnetically shielded region which encloses the top part of its trajectory and where the actual interferometer measurement takes place.

The interferometer phase shift manifests itself as a modulation of the fraction of atoms in the $F = 4$, $m_F = 0$ state. This fraction is determined, after the atoms have left the magnetic shield and have returned to the location of the original trap, by using normalized fluorescence detection. This detection takes place ~ 600 ms after the launch. Finally, after a short delay, the MOT will turn on again — starting the next measurement cycle exactly 1.3 s after the previous one.

3.2.2   Loading the MOT

The magneto-optic trap (MOT) uses three pairs of counter propagating trapping beams in a 1,1,1-configuration (threefold symmetry around the vertical axis, three beams directed upwards, three downwards), and the trapping coil axis is aligned with one of the pairs. The standard operating field gradient is ~ 6 G/cm. Each trapping beam is circular polarized, 4 cm in diameter ($\frac{1}{e^2}$-intensity contour), has a typical intensity of 15 mW/cm^2 and a frequency which is ~ 20 MHz red detuned from the $6s_{1/2}, F = 4 \leftrightarrow 6p_{3/2}, F = 5$ transition at ~ 852 nm. One of the trapping beams is nearly overlapped with a repumping beam which has an intensity of ~ 1.5 mW/cm^2 and is on resonance with the $6s_{1/2}, F = 3 \leftrightarrow 6p_{3/2}, F = 4$ transition.

Under normal operating conditions (cold finger at $+5°$C, 56 l/s turbo pump) this MOT has a loading time constant of 2.5 s and a steady state population of 3×10^9 atoms, determined by the very reliable method of optically pumping all the atoms from the $F = 4$ into the $F = 3$ state and measuring the total number of photons scattered in the process [28]. The trap diameter is ~ 5 mm, but it is relatively hard to measure because usually the MOT takes on weird shapes when optimized for a cold launch. After the standard loading time of 650 ms the trap contains 6×10^8 atoms.

At some point the 56 l/s turbo pump was replaced with a 30 l/s ion pump. The lower pumping speed resulted in a shorter trap lifetime ($\sim 1.0\,\mathrm{s}$) and an correspondingly smaller number of trapped atoms. In order to compensate the temperature of the cold finger was raised to $+15°$C, resulting in a similar number of atoms trapped after 650 ms of loading.

3.2.3   Launch

The launch process (see timing diagram in Fig. 3.3) begins by shutting off the magnetic field at the end of the loading phase. After a delay of 7 ms, which is necessary to allow magnetic field producing eddy currents to decay away, the main launch sequence starts by down shifting the frequency of the upper three trapping beams (traveling downward) by about $4.0\,\mathrm{MHz}^{†}$. This creates optical molasses in a frame traveling upwards at 3.00 m/s, and the atoms are allowed to accelerate and equilibrate at their new velocity for 2.0 ms. Then the detuning of all the trapping beams is increased to $\sim 60\,\mathrm{MHz}$ and their intensities simultaneously lowered to 1/3 of their original level. After another 0.4 ms the intensities are ramped down to zero over a period of 0.4 ms. During the whole procedure the intensity the repumping light is kept constant, and it is the last to be shut off, 0.2 ms later than the trapping light. This guarantees that all the atoms will be in the $F = 4$ hyperfine state after the launch.
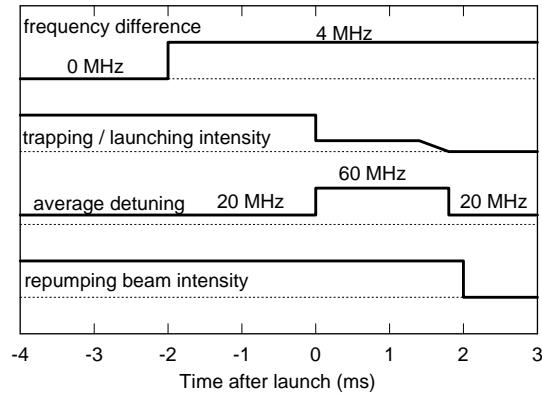
Figure 3.3: Launch sequence.
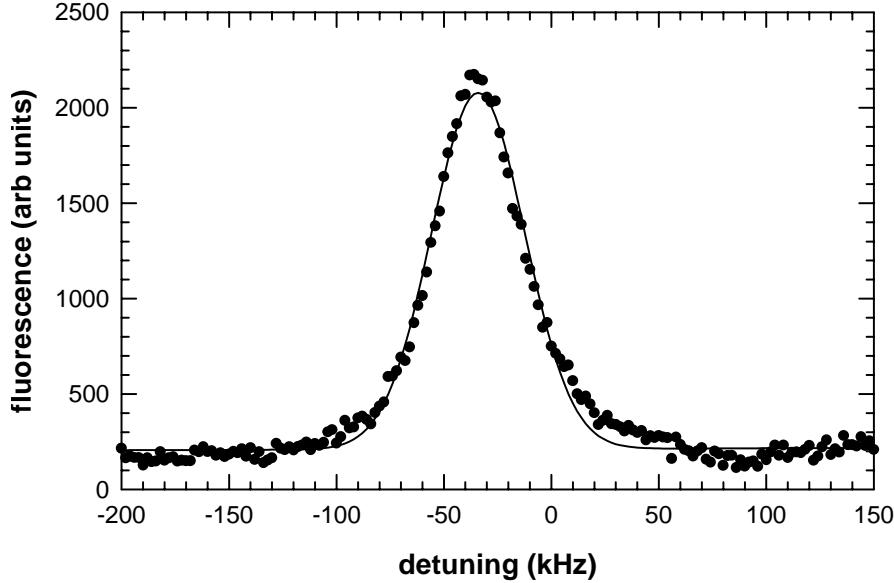
Figure 3.4: Velocity distribution of the atom after launch, measured using velocity sensitive Raman transitions. A Raman detuning of $100\,\mathrm{kHz}$ corresponds to a velocity of $4.25\,\mathrm{cm/s}$. The $1.31\,\mathrm{cm/s}$ $\frac{1}{e}$–width of the Gaussian fit corresponds to a temperature of $1.37\,\mu\mathrm{K}$

The final ramp down of the intensity is essential for achieving the lowest observed temperature of $\sim 1.5\,\mu\mathrm{K}$ (see Fig. 3.4 for temperature measurement). Without it, the temperature is closer to the usual steady state limit of $\sim 2.5\,\mu\mathrm{K}$ [30]. The probable cause of this improvement is adiabatic lowering of the temperature or atoms confined in local potential wells of the light field. Additionally, the temperature is very sensitive to beam alignment — and exactly overlapped and counter propagating beams do *not* give the best result. The best alignment is usually found by a lengthy process of trial and error, and it generally results in a MOT that is not spherical anymore, but rather pancake shaped and compressed along the symmetry axis of trapping coils. This indicates that the optical thickness of the cloud, or the ability of scattered photons to escape easily, might play a role in the process.

Also important is the cancelation of magnetic fields during the launch, which can be achieved using a set of three pairs of large magnetic field coils surrounding the apparatus. Initially, the fields can be zeroed to within a few milli Gauss by taking Zeeman spectra (using either microwave or Raman transitions), but ultimately they are adjusted to achieve the lowest temperature launch.

3.2.4 Preselection

Before the atoms enter the atom interferometer, they still need to be prepared in a well defined initial state. Most importantly, we only want all the atoms to be in a magnetically insensitive state with $m_F = 0$, while originally they are about equally distributed among all 9 possible Zeeman sublevels of the $F = 4$ hyperfine state. Optical pumping would be one option to transfer the atoms to the $m_F = 0$ state [14], but the associated heating prevent us from taking advantage of the benefits afforded by the low initial launch temperature. It is therefore better to just select the atoms already in the $m_F = 0$ state and get rid of the others.

We also would like to narrow down the vertical velocity distribution of the atoms, because this allows us to obtain higher contrast interferometer fringes and simplifies the search for systematic errors: Limited Raman laser power requires relatively long interferometer pulses, which means that their Fourier limited frequency width is not sufficient to address all the atoms in the velocity distribution, because of their Doppler shifts. It would still be possible to operate the interferometer under these conditions, but the contrast would be limited to 28 % [11]. Furthermore, some systematic errors are hard to identify if one always has to average over a wide velocity distribution. The goal is therefore to create an initial velocity distribution that is much narrower then the Fourier width of a typical Raman pulse.
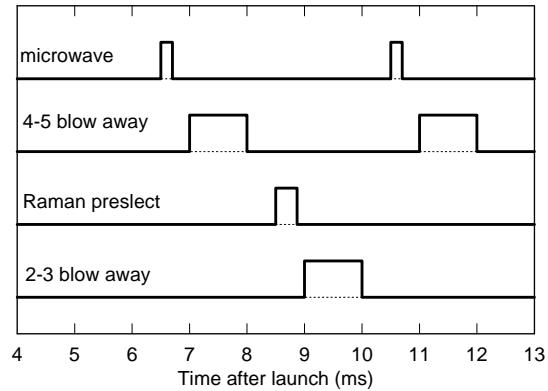
Figure 3.5: Atomic state preparation sequence.

To achieve both these goals, we apply the following procedure involving a rather complex sequence of microwave, velocity selective Raman and state selective blow-away pulses (see timing diagram in Fig. 3.5): First we first define a quantization axis by pulsing on a vertical

magnetic bias field of about $500\,\text{mGauss}$, $2\,\text{ms}$ after the launch (we choose to define the moment of the launch as the time when we switch to low intensity, far detuned optical molasses). At $6.5\,\text{ms}$ we then apply a microwave π-pulse ($\sim 100\,\mu s$ long) to transfer all the atoms in the $F = 4$, $m_F = 0$ state to the $F = 3$, $m_F = 0$ with very high efficiency (typically 98 %). All the other atoms remaining in the $F = 4$ state are then blown away by the scattering force exerted by a $1\,\text{ms}$ long pulse of light in resonance with the $F = 4 \leftrightarrow F = 5$ closed optical transition.

Then a $380\,\mu s$ long, velocity selective Raman π-pulse is applied. It transfers atoms in a narrow slice of the velocity distribution, corresponding to a 1D-temperature of only $\sim 10\,\text{nK}$, back into the $F = 4$, $m_F = 0$ state. Afterwards another blow-away pulse, this time in resonance with the $F = 3 \leftrightarrow F = 2$ closed transition, eliminates the atoms remaining in the $F = 3$ state.

Now we already have a velocity selected sample of atoms in a magnetic field insensitive state. However, because of our detection method we would prefer the atoms to be initially in the $F = 3$, $m_F = 0$ state. In that case we can detect low contrast signals as peaks on essentially zero background, instead of having to look for dips in a large, possibly noisy background signal. The 3–2 blow–away is also not quite as efficient as the 4–5 blow-away, leaving behind a few percent of atoms in the wrong states and velocity classes. Both problems can be easily rectified by using another microwave pulse to transfer the atoms back to the $F = 3$, $m_F = 0$ state, followed by another 4–5 blow–away pulse for clean up.

This whole preselection process reduces the number of atoms by a factor of about 135 (factor 9 from selecting Zeeman level, factor 15 from velocity selection), but this still leaves us with approximately 3×10^6 atoms. Even after taking into account another reduction by a factor of 10, due to selective detection (see below), the remaining 3×10^5 atoms are still enough to not limit the performance of the instrument (see Sec. 5).

At first glance one might argue that this whole, complicate selection sequence could be replaced with a single Raman pulse, which would be velocity as well as magnetic state selective, and a single 4–5 blow away pulse. The problem is, that under normal operating conditions the 1-photon Raman detuning is not large enough to make spontaneous emission totally negligible: A Raman π-pulse will typically transfer a fraction of a percent of the atoms via spontaneous processes, a number small enough to be of no concern under most circumstances. However, in the preselection process only 1 in 350 of the original atoms gets transfered via the proper Raman process. So even a small spontaneous transfer — which

can originate from *all* the original atoms, not just the selected ones — can result in a large fraction ($\sim 60\,\%$) of undesirable background atoms.

3.2.5 State selective detection

Basics

During the interferometer pulse sequence a variable fraction of the atoms is transfered from the $F = 3$ to the $F = 4$ state, depending on the interferometer phase shift. This fraction is measured once the atoms return to the approximate location of the original trap, where the magnetic field is zeroed to within a few milli Gauss.

The normalized fluorescence detection is implemented using a sequence of two identical probe pulses and an additional pulse for optical pumping in between (see timing diagram in Fig. 3.6). The $500\,\mu$s long probe pulses are on resonance with the $6s_{1/2}, F = 4 \leftrightarrow 6p_{3/2}, F' = 5$ transition, are circular polarized and have an actively stabilized intensity of typically $0.9\,\mathrm{mW/cm^2} \approx 0.8\,I_{\mathrm{sat}}$. Only atoms in the $F = 4$ state will scatter photons from this probe beam, so the detected fluorescence signal is proportional to the number of atoms in this state. Furthermore, since this is a closed optical transition, the atoms will still be in the $F = 4$ state after the pulse — as long as it is not to long or intense.
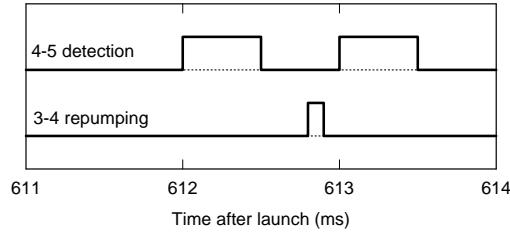
Figure 3.6: Detection sequence.

During the $500\,\mu$s time interval between detection pulses the atoms are illuminated by light resonant with the $6s_{1/2}, F = 3 \leftrightarrow 6p_{3/2}F' = 4$ transition. This pulse, which is $100\mu s$ long and has an intensity of $\sim 1.5\,\mathrm{mW/cm^2}$, is sufficient to transfer all the atoms originally in the $F = 3$ state to the $F = 4$ state via optical pumping. This means that *all* the atoms are in the $F = 4$ state when the second detection pulse is applied. Division of the two detection signals therefore yields the normalized fraction of atoms originally in the $F = 4$ state.

The signal to noise ratio of this detection scheme can be as high as 300/1. This is usually

not limited by intensity fluctuations of the probe beam, which is actively stabilized, but by frequency jitter. It is also very important set the probe frequency correctly, almost directly on resonance. While the noise is relatively insensitive to detuning towards the red (over a few MHz), it increases dramatically for even small detunings towards the blue (over only 200 kHz).

Details

The fluorescence is captured using a 3-inch diameter, f=1 condenser lens (Melles Griot 01-CMP-121) that is mounted at approximately 90° to the probe beam and covers a solid angle of about $4\pi/100$. The atomic cloud is first imaged (2:1) onto an adjustable, vertical slit and then (1:1) onto a PMT (Hamamatsu R943-02). A long pass filter is mounted in front of the PMT to reduce its sensitivity to room lights. The output signal of the PMT — which is operated at bias voltages between 700 and 1300 Volt, depending on the measurement — is first amplified by a current pre–amplifier (Keithley 427) and routed to two gated integrators to capture and store the signal due to both probe pulses. Ultimately, the output of the integrators is digitized and read into a computer using an 12-bit A/D board (Keithley-Metrabyte DAS-16).

The horizontal probe beam is retro-reflected to minimize the deflection of the atomic trajectories by light scattering forces. Its size and position can be controlled by a variable circular aperture and an adjustable vertical slit (same type as in front of the PMT). The optical repumping beam, actually the same one used for the MOT, has a much larger diameter ($\sim 4\,\mathrm{cm}$) and illuminates the atoms from a different direction. The diameter of the round aperture in the probe beam is usually set to 2.5 cm, except during time-of-flight temperature measurements when a probe beam much smaller then the cloud size is useful. The $\sim (1\,\mathrm{cm})^2$ photo-cathode of the PMT covers about the same vertical range, taking into account the magnification of the imaging system.

The slits are used to select only a narrow vertical column of the larger atomic cloud for detection. This improves the contrast of the interferometer (since these atoms are always within the central, uniform intensity area of the Raman beams) and is also useful when tracking down systematic errors due to coriolis forces (Sec. 6.5.1). Usually both slits are set to a width of 6 mm, which reduces the number of detected atoms by another factor of 10 to approximately 3×10^5.

The detection beam passes through the cesium source chamber, resulting in $\sim 30\,\%$

absorption. However, since this absorption is essentially constant it usually does not have any adverse effects. A bigger problem is caused by the strong background fluorescence — it can be bigger then some of the weaker signals — caused by thermal cesium atoms in the detection region. We actually perform our detection in the region of the main chamber with the highest cesium density simply because of the easy optical access. This probably should be changed in the future.

3.3 Additional atomic fountain details

3.3.1 Cesium source

The current MOT differs from an earlier, otherwise very similar version [28] in that it is not a pure vapor cell design. In the standard version, the MOT is loaded from a uniform cesium background vapor in equilibrium with a cooled cesium reservoir. In our version, the cesium vapor pressure is neither uniform nor in equilibrium with the cooled reservoir — responsible is the arrangement of the systems vacuum pump, combined with its relatively high pumping speed.

Figure 3.7 illustrates the situation: Cesium atoms originating from the supply in the cold finger first form a relatively high vapor pressure (still lower then the expected equilibrium vapor pressure) in the source chamber. They then enter the main chamber through a 1–1/2 inch diameter tube, effectively forming a large diameter, high divergence atomic beam. After only a few bounces these cesium atoms are removed from the system by the vacuum pump, without causing a significant rise in the cesium vapor pressure in other parts of the chamber. However, since they pass the capture volume of the MOT at least during their first pass they can still be trapped.

The strongest evidence for this model comes from optical thickness measurements of the cesium vapor. For a typical cold finger temperature of $+5°C$ ($+15°C$)[‡] the equilibrium vapor pressure [31] should be $\sim 1.5 \times 10^{-7}$ torr ($\sim 5 \times 10^{-7}$ torr). However, optical thickness measurements along a horizontal axis, going trough the source as well as the main chamber, indicate an average vapor pressure of only $\sim 7 \times 10^{-9}$ torr, or $\sim 2 \times 10^{-8}$ torr if the cesium is confined to the smaller source chamber only. A similar measurement along the vertical axis of the main chamber even indicate an average cesium partial pressure of less then 10^{-10} torr.

[‡]The numbers in parenthesis are the new operating parameters after the 56 l/s turbo pump was replaced by the 30 l/s ion pump
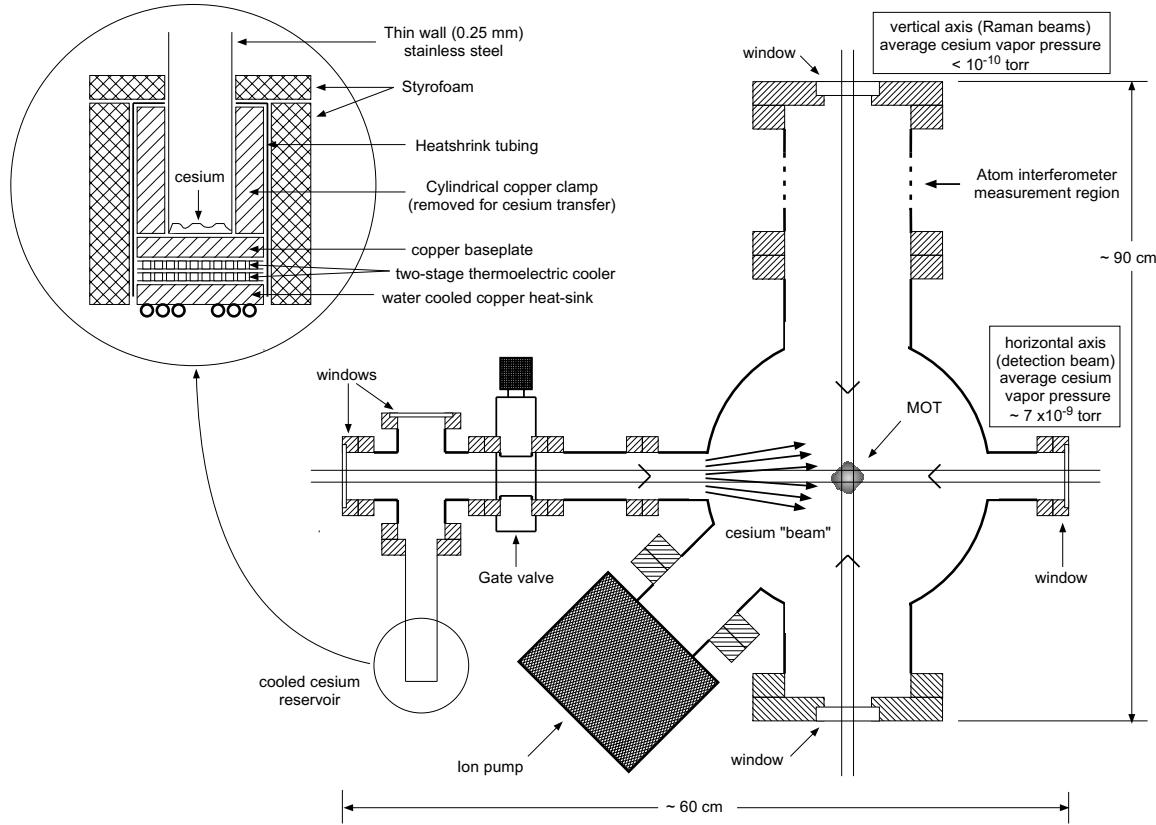
Figure 3.7: Cesium source.

3.3.2 Trapping magnet

The quadrupole trapping field is produced by two coils in anti "Helmholtz" configuration, wound directly on the outside of the vacuum chamber. The coils have a diameter of $\sim 10\,\text{cm}$ and are spaced $\sim 22\,\text{cm}$ apart. Note that this is far from the "correct" anti Helmholtz spacing of $5\,\text{cm}$, which makes this configuration very inefficient: In this limit the current necessary to achieve a specific field gradient at the center of the assembly increases as the 4th power of the coil spacing — and the dissipated power as the 8th power. The coils therefore have to be water cooled. They are made using 40 turns of 1/8–inch diameter copper tubing ($\sim$ 1/16–inch diameter water channel) which has been isolated using high temperature (so they can survive a vacuum chamber bake out), Teflon heat shrink tubing.

The coils produce a gradient of $0.14\,\text{Gauss/cm}$ for a drive current of one ampere. The water cooling is sufficient to allow currents up to $100\,\text{A}$, but the MOT is usually operated

at 45 A and a gradient of 6 Gauss/cm. The current is supplied by a 100 A / 10 V power supply (HP 6260b) operated in voltage control mode. It can be switched off in less then 1 ms using a parallel pair of MOSFET Power transistors (Motorola MTM50) in series with the supply. An RC filter in the control line slows down switching process in order to prevent the inductive spike from driving the transistors into avalanche mode. The switching time of the circuit is fast enough to insure that it doesn't dominate the decay time of the magnetic field, which is then mostly determined by eddy currents in the vacuum chamber.

To produce a well defined MOT it is important that the quadrupole field of the trapping coils is not disturbed. Originally the magnetic shielding assembly for the atomic fountain was to close too the MOT , resulting in a severely deformed trap, shifted by as much as 5 cm. Raising the shield by another ~ 10 cm solved this problem. Mounting the unshielded ion pump directly to the main vacuum chamber is also problematic; it produces field gradients up to 1 Gauss/cm at the location of the trap, but so far this effect happens to be just barely tolerable.

In addition to the trapping coils the setup includes three additional coil pairs to compensate Earth's magnetic field and, for short periods, provide a bias field for magnetic state selection. The system was originally designed to use a flux gate magnetometer and active feedback to deal with the effects of a cryogenic, 10 Tesla magnet located in a nearby laboratory, only ~ 5m from our setup, and able to produce fields of up to 100 mG at the location of the trap. However, in the end it turned out to be easier to coordinate the schedules of both experiments.

3.3.3 Laser system and optics

Ti:Sapphire laser

Figure 3.8 shows the laser system for the atomic fountain and the state sensitive detection. An Argon-Ion laser (Coherent Innova 100 or Innova 400) pumped Ti:sapphire ring laser (Coherent 899-21) provides all the light near the $6s_{1/2}, F = 4 \leftrightarrow 6p_{3/2}, F =?$ transitions of the cesium D_2 line at ~ 852 nm. This includes beams for trapping, optical pumping, detection and state selective blow-away. The single frequency, infrared output power of the Ti:sapphire laser is typically 2.0 - 2.5 Watts for 15 Watts of multi-line-visible pump power.

Because of concerns about vibrations, the Ti:Sapphire and Argon-Ion laser are installed on a separate table. The light is the transfered to the main optical table using a 2 m long

single-mode, polarization preserving optical fiber with pre-installed collimation lenses (Oz-optics LPSC-03-852-5/125-P-0.86-1.3-6DEG-1-3-2). By using a telescope for proper mode matching we are able to achieve a very high coupling efficiency and deliver 75 % of the laser output power to the optical table.

Using the optical fiber also comes with the *enormous* benefit of decoupling most of the setup from pointing fluctuations of the laser. This means that most of the optics after the fiber, if properly mounted, never have to be realigned. This property alone, despite the small power loss, would probably justify the use of the fiber, even if the Ti:Sapphire laser were located on the optical table itself. The arrangement is also extremely stable and needs very little realignment even at the input side: For daily operation only the input telescope mirrors, the birefringent filter and the thin-etalon need to be adjusted — with no need to touch up the fiber coupling. Major realignments are only necessary once every few months, mostly after cleaning the intra-cavity optics of the Ti:Sapphire laser.

FM saturation spectroscopy lock

The laser frequency is stabilized relative to the $F = 4 \leftrightarrow F' = 4$, $F = 4 \leftrightarrow F' = 5$ crossover line using a standard FM saturation spectroscopy lock [32]. A double-pass AOM in the saturation beam of the lock provides a tunable offset which is usually set at 67 MHz to place the laser output frequency 59 MHz below the $F = 4 \leftrightarrow F' = 5$ transition (Fig. 3.9). Some features of this lock that are worth pointing out: (a) No chopping of the saturation beam is used to eliminate a possible Doppler background. Instead, we find that this background is already low in the neighborhood of the 4/5 crossover resonance and can be made to vanish almost completely by slightly adjusting the probe beam polarization. (b) The lock has a relatively high bandwidth of $\sim 15\,\mathrm{kHz}$. To achieve this a second, fast control path is implemented by adding a voltage to the output of Ti:Sapphire lasers internal cavity lock photodiode. (c) The lock has a hold feature which is used to increase the molasses detuning during the final stages of the fountain launch. The lock receives a hold command. Simultaneously, an additional feed-forward voltage is added to the fast control output (see above). This decreases the laser output frequency by $\sim 40\,\mathrm{MHz}$. The hold command is removed after a few milliseconds, once the launch is complete, and the lock recovers without problems.

Downward Propagating MOT

(+40 MHz for trapping
+36 MHz for launching)

AOM

Upward Propagating MOT

(+ 2 x 89 MHz)

AOM   AOM

(-120 MHz)   (+40 MHz)   To FM lock

AOM

4-5 Detection

4-5 Blow Away

Intensity control
photodiode

Ti:Saph

Reference for Raman Beams

To Fast Dither Lock

(- 2 x 126 MHz)

AOM   AOM (+110 MHz)

3-4 Repump

DBR
Laser
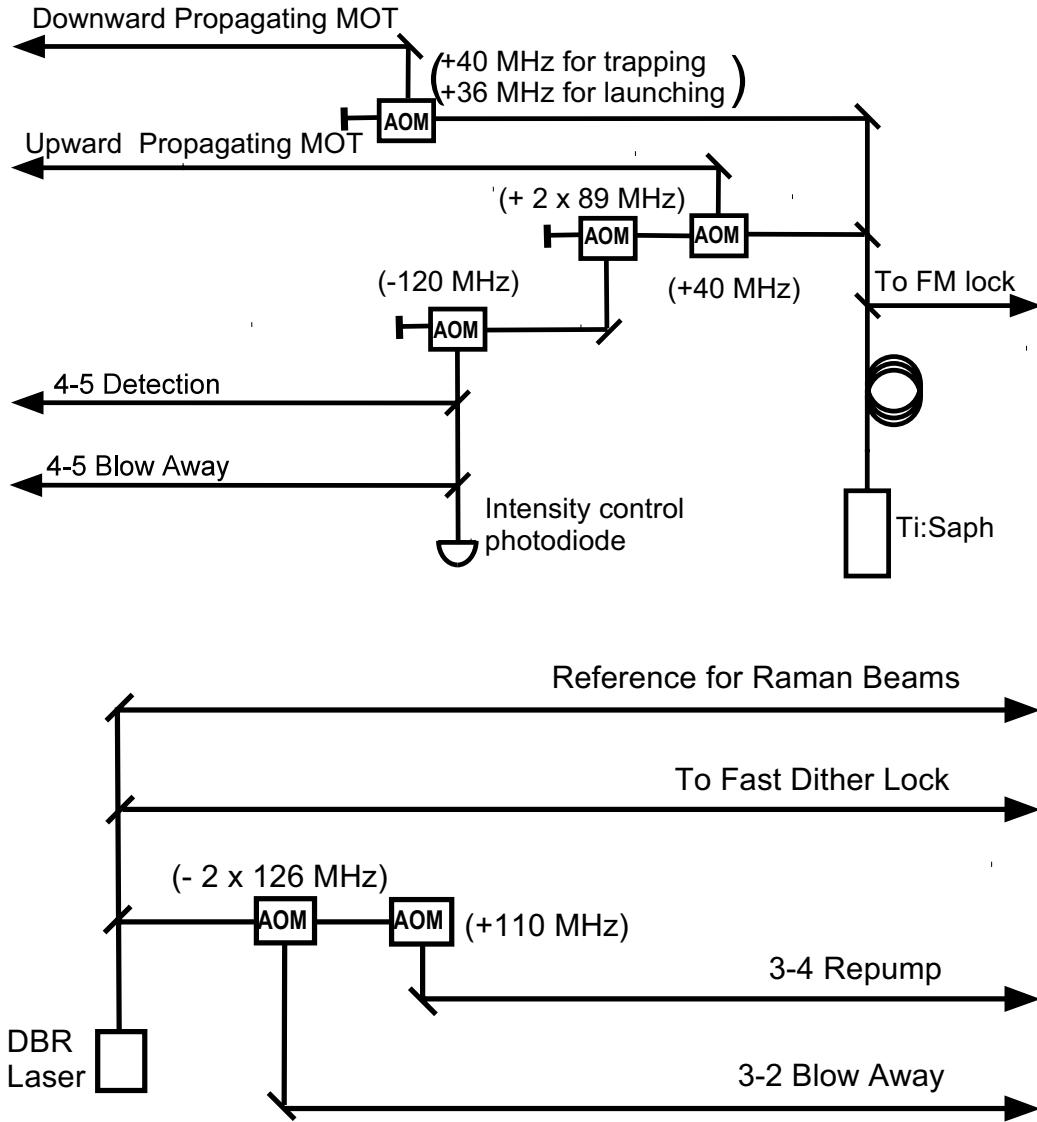
3-2 Blow Away

Figure 3.8: Schematic of laser system. All laser beams (trapping, detection, 4–5 blow-away) close to $6S_{1/2}, F = 4 \leftrightarrow 6P_{3/2}, F' = ?$ transitions (see Fig. 3.9 for energy level diagram) of the cesium D_2 line at $\sim 852\,\text{nm}$ are derived from a Ti:sapphire laser. All laser beams (repumping, 3–2 blow-away, Raman frequency reference) close to $6S_{1/2}, F = 3 \leftrightarrow 6P_{3/2}, F' = ?$ transitions are derived from a distributed–Bragg–Reflector (DBR) diode laser.
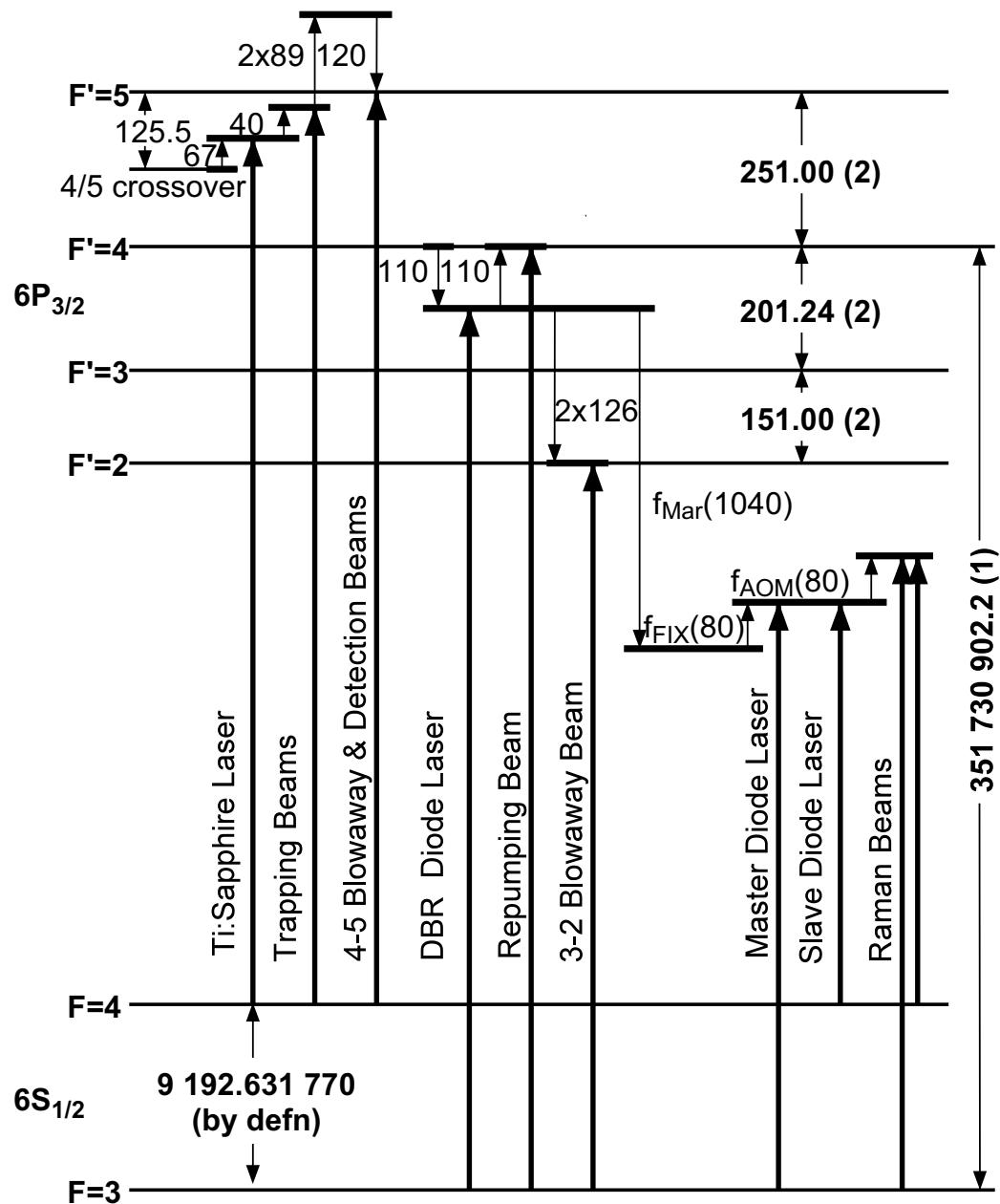
Figure 3.9: Atomic energy levels and laser frequencies. All laser frequencies are referenced either to the $F = 4 \leftrightarrow F' = 4 \,/\, F' = 5$ "crossover" resonance or the $F = 4 \leftrightarrow F' = 4$ resonance. Numerical values are in MHz.
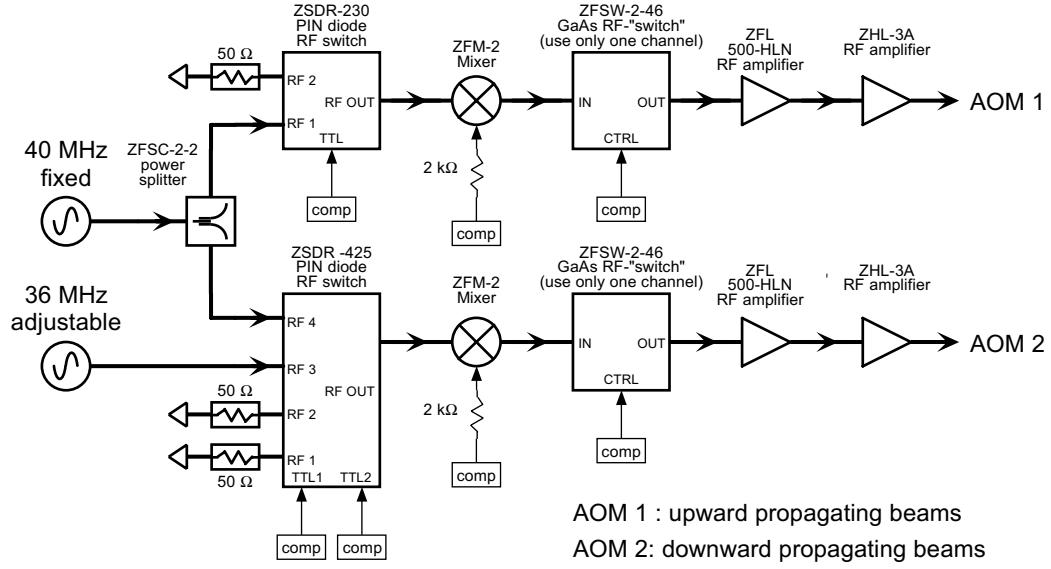
Figure 3.10: Circuitry for controlling launch frequencies. The GaAs RF–"switches" are used as variable attenuators. Compared to double balanced mixers they have the advantage that the attenuation does not depend on the RF input power, which is important for this circuit.

Trapping beams

There are two sets of trapping beams (3 upper beams, 3 lower beams), each derived from a single precursor beam containing about 50% of the total Ti:sapphire laser power after the fiber. Both beams can be controlled using single-pass AOM's. While the AOM for the lower beams always operates at a fixed frequency of 40 MHz, the frequency of the other one can be tuned to generate the moving molasses during the fountain launch (see Fig. 3.10 for control circuit). The AOMs are backed by a pair of mechanical shutters (nm LST 18) to prevent eventual leakage light from disturbing the interferometer measurement. Each beam is then expanded by a factor of 5, using a spatially filtered telescope, before being split into three equal intensity components by plate beam splitters. Each of the components is the converted to circular polarization by $\lambda/4$ wave plates and expanded by another factor of 8, using independent telescopes. Finally the beams are routed to the MOT using large gold coated mirrors to preserve their circular polarization.

Detection and blow–away beams

The detection and blow-away beams are derived from the same source. A small fraction of the Ti:Sapphire light is split off and frequency shifted a first time by a double–pass AOM operating around 89 MHz. This frequency can be tuned to put the detection beam exactly on resonance with the $F = 4 \leftrightarrow F' = 5$ transition. It then passes through another AOM, operating at a fixed frequency of 120 MHz and used to switch the light, as well as actively stabilize its intensity. To perform the latter task, a small fraction of the 1st order light is detected by a photo diode and held constant by a PID feedback circuit (~ 100kHz bandwidth) controlling the RF-power driving the AOM. The feedback is only used during detection, while for a blow-away pulse the intensity is simply set to maximum.

The beam is then spatially filtered and split into two components, one for the detection and one for the blow-away beam. Both beams would always be on at the same time, but two mechanical shutters (Uniblitz LS-2) select one at a time. The detection beam is then expanded, made circular polarized by passing through a polarizer followed by a $\lambda/4$ wave plate and apertured before it enters the vacuum chamber horizontally (see above). The blow-away beam is routed to the top window of the vacuum chamber, where it is focused on a small pick-off mirror (almost clipping the Raman beams) which then reflects the expanding beam down through the center of the magnetic shield.

Optical pumping beam

Another small fraction of the Ti:sapphire power is used to provide light on resonance with the $F = 4 \leftrightarrow F' = 4$ transition, which can be used to optically pump atoms into the $F = 3$ hyperfine state (see for example Sec. 3.2.2). This beam passes through a double pass AOM, operated at 96 MHz, which can pulse the light on or off and also shifts its frequency onto resonance. This AOM is also backed by a mechanical shutter.

DBR diode laser

A Distributed-Bragg-Reflector (DBR) diode laser provides all the light near the $6s_{1/2}, F = 3 \leftrightarrow 6p_{3/2}, F = ?$ transitions. This includes the repumping light applied while loading the MOT and during detection, as well as one of blow-away beams used during preselection. Additionally, the absolute frequencies of the Raman lasers are also referenced to the DBR laser by means of a frequency offset lock.

The DBR laser (SDL-5712-H1) can provide up to $100\,\text{mW}$ of stable, single frequency output power (we usually operate at $80\,\text{mW}$). It is well behaved and easily and continuously tunable over a large frequency range of several nm, simply by adjusting current and temperature. This convenience comes at the price of a substantially larger linewidth (measured as $\sim 8\,\text{MHz}$ using a heterodyne method) compared with an external cavity diode laser. It is also *very* sensitive to optical feedback, requiring an optical isolator in front of the laser which also has to be mounted very stably to prevent small reflections from its front window to disturb the laser. While the output beam is slightly elliptical and astigmatic, we found it unnecessary to correct these for our purposes.

Fast dither saturation spectroscopy lock

The DBR laser is locked relative to the $F = 4 \leftrightarrow F' = 4$ line using saturation spectroscopy and a fast dither lock. Again a double pass AOM in the saturation beam provides a tunable offset, but in this locking scheme it also does double by providing the frequency dither for the lock. This AOM is driven by the frequency quadrupled and amplified output of an DDS synthesizer (SRS DS345), which also provides the frequency dither ($\pm 6\,\text{MHz}$ frequency span after quadrupling, $10\,\text{kHz}$ modulation frequency). A lock-in amplifier (SRS 510) is the used to extract the lock error signal. The AOM center frequency is usually set at $110\,\text{MHz}$, placing the frequency of the DBR laser this far below the $F = 4 \leftrightarrow F' = 4$ transition.

The advantages of modulating only the saturation beam, compared with the standard practice of simply modulating the laser itself, are twofold: First, there will be no modulation sidebands on the main laser beam. Additionally, this method is intrinsically free of the Doppler broadened background that is usually associated with a modulated probe beam. One possible problem with this type of lock is its sensitivity to the alignment of the double pass AOM. Any amplitude modulation or slight beam movement associated with the dithering will generally result in shift of the lock-point. By doing spectroscopy on the cold atoms in the fountain, we actually find that the lock frequency is usually offset by $\sim 1\,\text{MHz}$ from its proper value, and that this offset may drift around by a few hundred kHz.

Repumping beam

Most of the DBR light is used for repumping. A single pass AOM operating at $110\,\text{MHz}$ is used to control the repumping beam intensity. It also up-shifts the light's frequency back into resonance with the $F = 3 \leftrightarrow F' = 4$ transition. The repumping beam is then spatially

filtered and nearly overlapped with one of the trapping beams. This is done by focusing it onto a pick-up mirror which is placed close to the focus of the trapping beam's final expansion telescope.

Blow–away beam

The main DBR beam is also used to generate a blow–away beam in resonance with the closed $F = 3 \leftrightarrow F' = 2$ transition. In that case the beam is switched and down-shifted in frequency using a double pass AOM operating at 121 MHz. It is then spatially filtered, routed to the vacuum chamber and is used to illuminate the atoms from the side, through one of the large windows.

Controlling stray light

The atom interferometer measurement is very sensitive to stray light close to resonance. For that reason, a large portion of the laser system is surrounded by boxes made from black cardboard, with only a few, small holes for the laser beams. To decrease the leakage light through the switching AOM's, they are usually combined with spatial filters and RF-switches to turn off the drive power completely. This results in leakage light levels which are typically less then 10^{-5} times of the input power. Since this might still be too much, all the AOM's are additionally backed by mechanical shutters.

3.3.4 Microwave pulses

The microwaves used during the preselection process are introduced into the system using a microwave horn mounted in front of one of the 4–1/2 inch viewports. They are generated by mixing the frequency doubled output of microwave synthesizer (Gigatronics 600) with a lower frequency generated by a DDS synthesizer (HP 33120 A). Both synthesizer are phase locked to a 10 MHz Loran-C reference signal. Before going to the microwave horn, the signal is amplified to ~ 400 mW by a high gain microwave amplifier (JCA 605). While the pulses are primarily controlled using GaAs RF-switches at the output of the DDS synthesizer, this is not sufficient to prevent interference with the interferometer measurements. We therefore also gate the supply voltage for the microwave amplifier, achieving surprisingly fast switching times of only a few μs.

3.3.5 Computer control and timing

This pulsed experiment involves a rather complex sequences of events and therefore requires a sophisticated control system, consisting of two computers in combination with several pulse generators and arbitrary waveform synthesizers.

Data acquisition computer

One of the computers (IBM compatible, 50 MHz 486, DOS 6.2) is responsible for data acquisition and controls most aspects of the experiment. It is fitted with a GBIB board (Keithley Metrabyte KM-488-DD) and an Multi function I/O board (Keithley Metrabyte DAS-16). The GBIP board is used to initialize the many different devices (synthesizers, pulse generators, oscilloscopes) necessary to run the experiment and then to scan several parameters (frequencies, pulse times) during data acquisition. Several digital lines of the multi function I/O board are uses for timing and synchronization purposes but its main function is to digitize the atomic fluorescence signal during detection. The software controlling the experiment is written in Microsoft QuickBasic, while some of the data analysis programs are implemented in Fortran and use least-squares fit routines from the IMSL numerical library.

Timing computer

The second computer (IBM compatible, passive backplane VESA system with 14 expansion slots, 66 MHz 486DX2, Windows for Workgroups 3.1) is used to implement a dedicated timing system for most of the experiment. The system was originally developed by Todd Gustavson and then slightly modified for use in our experiment. It uses four counter/timer boards (National Instrument PC-TIO-10) to provide up to 40 timing pulses with $10\,\mu$s resolution (for a maximum cycle length of $\sim 1.2\,$s). These pulses are then used to update the outputs of three 12-bit D/A boards (National Instruments AT-AO-10), always loading the next output value from their built in, cyclic hardware buffer. This providing us with 30 analog output lines to control the experiment. The hardware is controlled by a combination of low level routines, written in C, and a user-friendly graphical MATLAB user interface.

A nice feature of this system is that it is almost completely implemented in hardware. Thanks to the build-in hardware buffers of the analog output boards, no software intervention is required anymore after everything has been set up initially. This leaves the main

computer free for other purposes, mostly on-the-fly data analysis. To facilitate this mode of operation, we actually have the control computer write newly acquired data onto the hard disk of the timing computer immediately, using an Ethernet network connection (its own hard disk is not externally accessible, since it is running under DOS). This arrangement has proven to be very effective and useful.

Additional timing hardware

Some of the more critical timing signals (Raman pulses, microwave pulses), or those that need to be scanned (Detection time for TOF measurement, Raman nd microwave pulse length to measure Rabi frequency) pulse are still provided by a set of pulse generators (SRS DG535) and arbitrary waveform synthesizers (SRS DS345). These are generally phase locked to an $10\,\mathrm{MHz}$ Loran-C frequency reference and controlled via GPIB by the data acquisition computer. One of the pulse generators is also used as the master trigger for the experiment, mostly because it offers a line trigger feature that can be useful for certain measurements.

3.4 Interferometer

In this section we present the system for generating the laser pulses which form the beam splitters and mirrors of the atom interferometer. We also describe the magnetic shielding assembly surrounding the measurement region.

3.4.1 Phase–locked diode lasers

There are several possible ways to generate the two optical frequencies required for stimulated Raman transitions. They include using high frequency acousto–optic modulators, either directly (at $1.7\,\mathrm{GHz}$ for sodium [33]) or in combination with injection locked slave lasers (at $9.2\,\mathrm{GHz}$ for cesium [34]). Another option is to use the sidebands generated by a high frequency electro–optic modulator (at $1.7\,\mathrm{GHz}$ for sodium [11], at $9.2\,\mathrm{GHz}$ for cesium [35]), or even by direct current modulation of a single frequency diode laser.

For this experiment we choose to generate the Raman light by phase–locking two external cavity diode lasers [14, 36]. The general idea is to detect the beat note between the two independent diode lasers using a fast photo diode and compare it to a stable RF–reference frequency. Under certain conditions it is then possible to phase–lock them together using a

electronic feedback loop (PLL). To make this work it is essential that at least one of the two diode lasers has a frequency modulation bandwidth substantially larger than either of their intrinsic line widths. It must also be possible to keep all time delays within the feedback loop sufficiently short.

External cavity diode lasers

While diode lasers generally have large frequency modulation bandwidths, their intrinsic line widths are usually too large to allow phase-locking (This is true even for DBR diode lasers). The first goal is therefore to reduce the laser linewidth, and it can be readily achieved by using an external cavity configuration. We start with two laser diodes (SDL-5410-G1, 100 mW, GaAlAs) and build the external cavities using gold coated, holographic gratings in Littrow configuration. The output beams then have short term linewidth substantially smaller than 1 MHz, and we usually extract 80 mW of power. To improve the reliability and long term stability of the phase-lock, we stabilize the temperature of the external cavity in addition to that of the diode and use a lot of thermal insulation material. (Diode laser current and temperature controller are self made, cavity temperature controller: Wavelength Electronics TEC-5000)

In addition to the normal current modulation capabilities afforded by the diode current controller, we add an additional fast modulation port to the diode laser that is going to be actively phase locked (slave laser). This is done by simply bringing the modulation signal as close as possible to the diode before adding it to the diode current via AC-coupling. The frequency response of this current modulation onto the laser frequency, in both amplitude and phase, was measured previously by Kurt Gibble (for SDL and STC laser diodes). His data is presented in Fig. 3.11.

Phase lock

A fairly complete schematic of the phase-lock system is given in Fig. 3.14. The beat note is detected is detected using a fast photo diode (Antel S2), amplified and immediately mixed down to a convenient intermediate frequency. The local oscillator frequency for the mixer is itself tunable and its generation will be discussed in Sec. 3.4.2. The intermediate frequency is once again amplified and then distributed to various feedback components and monitoring equipment.
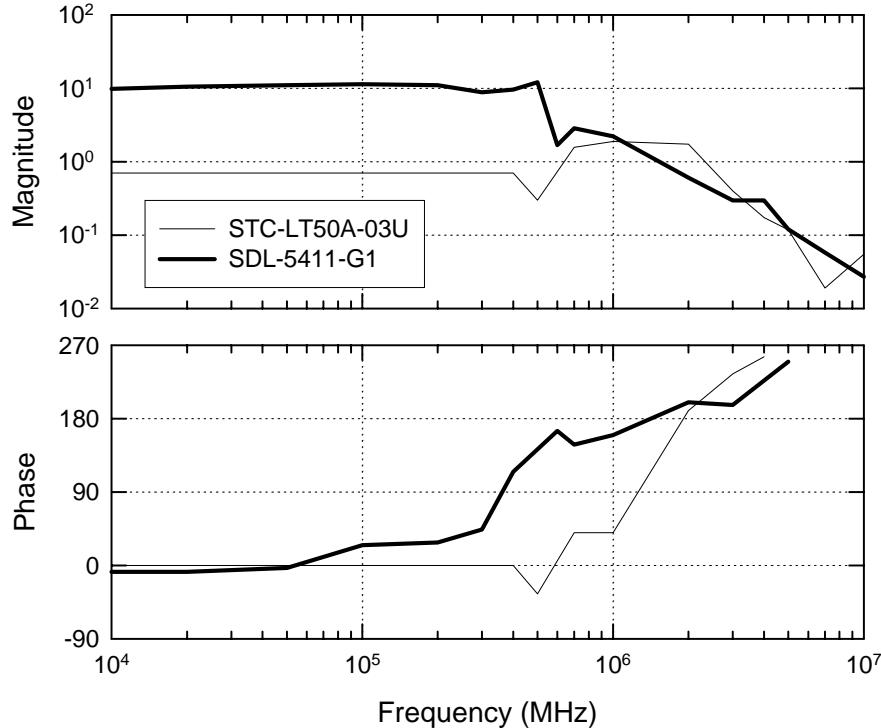
Figure 3.11: Frequency modulation response of diode lasers. Measured by Kurt Gibble for STC and SDL laser diodes.

The phase-lock system actually uses three different feedback paths: The fast path feeds the output signal of an analog phase detector directly back into the previously mentioned, fast modulation input of the slave laser. An RF-attenuator and compensation filter can be used to optimize the feedback. The filter is especially important since it provides a certain amount of lead compensation and increases the maximum feedback bandwidth substantially. The intermediate and slow feedback paths both obtain their error signal from a digital phase detector circuit (Fig. 3.12), which has better low frequency properties than the analog mixer and provides a bigger capture range for the phase-locked loop. The intermediate feedback path is implemented using the DC-modulation input of the diode laser current controller, while the slow path uses a piezo to adjust the length of the external diode laser cavity.

The crossover points between the three feedback bands are typically 25 Hz and 550 kHz, while the total feedback bandwidth is approximately $2.0 - 2.5$ MHz. While in principle it would be possible to generate all the signals independently, we instead choose to use the error signal of the intermediate path as the input for the piezo circuit. This automatically
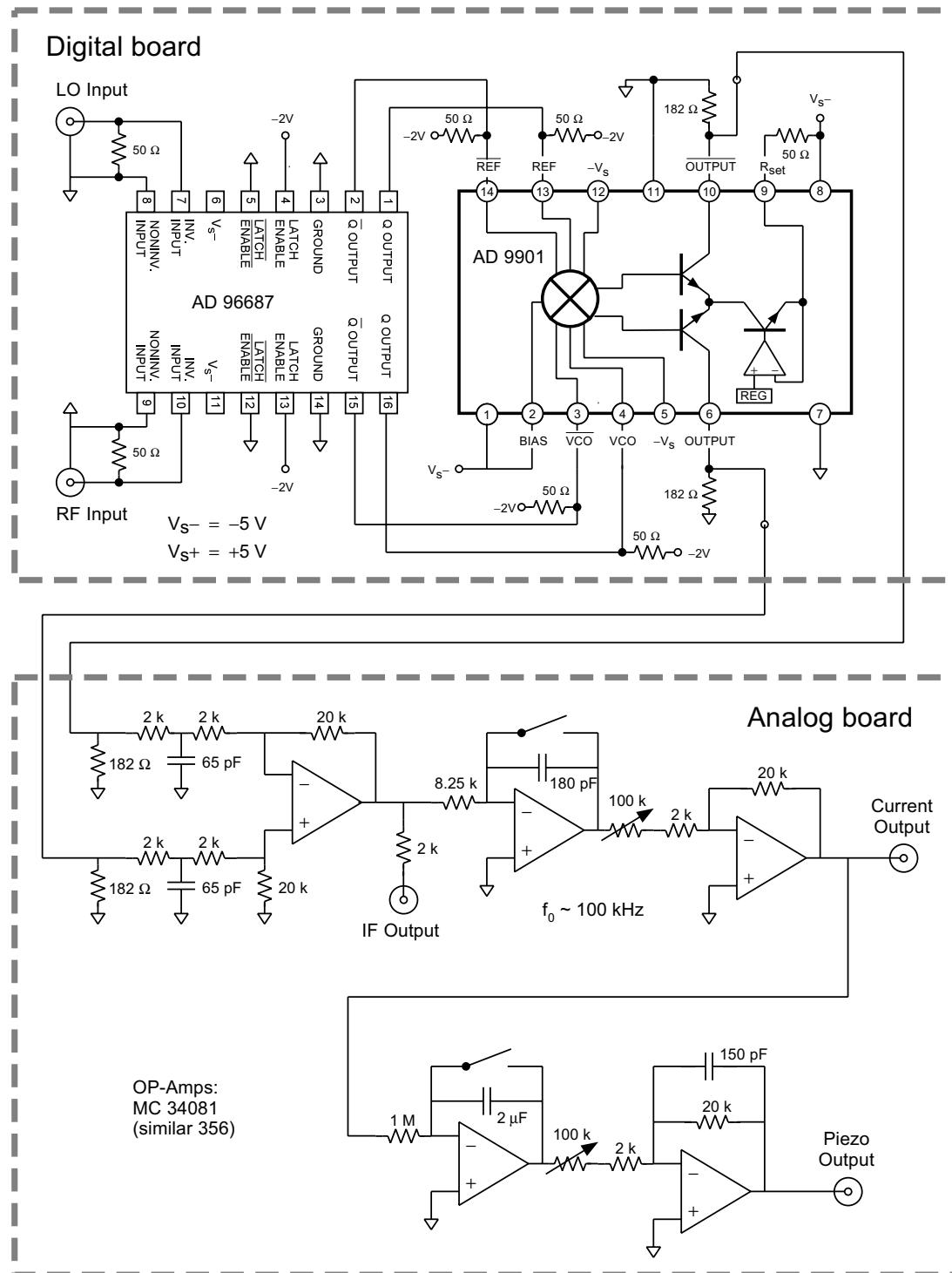
Figure 3.12: Digital phase–lock circuit.
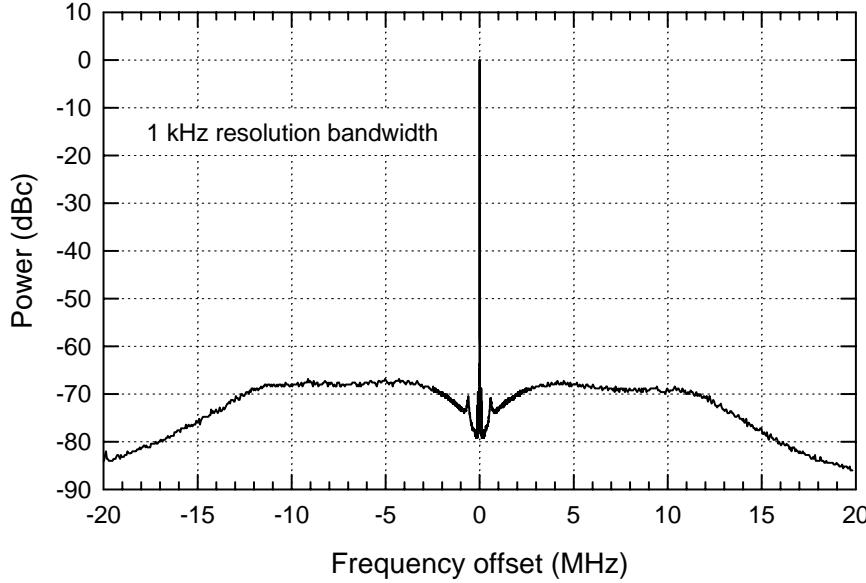
Figure 3.13: Phase noise of Raman laser beat note. Measured by Kurt Gibble for two phase locked STC laser diodes.

eliminates gain peaking and resonances at the crossover point of these two feedback bands. On the other hand, resonances are visible at the crossover point between the fast and intermediate bands. Figure 3.13 shows a typical beat note of two phase locked Raman lasers, with 99.8 % of the total laser power in the carrier. While this particular data was taken by Kurt Gibble who used two STC diode lasers, the signal is very similar for the current setup using SDL lasers. One noticeable difference is that the noise sidebands are substantially narrower, and slightly bigger, for the SDL lasers — probably because of their higher output power and accordingly lower intrinsic linewidth.

3.4.2   Frequency control

The relative phase of the Raman beams provides the reference against which all interferometer phase shifts are measured. Precise control of the Raman laser frequency difference and relative phase are therefore of ultimate importance — any noise in the Raman phase will directly translate into noise of the gravity data, and failure to control it properly could easily result in systematic errors in the measured gravity value. Further complications arise because the relative frequency and phase of the Raman lasers are not held constant during an actual gravity measurement. Instead, as discussed in the theory section (2.2.3), they

are adjusted to compensate for most of the gravity induced interferometer phase shift, so that only a small residual phase difference has to be derived from the atomic signal. Figure 3.14 presents the system that is used to control the Raman frequency difference and phase relationship.

All frequencies are ultimately derived from a 10 MHz Loran-C (SRS FS 700-01) frequency standard, which itself is ultimately referenced to atomic clocks. The Loran-C receiver was modified (by Brenton Young [16]) to address power supply related problems and reduce phase noise at 60 Hz harmonics by over 20 dB. With these modifications, the short term stability (1 s Allan Variance) of the reference was measured to be $\sim 1 \times 10^{-12}$, significantly better then the specification of 5×10^{-12}. There are still some problems with noise spikes during Loran-C updates which occur every 0.1 seconds. The frequency stability is also relatively poor at timescales of a few hours. So far, these problems didn't seem to have any effect on the interferometer performance, but they might become important in the future.

Microwave generation by frequency multiplication

The 10 MHz reference frequency is multiplied up to 9.18 GHz using a two-stage frequency multiplier chain, identical to the ones used in FTS (Frequency and Time Systems) atomic clocks. The first stage provides a clean, single frequency output signal at a 180 MHz. The second stage then uses a comb generator to produce many high order harmonics of the 180 MHz input frequency. One particular component, the one at 9.18 GHz, does then serve as our microwave frequency reference. Since it is generated using a straightforward multiplication process, its phase noise is almost completely determined by that of 10 MHz input signal.

We then generate a tunable microwave source by phase–locking a DRO (dielectric resonator oscillator) to the 9.18 GHz reference signal, with an adjustable, synthesized offset frequency f_{TEK} of typically 40 MHz. This phase lock has a bandwidth of ~ 300 kHz and uses a digital phase detector circuit very similar to the one used for the diode laser phase lock. The output of then mixed with beat note signal from the Photodiode to generate an intermediate frequency. The diode laser phase lock will then keep regulate the laser frequency to make the intermediate frequency equal to another synthesized reference frequency f_{SRS} of typically 52.631, 770 MHz. Overall, the Raman laser frequency difference is
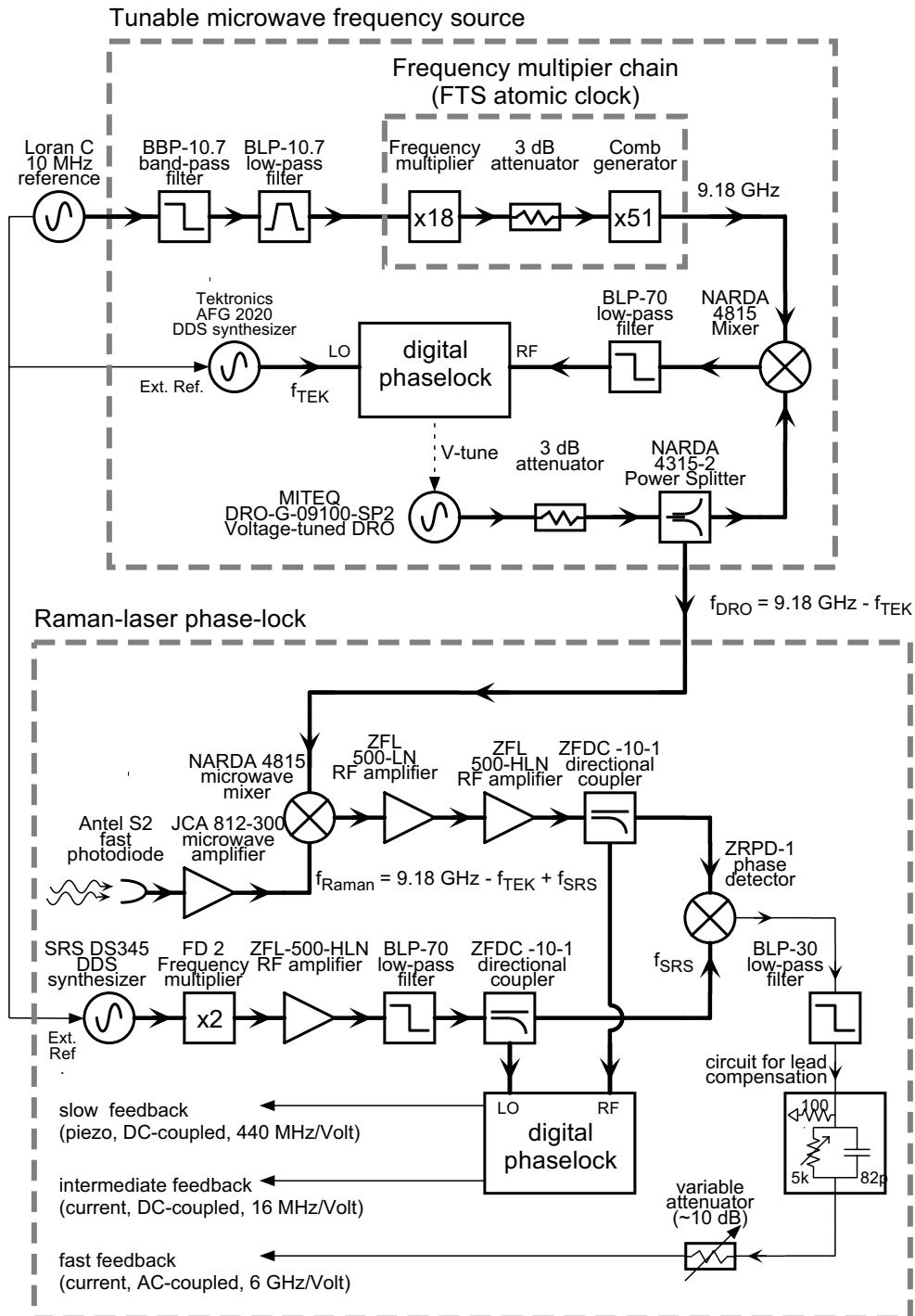
Figure 3.14: Raman laser phase-lock and system for controlling the Raman difference frequency and phase.

given by the formula

$$f_{\text{Raman}} \quad = \quad 9.18\,GHz \quad - \quad f_{\text{TEK}} \quad + \quad f_{\text{SRS}} \,. \tag{3.1}$$
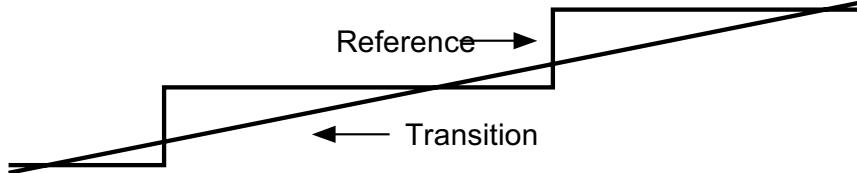
It is obvious that in principle the Raman frequency can be controlled by changing either one of the two frequencies, f_{TEK} or f_{SRS}. However, because phase shifts can lead to systematic errors, it is wise not to change the frequency f_{SRS} to much: The diode laser phase lock with its multiple feedback paths is very complex, and changing its intermediate frequency can easily result in rather unpredictable phase shifts. On the other hand, the DRO phase–lock has only one feedback path and behaves in a much more predictable way. One should therefore use its reference frequency f_{TEK} to control the Raman frequency.

Ideally, one would perform a gravity measurement by continously sweeping the frequency f_{TEK}, and thereby the Raman frequency, to exactly cancel the gravity induced Doppler of the atom. The exact g–value can then be calculated from the required chirp rate α. For a gravitational acceleration of 9.8 m/s this chirp rate would be ~ 23.0 MHz/s and a total interferometer time of 320 ms would require a 7.36 MHz frequency change. Regrettably, it is almost impossible to find a frequency source to generate such a chirp with sufficient resolution and accuracy. We have therfore implemented two slightly different alternative schemes.
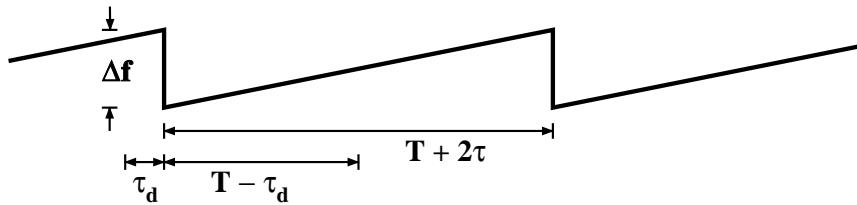
The first scheme makes use of the fact, that for sufficiently short Raman pulses a frequency chirp during the pulse itself is not important — only the accumulated phase between pulses matters. It is therefore possible to simply switch between three fixed Raman frequencies, a different one for each interferometer pulse, and adjust the step size Δf in order to best approximate the chirp rate α. If the timing of the frequency changes is exactly controlled and known, then it is possible to calculate the accumulated phase. This phase can also be fine tuned without changing the frequency step size, but by somehow shifting the phase during one of the pulses.

There are a number of important points to consider when implementing this method. The most important one is the correct synchronization between pulse timing and frequency changes in the case of finite pulse lengths. It turns out that the absolute time of the frequency changes is not important, only the time interval between them. And this interval has to be identical to $T + 2\tau$, and *not* to the dead time between pulses, T. The reason becomes most obvious when the interferometer sequence is modeled as two back to back ramsay sequences — $T + 2\tau$ then is the time interval any pair of equivalent points in the two partial sequences. Figure 3.15 illustrates the important timing relationships.

Reference and Transition Frequencies:

Frequency Difference:

Pulse Sequence:
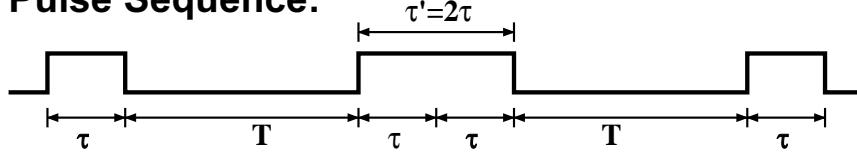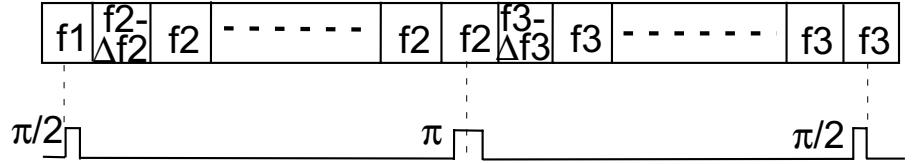
Figure 3.15: Timing relationship between interferometer pulses and frequency changes. The acceleration induced Doppler shift causes a continuous change of the atomic transition frequency. To compensate, the Raman frequency difference is adjusted in discrete steps. The exact delay τ_d of these frequency changes relative to the Raman pulses is not important, but they have to be spaced by exactly $(T + 2\tau)$.

All these frequencies are generated by a Tektronics AFG-2020 DDS (direct digital synthesis) synthesizer, which is also phase–locked to the Loran-C frequency reference. It has a 30-bit frequency resolution, which at a sampling rate of $250\,\mathrm{MHz}$ should rightfully correspond to ~ 0.23 Hz frequency steps. However, for reasons only known to the designers of the device, frequency control commands have to be given in multiples of $0.5\,\mathrm{Hz}$, further limiting the resolution and requiring a complicated rounding algorithm to figure out the *actual* output frequency. The changes in the output frequency can be implemented using the synthesizers FSK (frequency shift keying) modulation mode, which offers $10\,\mu s$ resolution for the time between changes. This time is also referenced to the external $10\,\mathrm{Mhz}$ reference, which absolute essential to make this method work. The relatively course frequency step size somewhat limits the phase resolution of the interferometer measurement. However, it

$$\Delta\phi = 2\pi \; (T+2\tau) \; [\; (N-1)(f3-f2) + (f3-f1)/2 + (\Delta f3-\Delta f2)\;]\;/\;N$$

Figure 3.16: Frequency changes of DDS synthesizer. Frequencies f_1, f_2 and f_3 are in resonance during the three Raman pulses. To allow a higher resolution in the relative phase we change the synthesizer frequency after the first and second pulses by a small amount Δf over a period of $(T+2\tau)/N$, where N is typically chosen to be 20. The phase difference $\Delta\phi$ is then given by the formula shown.

possible to work around this problem by using more than 3 frequencies and for shorter time intervals. This is illustrated in Fig. 3.16, which also give the formula for the total phase shift.

If the single Raman pulses become too long, then it is not possible anymore to ignore the gravity induced frequency chirp while the pulse is on. Our second scheme therefore has modifications to compensate for this chirp. This capability is also useful for systematic error checks, even when the Raman pulses are sufficiently short. We make use of the fact that we actually have a second handle to control the Raman frequency: The diode laser reference frequency f_{SRS}. Instead of holding it fixed, we use another frequency doubled DDS synthesizer (SRS DS-345) to sweep it for 1 ms at the correct chirp rate. A second SRS synthesizer, this one operating in square-wave burst, is used to repeatedly trigger this process once every 2 ms. Again, it is essential that both synthesizers are locked to the external 10 MHz Loran-C reference. Since these chirps only span a short frequency interval, and are furthermore identical for all pulses, the phase shifts in the diode laser circuitry are not a problem. This procedure guarantees that all the Raman pulses are correctly chirped, as long as they are applied during the correct 1 ms time intervals. Using this method also restricts the time $T+2\tau$ to multiples of 2 ms, but if this conditions is fulfilled the total phase shift is still given by the formula in Fig. 3.16.

Even though the velocity preselection pulse is not strictly a part of the interferometer sequence, it is generated by the same circuitry. Because of its long duration, it is always necessary to provide chirp compensation for this pulse. This is achieved by using another frequency doubled SRS DDS-synthesizer in sweep mode to provide the frequency f_{TEK}. An

RF-switch is used to switch between this synthesizer and the Tektronics AFG-2020.

While the absolute frequency of the Raman lasers is only of secondary importance, is has to be known to at least the targeted accuracy for the gravity measurement. The master laser frequency is therefore locked to that of the repumping diode laser. This is done by detecting their beat note on a fast photo diode, mixing it with an adjustable frequency f_{MAR} in the low GHz range, and then locking the resulting intermediate frequency relative to another reference frequency f_{FIX} using a frequency lock (here simply a low gain version of our digital phase lock circuit). The frequency f_{MAR} is typically 1.040 GHz and is generated by a frequency doubled Marconi synthesizer. We usually use a fixed frequency f_{FIX} of 80 MHz, generated from the 10 MHz Loran-C signal in three cascaded doubling stages. The absolute frequency of the master laser, including a final frequency shift f_{AOM} due to the switching AOM, is then given by

$$
\begin{aligned}
f_{\mathrm{master}} &= f_{3\leftrightarrow4} &-& \quad 110\mathrm{MHz} &-& \quad f_{\mathrm{MAR}} &+& \quad f_{\mathrm{FIX}} &+& \quad f_{\mathrm{AOM}} & \qquad (3.2)\\
&= f_{3\leftrightarrow4} &-& \quad 110\mathrm{MHz} &-& \quad 1040\mathrm{MHz} &+& \quad 80\mathrm{MHz} &+& \quad 80\mathrm{MHz}\,,
\end{aligned}
$$

where $f_{3\leftrightarrow4}$ is the absolute frequency of the $6s_{1/2}, F = 3 \leftrightarrow 6p_{3/2}, F = 4$ optical transition. Also see Fig. 3.9 for a illustration of all the atomic energy levels and laser frequencies.

3.4.3   Pulse generation

Another subsystem is responsible for controlling the timing and intensity of the Raman pulses. The actual switching of the light is done by an AOM operated at a fixed frequency f_{AOM} of 80 MHz, generated from the 10 MHz Loran-C signal in three cascaded doubling stages. The amount of RF-power driving this AOM controls the Raman beam intensity. It can be set to 3 different values (OFF, LOW for interferometer pulses, HIGH for preselection pulse) using a network of RF switches (see Fig. 3.17. All the timing signals for these switches are generated by a set of synchronized pulse generators (SRS DG 535) and several TTL logic gates. One of the pulse generator outputs is used to trigger all the hardware involved in generating the Raman frequencies.

3.4.4   Optics and beam path

Figure 3.18 gives an overview of the optical system for Raman beam generation and delivery to the atoms. The diode laser output beams are first circularized, overlapped using a
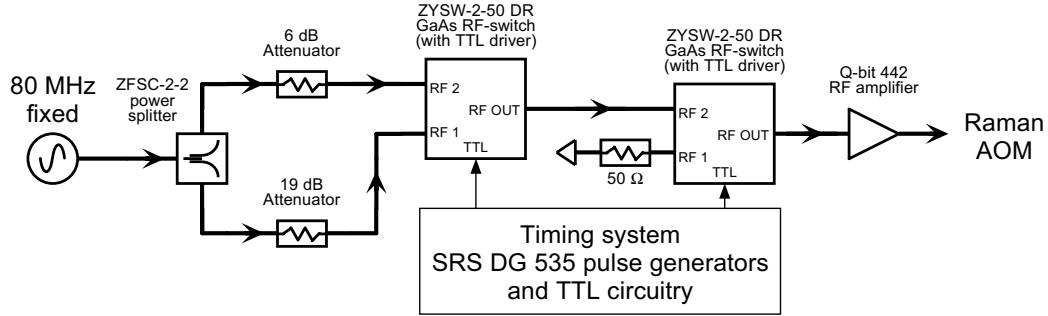
Figure 3.17: Circuitry for switching and controlling the intensity of the Raman beams. The Raman beams are collimated ($\sim 0.8\,\text{mm}$ Ø) when passed through the AOM (Isomet 1205-603F), resulting in a rise time of $\sim 200\,\text{ns}$.

polarizing beam splitting cube and then coupled into a 3.9 m long, polarization preserving optical fiber. This fiber (Oz optics LPC-04-852-5/125-P-0.86-3.9AS-40-1-3-3) comes with identical collimation already installed on both ends, and we usually achieve a coupling efficiency of $\sim 60\,\%$. The output beam is first passed through another polarizing beam splitting cube, to insure well defined polarization, and then a small fraction is picked up by a high quality beam sampler and sent to a fast photo diode to generate the beat note for the phase-lock. The collimated main beam then passes through a 80 MHz single pass AOM which is used to generate Raman pulses of controlled intensity.

The first order output beam of the AOM is then expanded to a diameter ($\frac{1}{e^2}$ intensity contour) of $\sim 2.7\,\text{cm}$. The beam expansion telescope is made using high quality singlet lenses of 7.5 cm and 150 cm focal length. Optionally, a 75-micron pinhole can be placed at the telescopes internal focus for spatial filtering. The output beam is carefully collimated using a shear-plate collimation tester (Melles Griot 009-SPM-003). It is then routed to the bottom window of the vacuum chamber using several high quality, gold coated mirrors. Two of these mirrors are mounted on translation stages, which allows for two dimensional beam movement without angular displacements. The whole beam path after the switching AOM is enclosed in lucite tubing in order to prevent wavefront deformations due to air currents.

The Raman beams then pass vertically through the vacuum system and the atom interferometer measurement region. They might first have to pass through an optional polarizing beam splitting cube before entering the vacuum chamber. The indium sealed entrance and exit viewports are both self made, using high quality AR-coated windows (fused silica, 2–inch diameter, 3/8–inch thick, $\lambda/20$, 2 arcsec parallelism). At the top of the vacuum
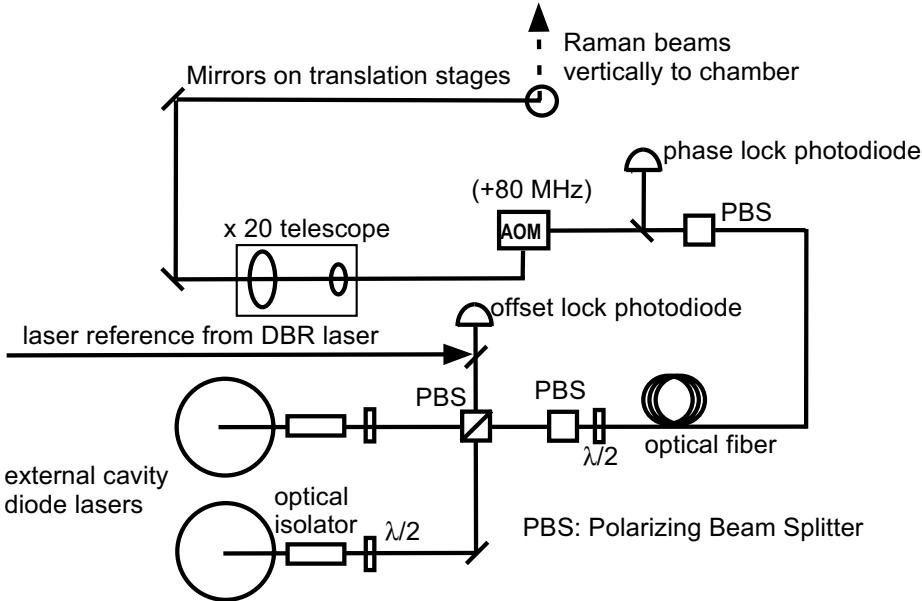
Figure 3.18: Raman lasers system.

chamber the Raman beams are retro reflected off a high quality, vibration isolated mirror (see Sec. 3.5.1). It also has to pass twice through high quality $\lambda/4$ – wave plate (zero-order, airspace, 2–inch diameter, $\lambda/20$, AR-coated, manufactured by Special Optics), which flips the beams polarization by 90 degrees. After leaving the vacuum chamber again, the beam is deflected onto a beam-dump if the optional polarizer is installed, otherwise continues to retrace its original path all the way back to the polarizer in front of the optical fiber.

This setup allows one to drive Doppler sensitive Raman transitions in a (lin $\perp$ lin) configuration: One of the two frequency components in the upward propagating beam together with the other, orthogonally polarized frequency component in the downward propagating beam can drive such a transition. All other combinations don't contribute because of polarization selection rules and detuning from the Raman resonance condition. It is also possible to drive Doppler insensitive ($\sigma^+ - \sigma^+$) Raman transitions, simply by inserting another $\lambda/4$ – wave plate into the beam before it enters the vacuum chamber and blocking the retro reflection.

Aluminum core
(graphite coated)

Bias field solenoid
(Kapton insulated wire)

four layers of
magnetic shielding
(1 mm thick Hipernom)

Aluminum spacers

14.5 "

12.5 "

10.5 "

8.5 "

1.5 "

2.0 "

2.5 "

3.0 "

3.5 "
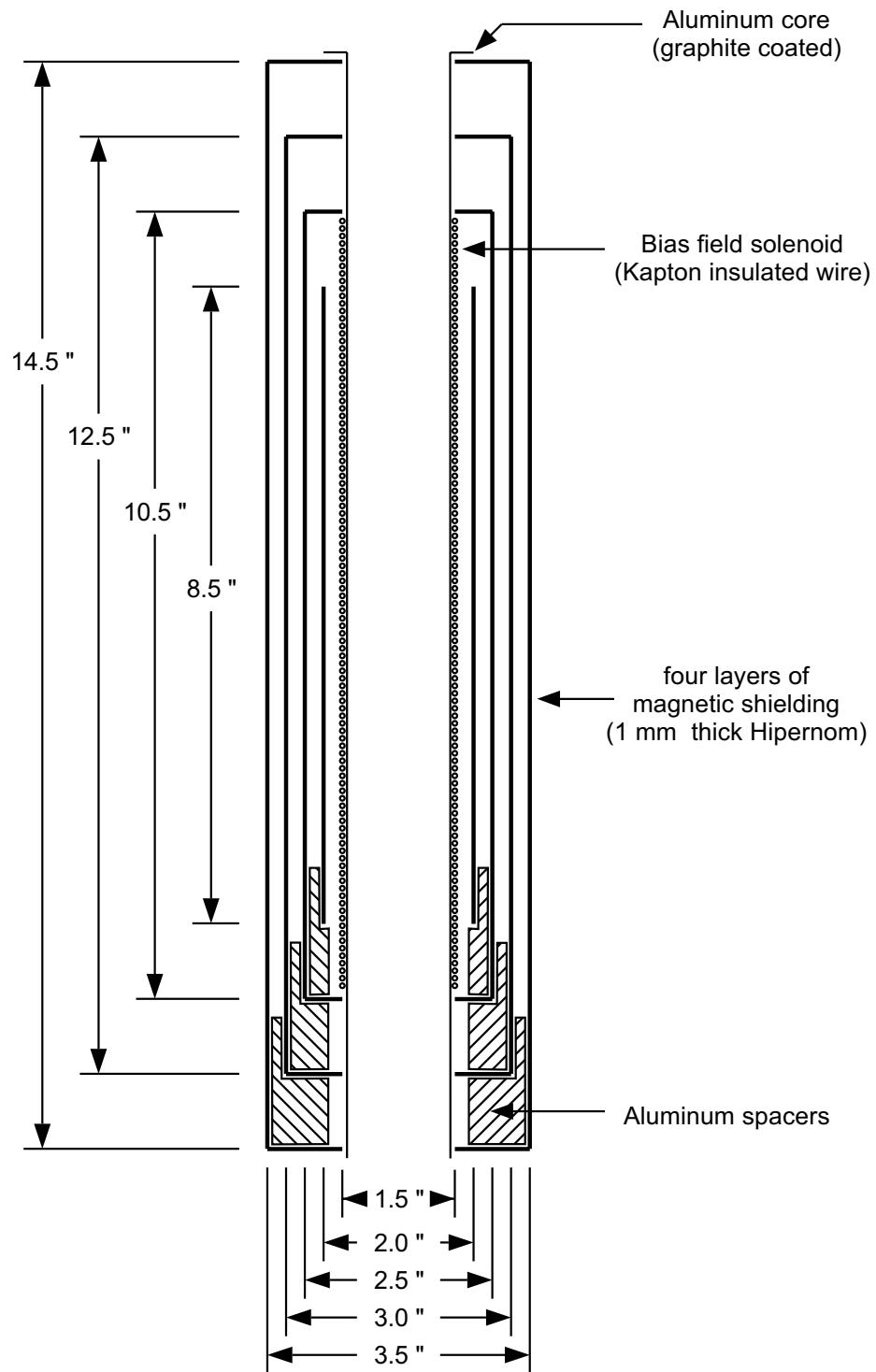
Figure 3.19: Magnetic shielding assembly.

3.4.5   Interaction region

The whole interferometer sequence takes place while the atom is inside a magnetically shielded interaction region. This is necessary since inhomogeneous magnetic fields can also cause an interferometer phase shift (see Sec. 6) and cause errors in the gravity measurement. The magnetic shield (see Fig. 3.19) consists of four cylinders made from $1\,\mathrm{mm}$ thick Hipernom. All but the innermost cylinder are also fitted with caps with $1.5\,\mathrm{inch}$ diameters holes. This shielding assembly should have theoretical radial and axial shielding factors of 1.6×10^9 and 2.9×10^7, respectively [37]. The fourth layer of magnetic shielding is only necessary because the MOT trapping coils can produce very strong ($\sim$100 Gauss), pulsed magnetic fields very close to the magnetic shield. In order to generate a uniform, vertical bias field a $10.5\,\mathrm{inch}$ long solenoid is installed inside the innermost shield. It consists of two layers of $1\,\mathrm{mm}$ diameter, Kapton coated wire which is wrapped on an aluminum core 1.5 inch in diameter. The solenoid can also be used for degaussing the two innermost magnetic shield layers.

The uniformity of the magnetic bias field is the quantity ultimately important for the experiment and we can actually measure it using the atoms in the atomic fountain. In order to do this, atoms in all possible $F = 4, m_F = ?$ Zeeman sublevels are launched with a slightly higher velocity than usual, taking then onto trajectories with reach all the way to the top of the vacuum chamber. We can then use Doppler *insensitive* Raman transitions to take Zeeman spectra at different points along atomic trajectories and use them to calculate the magnitude of the local magnetic field. The results for weak and strong bias fields are shown in Fig. 6.3. For strong fields the inhomogeneities are dominated by imperfections bias field generation, while the cause of the inhomogeneities at low field is not obvious.

3.5   Vibration isolation and tilt control

All atom interferometer measurements are easily perturbed by *relative* motions of their beam splitters and mirrors. It is therefore essential to implement these elements in an intrinsically stable way and protect them from external vibrations. For inertially sensitive interferometers, such as ours, it is furthermore necessary to protect against *common* movements of all elements, which is substantially harder to achieve. For our light pulse interferometer these requirements translate into the need to control and protect from disturbance the frequency and phase of the light field. Using stimulated Raman transitions is highly beneficial since

it replaces the resulting extremely tough requirement of milli-Hertz level laser frequency stability with a more easily achievable one for the difference frequency. Vibrations remain a problem since any movement of mirrors and other optical elements will induce Doppler shifts and thereby disturb the light.

Another peculiar complication arises for gravity measurements, since the equivalence principle explicitly states that locally it is impossible to distinguish between gravitational fields and accelerations of the measurement apparatus. Practically, this quandary is usually resolved by the fact that vibrational accelerations become negligible at frequencies well 0.1 Hz and can be eliminated by low-pass filtering the raw data using a time constant much longer than 10 s. This method is indeed used by classical spring/mass-type gravimeters, but it does not work for our atom interferometer measurements for two reasons. Most importantly, the measured signal is not a linear function of acceleration but takes the form of interferometer fringes. Large vibrations, corresponding to one or more fringe spacings, will therfore severely degrade the signal in a way that can not be compensated for. Furthermore, even small vibrations at high frequencies cannot simply be filtered out because the measurement is pulsed or, in other words, sampled. The Nyquist theorem then states that after sampling it is impossible to distinguish high frequency signals from low frequency ones, much less remove them by filtering.

The purpose of a vibration isolation system is therefore twofold. First, it has to ensure that any remaining vibrations are sufficiently small to keep the signal within a single interferometer fringe. This translates into allowing only displacements of much less than a single optical wavelength during a single interferometer sequence (~ 320 ms). Furthermore, the vibration isolator has to act as an anti-aliasing filter to reduce any vibrational noise above the Nyquist frequency (~ 0.4 Hz for 1.3 s between measurements) to acceptable levels before sampling. Standard optical table pneumatic isolators, while working nicely at high frequencies, do not provide any isolation at the required low frequencies and actually add noise around their typical resonance frequencies of 2 Hz. The situation therefore calls for a system with a much lower resonance frequency. Given the properties of the geological background noise — there are particularly strong vibrations, called micro–seism, at periods of ~ 5 and ~ 8 seconds — the resonance frequency should be substantially less than 0.1 Hz.

Independent of the exact nature of the vibration isolation system there are two different approaches (Fig. 3.20) to achieve stable Raman light fields. One options is to route the two beams to the interaction region independently. This has the advantage of being very clean
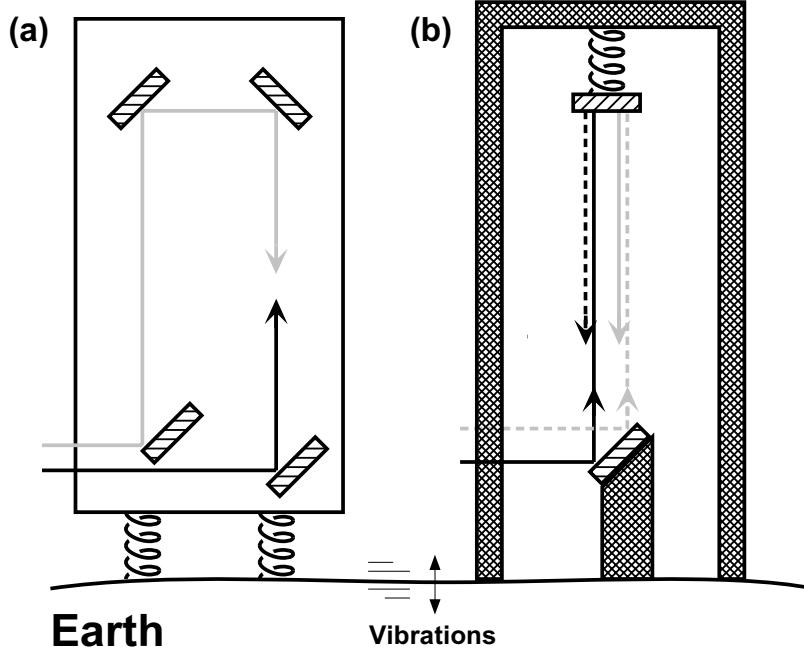
Figure 3.20: Different schemes for vibration isolation. (a) Without retro–reflection. (b) With retroreflection. Depending on their propagation direction different frequency components (light, dark) either do (solid) or do not (dotted) drive Doppler sensitive Raman transitions.

and avoiding some potential systematic errors due to standing wave effects. The disadvantage of the scheme is that it requires extreme stability of all optical components relative to each other and vibration isolation of the complete system. In our setup we employ the second method. Here, the two Raman beams are always co-propagating and are retro–reflected after passing through the interaction region. One frequency component in the upward propagating beam together with the other one in the downward propagating beam will drive Doppler sensitive Raman transitions. All other combinations do not contribute because of polarization selection rules and detuning from the Raman resonance condition. This scheme has the advantage that the vibrations of almost all optical components are common mode for both beams and cancel. The only exception are motions of the retro-reflection mirror which is therefore the only element that needs to be isolated against vibrations.
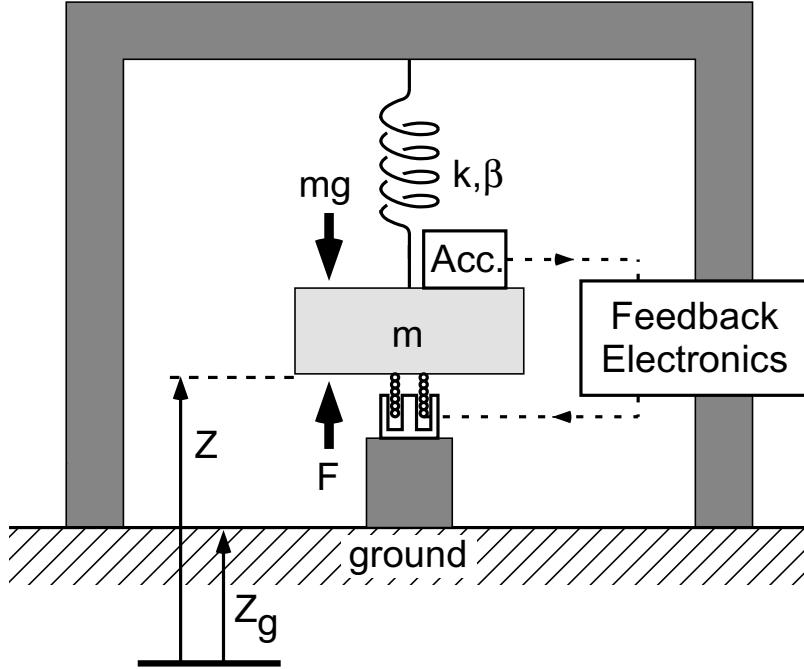
Figure 3.21: Vibration isolator schematic.

3.5.1 Vertical active vibration isolation

Since the interferometer is mainly sensitive vertical accelerations a single axis low frequency vibration isolation system is sufficient to achieve major reductions in measurement noise.

Passive vertical vibration isolation using a spring suspension is not possible at low frequencies. For a linear spring supporting a mass against a gravitational acceleration g the resonance frequency is $f_0 = \frac{1}{2\pi}\sqrt{g/L}$, where L is the spring extension from equilibrium. Achieving a resonance frequency of $0.1\,\mathrm{Hz}$ would thus require a prohibitively long spring extension of more than $25\,\mathrm{m}$. We have therefore constructed an active system that combines relatively short mechanical springs with an electronic feedback system to create an almost critically damped spring–mass system with an effective resonance frequency of $\sim 0.005\,\mathrm{Hz}$.

We now describe the basic theory, implementation and performance of the active vibration isolation system. A more detailed discussion of a very similar active vibration isolation can be found in [38].

We start with a mass m that is suspended from a linear spring (we assume that the spring suspension point and the ground are rigidly connected) with spring constant k and damping factor β (Fig. 3.21). We want to decouple its motion $z(t)$ from any motion $z_g(t)$

of the ground (both measured relative to a stable reference point). This system has the equation of motion

$$\ddot{z} + 2\zeta_0\omega_0(\dot{z} - \dot{z}_g) + \omega_0^2(z - z_g) = 0\,, \tag{3.3}$$

where $\omega_0^2 = k/m$ is the natural resonance frequency and $\zeta_0 = \beta/(2m\omega_0)$ the damping constant ($\zeta_0 = 1$ for a critically damped system). In our system we typically have a natural resonance frequency of $1\,\mathrm{Hz}$ and very little damping ($\zeta_0 = 0.03$).

In order to lower the resonance frequency of the system we use a magnetic actuator to apply two additional forces, F_a and F_v, to the suspended mass. $F_a = -mG\ddot{z}$ is proportional to the acceleration of the mass and $F_v = -2m\omega_0 H\dot{z}$ is proportional to its velocity. Here G and H are constants determined by the feedback electronics and $\ddot{z}$ and $\dot{z}$ are both derived from the signal of an accelerometer mounted to the suspended mass. The resulting equation of motion

$$(1 + G)\ddot{z} + 2\zeta_0\omega_0((1 + H)\dot{z} - \dot{z}_g) + \omega_0^2(z - z_g) = 0 \tag{3.4}$$

shows that the system now has a new resonance frequency $\omega_1 = \omega_0/\sqrt{G+1}$ and a new damping factor $\zeta_1 = (\zeta_0 + H)/\sqrt{G+1}$. Increasing the gain G lowers both the resonance frequency and the damping. To compensate for the loss in damping, it is also necessary to increase the gain H.

In the real system the acceleration of the mass is measured by a low noise, low frequency force feedback accelerometer (Guralp CMG-3V) and then digitized using a 16–bit data acquisition board (National Instruments AT-MIO-16X). The signal is then processed by a digital loop filter that implements the gains G and H (typically $G \approx 10000$, $H \approx 300$) but also contains additional compensators to maintain closed-loop stability at high ($\sim 80\,\mathrm{Hz}$) as well as low ($\sim 0.001\,\mathrm{Hz}$) frequencies [38]. To close the feedback loop the output signal is converted back into analog form and used to control the current through the solenoid actuator (BEI LA 12–12 A).

The physical implementation of the vibration isolator (Fig. 3.22) differs from the one in [38] mainly by using only two springs and a different permutation of components. Placing the air piston on top makes the system more stable. The axis of the air piston must be parallel to $\mathbf{k}_{\mathrm{eff}}$ and $\mathbf{g}$ to achieve optimal performance.

Alignment is critical for a single axis system such as this one. We have therefore expended substantial effort on making the axis of the air piston, the sensitive axis of the
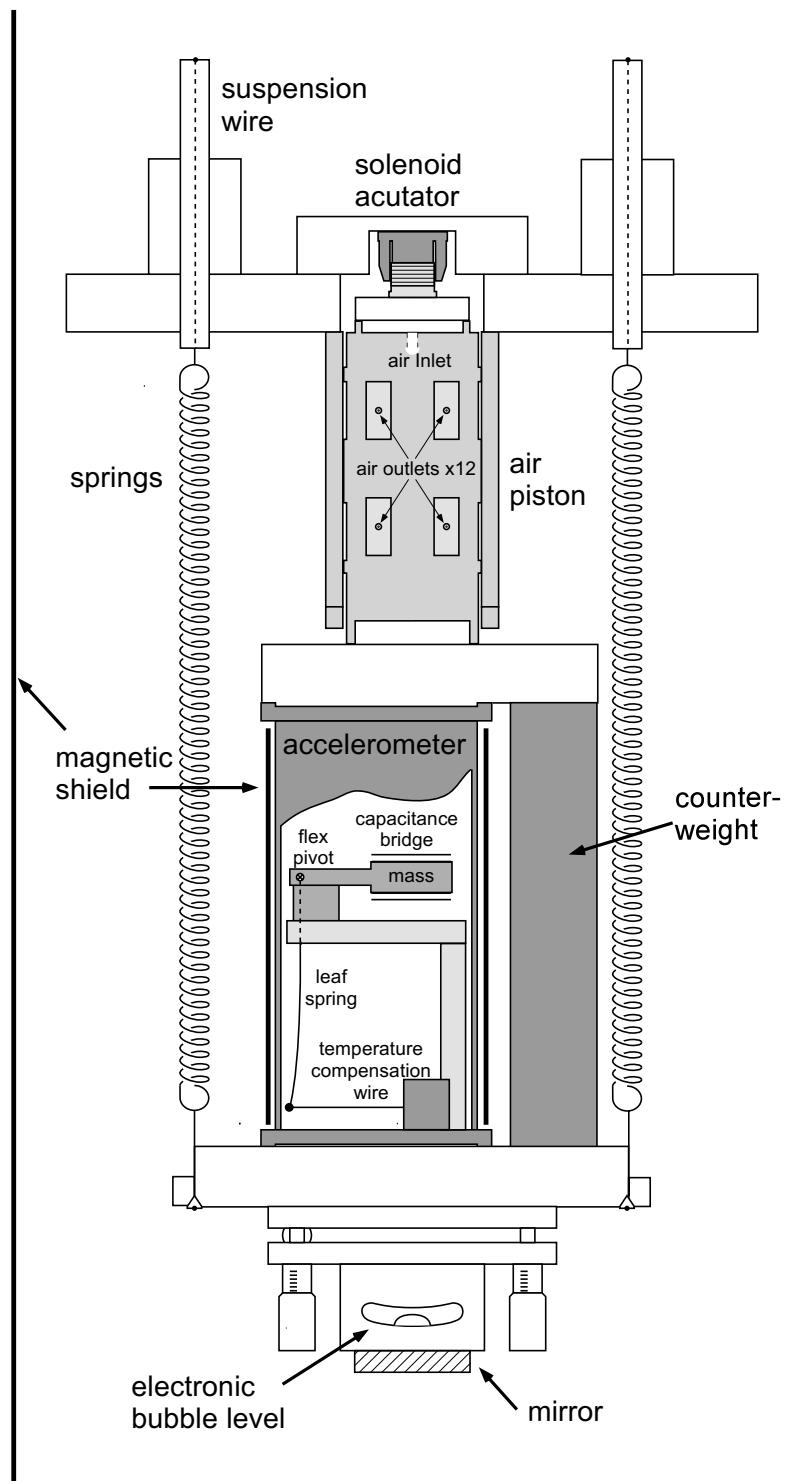
Figure 3.22: Vibration isolator mechanical system.

accelerometer and the direction of light propagation (normal to the mirror surface) parallel to each other and ultimately the vector of gravity. To aid this alignment we have also added an electronic tilt sensor (Sec. 3.5.3). The accelerometer is offset to the side so that its internal test mass is on the symmetry axis of the system. This is important, since otherwise the system would translate benign rotational noise into unwanted vertical vibrations. To reduce sensitivity to magnetic fields the accelerometer itself is fitted with a magnetic shield (Magnetic Shield Corp. 35P70) and additionally the whole vibration isolator is enclosed with magnetic shielding material.

Figure 3.23 shows the performance of the vibration isolation system. Without electronic feedback the combination of optical table pneumatic isolators and vibration isolator spring suspension already reduces vibrations substantially at frequencies above 3 Hz, but at the expense of some amplification at the mechanical resonance frequencies of 1.2 Hz (springs) and 1.8 Hz (table). Turning on the electronic feedback further reduces low vibrations in the 0.01 to 10 Hz frequency band. The error signal (bold line) indicates a reduction by as much as a factor of 300, but without an independent sensor we cannot be sure that the true performance is as good. However, the great improvement of our interferometer signal (Sec. 5.2) provides strong supporting evidence.

3.5.2   3D active vibration isolation of optical table

While the main vibration isolation system works well it has intrinsic performance limitations due to its one–dimensional nature. Most importantly, it cannot eliminate rotational vibrations around the two horizontal axes. Since the atom interferometer can also be sensitive to rotations (Sec. 5.3.5, 6.5.1), these rotational vibrations, particularly when enhanced close to the table resonance frequency (~ 2 Hz), could potentially dominate the interferometer noise.

To eliminate this potential problem we have added a 3D (vertical, x-tilt, y-tilt) feedback system to control and vibrationally isolate the whole optical table. The system uses three single-axis, force-feedback accelerometers (Kinemetrics FBA-11, 10 V/g, flat acceleration response to 90 Hz) to sense vertical accelerations at three different points of the L-shaped optical table (Fig. 3.24). Their amplified signal is then digitized, electronically filtered and fed back to a set of three magnetic actuators (loudspeaker coils) mounted directly underneath each sensor.

Each amplifier has a gain of 1000, includes 400 Hz low pass filters and an additional
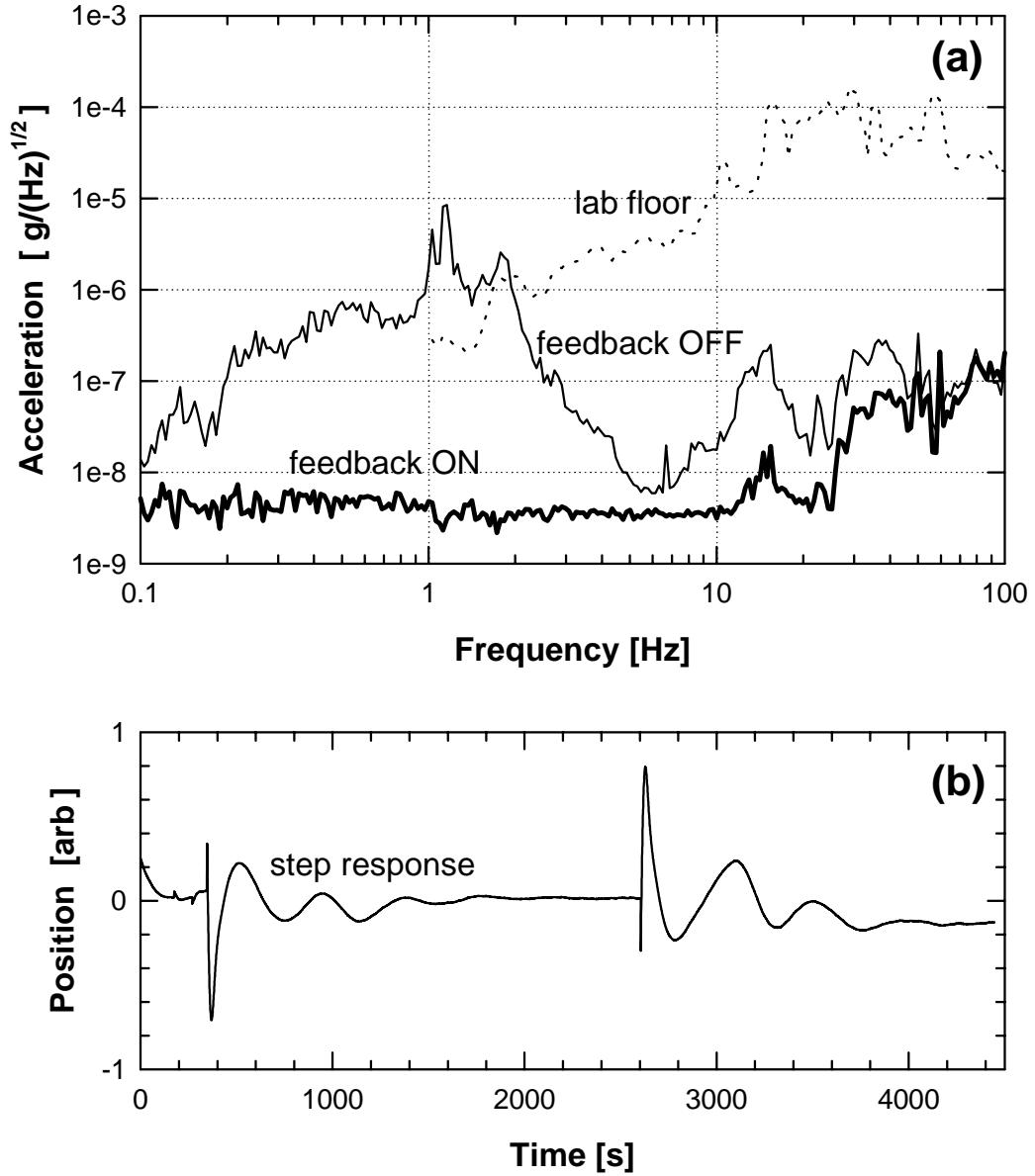
Figure 3.23: Vibration isolator performance. (a) Acceleration noise spectral density measured by the vibration isolator accelerometer. Passive spring isolation of the optical table and the isolator spring suspension (solid line) reduce the high frequency vibrations relative to the lab floor (dotted line). Turning on the electronic feedback (bold line) additionally suppresses low frequency vibrations. Below 10 Hz the error signal is smaller than the input noise of the spectrum analyzer used for this measurement. (b) Position response to two steps in the force acting on the suspended mass. It indicates an slightly under damped system with a natural resonance frequency of 0.0025 Hz. Achieving the same resonance frequency would require a 40 km long mechanical spring.

Cross-sectional view of one of the legs

Top View of Set-up
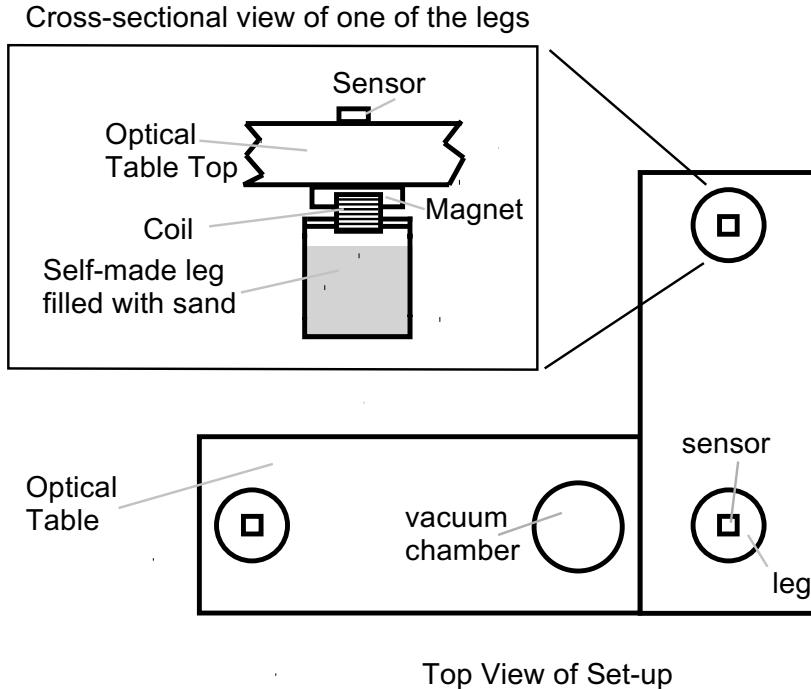
Figure 3.24: 3D active vibration isolation and tilt control system.

notch-filter to eliminate traces of the 7.5 kHz internal accelerometer excitation frequency. The amplified accelerometer signal ($10000\,\mathrm{V/g}$) is then digitized at 4000 samples/s using the same 16-bit analog input board and computer as the 1D system. The feedback software is also just an extension of the 1D version, but an additional 12-bit analog output board (National Instruments AT-AO-10) has been added to handle the new channels. The output signals are then converted into currents and drive three magnetic voice coil actuators, which in turn apply forces to the optical table.

In contrast to the $ 1000 BEI voice coil actuator in the 1D-system, the 3D-actuators are taken from old loudspeakers, purchased at a flea-market for $ 10 each. These cheap actuators have some drawbacks compared to actuators specifically designed for feedback applications: they need bigger magnets to achieve the same level of force, produce stronger stray magnetic fields, are hard to mount and have a very tight air gap. While the first points are of no concern for our application, it would be nice to have a wider air gap to allow bigger horizontal table movements before the coils start to rub. However, if one carefully aligns the coils properly and takes care not to bump the optical table too hard then the old loudspeakers are perfectly adequate.

The feedback parameters of the system can be adjusted to achieve new table resonance periods of 3 or 10 seconds. In either case the former, troublesome resonances at 2 Hz are completely suppressed. The system's performance at high frequencies is not as good as originally envisioned since the feedback bandwidth is currently limited to about 30 Hz by some not yet identified mechanical resonances. The optical table itself should be stiff enough to allow bandwidths of more then 100 Hz, so the problem probably lies with the voice coil actuators and their support structure. This could certainly be changed if better performance should be desired in the future, and it would also be possible to improve the not yet fully optimized feedback software: while the system currently uses three independent single input, single output (SISO) feedback paths it would benefit from a fully integrated multiple input, multiple output (MIMO) design which takes care of all possible cross couplings and might even include the additional 1D–stage.

3.5.3 Tilt control

The quantity of interest for local gravity measurements is usually the absolute magnitude, $|\mathbf{g}|$, of the local acceleration vector[§]. The atom interferometer, on the other hand, measures only the component of gravity in the direction of the effective Raman wave vector k_{eff}, which is evident from the formula for the interferometer phase shift

$$\Delta\phi \;\; = \;\; \mathbf{g} \cdot \mathbf{k}_{\text{eff}} T^2 \;\; = \;\; |\mathrm{g}||\mathbf{k}_{\text{eff}}| T^2 \cos\theta \,. \tag{3.5}$$

In order to measure the correct magnitude of local gravity, it is therefore important to have the effective Raman wave vector properly aligned along the vertical axis. This means that the misalignment angle θ has to be less than $45\,\mu$rad ($9\,$arcsec) to achieve a measurement accuracy of 1 μGal, and less than $14\,\mu$rad ($3\,$arcsec) for 1 μGal. This is not a trivial requirement since even the concrete floor of our laboratory shows daily tilt variations of typically $\pm\,20\,\mu$rad, probably caused temperature variations. And things are much worse on top of the optical table, which can easily tilt by more than $100\,\mu$rad. We have therefore implemented yet another feedback system to control tilt.

Since in our setup the effective wave vector is normal to the surface of the retro-mirror, we rigidly attach a 2-axis, high resolution electronic bubble level (Applied Geomechanics

---

[§]In principle all components of the vector $\mathbf{g}$ would be of interest, but to interpret them properly one would need to know their orientation relative to an gravity independent coordinate system, which is extremely hard to realize on Earth's surface.

755-1129, 0.1 μrad resolution, 1 μrad repeatability) to the back of this mirror and use it as the tilt sensor for our feedback system. To calibrate the bubble level we rotate the whole assembly through 360 degrees, using three ball bearings in contact with the mirror surface as our reference plane, and observe the sinusoidal modulation of the output signal. This method allows us to determine horizontal orientation to within $\pm\,5\,\mu$rad.

Any measured deviations of the retro-mirror from its proper horizontal orientation are compensated for by adjusting the tilt of the whole optical table. This is done by using two pairs of leak valves, one electronic, one manual. Each pair controls the airflow to the two pneumatic isolators at each end of the L-shaped optical table. The manual valve (Porter HRCVB1S, 1000 sccm Air max. at 75 psi) is set to allow a small amount of air to escape continuously, at a rate which would cause the table to tilt at about $1000\,\mu$rad/minute. Usually this outflow is exactly canceled by an equivalent inflow through the electronic valve (Porter EPCA08, 975 sccm Air max. at 75 psi). By electronically adjusting this inflow it is now easily possible to make the table tilt one way or the other. Since the inflow is also proportional to the input pressure, it is important to keep this pressure constant to prevent disturbances of the system. We use a high quality pressure regulator (Porter 8310-AMBF-100) to keep it fixed at 70 psi, approximately 15 psi higher than the maximum pressure inside the pneumatic isolators.

The loop filter for this feedback system is implemented using analog electronics and set for a slow time constant of approximately 2 minutes. Currently, the feedback for the two tilt axes is implemented independently and the electronic feedback system does not regulate the airflow to the central four air legs and has therefore no control over the average height of the table. There are two possible modes of operation: The central air legs can be valved off and the low leakage rate allows several days of runtime before the table settles too much (~ 1 mm). Alternatively, one can use a standard mechanical leveling valve if very long run times are necessary and the resulting disturbances can be tolerated. In principle it is also possible to add a third pair of valves for the central air legs and use an electronic position sensor[¶] to keep the table height constant. In this case it would also be necessary to change the loop filter in order to replace the two independent single-axis (SISO) channels with a more general 3-axis (MIMO) feedback method.

[¶]We have actually installed a LVDT (Linear Variable Differential Transducer) position sensor (Schaevitz 200 HR, $\pm\,5$ mm range, $<1\,\mu$m resolution), together with a signal conditioning unit (RDP E308). We don't currently use it for feedback, but it is very useful for several other purposes.

We have also tested the systems performance using a second, independent tilt sensor which is mounted to the main body of the optical table. The short term regulation is better than $1\,\mu$rad. Over periods of several days there are very slow drifts of up to $\pm\,20\,\mu$rad, but these are probably not due to a problem with the feedback system. Instead, they are most likely an indication for slight warping of the tower structure supporting the vibration isolator and the main tilt sensors attached to it. Such warping could, for example, result from small temperature fluctuations. In order to gather more information, one could use two tilt sensors mounted very close to each other.

In summary, the tilt control system is extremely reliable and a pleasure to work with. It can be turned on without problems and does not require any further user intervention.

Chapter 4

Experimental Results

In this chapter we present our experimental results, starting with the demonstration of simple Raman transitions and then proceeding to measurements of increasing complexity. While we briefly comment on the noise sources affecting these measurements, we otherwise defer the in depth discussion of this important topic to Chapter 5. Similarly, while we present the results of an experimental comparison between our atom interferometer and a classical "falling corner–cube" gravimeter, we leave the thorough investigation of potential systematic errors and their implications to Chapter 6.

Most of our measurements were performed using retro reflected Raman beams in $lin\perp lin$ configuration (Sec. 3.4.4) to drive Doppler sensitive Raman transitions. The exception are a few tests that were conducted using Doppler insensitive Raman transitions driven by co–propagating Raman beams in σ^+–σ^+ configuration. This modification is useful since it allows one to investigate noise and systematic errors in a somewhat simpler system that is not affected by vibrations or the initial velocity distribution of the atoms.

4.1   Rabi Oscillations

The decay of the Rabi oscillation amplitude for increasingly longer pulse lengths is a good indicator for the performance of our Raman pulses. Fig. 4.1 shows such Rabi oscillation decay under actual experimental conditions and Fig. 4.2 demonstrates how well the detuning dependence follows theoretical predictions.

The primary cause for the decay are the slightly different conditions encountered by different atoms in the atomic cloud. Examples are the variation of the Rabi frequency
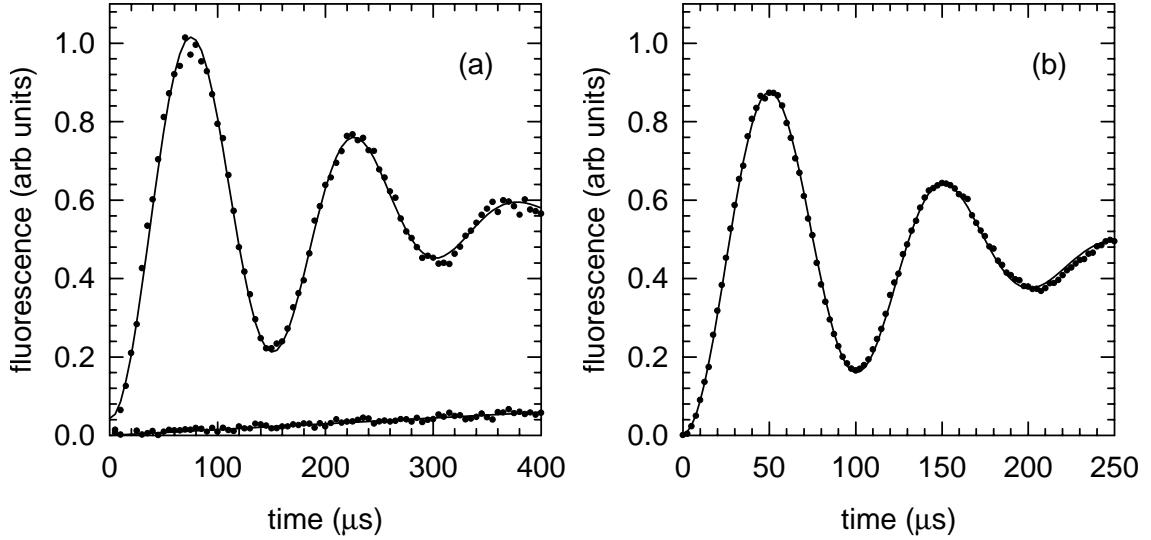
Figure 4.1: Rabi oscillations for Doppler sensitive (a) and Doppler insensitive (b) Raman transitions. The solid lines are experimental fits for a Gaussian decay envelope. (a) also shows the small population transfer caused by spontaneous emission due to the finite detuning Δ from the intermediate state. To obtain this data the laser difference frequency was detuned from the Raman resonance condition by $\sim 1\,\mathrm{MHz}$.
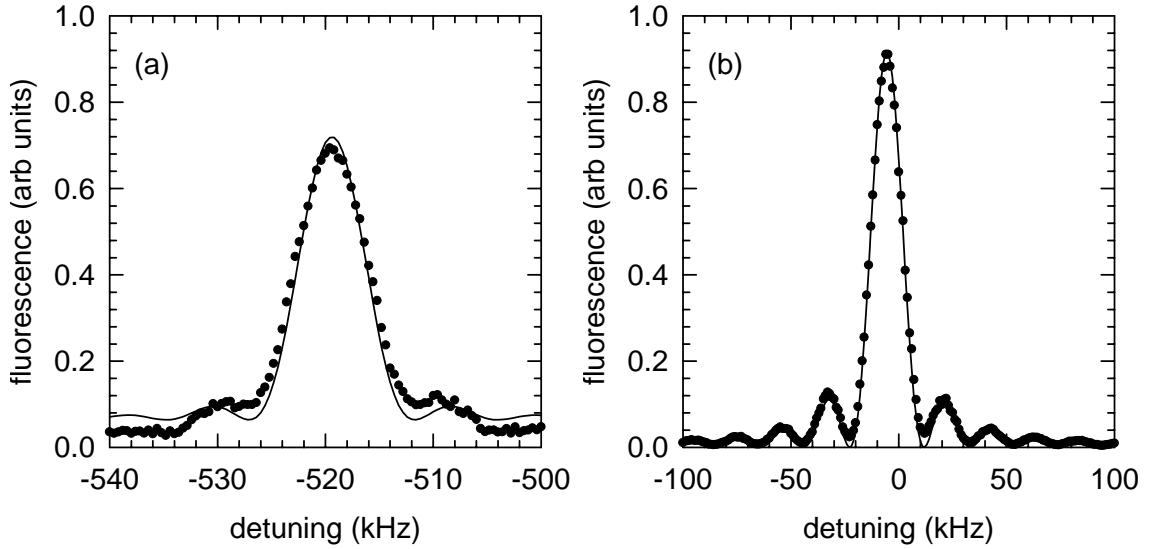
Figure 4.2: Frequency dependence of the transition amplitude for a square Raman π-pulse. In the Doppler insensitive case (b) the data (dots) is described extremely well by the theoretical Rabi formula (line) and side lobes are visible up to very high order (≈ 50). In the Doppler sensitive case (a) the atomic velocity distribution smears out the peak somewhat, even for severe velocity preselection. However, the first order side lobes are still visible.

depending on the position in the Gaussian Raman beam intensity envelope and, in the Doppler sensitive case, the different detunings for different atomic velocity classes. For our standard beam diameter of 2.7 cm displacements of as little as 1 mm can cause obvious differences in the decay rate.

We have achieved essentially the same performance for Doppler free and Doppler sensitive transitions, something that is only possible because of severe velocity preselection.

4.2   Interferometer Fringes

To measure gravity we combine the individual, optimized Raman pulses into the $\frac{\pi}{2} - \pi - \frac{\pi}{2}$ atom interferometer sequence. Fig. 4.3 shows a typical gravity fringe for an interferometer pulse spacing of $T = 160$ ms, close to the maximum permitted by the finite size of the magnetically shielded measurement region. Acquiring and fitting a sequence of such 1 minute fringes allows us to measure gravity with a resolution of 2.0×10^{-8} g/$\sqrt{\text{Hz}}$. Taking data by sitting on the slope of a fringe gives an even higher resolution of 1.5×10^{-8} g for a single launch or 1.7×10^{-8} g/$\sqrt{\text{Hz}}$.

4.3   Long Term Gravity Data

To perform useful measurements any gravimeter has to be able to operate continuously over extended periods of time. The gravity data in Fig. 4.4 demonstrates that our atom interferometer is indeed able to operate continuously for many days.

Figure 4.4 also illustrates the very important fact that the local acceleration due to gravity is definitely *not* constant. Instead, it displays a complicated time dependence caused mostly by tidal forces. Although these tidal effects are often an object of study themselves, they are considered a predictable perturbation in the context of absolute gravity measurements and are corrected for using theoretical tide models.

Since the tidal effects are large compared to the instrumental resolution and targeted accuracy it is essential to model them properly. At first glance the theoretical curve in Fig. 4.4 seems to match the experimental data extremely well. However, detailed examination of the data in Fig. 4.5 makes clear that standard tide models, even if they include the Earth's elastic response to tidal forces, are totally inadequate at this level of precision.

The obvious discrepancy between the standard tide model and the experimental data
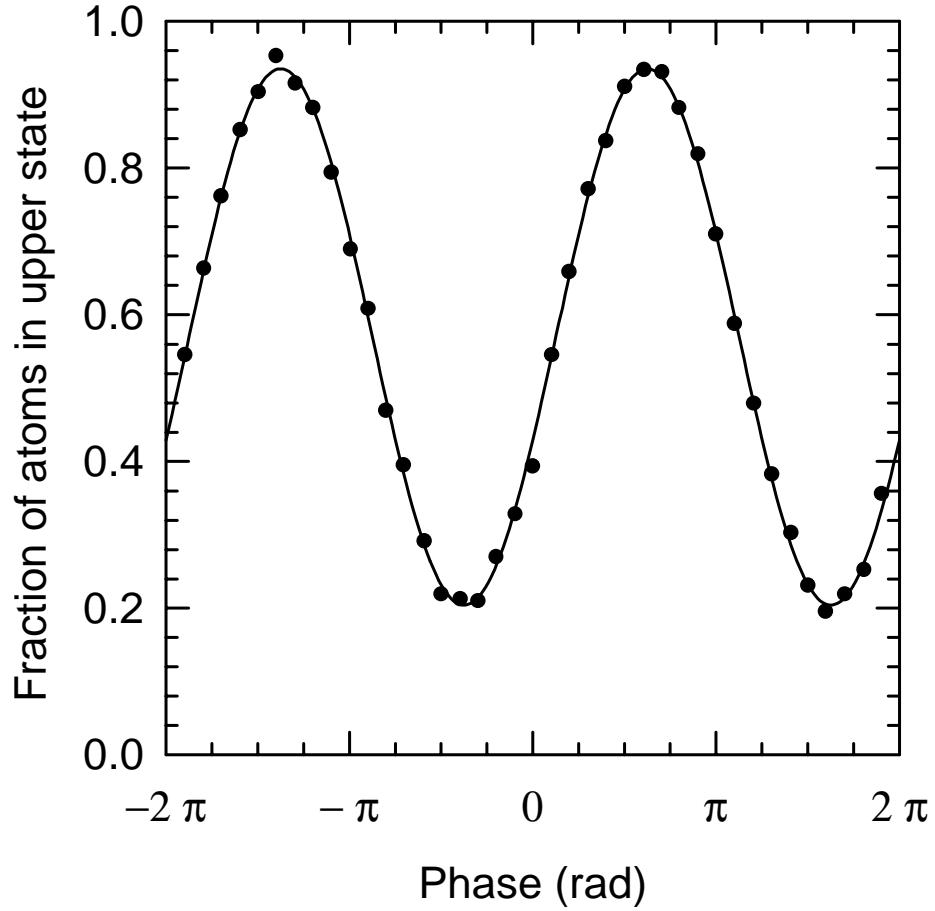
Figure 4.3: Typical Doppler sensitive interferometer fringe for a pulse spacing of $T = 160\,\mathrm{ms}$, the same as used for most of our gravity measurements. Plotted is the fraction of atoms excited from the $F = 3, m_F = 0$ state to the $F = 4, m_F = 0$ state. The phase of the fringe is scanned by adjusting the frequency step size Δf (see Sec. 3.4.2). The durations of the π and $\frac{\pi}{2}$ pulses are 80 and $40\,\mu\mathrm{s}$, respectively. The phase of the fringe is scanned by adjusting $\Delta f_2 - \Delta f_3$ (see Sec. 3.4.2, Fig. 3.16). Each of the 40 data points represents a single launch of the atoms, spaced 1.3 seconds apart and taken over a period of 1 minute. One full fringe period corresponds to $\sim 2 \times 10^{-6}\,\mathrm{g}$. Performing a least squares fit determines local gravity to approximately $3 \times 10^{-9}\,\mathrm{g}$.
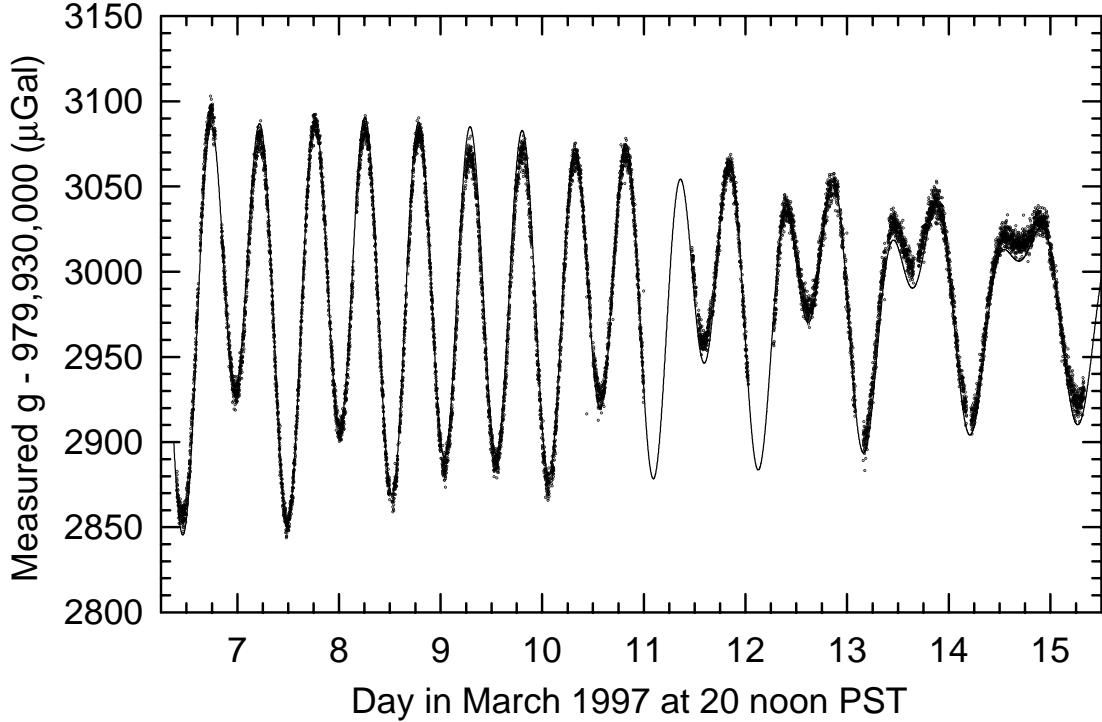
Figure 4.4: Gravity data taken over a period of several days. The data points are spaced approximately 1 minute apart and each corresponds to one of the interferometer fringes shown in Fig. 4.3. The data clearly shows the complex variations in g caused (mostly) by tides. The solid line is a single parameter (vertical offset) fit using a theoretical model of the gravity tides at our measurement site (Stanford, California).

can be attributed to a phenomenon that is known as ocean loading [39, 40]. Ocean loading is caused by the redistribution of the water in Earth's oceans in response to tidal forces. When more water is present at a certain location, its mass will increase the pressure at the ocean floor and depress it slightly. This minute change in the shape of the planet, not direct gravitational attraction by the water, is the cause of the periodic residuals in Fig. 4.5.

Including an ocean loading model [41, 42] reduces the discrepancy between data and theory significantly, but there still seems to be a slight periodicity visible in the new residuals, indicating that even this ocean loading model might not be good enough. However, one can reduce the influence of the essentially periodic imperfections by always averaging over an integer number of full cycles.
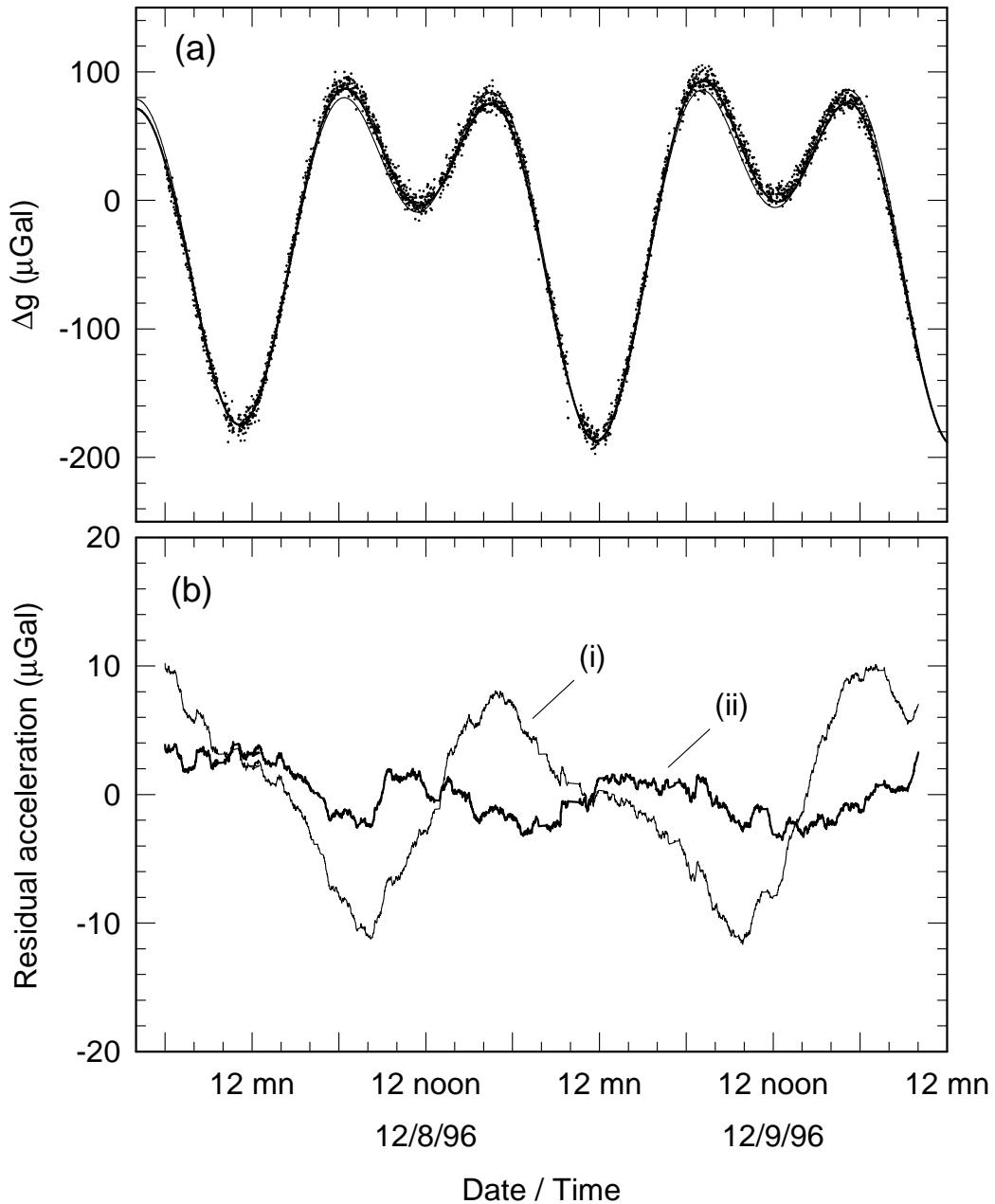
Figure 4.5: (a) A closer look at two days of gravity data. Each data point represents a one minute gravity measurement. The solid lines represent two different tidal models. (b) The residuals of the data with respect to a tidal model where (i) the Earth is modeled as a solid elastic object and where (ii) the effects of ocean loading of the Earth are taken into account. Effects at the few parts per billion level like changes in the local barometric pressure have not been included.

4.4   Comparison with Classical Gravimeter

The only sensible way to determine the atom interferometers accuracy is to compare it directly to other absolute gravimeters. The fact that local gravity, unlike the value of fundamental physical constants, is site dependent complicates such a comparison. Both instruments have to determine gravity at the same location and, since gravity values are sensitive to changes in the local environment, it is also desirable to perform the measurements simultaneously.

We have been able to perform such a comparison in our laboratory and over a period of 3 days, using an FG5 absolute gravimeter provided by the *National Science Foundation* (NSF) and operated by *National Ocean and Atmosphere Administration* (NOAA). The FG5, one of the most advanced absolute gravimeters currently available, measures gravity by monitoring the motion of a freely falling corner–cube acting as the retro-reflector in one arm of a Michelson laser interferometer. The accuracy of this instruments is usually specified as 2 μGal, but data from international gravity comparison measurements [43] indicates that 4 μGal is a more realistic number.

In addition to testing the atom interferometer's accuracy we were also interested in comparing the measurement noise of the two instruments. The resolution of the FG5 gravimeter is specified to be as good as 5 μGal for a single drop under ideal conditions (seismologically quiet site, far removed from civilization and related noise) and theoretically the repetition rate could be as high as 1 drop per second. This would mean a resolution of 5 μGal$/\sqrt{\text{Hz}}$, substantially better than the 20 μGal$/\sqrt{\text{Hz}}$ achieved by our atom interferometer. However, our laboratory is definitely not an ideal site as described above. It is located on the second floor of the busy physics building which itself is surrounded by major demolition and construction sites. It was therefore very interesting to see how the FG5 gravimeter would perform under these circumstances.

We also learned that the drop rate of the classical instrument is practically limited to about 1 drop every 15 seconds. Otherwise, mechanical wear would reduce the lifetime of the instrument and the lack of sufficient settling time for drop related vibrations could compromise the instruments accuracy. The repetition rate of our atom interferometer, on the other hand, is basically determined by the interferometer pulse spacing T and the loading time for the MOT. Currently it is limited to one launch every 1.3 s by the finite time necessary to reprogram the DDS synthesizer between launches.
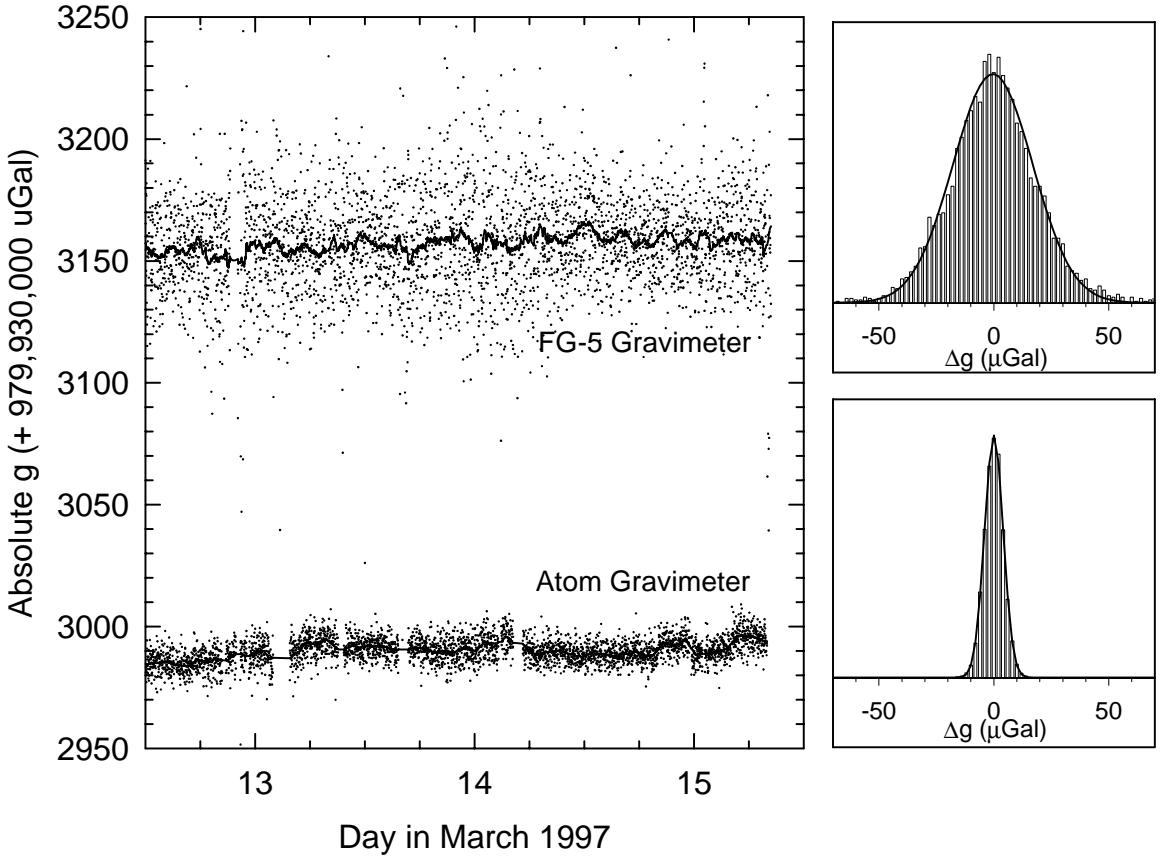
Figure 4.6: Comparison between atom interferometer (lower dataset) and classical gravimeter (upper dataset). Each point represents 1 minute of tide corrected gravity data, which corresponds to 4 drops of the corner–cube and 40 launches of the atoms. The continuous lines are running averages (30 minutes). The histograms show distribution of the 1 minute data points around the mean (for every 30 minute interval). Compared to the classical instrument, the measurement noise of the atom interferometer is smaller by a factor of 3 for equivalent measurement times. The noise per drop (launch), on the other hand, is comparable.

The original data from comparison measurement is summarized Fig. 4.6. To compare the resolution of the two instruments with their different sampling rates we binned the data into same length intervals (1 minute, corresponding to 40 atom launches and 4 corner-cube drops). Looking at the data it is immediately obvious that the noise of the atom interferometer measurement is lower by a factor of 3 when normalized to measurement time, even though the performance per drop is comparable.

Comparing the absolute gravity values is more complicated since the measurements were taken at slightly different locations and measurement heights (Sec. 6.5.2). After accounting for the different locations, we found that there was still an offset of approximately 175 μGal (Fig. 4.6). We later discovered that most of this discrepancy could be attributed an incorrect published value for the cesium D_2–wavelength (see Sec. 6.2.1). Using a better wavelength value to analyze our data immediately reduced the discrepancy to less than 40 μGal.

Subsequently, we have investigated many potential systematic errors (see Chapter 6). We found that two effects in particular, Coriolis forces due to Earth's rotation (Sec. 6.5.1) and disturbances of the vibration isolation system by the pulsed magnetic fields of the experiment (Sec. 6.4.2) were responsible for most of the residual 40 μGal offset. We have been able to essentially eliminate the second effect by enclosing the whole vibration isolator inside a magnetic shield. We have also put substantial effort into minimizing the effect of Coriolis forces by proper alignment.

After implementing these improvements and with a much better knowledge of the remaining problems we have performed another gravity measurement, the results of which we will present in the final chapter of this thesis (Chapter 7).

Chapter 5

Noise

Our atom interferometer currently has a resolution of $\sim 2 \times 10^{-8}$ g for a single launch of the atoms. As shown in Sec. 4.4 this is at least comparable, if not better, than the performance of classical absolute gravimeters. It is also a big improvement over the first atom interferometer measurements by Kasevich and Chu in 1991 [11], which had a resolution of $\sim 3 \times 10^{-6}$ g per launch.

For the early experiments the noise was clearly dominated by residual vibrations. Now, after many improvements and the implementation of an active vibration isolation system, the situation is substantially more complicated. We have investigated the effect of many noise sources, using theoretical analysis as well as experimental measurements.

The experimental measurements used both, counter–propagating Doppler sensitive and co–propagating Doppler insensitive* configurations to differentiate noise due to vibrations and rotations from noise contributions related to the phase measurement itself.

5.1 Definitions

We first define the term "resolution" of a gravity measurement in the context of this experiment. Assume we have a sequence of equally spaced gravity measurements $g_n = g(t_n)$ with $t_{n+1} = t_n + \tau$, where τ is the time between two consecutive measurements. One possible

---

*Even in Doppler "insensitive" mode our interferometer can measure the small residual Doppler shift with enough resolution to determine g to better than 1 part in 10^4!

characterization of the measurement noise would be to use the ordinary variance

$$\sigma_g^2 \quad = \quad \left\langle \left(g_n - \langle g_n \rangle \right)^2 \right\rangle . \tag{5.1}$$

However, this variance generally depends on the number of samples in a finite sequence of gravity measurements and might diverge for infinite sequences. The two–sample variance

$$\sigma_g^2(2, \tau) \quad = \quad \tfrac{1}{2} \left\langle \left(g_{n+1} - g_n \right)^2 \right\rangle , \tag{5.2}$$

on the other hand, does not depend on the number of samples. We therefore refer to this quantity as the resolution of the gravity measurement.

It is also possible to define the two–sample variance $\sigma_g(2, t)$ for longer time separations $t = N\tau$ by first taking the mean of N consecutive measurements. It is given by

$$\sigma_g^2(2, t) \quad = \quad \sigma_g^2(2, N\tau) \quad = \quad \frac{1}{2} \left\langle \left(\sum_{k=0}^{N-1} \frac{g_{n+k}}{N} - \sum_{k=N}^{2N-1} \frac{g_{n+k}}{N} \right)^2 \right\rangle . \tag{5.3}$$

If the noise of consecutive measurements g_n is uncorrelated, then we have

$$\sigma_g(2, N\tau) = \frac{1}{\sqrt{N}} \sigma_g(2, \tau) \quad \text{and} \quad \sigma_g(2, \tau) = \sigma_g . \tag{5.4}$$

Since this is the case for most of the noise sources that we have considered (except for very low frequency vibrations and rotations), we often do not distinguish between $\sigma_g(2, \tau)$ and σ_g.

We can also relate the variance of g to the signal–to–noise ratio of the experimentally observed interferometer fringes. Assume that the number of detected atoms is given by

$$x \quad = \quad A \left[1 + C \cos(\Delta\phi) \right] , \tag{5.5}$$

where $\Delta\phi = k_{\text{eff}} g T^2$ is the interferometer phase, C the fringe contrast and $A\,C$ the observed fringe amplitude. We then define the signal–to–noise ratio $(S/N) = A\,C/\sigma_x$ by comparing the variance σ_x of the signal on the slope of a fringe to the fringe amplitude $A\,C$. Assuming that neither A nor C fluctuate, the S/N–ratio and the variances of interferometer phase and gravity value are related by

$$(S/N)^{-1} \quad = \quad \sigma_{\Delta\phi} \quad = \quad k_{\text{eff}} T^2 \sigma_{\text{g}} . \tag{5.6}$$

When theoretically evaluating the effect of potential noise sources, we generally assume $100\,\%$ fringe contrast.

5.2   Evolution of interferometer performance

Figure 5.1 shows how interferometer contrast and noise evolved over time. The introduction of the active vibration isolation system was absolutely essential, allowing us to increase the time between interferometer pulses from 10 ms to more then 150 ms, corresponding to an automatic 225-fold increase in sensitivity. Without vibrations dominating the noise it soon became obvious that the microwave synthesizer controlling the Raman frequency difference was not really up to the task. Replacing it with a better system, including a frequency multiplier chain usually used for atomic clocks, allowed us to reach single launch reach resolutions of better than 1×10^{-7} g for the first time.

Further improvements over the course of several months then allowed us to reach our current noise level and a resolution of better than 2×10^{-8} g per launch. The main changes to the setup are illustrated in Fig. 5.2. Besides removing major sources of noise from the optical table and improving structural stability, meticulous alignment of the vibration isolator and the Raman beams proved to be extremely important.

Even after achieving this level of performance we continued for several months to search for additional noise sources and to implement several improvements to the apparatus — but, sadly, without any major gain in resolution. Some of the attempted modifications were admittedly more important with respect to eliminating systematic errors:

3D active vibration isolation, active tilt stabilization, counter-rotating table to cancel Coriolis forces due to Earth's rotation, better quartz frequency standard, different microwave synthesizer, canceling Doppler shift during individual interferometer pulses, moving phase–lock photo–diode to reduce phase noise, temporary elimination of all mechanical shutters, temporary shutter in Raman beams to eliminate leakage light, shielding of Raman beams from air currents, replacement of dirty vacuum chamber window for Raman beams, better beam dump for Raman beams, prevention of vibration isolator air bearing rotation, better pressure regulation for air bearing, damping of mechanical springs in vibration isolator, and magnetic shielding around vibration isolator.

5.3   Possible noise sources

Table 5.1 summarizes the most important noise sources and their estimated effect on the experiment. Their relative importance also depends on experimental parameters like the time T between interferometer pulses and, to a lesser degree, the length of those pulses.
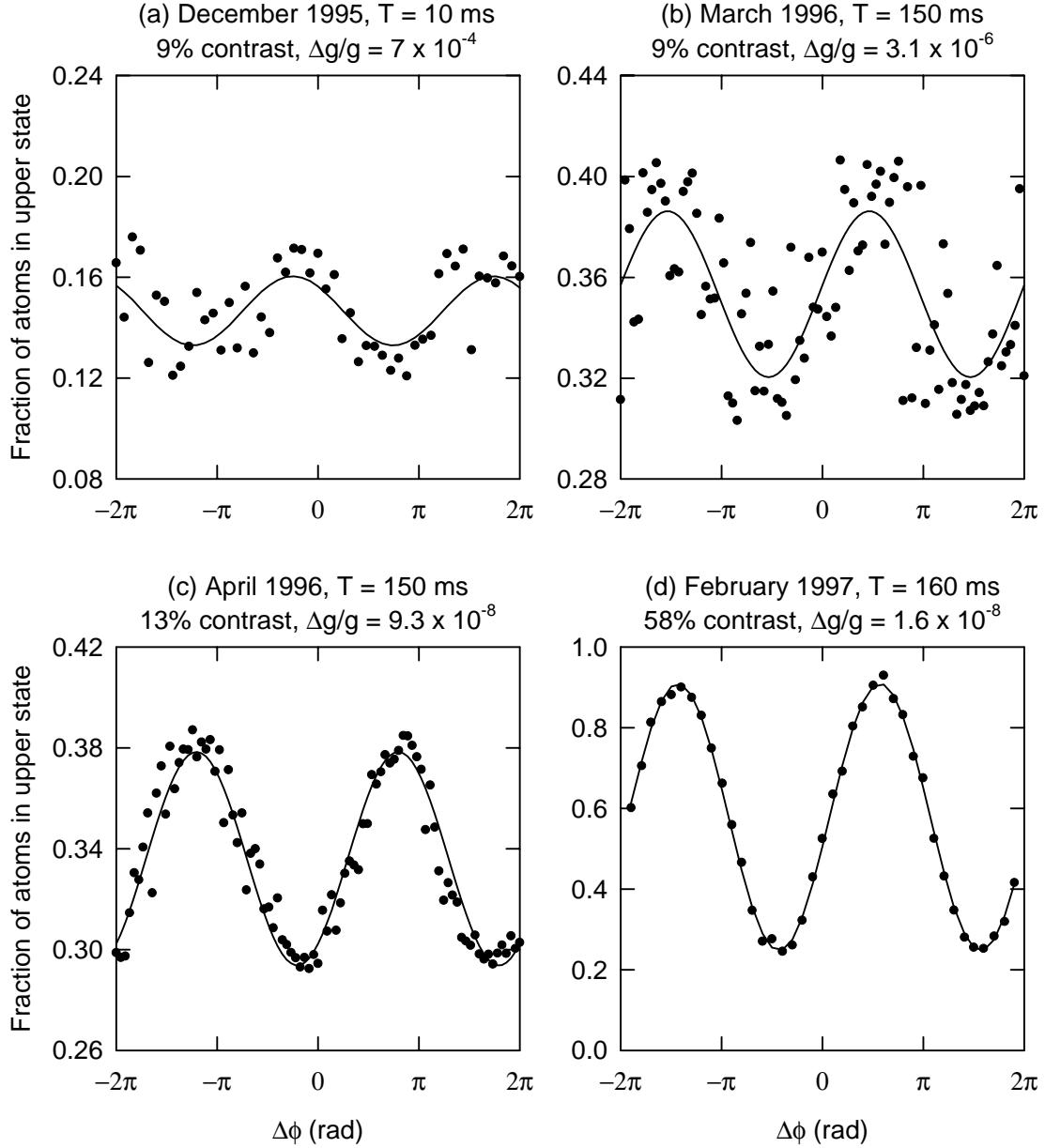
Figure 5.1: Evolution of interferometer noise and fringe contrast. T is the time between interferometer pulses, $\Delta g/g$ the measurement resolution for a single launch. Each data point also represents a single launch. (a) No active vibration isolation, optical table isolators only. (b) First result after installing vibration isolator. Note that increasing T from 10 ms to 150 ms alone results in a 225-fold increase resolution, even when the fringe looks the same. (c) After improving the Raman phase lock. (d) Final performance, after optimizing Raman beams and implementing many mechanical improvements (see text and Fig. 5.2). Improved contrast due to velocity preselection.
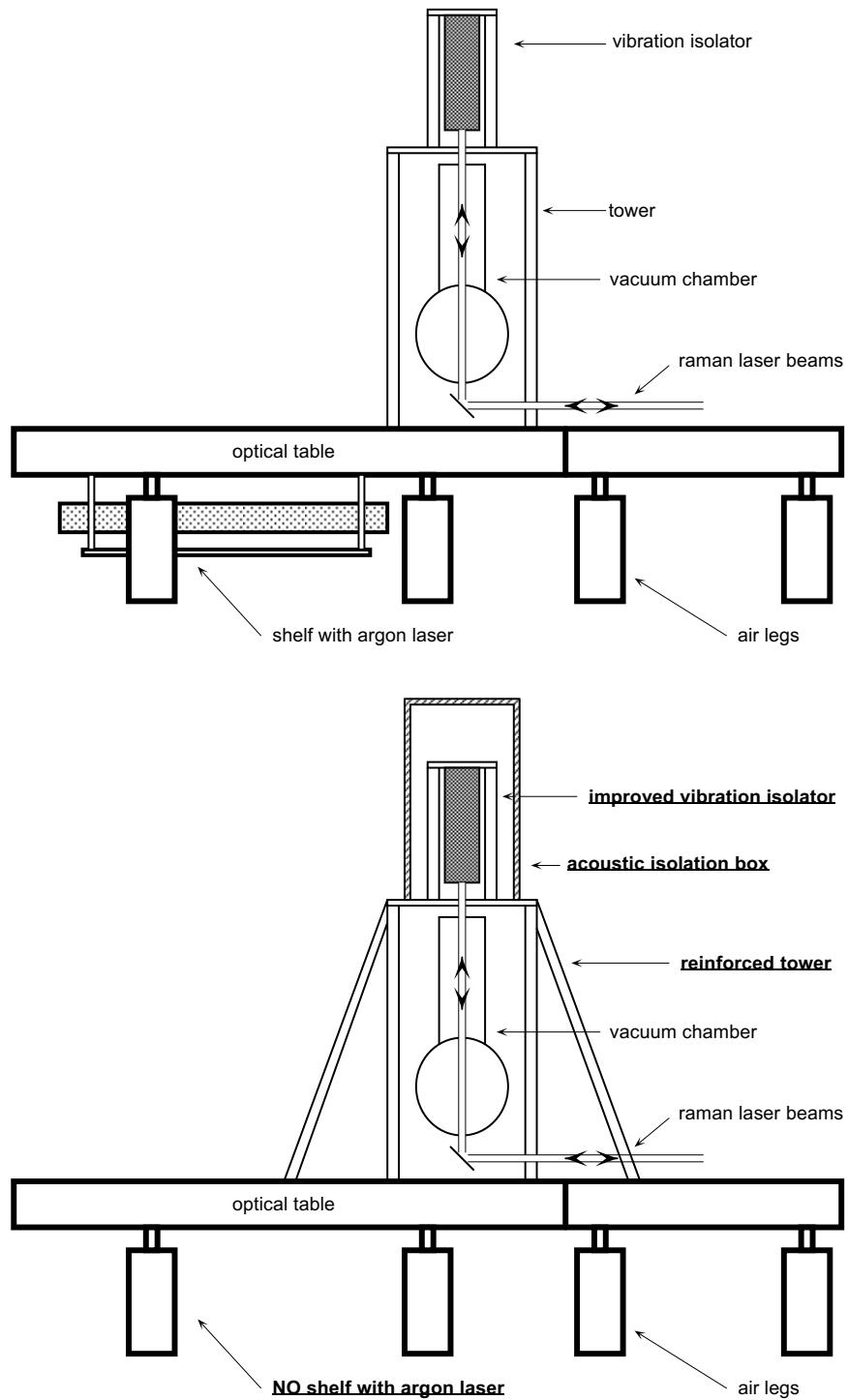
Figure 5.2: Evolution of the experimental setup to reduce noise levels. Underlined items indicate improvements.

Some effects, like shot noise or detection noise, are clearly not a problem at the current time. The remaining effects, although not large enough to fully explain the observed noise level, deserve further discussion and presentation of the experimental evidence.

Noise source	Signal/Noise	σ_{g} (μGal)
Atom shot noise (3×10^6 atoms)	1700	0.16
Detection noise	300	0.9
Loran-C frequency stability (8×10^{-13} at $1\,\mathrm{s}$, $100\,\mathrm{Hz}$ BW)	95	0.3
Raman-laser intensity noise ($\sim 0.5\,\%$)	75	3.5
High frequency phase noise ($2 \times 10^{-4}\,\mathrm{rad}/\sqrt{\mathrm{Hz}}$)	25	11
Residual vibrations and rotations	> 50	< 5
Observed noise	14	19

Table 5.1: Known noise sources and their estimated effect on a gravity measurement with $T = 160\,\mathrm{ms}$ between interferometer pulses of lengths $\tau_\pi = 100\,\mu\mathrm{s}$ and $\tau_{\pi/2} = 50\,\mu\mathrm{s}$.

5.3.1 Shot noise and detection noise

Without using specially prepared sources of atoms, like Bose–Einstein condensates, the atomic shot noise should ultimately limit the resolution of the interferometer at a level proportional to $1/\sqrt{N}$, where N is the number of contributing atoms. In our experiment $\sim 3 \times 10^6$ atoms contribute to the interferometer signal, corresponding to a shot noise limited S/N–ratio of 1700/1.

One necessary condition for shot noise limited performance is a detection efficiency sufficiently close to unity. Our fluorescence detection scheme fulfills this condition (~ 5 scattered photons detected per atom, including quantum efficiency of PMT), but is still limited by other problems. This is actually a very typical situation for pulsed experiments which use relatively large samples of atoms, since even the best detection methods seldom achieve S/N–ratios of better than 1000/1 (300/1 for our system) for a single measurement.

Continuous measurements, for example on atomic beams, achieve shot noise limit performance more readily, mostly because they generally have a better balance between number of atoms and detection noise. As an example, let us assume that we could perform our gravity measurement continuously, using the same average flux of 2×10^6 atoms per second

$(3 \times 10^6$ atoms, $1.3\,\mathrm{s}$ between launches). In principle it would take the detection system less than $1\,\mathrm{ms}$ to achieve a S/N–ratio of 300/1, but during this time only 2×10^3 atoms pass through, corresponding to a shot noise of $\sim 45/1$. The overall detection noise would therefore be shot noise limited. In other words, pulsed experiments suffer because they pile up unnecessarily many atoms in too short a time interval.

Some additional comments: The 300/1 detection S/N–ratio is probably limited by frequency fluctuations of the probe beam (its intensity is actively stabilized). For very small numbers of detected atoms fluorescence from the relatively dense cesium background vapor may dominate the noise. For Doppler sensitive measurements, including the actual interferometer, the normalization does not work as well, since atoms in different states arrive at slightly different times. Under some circumstances this can result in detection noise dominated by the $\sim 1\,\%$ fluctuations in the number of trapped atoms. While we currently only use $\sim 3 \times 10^6$ atoms per launch, this number could easily be increased to $\sim 5 \times 10^7$ atoms (using less severe velocity preselection and detection aperturing) if the shot noise limit should ever become a problem.

5.3.2   Raman–laser intensity noise

The Raman beam intensities are not actively stabilized and therefore show noticeable intensity fluctuations and the corresponding changes in the Rabi frequency affect the interferometer signal. The short term $(1\,\mathrm{Hz} - 1\,\mathrm{kHz})$ intensity fluctuations of the combined beams are typically $0.5\,\%$ or less. After the first $\frac{\pi}{2}$–pulse the fluctuations in the atomic inversion W are given by

$$\sigma_W \quad = \quad \frac{\pi}{2}\frac{\Delta\Omega}{\Omega} \quad = \quad \frac{\pi}{2}\frac{\Delta I}{I}\,. \tag{5.7}$$

After the complete interferometer sequence, and under the assumption that the intensity fluctuations for all three pulses are uncorrelated, the fluctuations at the slope of a fringe are given by

$$\sigma_{\Delta\phi} \quad = \quad \sigma_W \quad = \quad \frac{\sqrt{3}\pi}{2}\frac{\Delta\Omega}{\Omega} \quad = \quad \frac{\sqrt{3}\pi}{2}\frac{\Delta I}{I}\,. \tag{5.8}$$

Here the inversion W is also a direct measure for the interferometer phase shift $\Delta\phi$, and the $0.5\,\%$ intensity fluctuations therefore result in a S/N–ratio of 75/1.

5.3.3   Raman–laser phase noise

All the interferometer phase shifts are measured relative to the Raman phase and any Raman phase noise therefore translates directly into noise of the gravity measurement. According to $\Delta\phi = k_{\mathrm{eff}} g T^2$ the same amount of phase noise corresponds to different smaller amounts of acceleration noise at longer interferometer pulse spacings T. There are three basic contributions to the Raman phase noise:

Phase–lock noise

The phase–lock system can usually be neglected relative to the other contributions, especially when the two Raman beams are first sent through an optical fiber together before their beat note is detected by the fast photo–diode. If the photo–diode is placed before the fiber, as we have first tried, the Raman beams are not *perfectly* overlapped when part of the light is split off and sent to the photo–diode. This small imperfection causes the Raman phase at the photo–diode (controlled by the phase–lock) to differ from the one at the fiber coupler (seen by the atoms). Air currents and slight piezo movements in the external cavity lasers (Littrow configuration) affect this difference and cause noticeable, though usually still negligible, amounts of phase noise ($\sim 0.05\,\mathrm{rad}$ RMS when integrated from $1 - 100\,\mathrm{Hz}$).

Short-term stability of frequency reference

The short term stability of the quartz frequency reference, usually expressed in terms of the Allan variance $\sigma_y(T)$, is another possible problem. In fact, the atom interferometer could almost be used to measure this quantity, if there were not too many other noise sources. Let us now explain this relationship, starting with the definition of the Allan variance, or more precisely "the two-sample variance of the fractional frequency, without dead time, bandwidth limited at f_c" [25].

Let us assume that the nominal output frequency (possibly multiplied into the microwave range first) of the oscillator is f_0, that we divide time into equal intervals of length T and can somehow measure the average frequency $\bar{f}_n$ during each interval. Then the Allan variance is defined as

$$\sigma_y^2(T) \quad = \quad \left\langle \frac{(\bar{f}_{n+1} - \bar{f}_n)^2}{2 f_0^2} \right\rangle . \tag{5.9}$$

The average frequency can be expressed in terms of the phase difference between the beginning and end of each time interval,

$$\bar{f}_n \quad = \quad \frac{1}{2\pi T}(\varphi_{n,2} - \varphi_{n,1}). \tag{5.10}$$

We can now use the definitions

$$\varphi_1 = \varphi_{n,1}, \quad \varphi_2 = \varphi_{n,2} = \varphi_{n+1,1}, \quad \varphi_3 = \phi_{n+1,2} \quad \text{and} \quad \Delta\varphi = \varphi_3 - 2\varphi_2 + \varphi_3 \tag{5.11}$$

to express the Allan variance as

$$\sigma_y^2(T) \quad = \quad \frac{1}{(2\pi f_0 T)^2} \left\langle \frac{(\varphi_3 - 2\varphi_2 + \varphi_1)^2}{2} \right\rangle \quad = \quad \frac{1}{2(2\pi f_0 T)^2} \left\langle \Delta\varphi^2 \right\rangle. \tag{5.12}$$

or, using the fact that $\langle \varphi_3 - 2\varphi_2 + \varphi_1 \rangle = 0$, as

$$\sigma_y^2(T) \quad = \quad \frac{1}{2(2\pi f_0 T)^2} \left\langle \Delta\varphi^2 - \langle \Delta\varphi \rangle^2 \right\rangle \quad = \quad \frac{1}{2(2\pi f_0 T)^2} \left\langle (\Delta\varphi - \langle \Delta\varphi \rangle)^2 \right\rangle. \tag{5.13}$$

We can now compare expression for the Allan variance to the one for the interferometer phase shift,

$$\sigma_{\Delta\phi}^2 \quad = \quad \left\langle \Delta\phi^2 - \langle \Delta\phi \rangle^2 \right\rangle \quad = \quad \left\langle (\Delta\phi - \langle \Delta\phi \rangle)^2 \right\rangle, \tag{5.14}$$

and find that the two quantities are in fact proportional[†]. This means that the short term stability of the frequency reference sets a lower bound for the interferometer noise. If it is the dominant noise source, then an interferometer with time T between pulses can actually be used to measure the Allan variance $\sigma_y(T)$ of the reference.

We have measured the Allan variance of several quartz oscillators, including our Loran-C frequency reference, by comparing them to each other using the setup in Fig. 5.4. The results are shown in Fig. 5.3. The chosen measurement bandwidth of $f_c = 100\,\text{Hz}$ allows reliable measurements down to $T = 1\,\text{s}$ before being limited by white phase noise (see Section 5.3.3). We find that the Loran-C reference has the worst stability by far. It seems to have especially big problems at time scales of several minutes, probably because of badly designed system for locking the quartz to the Loran-C signal. Luckily we only care about the performance at shorter times where the Allan variance is actually pretty good. The measured value at 1 s is $\sigma_y(1s) = 8 \times 10^{-13}$, which is ~ 6 times better than the product

---

[†]For the interferometer $\langle \Delta\phi \rangle = k_{\text{eff}}gT^2 \neq 0$, but this does not make any difference for the noise. The Allan variance also depends on the measurement bandwidth f_c. For the interferometer f_c is approximately $1/(2\tau)$, where τ is the length of a single interferometer pulse.
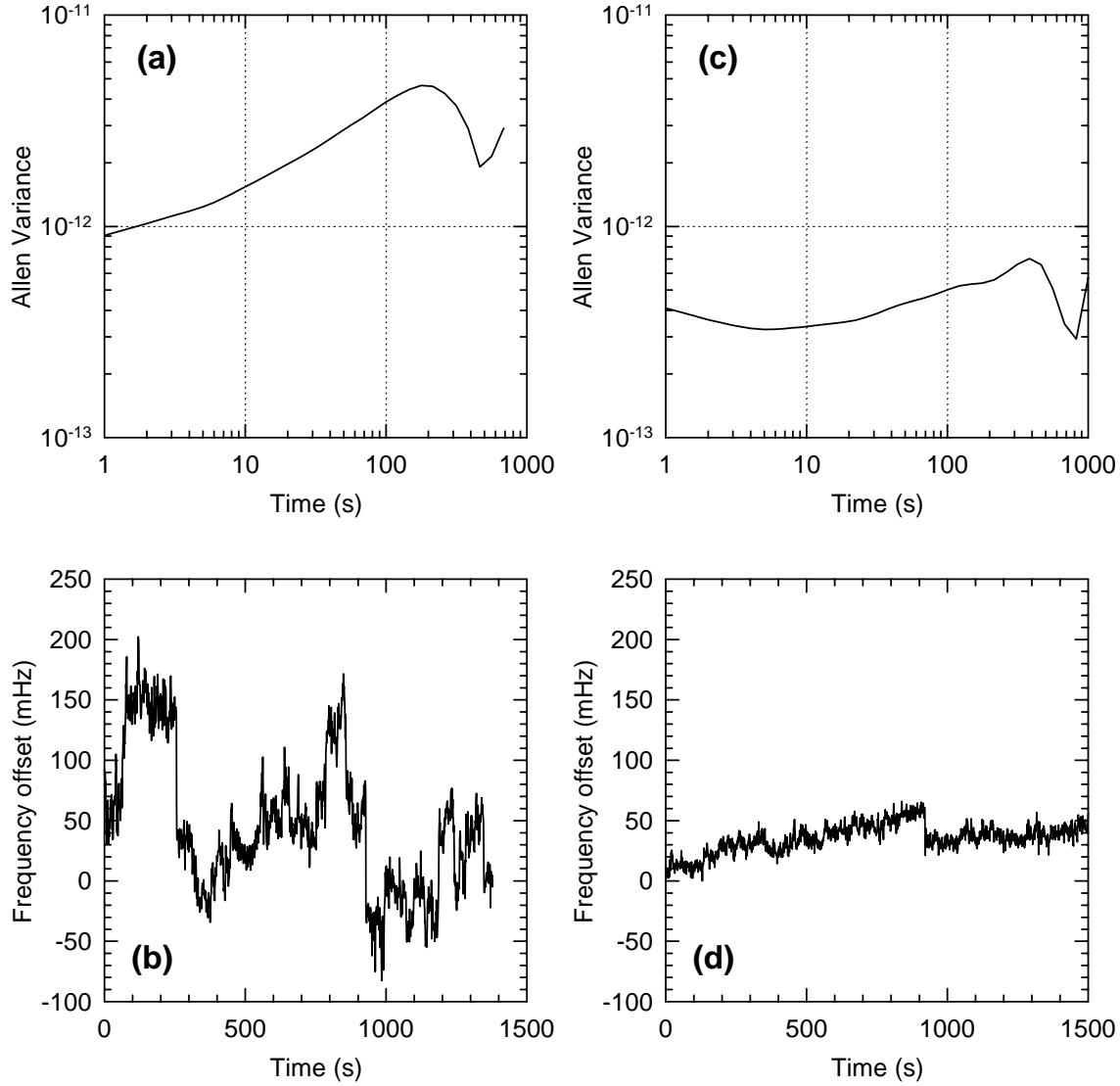
Figure 5.3: Short term stability of frequency standards. All measurements were performed using the setup in Fig. 5.4 and a measurement bandwidth of $f_c = 100\,\mathrm{Hz}$. We compared three different quartz frequency standards: an Oscilloquartz B-5400 (*OSC*), a FTS-1050-A (*FTS*), and our standard SRS FS-700-01 Loran-C receiver (*SRS*). (a) Allan variance *OSC* vs. *SRS*. (b) Frequency offset *OSC* vs. *SRS*. (c) Allan variance *OSC* vs. *FTS*. (d) Freqency offset *OSC* vs. *FTS*.
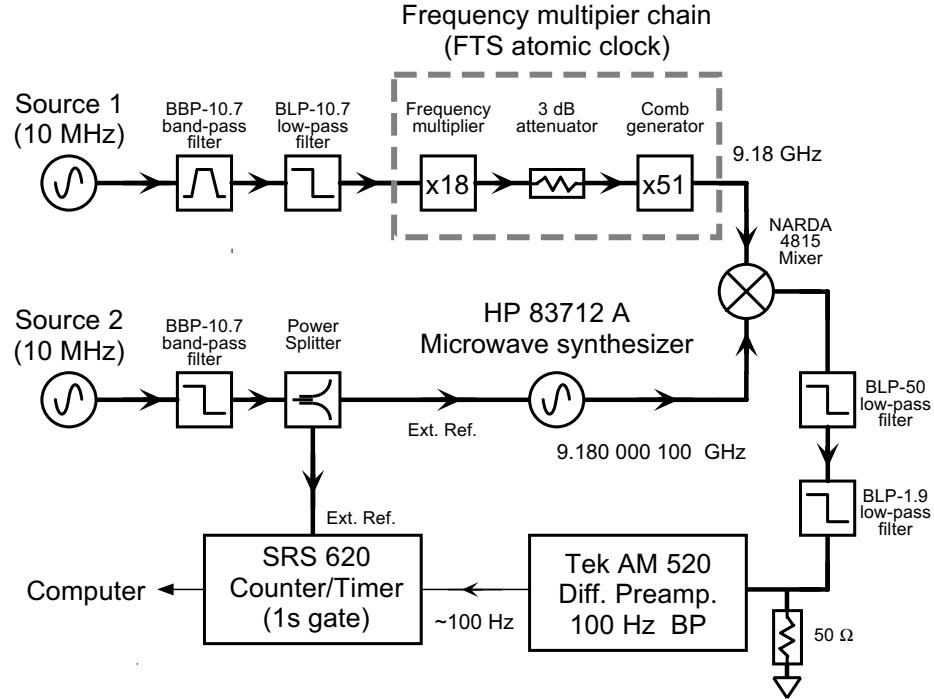
Figure 5.4: Setup for measuring Allan variance.

specification. Assuming that the Allan variance at 1 s and 0.1 s are similar (probably not a bad assumption given the graph in Fig. 5.3), then it would only limit our measurement noise to 95/1. If this should ever become a problem, then we always have the option of using one of the better quartz oscillators.

High frequency phase noise

White phase noise of our microwave frequency source turns out to be the biggest problem. It is dominated by the phase noise of our 10 MHz reference when multiplied up to microwave frequencies (frequency multiplication increases phase noise by 20 dB for every multiplication by 10 !). Our frequency multiplier chain does not provide any filtering to reduce this noise, since it was originally intended for use in atomic clocks where this noise was not the dominant problem. In this respect, a good microwave synthesizer (HP-8665-A) actually offers better performance.

We had one of these synthesizers available for a short time and used the setup in Fig. 5.6 to measure the relative phase noise between our standard microwave source and the
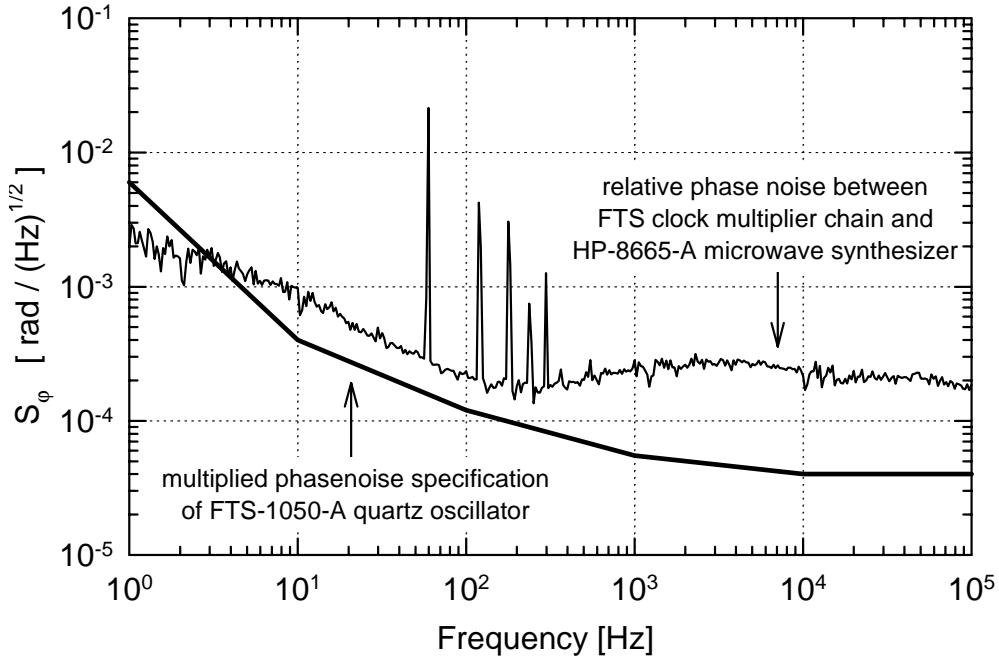
Figure 5.5: Phase noise of microwave frequency sources.

synthesizer (both phase-locked to the same $10\,\mathrm{MHz}$ reference). The result is shown in Fig. 5.5. Additional information from measurements with a third microwave source (Gigatronics 600) makes clear that the white phase noise at high frequencies is due to the frequency multiplier chain. The low frequency $1/f$–noise is due to the synthesizer, but in this region the overall noise is usually dominated by the phase noise of the multiplied quartz frequency reference. To illustrate this Fig. 5.5 also shows the multiplied phase noise specification for a good quartz oscillator (FTS-1050-A). The high frequency phase noise affects the interferometer measurement by causing uncorrelated phase fluctuations for each of the interferometer pulses. The variance $\sigma_\phi \simeq S_\varphi/\sqrt{2\tau}$ of these fluctuations depends on the pulse length τ, which determines the cut-off frequency f_c for integration of the white phase noise. up to which to integrate the white noise. It has thus slightly different values, $\sigma_\phi(\pi)$ and $\sigma_\phi(\frac{\pi}{2})$, for different interferometer pulses. On the slope of an interferometer fringe the variance of the total interferometer phase is then given by

$$\sigma_{\Delta\phi} \quad = \quad \sqrt{\sigma_\phi\big(\tfrac{\pi}{2}\big)^2 + 4\sigma_\phi(\pi)^2 + \sigma_\phi\big(\tfrac{\pi}{2}\big)^2} \quad \approx \quad \frac{2S_\varphi}{\sqrt{\tau_\pi}} \, . \tag{5.15}$$

For π-pulse lengths of $100\,\mu\mathrm{s}$ this would limit our S/N–ratio to 25/1. This noise contribution probably limits the performance of the interferometer when operated in Doppler insensitive
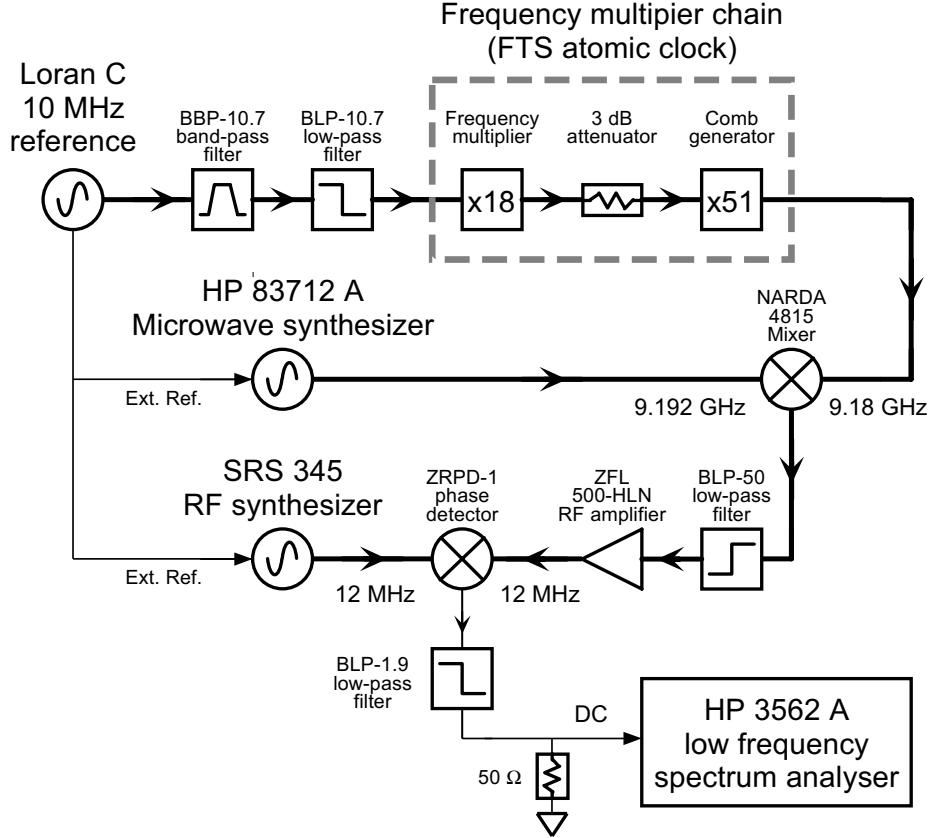
Figure 5.6: Setup for measuring phase noise.

mode. Replacing the frequency multiplier chain with the microwave synthesizer mentioned above (HP-8665-A), we have observed somewhat lower noise levels (see Table 5.2). The high frequency phase noise of this synthesizer should allow a S/N–ratio of $\sim 100/1$. However, other noise source start to dominate much earlier.

5.3.4 Vibrations

Since our setup uses retro–reflected Raman beams, only (vertical) vibrations of the retro–reflection mirror should be relevant. Let us initially assume that these vibrations have a fixed frequency and a well defined phase. We can then write the vibrational acceleration as

$$\mathbf{a}(t) = \hat{\mathbf{a}} \left(a_{\mathrm{c}} \cos \omega t + a_{\mathrm{s}} \sin \omega t \right), \tag{5.16}$$

where the time $t = 0$ coincides with the central π-pulse of the interferometer sequence ($\hat{\mathbf{a}}, \hat{\mathbf{v}}_{\mathrm{rec}}, \ldots$ are unit vectors). There are several ways to derive the resulting interferometer

phase shift, for example by using a perturbative treatment [44, 23] and the perturbation Lagrangian $\mathcal{L} = m\,\mathbf{a}\cdot\mathbf{r}$. For symmetry reasons the result is not affected by the cosine–component in Eq. 5.16, but the sine–component causes a shift of

$$\Delta g \quad = \quad \frac{4\,a_{\mathrm{s}}}{T^2}\,\hat{\mathbf{a}}\cdot\hat{\mathbf{v}}_{\mathrm{rec}}\,\frac{\sin^2\left(\frac{\omega}{2}T\right)}{\omega^2}\,, \tag{5.17}$$

which clearly depends on the vibration frequency as well as the interferometer pulse spacing (Fig. 5.7(a)). In fact, for each pulse separation T there are certain frequencies at which vibrations have no effect. This occurs whenever an integer number of vibrational cycles fits into the interval between π– and $\frac{\pi}{2}$–pulses. Another important property is the second order roll–off at frequencies higher than $1/T$, which means that the interferometer effectively low–pass filters the acceleration signal.

The frequency and time dependent sensitivity can actually be used to identify dominant vibrations of fixed frequency ω by comparing the measurement noise for different pulse spacings T. Since for certain times T the measurement is insensitive to this vibration, the magnitude of the measured noise will be modulated accordingly. For example, if $T = 40\,\mathrm{ms}$ then sinusoidal vibrations with a period of 40 ms would not contribute to the observed noise. The modulation of $\sigma_{\Delta\phi}$ in Fig. 5.8(a) would therefore indicate vibrations at $\sim 25\,\mathrm{Hz}$. The vibration isolator error signal in Fig. 5.7, on the other hand, shows major vibrations at $\sim 45\,\mathrm{Hz}$, suggesting some type of parametrically driven noise term. Removing the water cooled argon–ion laser from the optical table substantially reduced the noise $\sigma_{\Delta\phi}$ as shown in Fig. 5.8(b).

We can also use the above formula to calculate the noise of the interferometer signal (for a specific T) from the power spectrum of residual accelerations at the vibration isolator. One problem with this power spectrum is that the real accelerations in the lowest frequency decade are obscured by the digitization noise floor. We still find that the measurement noise due to residual vibrations should be between 4 and 8 μGal, corresponding to S/N-ratios of 66/1 and 33/1 (Fig. 5.7(b)(c)).

5.3.5   Rotations

In addition to vibrations the interferometer can also be sensitive to rotations. In addition to systematic errors due Earth's rotation this sensitivity can also cause noise problems. The level of rotational noise is mostly determined by the performance of the optical table, which reduces rotations at high frequencies but actually enhances them close to its resonance
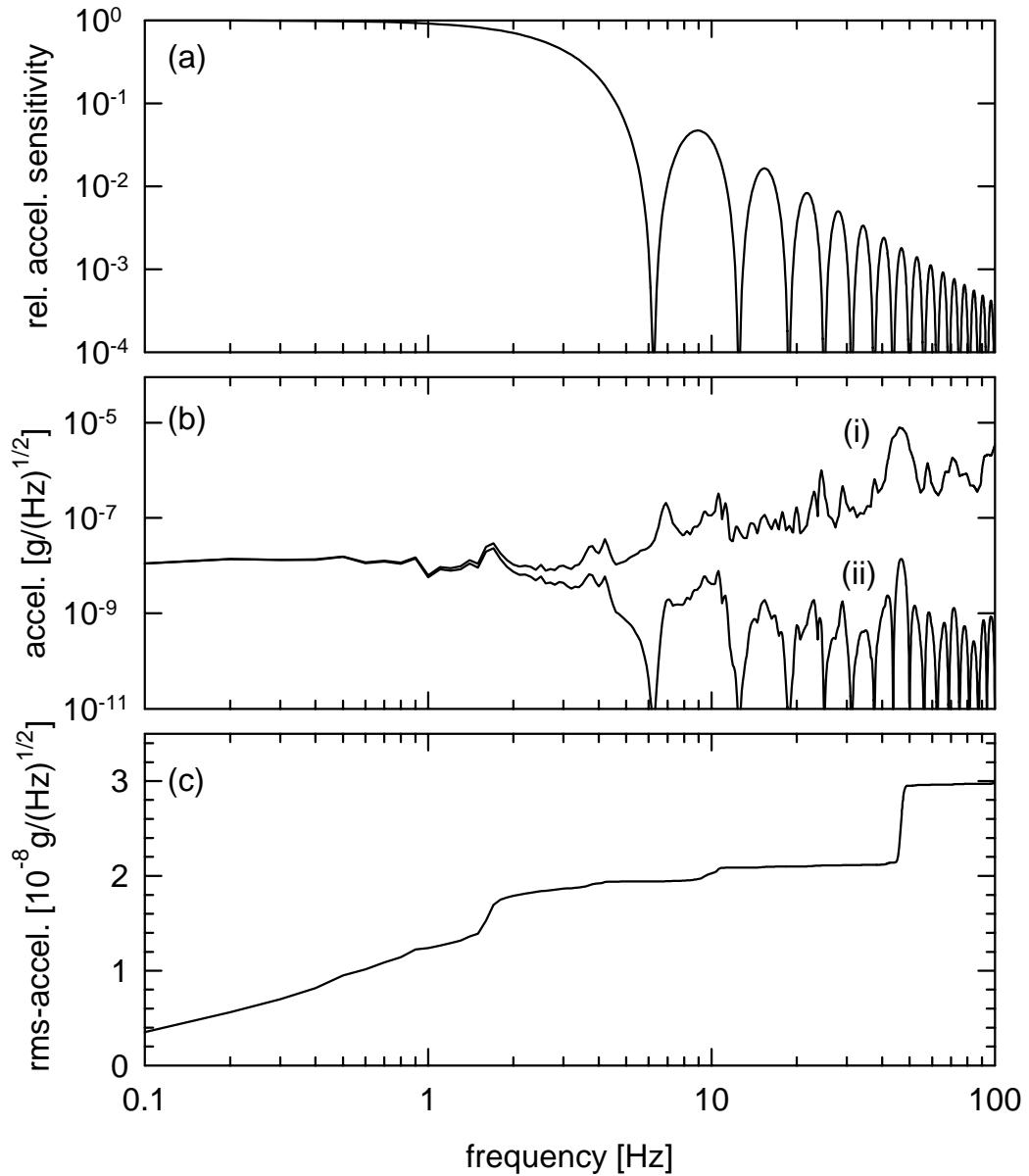
Figure 5.7: Effect of vibrations. (a) Relative sensitivity to different vibrational frequencies for an interferometer pulse spacing of $T = 160\,\text{ms}$. (b) Vibration isolator error signal before (i) and after (ii) multiplication by sensitivity function. (c) Predicted noise of interferometer signal due to vibrations (weighted by sensitivity function) integrated up to a certain frequency. All the data in this figure was taken before implementing the improvements outlined in Fig. 5.2.
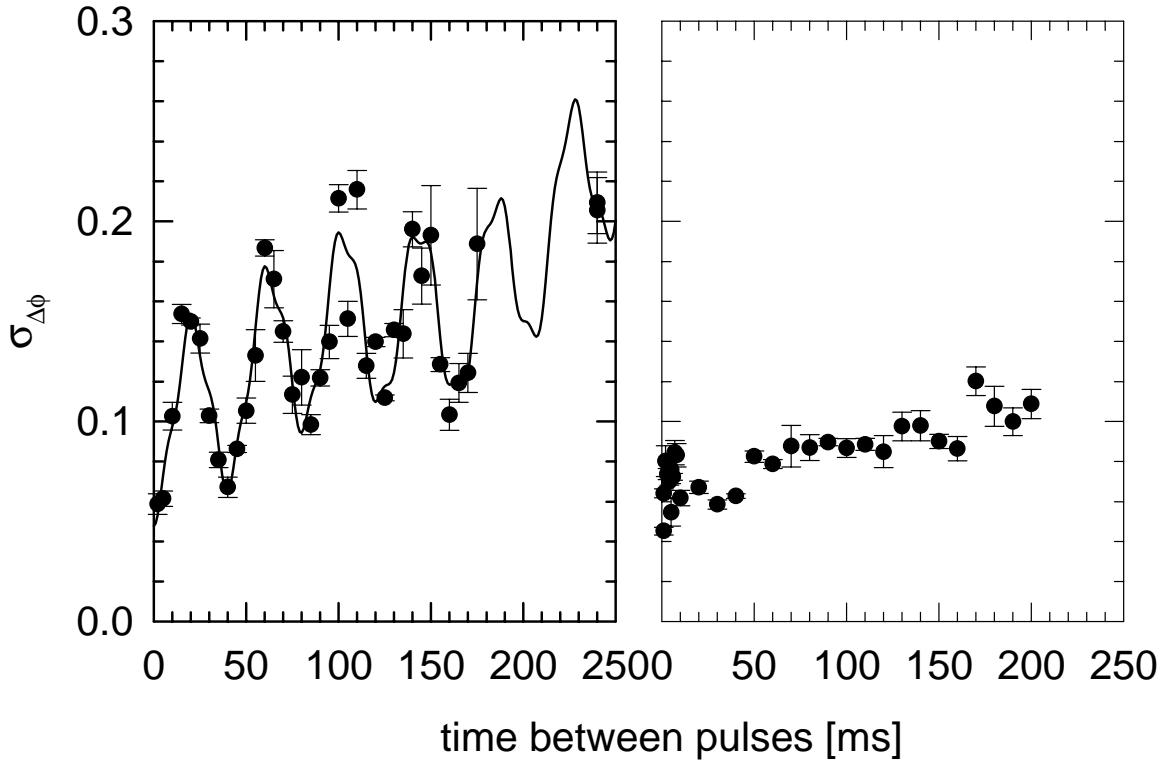
Figure 5.8: Noise modulation due to vibrations. (a) Before Improvements. (b) After improvements: removed Argon–ion laser from optical table, stiffened tower structure supporting vibration isolator, ... (Fig. 5.2). The solid line is a theoretical fit using 4 discrete vibration frequencies.

frequency of $\sim 2\,\mathrm{Hz}$. The main active vibration isolator suppresses the $\sim 2\,\mathrm{Hz}$ vibrational resonance but does nothing to suppress rotations. This is one of the reasons why we added an active 3D vibration isolation system for the optical table. While this system thoroughly eliminates problems at the original table resonance, it currently does nothing at frequencies above $10\,\mathrm{Hz}$.

Since the main vibration isolator performs very well over a wide frequency range, we can assume that it eliminates all vertical movement at the sensor location. Effectively, we therefore have to consider only rotations around this point. We first consider rotational noise with a well determined frequency ω and phase which can be written as

$$\boldsymbol{\Omega}(t) \quad = \quad \hat{\boldsymbol{\Omega}}\ (\Omega_{\mathrm{c}}\ \cos \omega t + \Omega_{\mathrm{s}}\ \sin \omega t)\ , \tag{5.18}$$

where the time $t = 0$ coincides with the central π-pulse of the interferometer sequence. As

in the case of vibrations we can derive the resulting interferometer phase shift by using a perturbative treatment and the perturbation Lagrangian $\mathcal{L} = m\,\boldsymbol{\Omega}\cdot(\mathbf{r}\times\mathbf{v}) + \frac{1}{2}m\,(\boldsymbol{\Omega}\times\mathbf{r})^2$. The sine– and cosine–components in Eq. 5.18 give rise to different shifts in the measured acceleration:

$$\Delta g_{\mathrm{c}} \quad = \quad \frac{2\,\Omega_{\mathrm{c}}}{T}\,\hat{\boldsymbol{\Omega}}\cdot(\mathbf{v}_0\times\hat{\mathbf{v}}_{\mathrm{rec}})\,\frac{\sin\left(\omega T\right)}{\omega} \tag{5.19}$$

$$\Delta g_{\mathrm{s}} \quad = \quad -\frac{4\,\Omega_{\mathrm{s}}}{T^2}\,\hat{\boldsymbol{\Omega}}\cdot(\mathbf{x}_0\times\hat{\mathbf{v}}_{\mathrm{rec}})\,\frac{\sin^2\left(\frac{\omega}{2}T\right)}{\omega} \tag{5.20}$$

Here $\mathbf{x}_0$ and $\mathbf{v}_0$ are the atomic position (relative to the sensor in the vibration isolator) and velocity (taking the mean of both interferometer paths) at the time of the central interferometer π-pulse. We have neglected the centrifugal force terms since they are small compared to the other contributions.

Note that while for constant rotation rates ($\omega = 0$) the first contribution reduces to the familiar coriolis force term, $\Delta g_{\mathrm{s}} = 2\,\boldsymbol{\Omega}\cdot(\mathbf{v}_0\times\hat{\mathbf{v}}_{\mathrm{rec}})$, the second contribution will vanish. It is therefore easily overlooked when making theoretical predictions.

Both effects only become relevant when the experimental apparatus is misaligned in one way or another. The first one is proportional to the horizontal velocity $\delta v = \mathbf{v}_0\cdot\hat{\mathbf{v}}_{\mathrm{rec}}$, the second one to the horizontal offset $\delta x = \mathbf{x}_0\cdot\hat{\mathbf{v}}_{\mathrm{rec}}$ between atoms and sensitive point of the vibration isolator ($\hat{\mathbf{v}}_{\mathrm{rec}}$ is vertical). The horizontal velocity δv is generally very small ($< 2\times 10^{-4}\,\mathrm{m/s}$), since it is carefully adjusted in order to avoid systematic errors caused by Earth's rotation. The horizontal displacement is harder to quantify and probably substantial. We have actually been able to reduce the measurement noise by horizontally translating the vibration isolator in increments of $5\,\mathrm{mm}$, so $5\,\mathrm{mm}$ should be a good estimate for δx.

We have measured the rotational noise of the optical table and used the above formulas with explicit values for δx and δv to predict the resulting interferometer noise. We found that the effect proportional to δv is almost certainly irrelevant, even for unrealistically large horizontal velocity of $1\,\mathrm{mm/s}$. The effect proportional to δx, however, can be more substantial, especially if the active feedback is turned off. In that case it might cause fluctuations of up to $3\,\mu\mathrm{Gal}$, corresponding to a S/N–ratio of 90/1.

5.3.6   Measured noise

The noise observed during an interferometer measurement depends on the exact operating parameters such as pulse separation and pulse length. Varying these parameters for both, Doppler sensitive and Doppler insensitive interferometer configurations, provides useful information for disentangling the effects the various noise sources such as vibrations, phase noise, etc. .

Our standard method of determining the S/N–ratio is to sit on the slope of an interferometer fringe and determine the variance within sets of 40 consecutive launches. While this variance could potentially depend on the number of launches (see Sec. 5.1), we find that this is not the case for our experiment and for fewer than ~ 100 launches (see Fig. 5.9(a)).

Calculating the two–sample variance $\sigma_g(2, t)$ defined in Eq. 5.3 (or $\sigma_{\Delta\phi}(2, t)$ for Doppler insensitive fringes) of a long sequence of measurements provides additional information. Figure 5.9 shows these variances for a variety of measurement conditions.

One obvious feature is the clear $1/\sqrt{t}$ dependence for fewer than ~ 100 launches. This result justifies our previous definition of the S/N–ratio, since it shows that for sets of fewer than 100 launches the noise of different launches is uncorrelated[‡]. It also means that all the noise can be attributed either to high frequency sources, with periods shorter than the 1.3 s interval between launches, or to very low frequency effects with typical timescales of several minutes or more. No dominant noise sources seem to exist with periods between 1 and 100 seconds.

Our main reason for calculating the two–sample variance was to determine up to what time the $1/\sqrt{t}$ dependence holds and to find the eventual flicker noise floor. For data taken by sitting on the slope of a fringe (thin line in Fig. 5.9(a)) the increase of the noise around $t = 100$ s is probably caused by drifts (mostly PMT dark current) in the detection system.

Taking data by fitting full interferometer fringes is not vulnerable to such drifts and therefore better suited for long term measurements. However, since data points at the extrema of a fringe provide no phase information, and because of experimental overhead, this method has slightly lower resolution at short times.

The thick line in Fig. 5.9(a) is for one of our multi–day gravity datasets which was acquired this way and corrected for tides using a model that includes ocean loading effects (see Sec. 4.3). The increase in noise around $t = 2 \times 10^3$ s is probably due to residual tidal

---

[‡]In this case we have $(S/N)^{-1} = \sigma_{\Delta\phi}(t_l)$, where $\Delta t_l = 1.3$ s is the time between launches.
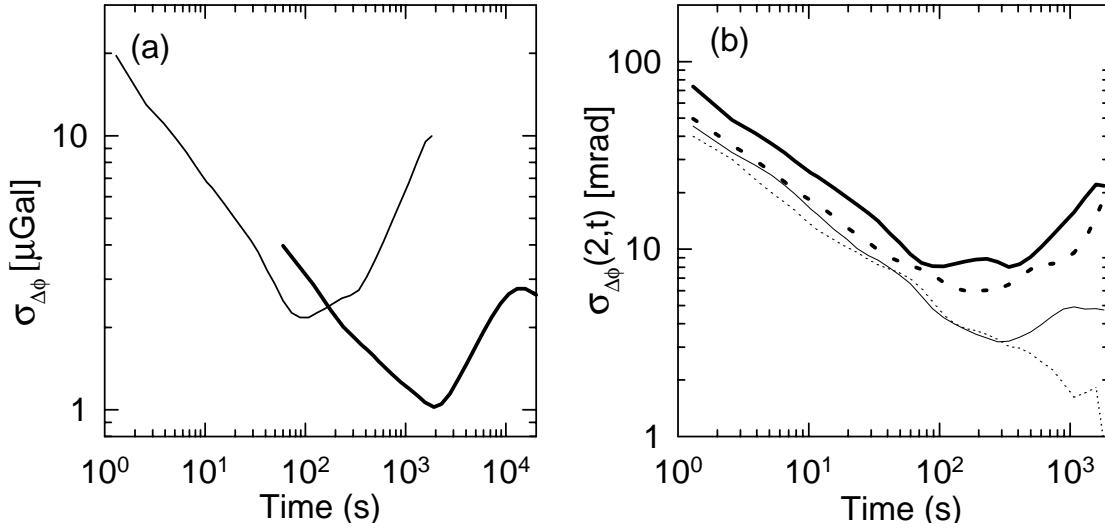
Figure 5.9: Allan variance of interferometer measurements. (a) For Doppler sensitive configuration with pulse separation $T = 160\,\text{ms}$ and data taken either by sitting at the side of a fringe (thin line) or by fitting 1 minute gravity fringes (thick line). (b) Comparison between Doppler sensitive (thick lines) and insensitive (thin lines) configurations for pulse spacings of $T = 160\,\text{ms}$ (solid) and $T = 2\,\text{ms}$ (dotted).

effects. A diurnal ($\sim 12\,\text{hour}$ period) component with an amplitude of $4.5\,\mu\text{Gal}$ (compare Fig. 4.5) would explain the peak at $t = 4 \times 10^3\,\text{s}$.

The high frequency noise, which affects every single launch in the same way, shows very little dependence on the time between pulses and is also not very different for Doppler sensitive and Doppler insensitive mode. The only times we have seen substantially lower noise levels is when we either replaced our frequency multiplier chain with a microwave synthesizer (HP-8665-A) or used much longer pulse lengths (up to $5\,\text{ms}$, only possible in Doppler free mode).

Table 5.2 shows some S/N–ratios obtained when using the microwave synthesizer. Note that the changes in the noise level are rather small for the large pulse separation Doppler sensitive fringes that we use for our gravity measurements.

	Frequency multiplier		Microwave synthesizer		
	Dop. sen. $80\,\mu\mathrm{s}$ π-pulse	Dop. insen. $80\,\mu\mathrm{s}$ π-pulse	Dop. sen. $80\,\mu\mathrm{s}$ π-pulse	Dop. insen. $80\,\mu\mathrm{s}$ π-pulse	Dop. insen. $2\,\mathrm{ms}$ π-pulse
$T = 1\,\mathrm{ms}$			39	46	
$T = 2\,\mathrm{ms}$	20	25			
$T = 160\,\mathrm{ms}$	14	22	18	33	50

Table 5.2: Signal–to–noise ratios for various interferometer configurations.

5.4 Discussion

The reasons for the current limitation of the measurement sensitivity are still not completely clear. It is very likely that phase noise in the Raman beams, and to a lesser degree intensity fluctuations, are the limiting factor for all Doppler insensitive measurements and short time Doppler sensitive measurements. However, long time Doppler sensitive measurements, which we use to measure gravity, suffer from an additional, yet unexplained noise contribution. Possible candidates are high frequency vibrations or rotations, as well as potential problems caused by the generation of the necessary frequency steps and chirps.

While it should be relatively easy to improve the Doppler free performance (by using a better microwave source and actively stabilizing the Raman laser intensity), it is harder to conceive improvements for the actual gravity measurements. Improving vibration isolation at high frequencies would be one option. Another course of action would be to change the setup to allow higher repetition rates or longer pulse separations in order to explore a larger parameter space in pursuit of the noise source.

Chapter 6

Systematic errors

An important property of the atomic fountain gravimeter is its ability to obtain an absolute gravity value which is directly referenced to atomic standards. However, the ultimate accuracy of the measurement still depends on our understanding of potential systematic errors.

Gravity measurements differ from those of fundamental constants (Rydberg constant, fine structure constant, ...) in that g is a site dependent quantity that also varies with time and is affected by environmental conditions. Theoretical models of these effects are therefore required to interpret the measurement results and their quality can be an important factor in determining the final measurement precision and accuracy. The variable nature of g also makes it more difficult to identify systematic errors of the instrument itself.

In this chapter we present our analysis of potential systematic errors. Related discussions of systematic effects for atom interferometers and atomic clocks can be found in references [14, 25].

6.1 Displacements of the atomic transition frequency

6.1.1 AC Stark shifts

AC Stark shifts are of profound importance for light pulse atom interferometers. In the case of 2–photon off-resonant Raman transitions they are intrinsically related to the Rabi frequency and cannot be avoided.

The average AC Stark shift $\Omega_{\mathrm{avg}}^{\mathrm{AC}} = (\Omega_{\mathrm{a}}^{\mathrm{AC}} + \Omega_{\mathrm{b}}^{\mathrm{AC}})/2$ (see Sec. 2.2) is always the same

for atoms in both paths of the interferometer, as long as one can neglect the intensity variations of the Raman beams over the path separation. This component of the AC Stark shift therefore leads to no observable phase shift.

The differential AC Stark shift $\delta^{AC} = \Omega_a^{AC} - \Omega_b^{AC}$, on the other hand, can lead to an observable phase shift. Combining the results for π and $\frac{\pi}{2}$ pulses from Ref. [14], we find that the resulting first order phase shift for a Mach–Zehnder type interferometer is given by

$$\Delta\phi^{AC} \quad = \quad \frac{\delta_3^{AC}}{\Omega_{\text{eff}}} - \frac{\delta_1^{AC}}{\Omega_{\text{eff}}}, \tag{6.1}$$

where Ω_{eff} is the effective Rabi frequency and δ_1^{AC} and δ_3^{AC} are the Stark shifts during the first and last $\frac{\pi}{2}$–pulse, respectively. The interferometer is therefore only sensitive to the *difference* in shifts during the two $\frac{\pi}{2}$–pulses. Since the Raman beam parameters are generally the same for both pulses this means that the effects of AC Stark shifts mostly cancel. However, the spreading of the atomic cloud with respect to the Gaussian Raman laser intensity profile breaks the symmetry of the situation and causes a residual shift large enough to be problematic.

This residual shift can be essentially eliminated by properly adjusting the detuning and intensity of the Raman beams. To see how, we first write out both the differential AC Stark shift

$$\delta^{AC} \quad = \quad \Omega_a^{AC} - \Omega_b^{AC} \quad = \quad \sum_{k,i} \frac{|\Omega_{kai}|^2}{4\Delta_{iak}} - \sum_{k,i} \frac{|\Omega_{kbi}|^2}{4\Delta_{ibk}} \tag{6.2}$$

and the 2–photon Rabi frequency

$$\Omega_0 \quad = \quad \sum_i \frac{\Omega_{1ai}^* \Omega_{2bi}}{2\Delta_{1ai}} \tag{6.3}$$

in terms of the 1–photon Rabi frequencies Ω_{kji} and detunings Δ_{iak} (see Sec. 2.2 or Ref. [14]). The Ω_{kji} are determined by the Raman beam intensities and polarizations and can be calculated using selection rules and the appropriate Clebsch–Gordon coefficients. For a fixed ratio of Raman beam intensities (i.e., 1–photon Rabi frequencies) the AC Stark shift is directly proportional to the effective Rabi frequency. As long as the Raman detuning Δ is smaller than the hyperfine splitting of $\sim 9.2\,\text{GHz}$, the minus sign in Eq. 6.2 makes it possible to make the proportionality factor zero by choosing the correct intensity ratio. This eliminates the differential AC Stark shifts, independent of the atoms position in the Raman laser intensity profile.

We have also determined the correct intensity ratio using an experimental method that involves adding an additional Raman pulse to the interferometer sequence. It is illustrated in Fig. 6.1. Figure 6.2(a) shows that the experimentally determined intensity ratio is a function of the detuning Δ, in good agreement with the theoretical result obtained by solving Eq. 6.2 for $\delta^{\mathrm{AC}} = 0$.

The Raman laser intensities are not actively stabilized and can change over the course of an experiment. Even after the differential AC Stark shift has been eliminated by balancing the Raman beams, it is therefore still important to know the residual sensitivity to small changes in the intensity ratio. Figure 6.2(b) shows that for our standard experimental configuration the measured gravity value is rather insensitive to changes in the intensity ratio (which typically stays between 1.6 and 1.8). The associated uncertainty is $\pm 2\,\mu$Gal. To achieve sub μGal resolution it would be necessary to either reduce the sensitivity even further or to implement active intensity stabilization.

6.1.2 DC Stark shifts

Two different effects of a static electric field have to be considered. The differential DC Stark shift of the two involved hyperfine levels ($F = 4$, $m_F = 0$ and $F = 3$, $m_F = 0$) may be important since the atoms in the two interferometer paths are always in opposite different states. The absolute (common mode) DC Stark shift of the two hyperfine levels may also be important since the two interferometer paths are spatially separated. As long as this separation is small, the resulting effect is proportional to the gradient of the absolute DC Stark shift.

The differential DC Stark shift of the cesium ground state hyperfine splitting ($m_F = 0$ sublevels) is given [25, 45] by

$$\frac{\Delta\omega_{hfs}}{\omega_{hfs}} = -2.5 \times 10^{-20} E^2 \qquad \text{or} \qquad \frac{\Delta\omega_{hfs}}{2\pi} = -2.3 \times 10^{-10} E^2 \frac{\mathrm{Hz}}{(\mathrm{V/m})^2}, \qquad (6.4)$$

where the electric field E is in units of V/m. For a worst case estimate we assume that an electric field of strength E is turned on only during the second half of the interferometer, so that there is no cancelation due to reversal of the internal states. For a time T between pulses this causes a gravity offset of

$$\Delta g = \frac{\Delta\phi}{k_{\mathrm{eff}} T^2} = -1.4 \times 10^{-9} \frac{E^2}{k_{\mathrm{eff}} T} \frac{1}{\mathrm{s}\,(\mathrm{V/m})^2}. \qquad (6.5)$$
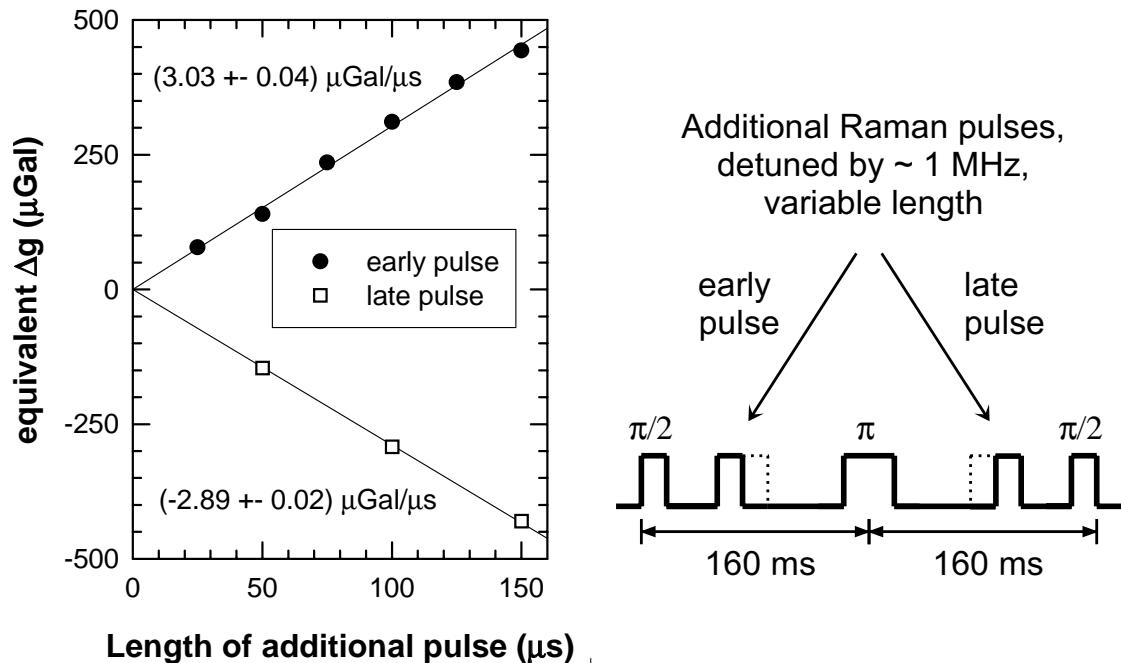
Figure 6.1: Measurement of the differential AC Stark shift caused by imbalanced Raman beams. An additional Raman pulse of variable length is added to the interferometer sequence. It is substantially detuned ($\sim 1\,\text{MHz}$) from the Raman resonance so that it does not actually drive a Raman transition. On the other hand, this detuning is small compared to the 1–photon detuning Δ and the AC Stark shifts are therefore the same as during normal interferometer pulses. If the intensities of the beams are not properly balanced, then the additional pulses cause an interferometer phase shift which is proportional to the pulse length. The sign of the shift is different for pulses introduced during the first and second half of the interferometer.

The results shown are for a detuning of $\Delta = 0.99\,\text{GHz}$ from the $F' = 4$ excited state and for $I_{F=4}/I_{F=3} = 2$ ($I_{F=4}$ and $I_{F=3}$ are the intensities of the Raman lasers coupling primarily to the $F = 4$ and $F = 3$ ground states, respectively). One can now eliminate the differential AC Stark shift by adjusting the intensity ratio until the phase shifts caused by the additional pulses disappear ($I_{F=4}/I_{F=3} = 1.67$ for $\Delta = 0.99\,\text{GHz}$).
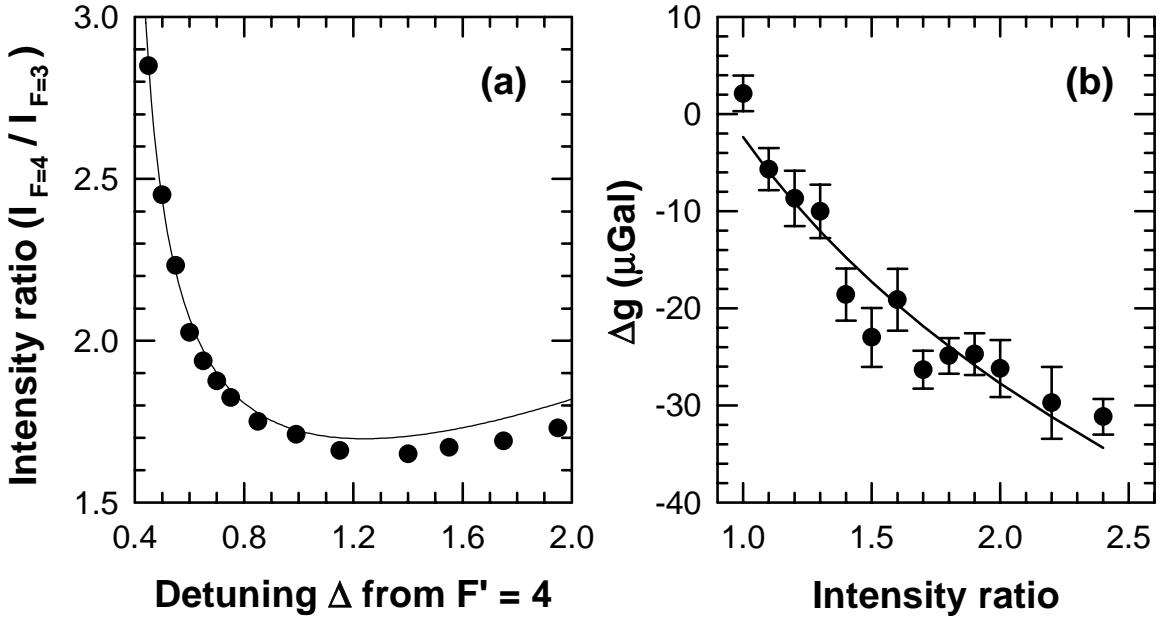
Figure 6.2: (a) Detuning dependence of the Raman laser intensity ratio at which the differential AC Stark shift vanishes. The data points are obtained using the method from Fig. 6.1, the solid line is the theoretical model described in the text. (b) Residual sensitivity of the gravity measurement to small changes in the Raman laser intensity ratio, for a pulse separation of $T = 160$ ms and a 1–photon detuning $\Delta = 0.99$ GHz from the $F' = 4$ excited state. The solid line is a two parameter (offset, amplitude) fit using the theoretical model.

Accordingly, a field of 32 V/cm would be necessary to cause a 1 μGal gravity shift for a typical pulse separation of $T = 160$ ms. For a more realistic situation, where the contributions from the first and second half of the interferometer would partly cancel, even stronger fields would be required. Since the interaction region is surrounded by a graphite coated aluminum tube, we can rule out electric fields of such magnitude. Therefore the differential DC Stark shifts should not be an issue in our experiment.

The effect caused by the gradient of the absolute DC Stark shift is substantially more problematic. The reason is that total the common mode DC Stark shift of both hyperfine ground states, given by [46]

$$\Delta\omega_{F=3} \simeq \Delta\omega_{F=4} = 2\pi\alpha E^2 \quad \text{with} \quad \alpha = -1.00 \times 10^{-5} \frac{\text{Hz}}{(\text{V/m})^2} , \tag{6.6}$$

is much bigger than the differential frequency shift in equation (6.4). To find the gravity offset caused by this effect we could first calculate the interferometer phase shift. But it is possible to skip this step and get the same result by simply calculating the classical force

on the atom in an inhomogeneous field:

$$\Delta g \quad = \quad \frac{F}{m_{Cs}} \quad = \quad \frac{1}{m_{Cs}}\frac{\partial U}{\partial x} \quad = \quad \frac{2h}{m_{Cs}}\frac{\alpha}{2}\frac{\partial E}{\partial x}E\,. \tag{6.7}$$

Using this formula we can calculate the effect of an electric field E_0 with a constant gradient $\frac{\partial E}{\partial x} = E_0/0.2\,\text{m}$ (reasonable given the dimensions of the interaction region). Under this assumption a field of $1.8\,\text{V/cm}$ would be necessary to cause a $1\,\mu\text{Gal}$ gravity offset. While this field strength is much lower then the $32\,\text{V/cm}$ from above, it is still bigger than what one would expect in the interaction region. We therfore can also rule out this effect.

6.1.3   Zeeman shifts

In our interferometer the atoms are always kept in magnetic field insensitive states with $m_F = 0$. However, these states still show a quadratic Zeeman shift and for small magnetic fields the resulting change of the cesium hyperfine frequency is given by

$$\Delta f_{\text{hfs}} \quad = \quad 427.45\,\text{Hz/G}^2\,. \tag{6.8}$$

This effect is big enough to require well controlled magnetic fields and extensive magnetic shielding to achieve the millihertz frequency stability necessary for gravity measurements at the $1\,\mu\text{Gal}$ level. Since the effect is quadratic in the magnetic field, it is desirable to operate at the smallest possible bias field. However, a certain bias field strength is necessary to define a proper quantization axis and to prevent Majorana spin flips when the atoms enter the magnetically shielded region. Preferably, the field should also be big enough to separate the frequencies of magnetic field sensitive transitions from the magnetic field insensitive ones. Since we have to use relatively short Raman pulses ($80\,\mu\text{s}$ π–pulse, $40\,\mu\text{s}$ $\frac{\pi}{2}$–pulse) to address a reasonably wide atomic velocity distribution, this would require a bias field of at least $0.15\,\text{Gauss}$.

In principle, it would be possible to estimate the estimate the effect of residual magnetic field inhomogeneities theoretically. However, since the magnetic field distribution inside the magnetic shield is relatively complex (see Fig. 6.3), experimental tests are easier and more conclusive. The results in Fig. 6.4(a) indicate that the measured gravity value changes substantially at strong bias fields. This makes it necessary to operate at weak bias fields where, as shown in Fig. 6.4(b), there is no significant field dependence of the measured gravity value.

While the data indicates that we could use bias field values up to 50 mG, this would not be strong enough to separate the Zeeman components. To avoid partially overlapping
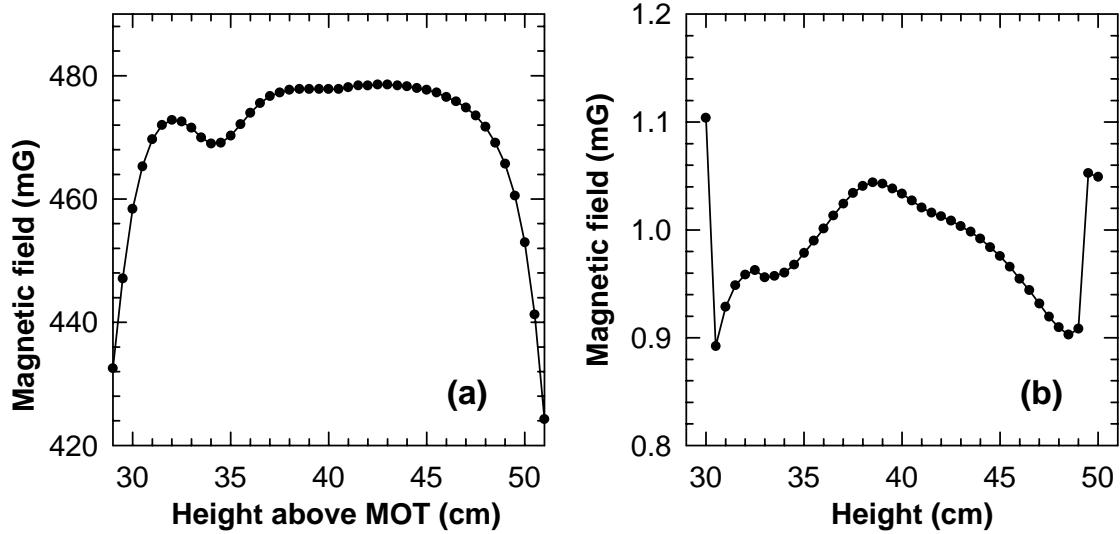
Figure 6.3: Magnetic field inside magnetic shield assembly. Measured using magnetic field sensitive Raman transition. (a) Strong bias field. Inhomogeneities dominated by solenoid field. (b) Weak bias field. Inhomogeneities dominated by other field sources.
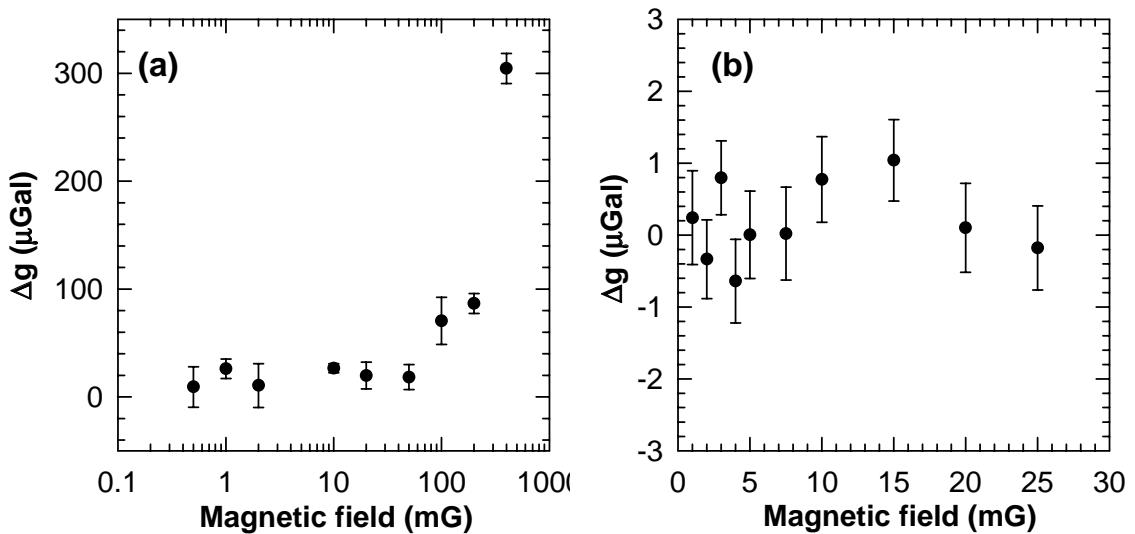
Figure 6.4: Magnetic field dependence of gravity measurement. The Δg–axis has an arbitrary offset.

Zeeman components we therefore choose to operate at a very small bias field, typically 2 mG, where all the Zeeman components are completely overlapped. Under these conditions, to avoid problems with magnetic field sensitive transitions, only atoms in the $m_F = 0$ state can be allowed to enter the interferometer. This is taken care of by our elaborate pre–selection sequence (Sec. 3.2.4). There could be some additional problems, like transfer into other magnetic sublevels, but due to the many inherent symmetries of the measurement these effects tend to cancel. More importantly, they would cause shifts that depend strongly on the overall detuning Δ or the Raman beam polarizations, and no such dependence has been observed experimentally. Therefore we conclude that magnetic fields are currently not a problem.

There is an important difference between the quadratic Zeeman shift and the quadratic Stark shift discussed earlier: The differential DC Stark of the two hyperfine levels is much smaller than the common mode shift, which causes the second contribution discussed in Sec. 6.1.2 to dominate. This is very different for the quadratic Zeeman shift, where the two magnetic field insensitive hyperfine states shift by equal and opposite amounts*. This contribution, equivalent to the classical force on the atom in an inhomogeneous magnetic field, can therefore be neglected.

6.1.4   Cold collisions

There is one substantial drawback of using laser cooled atoms for atom interferometry. For bosonic atoms at μK temperatures the collisional cross–sections, including those that cause hyperfine frequency shifts, can get devastatingly large [47, 48]. For ^{133}Cs atoms in a equal superposition of the $F = 3, m_F = 0$ and $F = 4, m_F = 0$ hyperfine ground states it has been measured by Gibble *et. al.* [47] to be (-15.8 ± 1.4) mHz at a density of $(1.0 \pm 0.6) \times 10^9$ cm^{-3}.

We now estimate the effect of such cold collisions on our atom interferometer, assuming

---

*This can be seen from the Breit-Rabi formula [25],

$$\omega_{\mathrm{hfs}}(F, m_F) = -\frac{\omega_{\mathrm{hfs}}}{2(2I + 1)} - \frac{g_I \mu_B B_0 m_F}{\hbar} \pm \frac{\omega_{\mathrm{hfs}}}{2} \sqrt{1 + \frac{4 m_F}{2I + 1} x + x^2} \,,$$

where

$$x = \frac{(g_j + g_I)\mu_B B_0}{\hbar \omega_{\mathrm{hfs}}} \qquad \text{and} \qquad \omega_{\mathrm{hfs}} = \frac{A(2I + 1)}{2\hbar} \,.$$

The minus sign in front of the square root applies when $F = I - S$, whereas the plus sign corresponds to the case $F = I + S$.

that the spatial separation of the two paths does not affect the collisions. The MOT originally captures about 5×10^8 atoms at a density of $8 \times 10^9\,\mathrm{cm^{-3}}$, but magnetic state and velocity preselection reduce the number of atoms to approximately 3×10^6 (Sec. 3.2.4). Because of the severe vertical velocity preselection we can neglect the spreading of the atomic cloud along the vertical axis. We furthermore neglect the initial horizontal size of the cloud and assume that its horizontal radius is proportional to the time after launch. We then find that the average atom density is $\bar{\rho}_a = 6 \times 10^7\,\mathrm{cm^{-3}}$ during the first half of the interferometer ($130\,\mathrm{ms} - 290\,\mathrm{ms}$ after launch) and only $\bar{\rho}_b = 1.5 \times 10^7\,\mathrm{cm^{-3}}$ during the second half ($290\,\mathrm{ms} - 450\,\mathrm{ms}$ after launch). Because of cold collisions and according to the formula

$$\Delta\phi \quad = \quad \kappa T(\bar{\rho}_b - \bar{\rho}_a), \tag{6.9}$$

where κ is the frequency shift cross–section from above and T the interferometer pulse spacing, this results in a phase shift of $0.6\,\mathrm{mrad}$ and an equivalent gravity offset of 0.2 μGal.

The effect would be approximately 15 times bigger without vertical velocity preselection, and bigger by another factor of 3 without magnetic sublevel preselection (the cross–sections for the other m_F states are somewhat smaller). These preselection steps are therefore essential.

6.2 Raman beams

6.2.1 Determination of the cesium D2–wavelength

From the formula $\Delta\phi = k_{\mathrm{eff}} g T^2$ it is apparent that to obtain a gravity value one has to know the Raman wave vector $k_{\mathrm{eff}} = |\mathbf{k}_2| + |\mathbf{k}_1|$ or, in other words, the $6S_{1/2}$, $F = 3$ to $6P_{3/2}$, $F = 4$ transition frequency to the same level of accuracy. At the time of our measurement this frequency had only been determined by several wavemeter measurements with a range of uncertainties between $\sim 10\,\mathrm{MHz}$ and $\sim 40\,\mathrm{MHz}$ (Fig. 6.5).

Using the frequency value by Avila *et.al.* [50] resulted in a big discrepancy between the atom interferometer gravity value and the one measured by the falling corner–cube gravimeter (see Sec. 4.4). However, Ted Hänsch and coworkers at the Max-Planck-Institute for Quantum optics have recently performed a direct measurement of the cesium D$_2$– frequency and their preliminary result is about $50\,\mathrm{MHz}$ lower than the weighted average
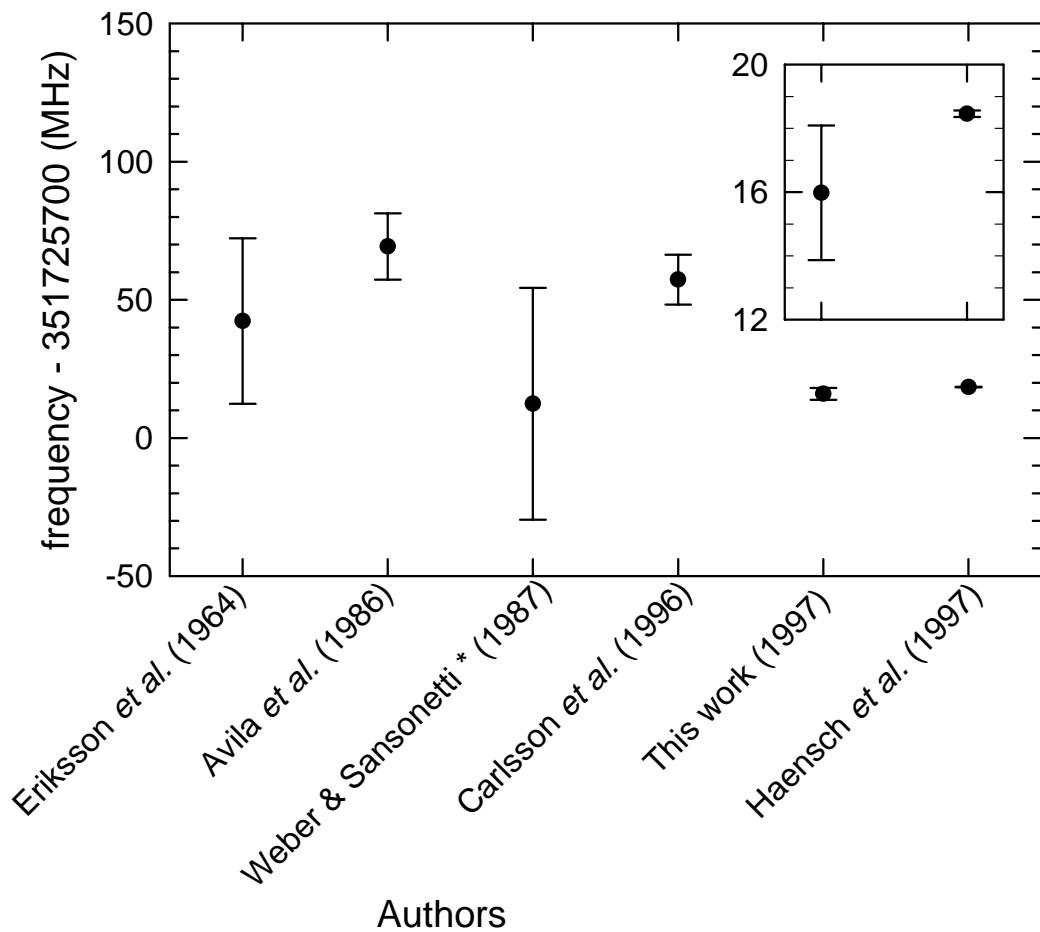
Figure 6.5: Measured values for the cesium D_2–frequency ($6S_{1/2}$, $F = 3$ to $6P_{3/2}$, $F = 4$ transition). Erikson *et.al.* [49], Avila *et.al.* [50] and Carlson *et.al.* [51] used wavemeters to measure the D_2–wavelength. Weber & Sansonetti [52] performed a wavemeter measurement of the D_1–wavelength, the large error bars shown are due to the transfer. Hänsch *et.al.* measured the D_2–frequency directly. Our own value is calculated by comparing atom interferometer and falling corner–cube measurements of g.

of the wavemeter measurements. Using this value reduces the discrepancy between the atom interferometer and classical gravity measurements to $7 \pm 7\,\mu$Gal (see Sec. 7).

Figure 6.5 also shows a value for the cesium D_2–frequency calculated by comparing the gravity measurements and assuming that both are correct.

6.2.2 Vertical alignment

To obtain the correct absolute gravity value the Raman wave vector has to be exactly parallel to the local vector of gravity. The relation

$$\Delta\phi \quad = \quad \mathbf{g} \cdot \mathbf{k}_{\text{eff}} T^2 \quad = \quad |\mathbf{g}||\mathbf{k}_{\text{eff}}|T^2 \cos\theta \tag{6.10}$$

shows that misalignment by an angle θ will result in too low a gravity value. For small angles this error is quadratic in θ. In order to achieve an accuracy of 1 μGal, the deviation of the Raman beams from vertical must be less than $45\,\mu$rad. This direction is effectively determined by the orientation of the retro reflection mirror, which in turn is controlled by an active tilt stabilization system (Sec. 3.5.3). The electronic bubble level, mounted rigidly to the mirror and ultimately responsible for the performance of the system, has been calibrated to approximately $5\,\mu$rad and the tilt error should therefore remain well below the critical value.

It is possible that the calibration of the bubble level could change over time. Furthermore, a wedge in the top vacuum window could deflect the wave vector at the location of the atoms relative to its direction at the mirror surface. To avoid this, we use windows that are plane parallel to better than $10\,\mu$rad, but they might be deformed by the pressure difference.

The most straightforward experimental test of the tilt alignment uses the atomic signal itself. Fig. 6.6 shows the change in measured gravity when the whole experimental setup is tilted over a substantial angular range. Using relation 6.10 we can use this data to find the correct setpoint for the active tilt control system and check the calibration of the tilt sensor. Since the result agrees to $10\,\mu$rad with the previous calibration of the tilt sensor we expect the resulting gravity error to be less than $0.05\,\mu$Gal.

6.2.3 Retro–reflection alignment

Any failure to properly retro-reflect the Raman beams affects the measurement result by changing the magnitude of the wave vector. If the angle of incidence of the incoming Raman
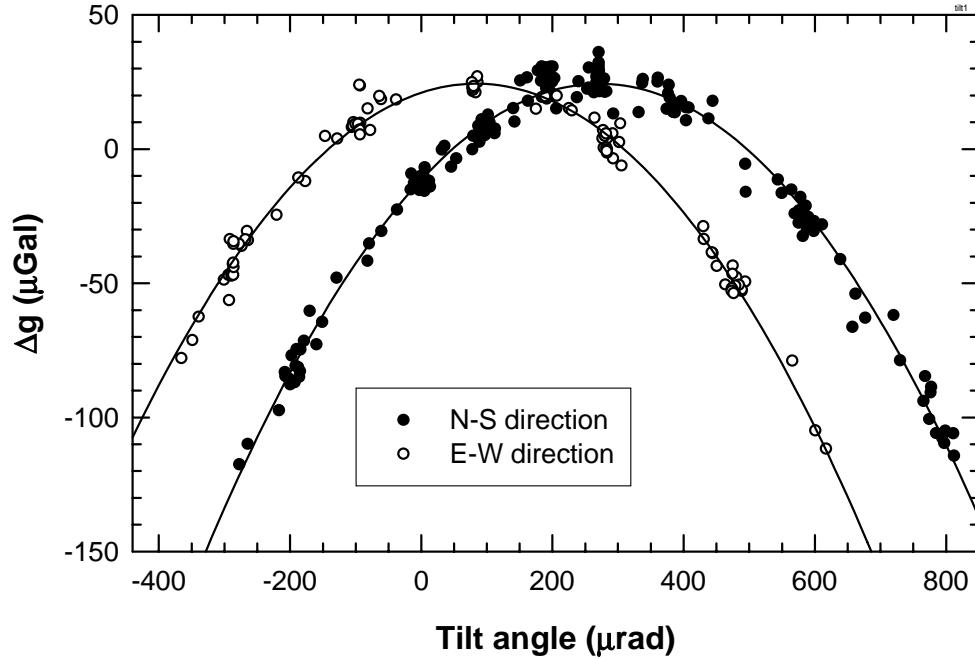
Figure 6.6: Tilt dependence of gravity measurements. The active tilt control system is used to tilt the whole experiment in the East-West as well as the North-South direction. The measured gravity value (dots) varies as a function of tilt. Using to equation 6.10 to fit (solid lines) this data allows us to find the proper setpoint (Apex of the parabolas) for the control system and check the calibration of the electronic tilt sensor.

beams at the mirror deviates from 90 degrees by an angle ϑ we have

$$|\mathbf{k}_{\text{eff}}| \quad = \quad (|\mathbf{k_1}| + |\mathbf{k_2}|)\cos\vartheta \,, \tag{6.11}$$

which for small angles causes an error quadratic in ϑ.

Currently, this retro reflection is checked rather crudely by aperturing the Raman beams down to 2 mm at a distance of approximately 3 m from the retro–reflection mirror and then centering the reflected beams on the same aperture. This can be done quite easily with an error of less then 0.2 mm, corresponding to an angle of $30\,\mu$rad and a measurement error of less than 1 μGal.

In order to validate this alignment procedure we have intentionally tilted the incoming Raman beam and observed the change in the measured gravity value (Fig. 6.7). Fitting this dataset using equation 6.11 we typically find an tilt angle for proper retro reflection that differs from the one obtained by the aperture method by less than 40 μrad.
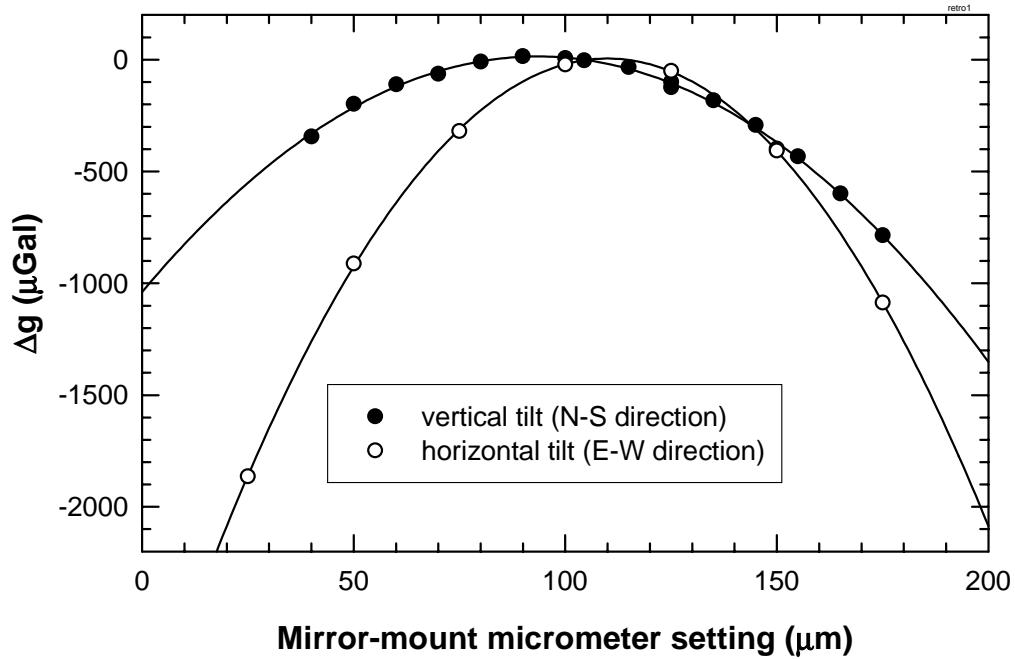
Figure 6.7: Retro-reflection of the Raman beams. The measured gravity value (dots) varies when one of the folding mirrors in the Raman beam path is used to misalign the retro-relection. We can use equation 6.11 to fit (solid lines) this data and find the proper alignment (Apex of the parabolas). The curvature of the two parabolas is different because of the geometry of the mirror mount.

Even after using the aperture alignment method we still have to expect an error as large as $-1\,\mu$Gal. Since the angular direction of the incoming Raman beams tends to drift, one has to check this alignment frequently.

6.2.4 Wavefront curvature

The theoretical derivation of the interferometer phase shift assumes the Raman beams to be ideal plane waves. Our Raman beams, on the other hand, are Gaussian laser beams (Bessel beams when a pinhole is used for spatial filtering). The wavefronts of Gaussian beams are spherical and can be approximated by plane waves only for distances from the beam waist that are much smaller than the Rayleigh length $z_0 = \pi w_0^2/\lambda$. For sufficiently large, well collimated Gaussian beams this distance can be rather large — $575\,$m for the $2.5\,$cm diameter beams in our setup — but our extreme accuracy requirements make further investigation necessary.
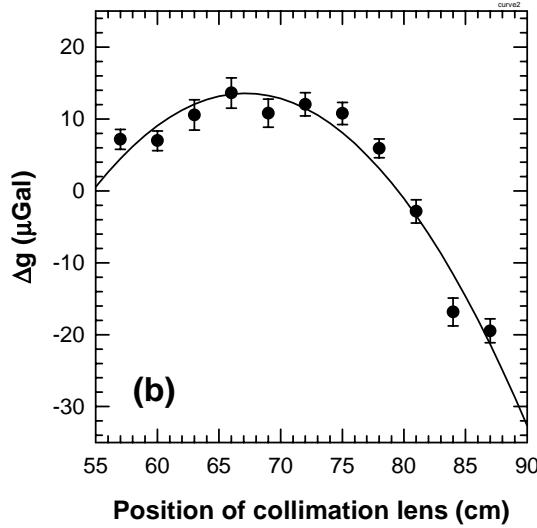
Figure 6.8: Change in the measured gravity value (dots) when changing the Raman beams wavefront curvature by moving the collimation lens. The solid lines are parabolic fits. The x-axis has an arbitrary offsets.

We have investigated this effect by moving the collimation lens (1.5 m focal length) over some distance, which causes substantial changes of the wavefront curvature in the interaction region. The parabolic dependence of the observed shift (Fig. 6.8) agrees with theoretical predictions [14]. It is also obvious that rather extreme movements of the lens are required to produce a relevant effect. Since we usually collimate the Raman beams at a level that corresponds to a lens displacement of only 1 mm, we conclude that errors because of wavefront curvature are well below 1 μGal.

6.2.5   Speckle

We have also considered the effect of the more local wavefront perturbations caused by optical scatterers and imperfect optical elements. They can be very complicated and in more severe cases are generally referred to as speckle [53, 54].

We have investigated this effect by looking for observable changes while making things worse intentionally — here by sprinkling baby powder (Longs Drugs store brand) onto a glass plate inserted into the beam path. Fig. 6.9 shows the effect of this rather drastic procedure as observed by a CCD chip illuminated directly by the Raman beams.

Amazingly, this procedure did not result in any significant gravity offsets (Fig. 6.10),
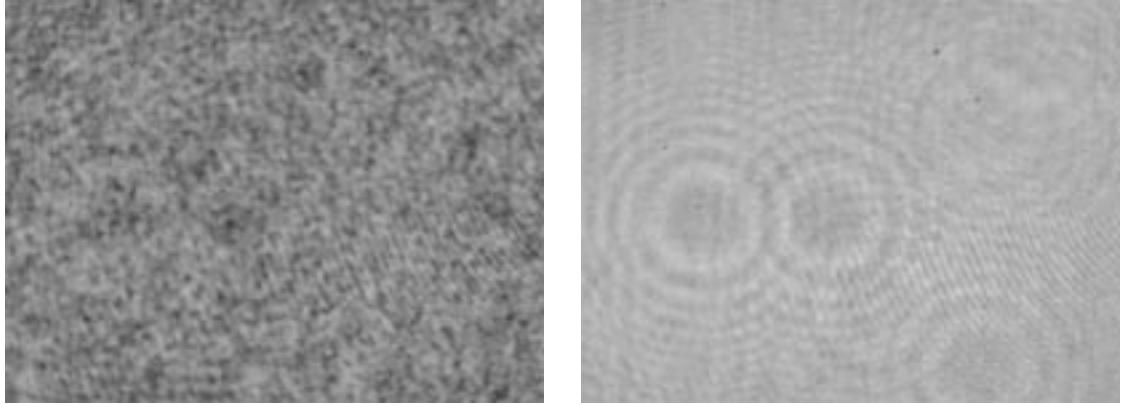
Figure 6.9: Local intensity variations of the Raman beams, observed by direct illumination of a CCD (1/2–inch wide) inserted into the beams after they passed through the vacuum chamber. (a) The first picture shows the speckle pattern generated by a baby-powder covered glass plate inserted into the beams. (b) The second picture shows the intensity distribution without this additional plate. Only a few diffraction rings, caused by small dirt particles on the lower vacuum chamber window, are visible.
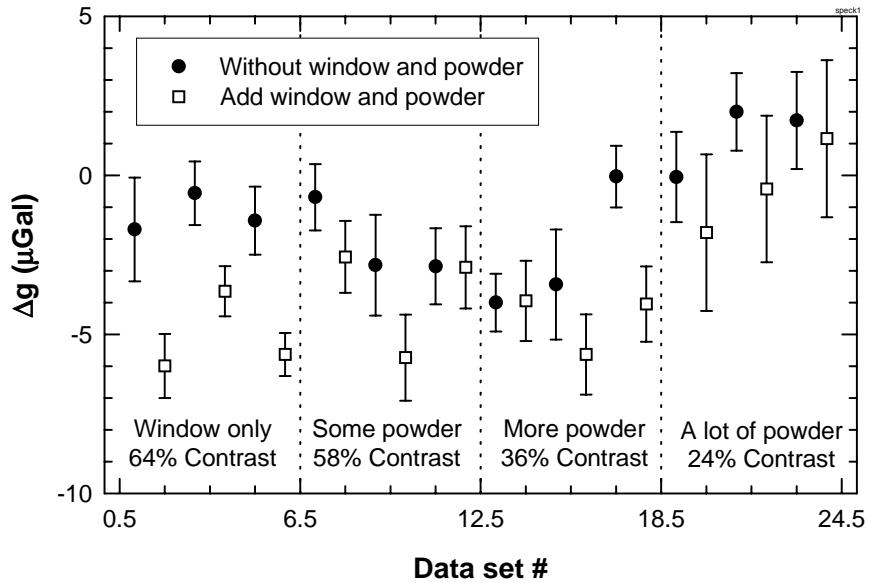
Figure 6.10: Effect of speckle on the measured gravity value. The open squares are measurements taken with a glass plate, covered with variable amounts of baby powder, inserted into the Raman beams before the vacuum chamber. The solid dots are measurements without this additional plate. They are necessary for comparison, since gravity changes over the course of the measurement. While adding more powder decreases the fringe contrast substantially, it does not have any significant effect on the measured gravity value. The small offset between the two datasets is caused by the small wedge of the glass plate.

even in extreme cases with enough powder on the window to reduce the interferometer contrast to less than 25 %. Therefore, given that our optics are generally much cleaner, we rule out speckle as the cause of any relevant error.

6.2.6 Standing waves and polarization quality

The presence of a strong standing wave component in the Raman beams can cause substantial systematic errors, mostly caused by spatially varying AC Stark shifts. The worst case scenario, direct retro-reflection without change of polarization, has been discussed elsewhere in great detail [14].

It would be ideal to avoid standing waves by using two independent Raman beams, but then we would loose the many benefits and ease of alignment afforded by our current retro–reflection setup (Sec. 3.5). Instead, we use a setup that substantially reduces the standing wave effect by inserting a $\frac{\lambda}{4}$–waveplate in front of the retro-reflection mirror. The resulting lin⊥lin or $\sigma^{\pm}-\sigma^{\pm}$ polarization configurations do not cause spatially varying AC Stark shifts for atoms in $m_F = 0$ states and therefore eliminate the primary cause of systematic errors.

Misalignment of the $\frac{\lambda}{4}$–waveplates and unwanted reflections from optical surfaces can reintroduce small AC Stark shift variations. Reflections from tilted surfaces will also introduce light field components with different wave vectors. The systematic errors caused by these effects are probably small. This is confirmed by experimental tests which show no significant effect due to misaligned waveplates or partially reflecting glass plates introduced into the beam path. Therefore we conclude that standing waves are not a problem at our current accuracy level.

6.2.7 Refractive index of background vapor

The refractive index of the background vapor can potentially modify the wave vector of the Raman beams and thereby cause a shift in the measured gravity value.

Generally one would assume the refractive index inside an ultra high vacuum system to be sufficiently close unity. However, a substantial fraction of the vapor pressure is due to cesium vapor. This will cause a substantially increased refractive index for the Raman beams since their frequency is close to a cesium transition. We therefore estimate at what cesium partial pressure this would become a problem.

The refractive index is related to the complex absorption coefficient by $\Delta n_{\mathrm{ref}} = n_{\mathrm{ref}} - 1 =$

$\operatorname{Im}\alpha/k$ [26]. We have

$$\operatorname{Im}\alpha \quad = \quad \frac{n\sigma}{2}\frac{1}{(1+s)}\frac{\delta}{(\Gamma/2)}\frac{1}{1+(\frac{\delta}{(\Gamma/2)\sqrt{1+s}})^2}\,, \tag{6.12}$$

which in the far detuning limit reduces to

$$\operatorname{Im}\alpha \quad = \quad \frac{n\sigma}{2}\frac{(\Gamma/2)}{\delta}\,. \tag{6.13}$$

Here s is the saturation parameter, n the atomic number density and σ the absorption cross section on resonance. For circular polarized light, and after averaging over all excited states, the absorption cross section is $2.37\times10^{-9}\,\mathrm{cm^2}$ for atoms equally distributed among all magnetic sublevels of the $F=4$ state and $2.65\times10^{-9}\,\mathrm{cm^2}$ in case of the $F=3$ state. We approximate both numbers by $2.5\times10^{-9}\,\mathrm{cm^2}$, assume that each Raman beam interacts only with atoms in one of the two hyperfine state and that the atoms are equally distributed among these, neglect the Doppler broadening as well as the excited state hyperfine splitting, use the relation $10^{-9}\,\mathrm{torr}\sim3.2\times10^7\,\#/\mathrm{cm^3}$ for cesium at room temperature, and assume a detuning Δ of $1\,\mathrm{GHz}$. This leads to the relation $(\Delta g/g)/p = 0.8\,\mathrm{torr^{-1}}$ and implies that the partial pressure of cesium has to be less then $1.2\times10^{-9}\,\mathrm{torr}$ to keep the gravity offset below $1\,\mu\mathrm{Gal}$.

Our system, which is a hybrid between vapor cell MOT and beam loaded MOT, exhibits large differences in the local cesium density. It is therefore difficult to estimate the cesium partial pressure in the interaction region itself, but absorption measurements indicate that it is less than $10^{-10}\,\mathrm{torr}$. The refractive index of the background vapor should therefore cause a shift of less than $0.1\,\mu\mathrm{Gal}$.

6.2.8 Refractive index of cold atom cloud

The refractive index of the cold atoms themselves could also cause problems. Luckily, a constant refractive index does not have any substantial effect, since the atoms cause only a local deformation of the light field "ruler" that travels together with the atoms and therefore cancels in the final measurement. However, the density and optical thickness of the atom cloud changes along its trajectory (Sec. 6.1.4), causing time dependent phase shifts and variations of the refractive index.

We now estimate the most important effect, which is the phase delay of the retro-reflected Raman beam as it passes the cloud on its way up. Since the optical thickness of the cloud decreases as a function of time, so does the phase delay. This is equivalent to reducing

the optical path length the Raman beam has to travel, which in turn is indistinguishable a downward movement of the retro-reflection mirror. Since this decrease of the optical thickness is nonlinear, this corresponds to an apparent upward acceleration and therefore causes a measurement error. Under the same assumptions for the expanding atomic cloud as in Sec. 6.1.4 and using the appropriate cross section of $2.31 \times 10^{-9}\,\mathrm{cm}^2$ for atoms in the $m_F = 0$ sublevel, we find a gravity shift of $2 \times 10^{-13}\,\mathrm{g}$ at a detuning of $\Delta = 1\,\mathrm{GHz}$. Therefore we can surely neglect this effect, even without any initial preselection.

6.2.9   Leakage light

During the interferometer measurement the even very low levels of light close to the cesium resonance can cause substantial measurement errors. Leakage light from the trapping, repumping and detection beams is especially dangerous since it has the smallest detuning. Most of the laser system is therefore enclosed in black cardboard boxes and mechanical shutters are used complete shut–off of all such beams.

The Raman beams, however, are only switched off by an AOM and the atoms are therefore exposed to some leakage light in between Raman pulses. The only realistic influence of this light, which for the majority of time it is far detuned from any possible Raman transition, would be due to AC Stark shifts.

The AOM (with an additional RF switch in its driving circuitry) reduces the Raman beam intensity by at least a factor of 10^5 when turned off . On the other hand, the leakage light is on for about 160 ms between pulses, much longer than the $80\,\mu$s duration of a typical Raman pulse. From the data in Fig. 6.1 we know that even for not well balanced beam intensities a 0.1 ms pulse at full intensity would cause a gravity shift of maximally 250 μGal. A 160 ms pulse of light, attenuated by a factor of 10^5, would therefore cause a maximum shift of 4 μGal. Usually, though, the intensities are usually substantially better balanced and cancelation due to the inherent symmetry of the interferometer should reduce this effect by at least another order of magnitude. We therfore conclude that the resulting gravity offset should be less than 0.1 μGal.

6.3   Frequency control and pulse timing

Among all physical quantities, time and frequency are generally the ones most accessible to current experimental methods and can be measured to the highest precision and accuracy.

Many precision experiments therefore transform the ultimately intended measurement into one of time and frequency. Following this philosophy, our atom interferometer effectively measures g by converting it into a phase shift value that depends only on the frequency of the Raman beams and the time between light pulses.

Certain features of our experiment further tailor this process to operate in a regime where current technology works best. The use of stimulated Raman transitions alleviates the requirement of milli–hertz level optical frequency control and requires such precision only in the microwave and radio frequency range where it is much easier to achieve. Chirping the Raman frequency difference to nearly cancel the gravity induced Doppler shift, in addition to keeping the atoms in resonance, reduces the sensitivity to the timing of the light pulses. This is highly beneficial, since frequencies can be controlled even better than short time intervals.

Even with these methods timing and frequency control are not trivial at the level required to achieve the targeted accuracy of $1\,\mu$Gal. In marked contrast to most atomic physics experiments where RF and microwave components can usually be considered ideal, we therfore have to scrutinize every single component of the frequency control and timing system.

6.3.1   Frequency dependent phase shifts

Changing the Raman frequency to keep the atoms in resonance can introduce severe systematic errors since then group delay (second or higher order phase shifts as a function of frequency) exactly mimics an additional gravity signal. Such frequency dependent phase shifts can for example be introduced through filters, spurious frequency components from the direct digital synthesis process, interference effects due to back reflections of RF power or RF leakage along alternate paths.

We attempted an independent measurement of this effect. Ideally, a group delay measurement would look at the system as a whole, starting with the mathematical description of the frequency chirp and then analyzing the phase shift of the Raman beams themselves. But technical reasons, mainly due to the nature of the DDS process, require that measurement be divided into at least two parts.

The phase shifts of the DDS synthesizer are the hardest to determine, because the chirped output frequency is different from the input frequency, i.e. the fixed $10\,$MHz reference. This precludes using standard vector network analysis techniques. Instead, we use
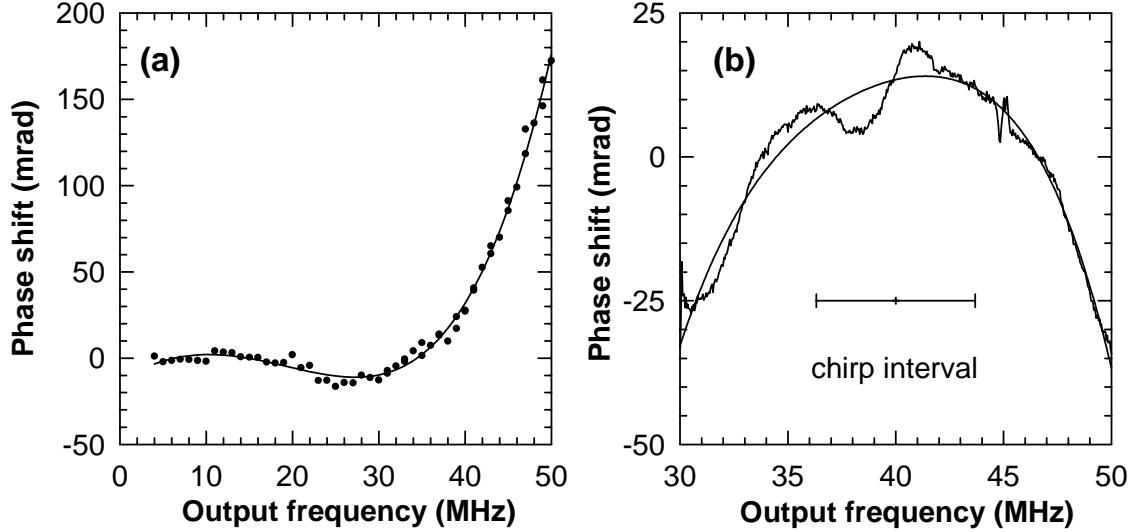
Figure 6.11: Frequency dependent phase shifts. (a) Tektronics AFG 2020 DDS synthesizer with internal 100 MHz anti-aliasing filter. Measured using fast digital scope. (b) Remaining system, from output of the DDS synthesizer to Raman beams. Measured using vector network analysis.

a fast digital scope to measure the delay from a frequency update command to the next zero crossing of the output waveform. Since the update command is internally synchronized with the phase accumulator of the Tektronics DDS synthesizer, and therefore the *theoretical* phase, this measurement of the *real* output phase allows us to determine the frequency dependent phase shift introduced by the synthesizer. Fig. 6.11(a) shows the measured phase shifts. For our standard chirp centered around 40 MHz we find an additional phase shift $\Delta\phi_{\mathrm{RF}} = \phi(43.68\,\mathrm{MHz}) - 2\phi(40\,\mathrm{MHz}) + \phi(36.32\,\mathrm{MHz}) \simeq 15\,\mathrm{mrad}$, corresponding to a 4 μGal gravity offset. For some of our most recent measurements we have therefore moved the chirp center frequency to 16 MHz where the group delay is minimal and we only expect a gravity offset of 0.4 μGal.

The remaining system (starting at the output of the DDS synthesizer) can be investigated by standard vector network analysis. The result is plotted in Fig. 6.11(b). The global curvature of this response graph would correspond to a gravity offset of 2.2 μGal. The smaller scale wiggles visible in the graph would cause additional μGal scale offsets depending on details like the central frequency of the chirp or the time between Raman pulses. However, since we had to introduce many additional components to perform this measurement we can not be sure (without much more involved calibration procedures) if
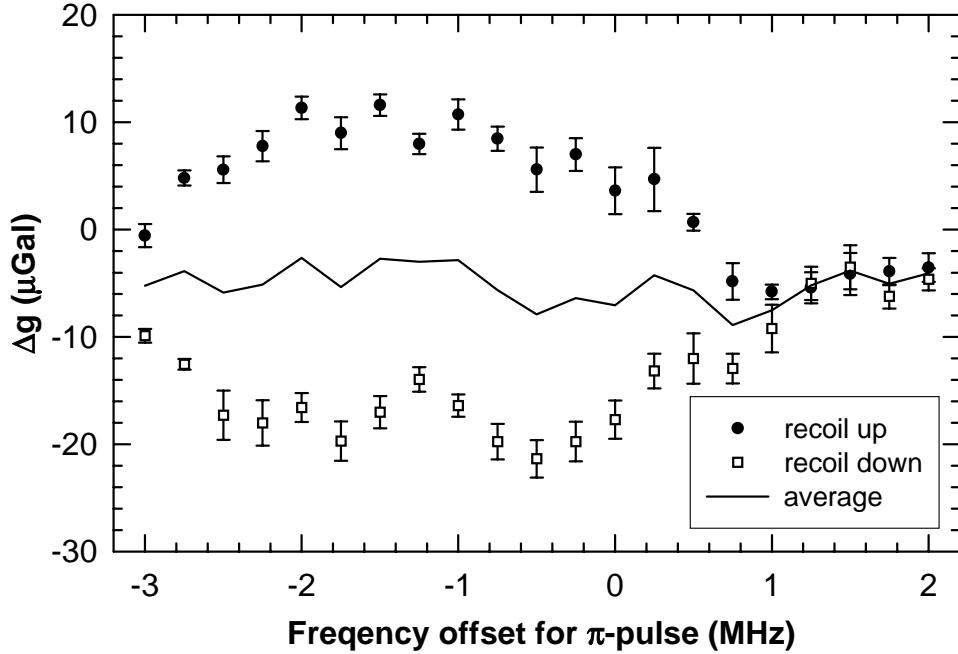
Figure 6.12: Effect of frequency dependent phase shifts. The measured gravity value changes if the center frequency of the DDS synthesizer chirp is changed from its usual 40 Mhz value (compensated for by changing the offset frequency of the Raman laser phase lock, see Sec. 3.4.2). Reversing the direction of the photon recoil also means reversing the direction of the chirp and the sign of the gravity shift. The average value is therefore much less sensitive to this effect. Interferometer pulse separation $T = 160\,\text{ms}$.

all of the observed features are real or if they might be artifacts.

Since the measurements described above are not fully conclusive we use a nice property of atom interferometer to measure and cancel the group delay effect. Reversing the direction of the photon recoil also means changing the direction of the RF chirp and the sign of the gravity offset. One can therefore alternate between the two interferometer configurations and calculate the average value, which should be free group delay related offsets. The differential value is actually a measurement of the group delay. Fig. 6.12 illustrates the effectiveness of this method. However, changing the recoil also introduces some other changes, like slightly altered trajectories or pulse times, which may cause additional offsets. In order to exactly reverse the chirp, with the same center frequency, it is for example necessary to apply the middle interferometer pulse *after*, instead of *before* the atoms reach
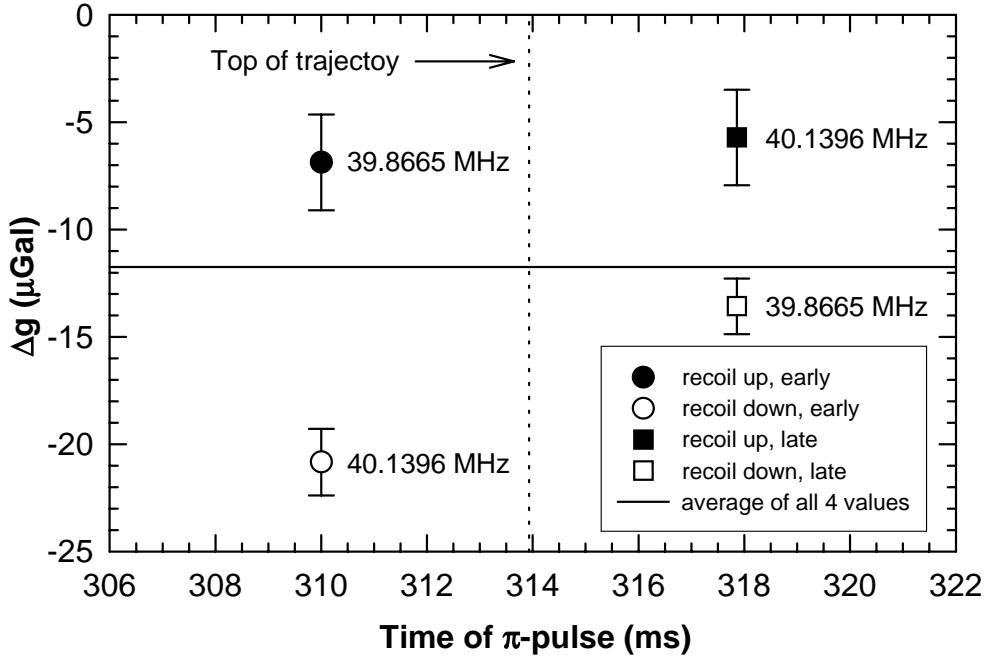
Figure 6.13: Changing the direction of photon recoil and RF chirp cancels most RF phase shift related gravity offsets. But one either has to change either the time of the interferometer π–pulse (early = before apex of trajectory, late = after) or the center frequency of the RF chirp (see graph). The graph shows measurement results for all four possible combinations. They are usually averaged to cancel most of the effect.

the apex of their trajectory (or vice versa)[†]. To account for this, we often take gravity data for all four possible combinations of recoil direction and pulse time, as shown in Fig. 6.13.

In summary, the method of alternating between differential recoil configurations can reduce the sensitivity to imperfections of the RF system substantially, but the remaining uncertainties are still some of the most important ones affecting the atomic fountain gravimeter. From the uncertainty of measurements using different center frequencies and recoil directions we estimate a residual uncertainty of 2 μGal.

6.3.2   Transient phase shifts

The necessity to pulse the Raman beams introduces another potential pitfall. Essentially all methods for switching RF power or light fields also show some amount of phase modulation.

[†]Since we use retro-reflected Raman beams this pulse can not be applied exactly at the apex. Otherwise, it would also drive unwanted Doppler insensitive Raman transitions.
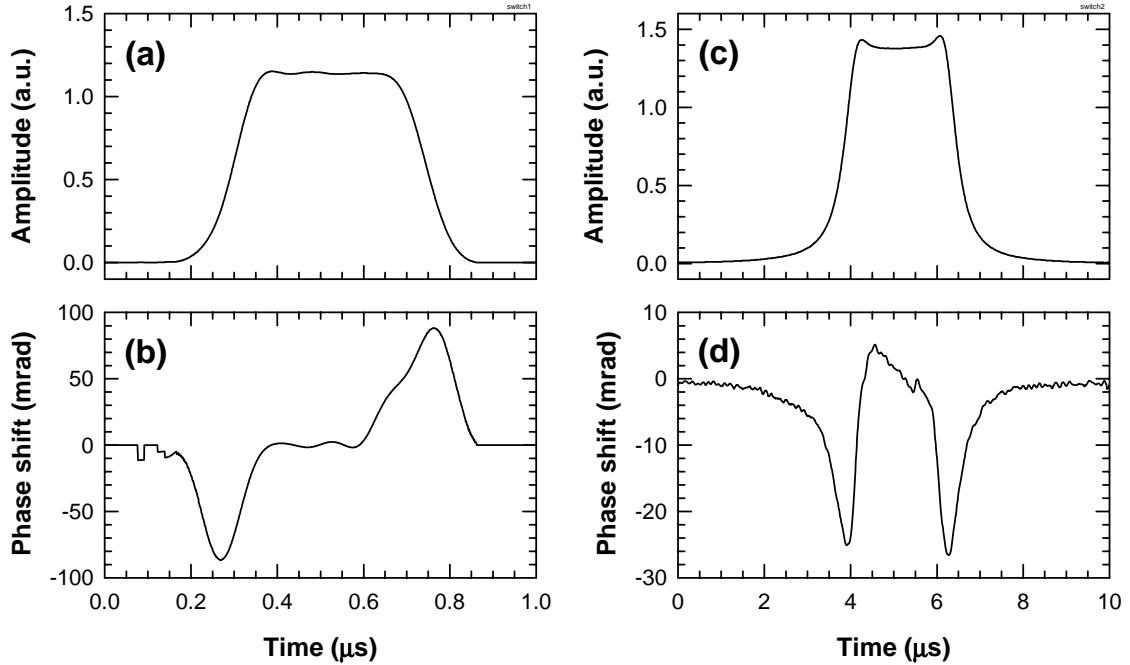
Figure 6.14: Transient phase shifts during Raman pulses. (a)(b) Amplitude (not intensity) and amplitude weighted phases shift of the Raman beat note during a short pulse. The rise and fall times are determined by the finite beam size and the speed of sound in the switching AOM. The RF power driving the AOM is switched much faster ($\sim 5\,\mathrm{ns}$) by an GaAS RF switch. There are substantial phase shifts, but the integrated effect is small because of the asymmetry. (c)(d) Similar data for a longer pulse that is turned on and off slowly($\sim 50\,\mathrm{ns}$) by ramping the control voltage to the RF switch. The amplitude weighted phase shifts are smaller, but persist for longer times. Since the trace is not anti–symmetric anymore, the integrated effect is substantially bigger.

In our experiment the Raman light is controlled by an AOM and phase transients could be introduced by the GaAs switch controlling the RF drive power or by intrinsic properties of the AOM itself. It is advisable to make the switching process for both Raman beams as identical as possible. Our current setup therefore uses a single AOM to switch both beams which also have identical polarizations.

To investigate this effect we irradiate an independent fast photodiode with a short pulse of Raman light, mix the observed beat note down to a convienient frequency of $80\,\mathrm{MHz}$ and digitize the signal at 2 Gsamples/s. Using a Fourier transform method [55] we can then extract both phase and amplitude information independently. We can also calculate the amplitude weighted phase shifts as shown in Fig. 6.14. This data shows that substantial

phase transients are present. The actual experiment, however, uses much longer square pulse which reduces the relative duration of the switching transients. Averaged over a 40 mus pulse, one of the transient phase shifts in Fig. 6.14 would only be ~ 0.25 mrad, corresponding to $0.07\,\mu$Gal. Additional cancelation due to the anti–symmetry of the phase shifts during a single pulse and the symmetry of the pulse sequency would reduce this effect even further.

There are situations, though, where these transient effects might become important. It would definitely be dangerous to switch the two Raman beams separately, using different AOM. Furthermore, it would be problematic to use very short pulses or to replace the square pulses with such of shaped intensity profiles, for example Blackman pulses.

From the formula $\Delta\phi = gk_{\text{eff}}T^2$ one would naively expect that a 1 part in 10^9 measurement of g would require knowing the interferometer pulse spacing T with similar accuracy. For our typical 160 ms spacing this corresponds to only 80 ps, a requirement that is essentially impossible to fulfill using standard beam switching methods.

Fortunately, the chirping of the Raman frequency makes the timing requirements much less severe. This is easy to see in the case where the chirp is adjusted to *exactly* cancel the Doppler shift due to gravity. A change in the time T will change the fringe period, but the position of the central fringe remains the same since it only depends on the chirp rate, a condition that is obviously independent of the time between pulses.

The situation is slightly different when the continuous chirp is approximated by switching between three fixed frequencies. In that case we are once again sensitive to the pulse timing, but now small timing errors enter only quadratically. For small errors δt_i in the time of the three interferometer pulses we find

$$\frac{\Delta g}{g} \quad = \quad \frac{\delta t_1^2 + \delta t_2^2 + \delta t_3^2}{2T^2} \,. \tag{6.14}$$

This is confirmed by the experimental data in Fig. 6.15. Since we can easily achieve a timing accuracy of 200 ns (AOM rise time), the possible error due to pulse timing is less than 0.01 μGal.

6.3.3   Length and Intensity of Raman pulses

Variations in the length and intensity of the Raman pulse are another potential sources of trouble. For a single pulse the effect of such variations has been worked out in [14]. A priori, it is big enough to be of concern if the Raman beam intensities, as in our setup, are
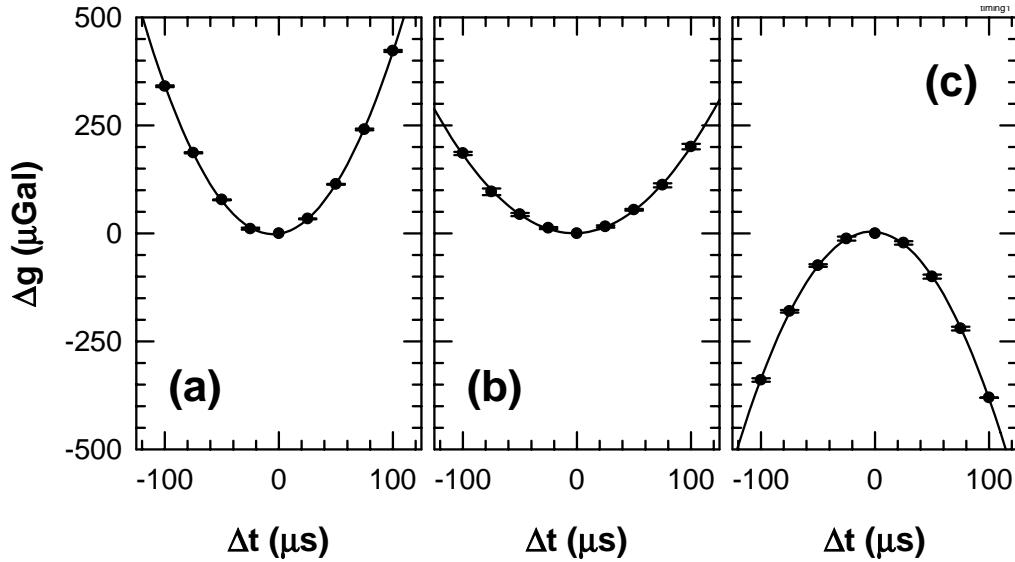
Figure 6.15: Effect of small error in the Raman pulse timing on the measured gravity value (dots). The solid lines are parabolic fits, in agreement with the theoretical predictions. (a) Changing the time of both $\frac{\pi}{2}$–pulses by equal but opposite amounts. (b) Changing the time of the first $\frac{\pi}{2}$–pulse only. (c) Changing the time of the π–pulse.

not actively stabilized. But as long as these variations happen for all three interferometer pulses simultaneously, the effects chancel almost completely due to the symmetry of the $\frac{\pi}{2} - \pi - \frac{\pi}{2}$ pulse sequence. Even when we use a $\frac{\pi}{4} - \frac{\pi}{2} - \frac{\pi}{4}$ pulse sequence, corresponding to a rather drastic error in intensity, the shift in measured gravity is at most a few μGal.

Other tests also confirm that the measured gravity value remains unchanged when short, high intensity pulses are replaced with longer, low intensity pulses while keeping the pulse area constant and maintaining the correct time between pulses (Sec. 2.2 for the proper definition of T). Intensity variations among the pulses of the interferometer are sufficiently small to be neglected. We therefore conclude that the error due to these effects is less than 1 μGal.

6.3.4 Chirp of Raman pulses

We often perform gravity measurements by simply switching between fixed Raman frequencies instead of applying a continuous chirp. In this case the atoms, in their own free falling reference frame, see an apparent chirp of the Raman beams during each single pulse. For
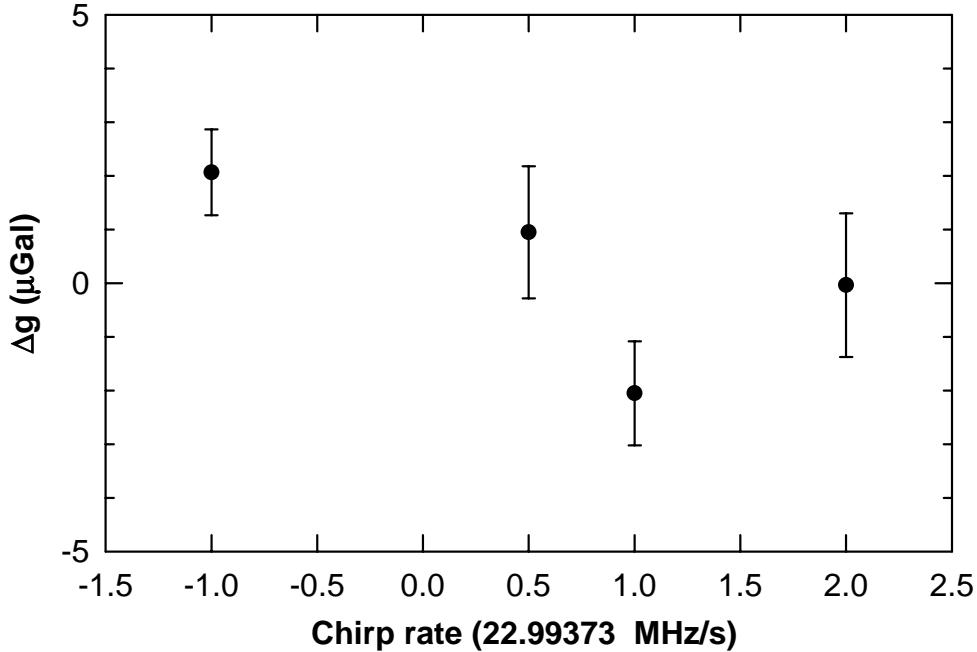
Figure 6.16: Effect of chirp during Raman pulses. We can introduce chirps of the Raman frequencies during each interferometer pulse. A chirp rate of 22.99373 MHz/s exactly cancels the gravitational chirp, the ideal situation. But even for very different chirp rates the gravity value is almost unaffected.

finite length pulses this will cause phase shifts (Sec. 2.2). For typical experimental parameters the effect of these shifts is rather small as a result of the symmetry of the $\frac{\pi}{2} - \pi - \frac{\pi}{2}$ pulse sequence.

It is still preferable to eliminate this concern completely by using the second phase locked loop in our setup (Sec. 3.4.2) to cancel the gravitational chirp during each individual pulse. The same method can also be used to deliberately introduce chirps of the wrong sign or magnitude. The result is shown in Fig. 6.16 and clearly confirms the theoretical prediction that the measurement is rather insensitive to such chirps.

6.3.5 Detuning of Raman pulses

Using the $\frac{\pi}{2} - \pi - \frac{\pi}{2}$ pulse sequence makes the interferometer intrinsically insensitive to detunings from the exact Raman resonance condition, a feature absolutely necessary considering the velocity spread of the atoms and the corresponding Doppler shifts. This does not rule out small residual offsets when the Raman frequency is not properly centered with

respect to the atomic Doppler distribution. We found experimentally that this gravity offset is linearly proportional to the average detuning with a slope of $\sim 1\,\mu\mathrm{Gal/kHz}$.

We now estimate if frequency offsets of this size could occur. Since all the Raman frequencies are referenced to a Loran-C receiver, and thereby ultimately an atomic clock, they are generally known to better than 5×10^{-12}, or $0.05\,\mathrm{Hz}$. The resonance can be easily located to better than $100\,\mathrm{Hz}$ and, because of the velocity preselection, is mostly insensitive to small changes in the atomic velocity distribution. This resulting gravity offset would be approximately $0.1\,\mu\mathrm{Gal}$.

6.4 Synchronous noise

In contrast to a continuous measurement, noise synchronized with the data taking process of a pulsed experiment does generally not average out over time but causes an systematic offset. Vibrations, stray light and electromagnetic interference are just a few examples of the multitude of possible culprits. Modifying the timing of the experiment to ascertain which of them are present is limited by the existence of many timing constraints and the unavoidable interdependence of timing parameters with others, for example spatial position and frequency.

6.4.1 60 Hz Line noise

If the experiment is line triggered, then line noise (60 Hz) is an obvious source of trouble, and Fig. 6.17 shows that it indeed has an substantial effect (up to $5\,\mu\mathrm{Gal}$) on our gravity measurement. We therefore do *not* line trigger our experiment during gravity measurements in order to make the effect average out over time, assuming that the system's response to the 60 Hz disturbance is linear. In this mode of operation the effect then becomes just another source of noise.

6.4.2 Magnetic sensitivity of Seismometer

The central component of the active vibration isolation system is a commercial low frequency accelerometer, not specifically designed for use in feedback systems but for applications in seismology and geophysics. When performing measurements for these purposes, the seismometer is usually located either out in the field or in specially constructed seismic vaults.
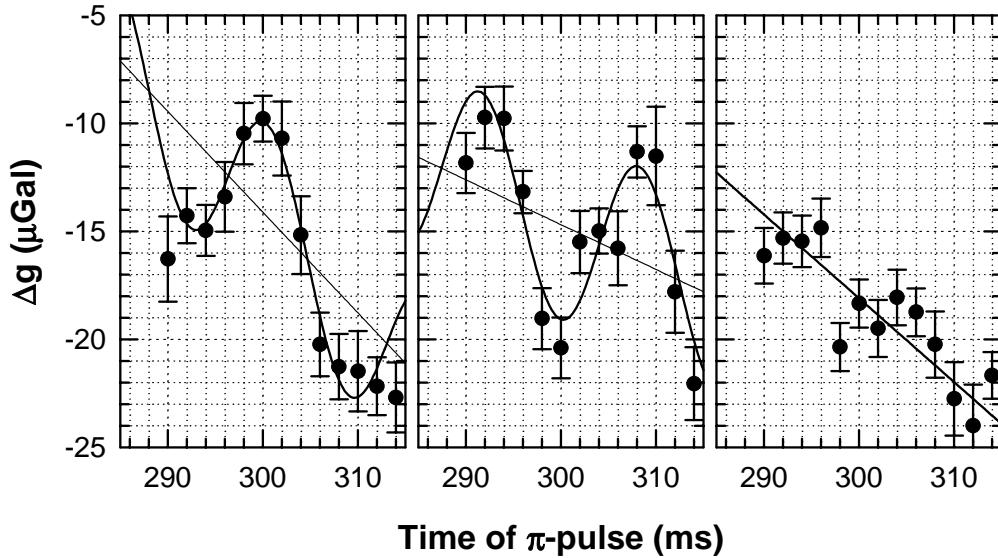
Figure 6.17: Effect of 60 Hz line noise. Graphs (a) and (b) show the changes in the measured gravity value as a function of the delay between interferometer pulse sequence and line trigger. The line trigger phase differs by 172.8°, and the resulting change in the sign of the sinusoidal offset clearly indicates that it is due to 60 Hz line noise. The linear slope is caused by other effects. Graph (c) demonstrates that the effect line noise effect averages out if the experiment is not line triggered.

In neither case is it subjected to substantial electromagnetic interference and accordingly the instrument has not been designed with special precautions to control such influences.

The situation in the laboratory is very different, with the seismometer exposed to external disturbances of various types. Many of them are synchronized with the experimental cycle and could therefore not just lead to increased noise but result in systematic errors. In the following we will analyze the effect due to pulsed magnetic fields to which the seismometer is especially susceptible.

The seismometer will mistakenly interpret any change in the external magnetic field as an acceleration and the feedback loop, attempting to compensate, will introduce a real acceleration of the retro reflection mirror in the opposite direction. Since the acceleration of the atoms is measured relative to this mirror this in turn will cause a systematic measurement error. The precise size of this error will depend on details like the parameters of the feedback loop or the duty cycle of the magnetic field, but it will generally be of the same magnitude as the fake acceleration.

For our setup pulsing of both the trapping coils and the Helmholtz coil assembly can
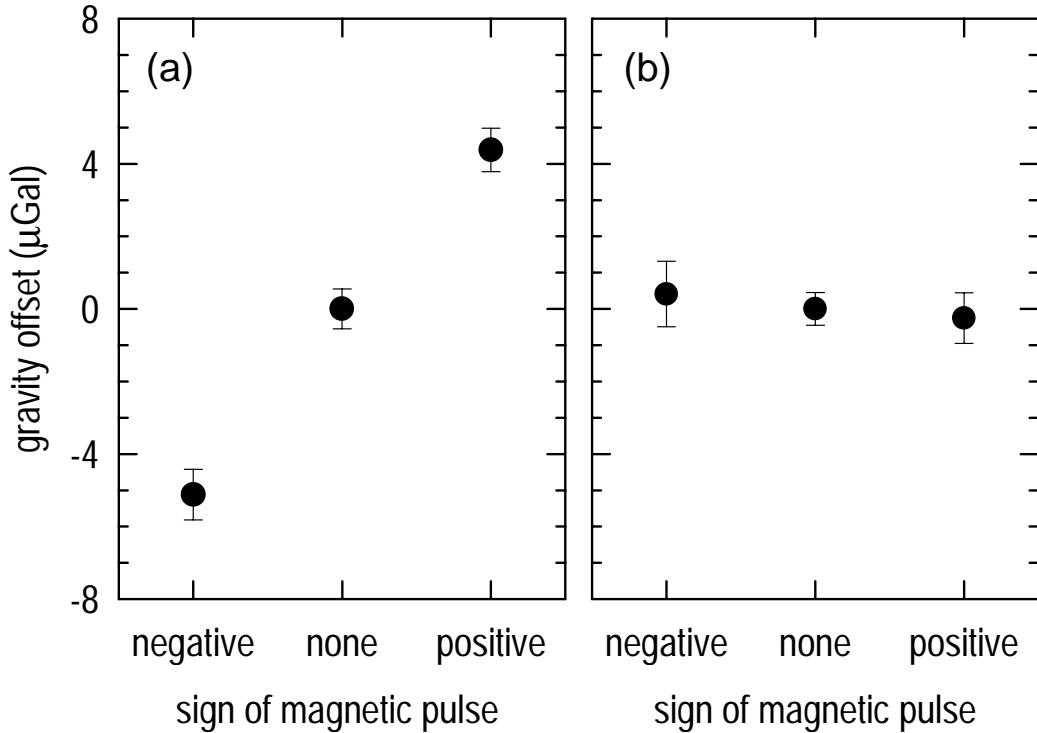
Figure 6.18: Effect of pulses magnetic fields due to the magnetic field sensitivity of the seismometer in the vibration isolation system. In order to test the effect, we extended the normal cycle time of the experiment from 1.3 s to 2.0 s by inserting a delay before reloading the MOT. During this time interval we can pulse on the Helmholtz coils to produce a magnetic field either equivalent to that used for ~ 600 ms during the normal experimental cycle, or with opposite sign. Graph (a) shows that even with a magnetic shield around the seismometer itself the measured gravity value is strongly affected by these pulses. If we pulse on the MOT trapping coils during the additional time interval, we find a similar effect. For standard measurement sequence the expected gravity shift due to this effect should be of approximately the same magnitude. Graph (b) shows that adding additional magnetic shielding around the vibration isolator reduces the effect to below our current measurement resolution. The global slope of the data is there since we did not correct for tidal effects during this measurement.

result in field strengths of several hundred mG at the location of the vibration isolator. Together with the measured magnetic field sensitivity of $\sim 150\,\mu\mathrm{Gal/Gauss}$ of our particular version of the CMG-3 seismometer this implies unacceptably big errors. Therefore the seismometer was fitted with a magnetic shield (Sec. 3.5.1) even before assembling the system, reducing its magnetic field sensitivity by at least a factor of 10. However, even this improvement does not reduce the effect sufficiently, as is clearly demonstrated by the experimental test data in Fig. 6.18 which predicts an gravity offset as big as $10\,\mu\mathrm{Gal}$ for a typical measurement configuration.

To reduce this effect to acceptable levels we have therefore enclosed the whole vibration isolator assembly with an additional magnetic shield. The second graph in Fig. 6.18 indicates that this is sufficient down to the $1\,\mu\mathrm{Gal}$ level.

Other noise sources

Problems due to other sources of synchronous noise are much harder to identify. Some of irregularities in the data presented in Sec. 6.7 might be related to this problem.

6.5 Fundamental

6.5.1 Coriolis force and Sagnac effect

Atom interferometers are intrinsically sensitive to all types of inertial forces. Our setup is specifically designed to be sensitive only to the acceleration due to gravity, but even small misalignments can make it susceptible to Coriolis forces. Some Coriolis forces, for example those caused by rotational noise of experimental setup, are avoidable. But since our experiment is performed in a terrestrial laboratory, the Coriolis forces due to Earth's rotation are always present and can cause severe systematic errors if not properly accounted for.

The atoms in the atomic fountain, though laser cooled, still have a certain horizontal velocity spread. If we trace the trajectory of an atom that has a non zero initial horizontal velocity, we find that the two interferometer paths to enclose a finite *spatial* area (Fig. 6.19). Whenever this happens the atom interferometers becomes sensitive to rotations. This is also known as the Sagnac effect. For a Mach-Zehnder type configuration the resulting phase

shift is given by

$$\Delta\phi \quad = \quad \frac{2m}{\hbar}\,\mathbf{\Omega}\cdot\mathbf{A} \quad = \quad 2\,\mathbf{\Omega}\cdot(\mathbf{v}_0\times\mathbf{k}_{\text{eff}})\,T^2\,, \tag{6.15}$$

where $\mathbf{v}_0$ is the initial velocity and $\mathbf{A}$ a vector normal to the enclosed area and with a length proportional to its size. The corresponding gravity offset,

$$\Delta g \quad = \quad 2\,\mathbf{\Omega}\cdot(\mathbf{v}_0\times\hat{\mathbf{v}}_{\text{rec}})\,, \tag{6.16}$$

is exactly what one would find by calculating the classical Coriolis acceleration. All these formulas also remain valid in the presence of a constant gravitational field.

Substituting the Earth's rotation rate $\Omega = 7.292 \times 10^{-5}\,\text{rad/s}$ (one rotation per one 23hrs 56min 4sec sidereal day, not one solar day) and the geographical latitude of our laboratory ($37°\text{N}$) we find that the initial East-West transverse velocity has to be less than $8.6 \times 10^{-5}\,\text{m/s}$ to achieve 1 μGal accuracy. In other words, since the total time of flight is $610\,\text{ms}$, the atoms have to return to within $52\mu\text{m}$ of their initial position.

The atoms in the atomic fountain have a certain velocity distribution, so what matters is the *average* horizontal velocity of all the *detected* atoms. Within limits, we can adjust this average velocity by changing the size and position of the detection region, either by moving the excitation beam or the aperture in front of the PMT. Fig. 6.19 shows that we can easily detect Earth's rotation using this method. It also demonstrates that the effect is big enough to cause devastating systematic errors even for small misalignments.

It would be possible to reduce this effect by transverse velocity preselection, but we could not use this method due to lack of optical access. Instead, we use the interferometer signal itself to achieve the proper alignment. The effect of Earths rotation is linear in the detection position and cannot give us the required information. However, we can find the correct position of the detection region — where the Coriolis effect vanishes — by intentionally introducing additional, well-defined rotations. Fig. 6.19 demonstrates how this can be done by shaking the table so that is rotating clockwise and counter–clockwise during alternating launches of the atoms.

This method can in principle provide the required alignment accuracy, but only if it is implemented with extreme care. It is extremely important to rotate the experimental setup around a point directly below the sensitive spot of the vibration isolator. Otherwise even the excellent performance of the 1D vibration isolation system is not sufficient to suppress the vertical accelerations introduced by the shaking, and as a result we find an erroneous value for the Coriolis insensitive detection beam position.
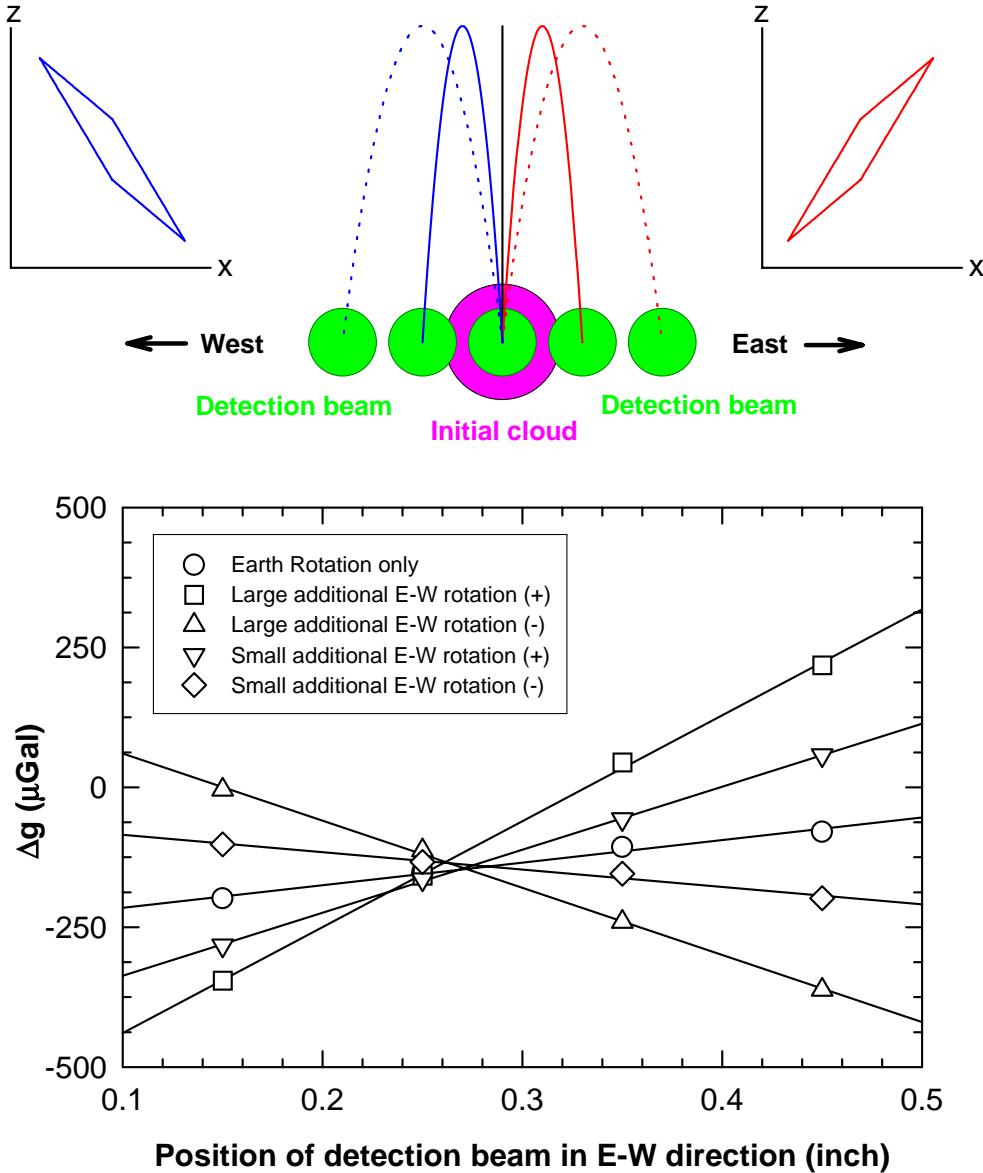
Figure 6.19: Effect of Coriolis forces on the measured gravity value. (a)(b) For atoms with non zero horizontal velocities the two interferometer paths enclose a *spatial* area , which makes the interferometer sensitive to Coriolis forces. (c) By moving the detection beam, we can preferentially select atoms which have different horizontal velocity components, resulting in a different magnitude and sign of the interferometer phase shift (which corresponds to a certain gravity offset) cause by the same rotation. (d) Using this method, we can easily detect Earth's rotation (circles). The other symbols show the additional gravity shifts produced by intentionally rotating the optical table clockwise and counter-clockwise. The intersection of the lines marks the detection beam position at which the Coriolis effect vanishes. All measurements use a pulse separation of $T = 160 \, \mathrm{ms}$.

It is also important to adjust the phase of the sinusoidal table rotation such that the instantaneous angular velocity is maximal ($\dot{\boldsymbol{\Omega}} = 0$) at the time of the π–pulse. Otherwise, the measurement becomes sensitive to horizontal displacements of the atoms with respect to the sensitive spot of the vibration isolator (Sec. 5.3.5). This in turn can result in a wrong value for the correct detection beam position.

Finally, since our laboratory is not *exactly* North-South oriented, it is also important to perform the Coriolis calibration by shaking the table along both axes.

We have found that the direction of the launch changes over time scales of several hours. Long term gravity measurements using the current setup therefore require frequent checks of the Coriolis calibration. Overall, sensitivity to Coriolis forces remains the dominant problem for the current experimental setup and seems to limit the current accuracy to approximately 2 μGal.

6.5.2 Gravity gradients

Gravitational fields are typically not uniform but exhibit some degree of spatial variation. The inverse square law dependence of Earth's gravitational field results in a vertical gravity gradient of approximately $300\,\mu$Gal/m at its surface. Variations in the local mass distribution due to geological features can change this value significantly.

This effect has to be taken into account when analyzing the interferometer data since along their trajectory the atoms encounter changes in gravity that are large compared to the targeted measurement accuracy of 1 μGal. As long as the gravity gradient can be considered linear over the $\sim 10\,$cm length scale of the atomic fountain, we easily treat it using Eq. 2.12 from the theory section. Nonlinearities in the gravity gradient, on the other hand, would complicate the analysis of the atom interferometer data substantially. They could be caused by local mass distributions in the building, the laboratory or even the measurement apparatus itself.

The gravitational gradient in the measurement region was estimated to be slightly higher than the free space gravity gradient due to the proximity of the apparatus. Some nonlinearities may also be introduced by the magnetic shield and the aluminum spacers holding it together. We have attempted to measure this gradient experimentally, using the atom interferometer itself.

To vary the vertical position of the interferometer within the measurement region, we change the timing and velocity of the atomic launch. We keep all other parameters (Raman
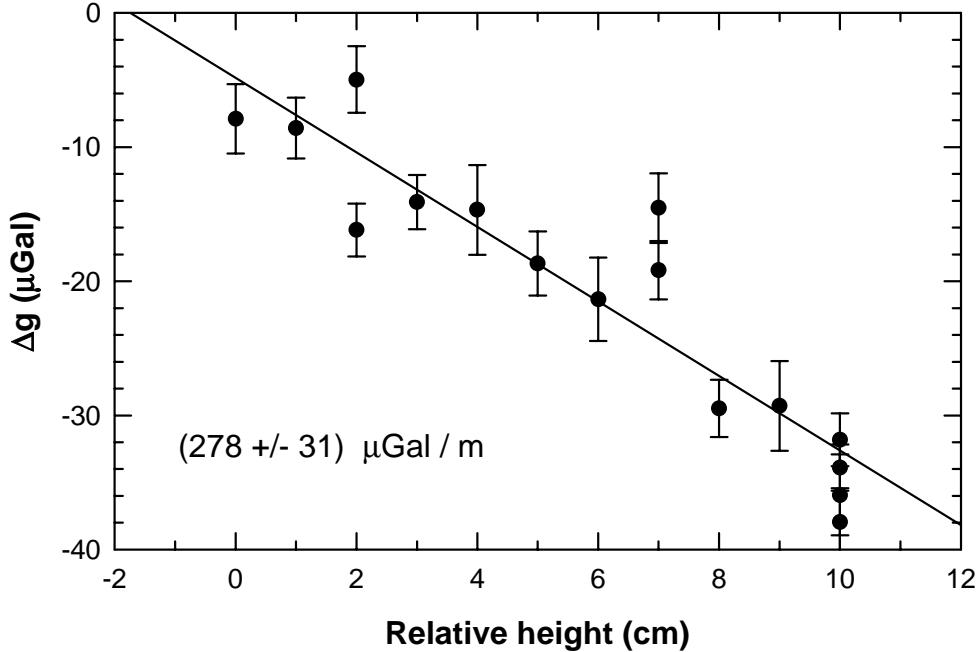
Figure 6.20: Measurement of gravitational gradient inside the interaction region. The data is obtained by using a smaller atomic fountain (pulse spacing $T = 90\,\mathrm{ms}$) and moving it up and down inside the measurement region by adjusting the launch parameters. The solid line is a linear fit.

frequency, pulse timing, ...) constant to insure that any small systematic effects associated with them cancel. The particular method that we employ to achieve this rules out using velocity preselection, but this mostly results in a loss of fringe contrast with no further bad consequences.

We also rotate the optical table to cancel Earth's rotation. Otherwise, the changes in the atomic trajectories could make the measurement sensitive to Coriolis forces. Since the magnetically shield region has a finite length, we have to reduce the time T between Raman pulses to 90 ms in order to get a smaller fountain and gain some space to move it up and down. This reduces the measurement sensitivity substantially. Together with the fact that the table rotates in the correct direction only for every second launch, this leads to measurement times 20 times longer than under normal circumstances and makes it very difficult to obtain a good measurement resolution.

The result of the measurement is shown in Fig. 6.20. It demonstrates that the gravity gradient in the measurement region is essentially linear. From a linear fit of the data

we obtain a value of $278 \pm 31 \,\mu\mathrm{Gal/m}$. This agrees well with the independently measured $293 \pm 10 \,\mu\mathrm{Gal/m}$ outside the vacuum chamber. Given these results conclude that the gravity gradient inside the measurement region is known well enough not to cause problems at our current measurements accuracy.

Gravity gradients are also important if one wants to compare gravity values obtained by different instruments. Since the two instruments cannot (at least for simultaneous measurements) operate at exactly the same location, one has to transfer both gravity values to a common spatial reference point.

Since we have substantial masses in our laboratory, for example the optical table, we could not assume the gravity gradient to be linear and constant. But the atomic fountain apparatus is also stationary, which precludes access to the exact measurement site. We therefore moved a LaCoste-Romberg type G gravimeter with manual readout between the reference location of the FG5 absolute gravimeter measurement ($\sim 1.308\,\mathrm{m}$ above floor level, $\sim 2.5\,\mathrm{m}$ horizontally from the atomic fountain) and a point at the same height as the top of the atomic fountain and as close to it as possible ($1.810\,\mathrm{m}$ above floor level, $\sim 30\,\mathrm{cm}$ horizontally from atomic fountain). Repeating this procedure 15 times we measured a gravity difference of $147 \pm 5 \,\mu\mathrm{Gal}$, corresponding to a linear gravity gradient of $293 \pm 10 \,\mu\mathrm{Gal/m}$. The relatively large error is mostly due to the limited readout resolution of the gravimeter and the large vibrational background noise.

6.5.3 Finite speed of light

Retardation effects due to the finite speed of light can introduce substantial systematic errors for certain measurement configurations. This problem is not specific for atom interferometric measurements, it also afflicts classical gravimeters that monitor the position of a freely falling retro-reflector using a laser interferometers.

The effect is most easily understood for a measurement in which the frequency of just one Raman beam, lets say the upward pointing one, is chirped at a rate $\alpha = k_{\mathrm{eff}} g$ that, when neglecting retardation effects, would exactly cancel the Doppler shift of the accelerating atom. This chirp rate is defined as the rate of change of the instantaneous laser frequency at some point early on in the laser path, somewhere close to the location of the phase lock photodiode. Because of the finite speed of light any change in the instantaneous frequency takes a certain amount of time to propagate to the actual location of the atom. This would be of no consequence for a stationary atom since the constant propagation delay

would produce an identical chirp, just centered around a slightly different frequency, at the location of the atom itself. However, if the atom is moving towards the laser source the propagation delay will shrink constantly and the apparent chirp rate is higher at the location of the atom — it sees the changes in frequency with less and less delay. Accordingly, movement away from the laser source will result in a lower apparent chirp rate. Both effects reverse sign if the downward pointing Raman beam is chirped instead of the upward pointing one.

By making the measurement as symmetric as possible, either by chirping both Raman beams by equal amounts in opposite directions or by applying the central Raman pulse exactly at the top of the fountain, one can all but eliminate this effect. Otherwise one has to correct the measured gravity value by

$$\frac{\Delta g}{g} \quad = \quad \frac{2v_0}{c}\frac{\alpha_\mathrm{up} + \alpha_\mathrm{down}}{\alpha_\mathrm{up} - \alpha_\mathrm{down}}, \tag{6.17}$$

where v_0 is the atomic velocity at the moment of the π-pulse and α_up and α_down are the chirp rates of the upward and downward pointing Raman beams, respectively.

For our typical fountain configuration we chirp only one of the Raman beams. We also have to make the interferometer slightly asymmetric in order to prevent the central Raman pulse from driving Doppler insensitive transitions. The velocity v_0 corresponding to this asymmetry is about $0.04\,\mathrm{m/s}$ and results in a minute $0.3\ \mu\mathrm{Gal}$ correction. If, instead of using an almost symmetric fountain, we would simply drop the atoms (using the same pulse spacing), then this effect would cause a much larger offset of $10.4\ \mu\mathrm{Gal}$.

6.5.4   Other relativistic effects

Relativistic effects that arise in the context of our atom interferometric measurement of gravity, or inertial forces in general, can be divided into two fundamental classes: Those that would also apply to an equivalent measurement using classical objects, and others that are intrinsically related to the quantum mechanical nature of the measurement. In this section we use classical calculations to deal with contributions from the first class only, show that they are negligible and then assume that additional contributions from the second class can be neglected as well.

In the classical description of our system the atom is modeled as a freely falling classical object, able to measure the phase of the Raman light field along it's space-time path and comparing it to the phase of an internal clock (see Section 2.1.3).

Relativistic effects can show their influence in several different ways: The internal clock of the atom will experience time dilation effects because of its change in velocity as well as its changing position in Earths gravitational potential. Fully relativistic dynamics result in a slightly different atomic trajectory. The Raman light is propagating in curved space time, which slightly modifies the electromagnetic wave equation. At higher atomic velocities the fully relativistic treatment of the Doppler effect has to be applied. Finally, there are retardation effects because of the finite speed of light, as discussed in the previous section.

All these effects are not independent but intermingled intimately. One therefore has to be very careful not to double-count or to neglect anything when estimating their importance. Instead of trying to estimate the effects separately it is much safer to start with a fully relativistic description in curved space time and then to apply the necessary approximations to the system as a whole.

Luckily, it is not necessary to go through this elaborate process in the context of this work. Since the maximum atomic velocity v during the interferometers sequence is less than $1.6\,\mathrm{m/s}$, and since the altitude change δh of the atom is less than $15\,\mathrm{cm}$, we find

$$\frac{1}{2}\frac{v^2}{c^2} \quad < \quad 2 \times 10^{-17} \tag{6.18}$$

for the scale factor which is relevant for the second order Doppler shift and the velocity dependent time dilation. We also have

$$\frac{g\,\Delta h}{c^2} \quad < \quad 2 \times 10^{-17} \tag{6.19}$$

for the scale factor which is relevant for the gravitational redshift of the Raman light and the gravitational time dilation of the atom.

These numbers are so small that even without complete understanding of the theory we can safely assume that they will not cause problems. Even if somehow the gravitational redshift of the *optical* frequency of the Raman beams instead of just that of their frequency difference should be a relevant quantity, something that is not supported by our current theoretical analysis, it would only lead to effects of the order of 10^{-12}.

A more complete treatment, necessary in particular to include the second class of effects mentioned above, would require a framework for doing relativistic quantum mechanics in curved spacetime. Since to the best of our knowledge there are no universally accepted and uncontested methods, it is by no means trivial to perform such calculations. Several authors [56, 57, 58] have nevertheless endeavored to do so and have predicted possible effects. These

are generally too small to affect our gravity measurement, but it might be possible observe them in future atom interferometers.

Since little work has been done using the underlying theoretical framework, limiting the opportunity to encounter many of the possible caveats, these treatments should be approached with some caution. It is always possible that something important might have been left out, or maybe has fallen victim to one of the many approximations that were used. Furthermore, it is usually hard to apply these models to the actual experimental situation with its added complexities and complications.

Given the predictions from such theories, it is not always easy to disentangle the purely quantum mechanical part from the one that has a classical equivalent. It is important to note, though, that these theories clearly indicate that the quantum nature of the system leads to a much richer set of effects, for example such that depend on spin. They also nourish the hope that atom interferometry might allow us to encounter some new physics in the future.

6.5.5   Berry phase

A Berry phase, or geometrical phase, can be important for many quantum mechanical systems, including atom interferometers [59, 60, 61, 62]. Most commonly, it will arise in the context of adiabatic processes. If a Berry phase is relevant for an atom interferometric measurement, but is overlooked when analyzing the system, it will most likely lead to very substantial measurement errors.

Solving the time dependent Schrödinger for the system under study does essentially rule out making such a mistake. Although it might still be difficult to identify and isolate Berry phase contributions, they will be handled automatically by this procedure. But other approaches, including path integral formalism and perturbation theory, might ignore important Berry phase contributions completely.

These statements should mostly serve as a general warning about the importance of Berry phase effects. They do not seem to be a problem for our particular interferometer configuration — the atom–light interactions *are* treated by solving the time dependent Schroedinger equation and there are no obvious adiabatic processes, except maybe because of the atoms movement in external electromagnetic fields (i.e. Aharanov-Bohm or Aharanov-Cashier type effects). Since these field are very weak, they should not cause substantial errors, even if there is a related Berry's phase.

Source	Magnitude (μGal)	Uncertainty (μGal)	Time scale
Solid Earth tides	300	$0.2 - 0.5$	Diurnal
Ocean loading	20	0.2	Diurnal
Air pressure	8	$1 - 5$	Hours–Diurnal
Water-table	Site-dependent	Site-dependent	Seasonal
Polar motion	10	< 0.01	12, 14 months

Table 6.1: Environmental effects

The situation might be different for interferometers using adiabatic transfer processes in their beam splitters[‡] or employing more complicated pulse sequences, especially such that address only a single arm of the interferometer at a time.

6.6   Environment

Environmental effects have an substantial impact on absolute gravity measurements and play a somewhat special role. Whether the resulting gravity offsets are considered systematic errors or valid measurement of environmental conditions is somewhat arbitrary. By convention, uncertainties due to environmental signals are generally not included in the error estimate for any absolute gravimeter.

Aside from these fundamental considerations it is important to understand the various environmental effects for purely practical reasons. Otherwise, it would not be possible to compare gravity measurements taken at different times and locations. Gravity variations due to environmental effects could also mask those caused by instrumental flaws. Table 6.1 summarizes some of the most important effects [5].

6.6.1   Tidal effects

The biggest environmental effect by far ($\sim \pm 150\,\mu$Gal) are gravity tides, caused by the relative motion of Earth, Moon and Sun [63]. We have already discussed tides, including the complications cause by ocean loading effects [39, 40, 41, 42, 64] in Sec. 4.3. Here we only mention one more subtlety that arises in the context of absolute gravity measurements, the treatment of the so called permanent tide.

[‡]Preliminary analysis shows no problems for the specific method used in the atom interferometric measurement of $\hbar/m_{\mathrm{Cs}}$ [16].

This DC term can be understood when considering the really long term average of lunar and solar positions relative to Earth. The gravitational force exerted by the resulting average mass distribution, which is toroidal, gives rise to the permanent tide. Not all computer tide models retain this term, and if one wants correct for it in absolute gravity measurements is purely a matter of convention.

6.6.2 Atmospheric pressure

Variations in atmospheric pressure also affect local gravity. The basic mechanism behind this effect is easy to understand. Higher air pressure corresponds to an increased density of air over the measurement site. The additional mass will exert an upward directed gravitational force on the gravimeter, counteracting Earth's gravitational pull and therefore causing a slightly lower total gravity value. The size of this effect is approximately $0.3\,\mu\text{Gal/mbar}$ and typical weather induced pressure variations will therefore change local gravity values by several μGal, making it necessary to keep detailed pressure records in order to apply the appropriate corrections.

The $0.3\,\mu\text{Gal/mbar}$ sensitivity factor is only a semi-empirical quantity, but it will usually suffice to make gravity measurements accurate to a few μGal. If one wants to achieve even higher accuracies, then one has to use much more elaborate models that also include elastic deformations of the continental crust, and the behavior of nearby oceans, in response to air pressure changes [65].

Even after selecting appropriate model for air pressure effects the gravity readings still need to normalized to a standard pressure. The usual convention is to use the nominal pressure computed from the topographic elevation of the measurement site following DIN standard #5450 and using the formula [66]

$$p_n \quad = \quad 1013.25 \left(1 - \frac{0.0065\,h_m}{288.15} \right)^{5.2559} \tag{6.20}$$

where p_n is the nominal pressure in mbar and h_m the topographic elevation in meters.

Water table

Gravitational attraction from a fluctuating water table and easily cause gravity changes of several μGal. These variations are very site depend and generally hard to predict. If the water table is modeled as an infinite plane then the effect is $42\,\mu\text{Gal/m}$, scaled by the bulk

porosity. The Bulk porosity can vary from $< 3\,\%$ in competent granite to $> 50\,\%$ in sands [5].

6.6.3 Polar motion

Another problem arises because Earth's rotational axis is not absolutely stationary but moves around by small amounts relative to Earth's body. Correspondingly, the position of the rotational poles relative to Earth's geography will change; hence the term polar motion. Local gravimetric measurements are sensitive to this motion because the centrifugal component of the measured acceleration will change due to variations in the distance of the measurement site from the rotational axis. The gravity changes due to this effect are typically a few μGaland have a characteristic time scale of 1 year. Since the pole positions are known with exquisite accuracy, this effect can be computed precisely using the following formula [66, 67]:

$$\Delta g \quad = \quad -1.164 \times 10^8 \; \omega^2 \; R \; 2\sin\phi\cos\phi(x\cos\lambda - y\sin\lambda) \tag{6.21}$$

where

$$
\begin{aligned}
\Delta g &= \text{polar motion correction } (\mu\text{Gal}) \\
\omega &= \text{Earth's angular rotational velocity (rad/s)} \\
R &= \text{equatorial radius (semi-major axis) of reference ellipsoid (m)} \\
\phi &= \text{geodetic latitude of the observation station} \\
\lambda &= \text{geodetic longitude of the observation station} \\
x, y &= \text{pole coordinates in IERS}^{\S}\text{system (rad)}
\end{aligned}
$$

The pole positions are frequently determined with milli arc second resolution by VLBI[¶] measurements of Quasar positions. They are published in the monthly IERS Bulletin A which can be obtained from via the Internet (**http://maia.usno.navy.mil/**) from the US Naval Observatory Earth Orientation Department.

Also available from this site is a IERS publication [40] which not only describes this data in detail but also deals with tidal effects, ocean loading, atmospheric loading, postglacial rebound, tectonic plate motion, and even general relativistic models for time and coordinate

---

[§]International Earth Rotation Service
[¶]Very Long Baseline Interferometry

systems. In short, it contains almost everything one would ever want to know about the motions of the planet Earth. An enormous number of related references can also be found in this publication.

6.6.4 Postglacial Rebound

Gravity measurements are taken in regions that were covered by glaciers during the last ice age will usually show the effects of postglacial rebound [68]. When the glaciers were present their enormous weight caused deformations of the underlying continental crust, depressing it by up to several hundred meters. Now that the glaciers are gone the crust is rebounding slowly, typically by a few millimeters a year. This change in altitude then causes μGal level changes in the local gravity value.

Scandinavia and the Canadian shield of North America are exemplary sites showing postglacial rebound. But since our gravity measurements are taken in California, far away from regions of previous glaciation, we need not worry about this effect.

6.6.5 Tectonic plate motions

An effect that could be more relevant in California are potential vertical displacements of the measurement site following a major earthquake. However, no such earthquake happened during the lifetime of this experiment. Measurements in other regions might be more susceptible to tectonic movements, for example in mountain ranges like the Andes that experience substantial tectonic uplift.

6.6.6 Local mass distribution

Local mass distributions, especially when they change over time, become important when gravity is measured at the μGal level. Most absolute gravity measurements taken in the context of geophysical research are therefore conducted at sites specifically selected to control these influences.

One of the primary characteristics of a good site is remoteness from any human activity, a criterion definitely not fulfilled by our instruments location inside a busy university physics building. To make things worse, the physics building is currently surrounded by huge construction site — demolition of multiple nearby buildings, excavation of big holes in

the ground and construction new structures do obviously not constitute an undisturbed environment.

Table 6.2 lists several local objects whose gravitational fields could affect our experiment. The more distant objects simply modify the absolute gravity value at the measurement site. The closest objects could also cause additional problems by producing nonlinear gravity gradients (Sec. 6.5.2).

Object	mass (kg)	distance (m)	gravity (μGal)	gradient (μGal/m)	angle (deg)	gravity change (μGal)
Earth	6.0×10^{24}	6.4×10^{6}	9.8×10^{8}	308	0	9.8×10^{8}
Optical table	1000	1.5	3.0	4	0	3.0
Aluminum spacers	1	0.1	0.7	13	0	0.7
Experimental physicist	90	1.0	0.7	1.2	45	0.5
Theoretical physicist	120	3.0	0.1	0.06	0	0.1
Loaded truck	40000	10	2.7	0.5	45	2.0
Physics lecture hall (demolished)	2.0×10^{6}	50	5.0	0.2	90	0.0
Hole (excavated)	2.0×10^{7}	100	13.3	0.3	85	1.3

Table 6.2: Gravitational effects of various nearby objects

The nearby construction activities are currently our biggest concern. We have made substantial progress in eliminating systematic offsets in our own instrument since the comparison measurement with the falling corner cube gravimeter (Sec. 4.4). The only classical reference value we have available to compare with our new atom interferometric gravity measurements is therefore several months old and might not be valid anymore because of the construction activities.

6.6.7   Motion of building

Another problem with our instruments location on the second floor of the physics building are possible movements of the building and the resulting changes in the measurement height.

One possible cause for building movements would be temperature changes. We can make a rough worst case estimate for the effects of pure thermal expansion. Assuming that the floor of our laboratory is about 10 m above the foundations of the building, daily temperature variations of 10° Celsius, and using the thermal expansion coefficient of 1.4×10^{-5}/K for concrete, we find a vertical displacement of 1.4 mm. The corresponding change in gravity of $0.4\,\mu$Gal would be to small for us to detect. However, the number is big enough

to raise concerns about additional, possibly larger, vertical motions caused by thermal deformations of the building.

The building might also move for a variety of other reasons, for example ground motions related to a nearby construction site or changes in the mechanical properties of the soil after rainfall. However, these effects would be hard to identify and so far we have seen no clear evidence for their existence.

6.6.8   Arbitrary conventions

Although not important when directly comparing two instruments, as long as the measurements are taken simultaneously and at approximately the same location, certain conventions have to be followed in most other cases. They are especially important when comparing new measurements with previous gravity values obtained from independent sources. The problem is that these conventions are somewhat arbitrary and that not everybody uses the same ones. Furthermore, it is often difficult to determine which set of rules was applied for a particular published value.

The most important convention by far is the definition of a standard measurement height. Since vertical gravity gradients of $300\,\mu\mathrm{Gal/m}$ are typical, it makes a big difference if a gravity measurement is at a height of $15\,\mathrm{cm}$ or $100\,\mathrm{cm}$ above ground. We are aware of three different standards: $1\,\mathrm{m}$ above ground, $80\,\mathrm{cm}$ above ground or at ground level. Because of this confusion, for serious work with absolute gravity data it is necessary to obtain all accessible documentation about the earlier measurements, including a site map and gradient data.

6.7   General tests and observations

Most of the experimental tests described so far were specifically tailored to investigate known, or at least suspected, systematic effects. But even without such prior suspicion one can perform other, more general tests in the hope of finding additional problems.

6.7.1   Varying the interferometer pulse spacing

One possibility is to check if the measurement results are consistent for different spacings of the interferometer pulses. Fig. 6.21(a) shows the result of such a test for the Doppler

sensitive interferometer configuration. Ideally, the measured gravity value should not depend on the pulse spacing, except for a very small contribution (0.64 μGal at $T = 160$ ms, 0.16 μGal at $T = 80$ ms) due to the change in the average height of the atoms in the presence of the local gravity gradient. Within the error bars this seems to be the case, but only if the effects of nonlinear RF phase shifts are removed by averaging measurements for two directions of the photon recoil (Sec. 6.3.1).

It is also useful to perform the same test using the equivalent Doppler insensitive interferometer configuration, which might be sensitive to some of the same problems but is not complicated by RF phase shifts and tidal gravity variations. The results in Fig. 6.21(b) indicate that there might be indeed some problem for pulse separations of less than 100 ms, and looking back at the Doppler sensitive data we find indications for this as well. Since for shorter pulse separations the same shift in gravity corresponds to ever smaller shifts in phase, this seems to indicate that there may be problems with the phase of the Raman beams, for example caused by synchronous noise in the RF-system.

6.7.2 Varying the time of the central interferometer pulse

Another possible approach is to keep the pulse separation constant, but to vary the time of the central π-pulse. This changes where along their fountain trajectories the atoms are during the interferometer sequence, and consequently any effect related to spatial position should manifest itself in the data. The method is also sensitive to any form of synchronous noise since it changes the timing relationship between the interferometer sequence and the rest of the experiment.

Again it is possible to perform Doppler sensitive as well as Doppler insensitive versions of this experiment. In both cases the limited vertical extend of the magnetic shield forces us to reduce the pulse spacing T to 80 ms. This increases the measurement time necessary to achieve a given noise level in g by a factor of $\sim$16.

The Doppler sensitive measurement is complicated by RF phase shifts, which are a function of the time dependent Raman difference frequency. In our setup we have two phase-locks that determine the Raman difference frequency (Sec. 3.4.2). To eliminate the RF phase shift effects we can adjust the reference frequency f_{SRS} to accommodate the changes in the pulse time, while keeping the sweep of the other reference frequency f_{TEK}, which is responsible for most of the RF phase shift effect, untouched.

The results for Doppler sensitive and Doppler insensitive cases are shown in Figures
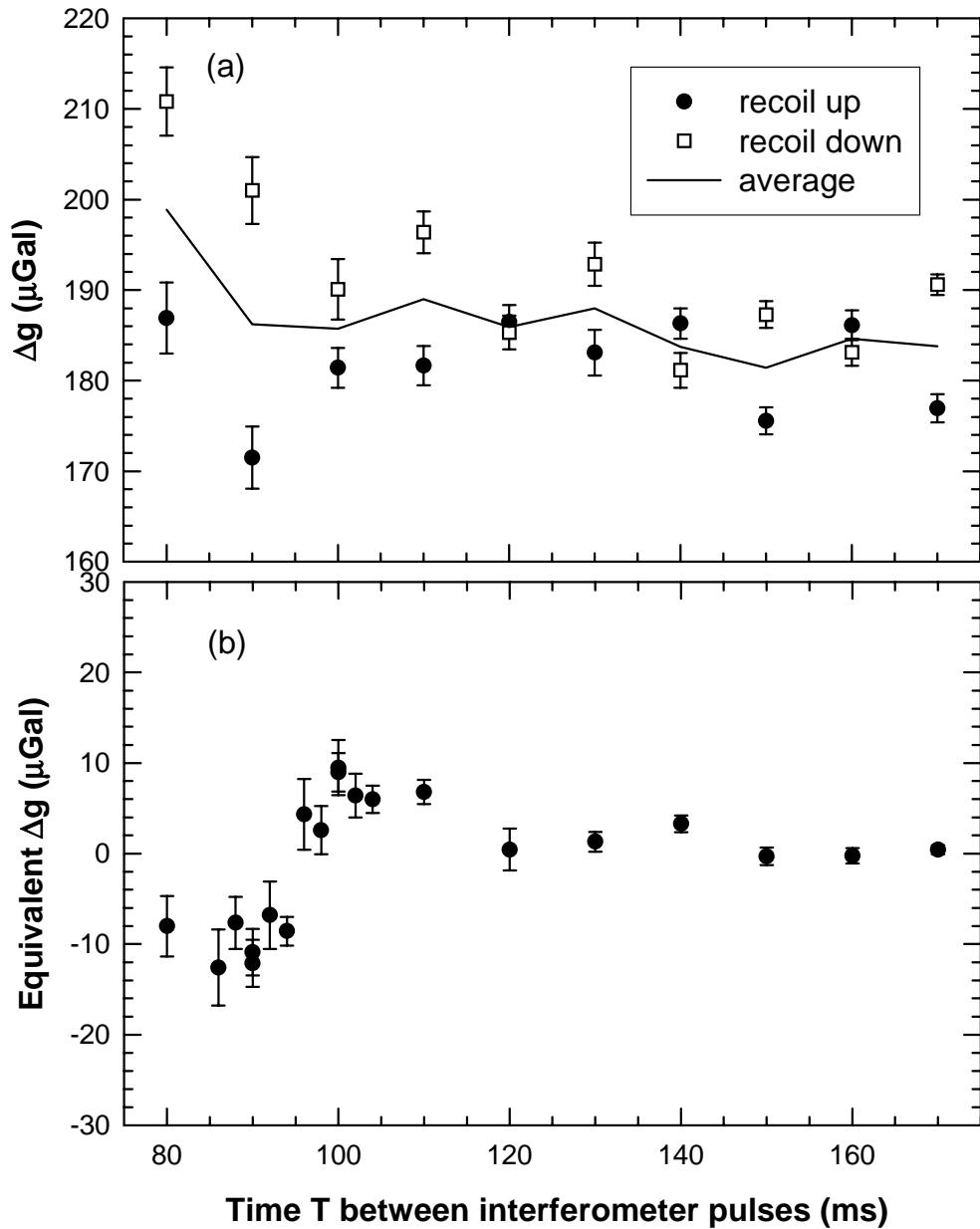
Figure 6.21: Effect of varying the interferometer pulse spacing. (a) Doppler sensitive configuration. $1\,\mu Gal \;\hat{=}\; 66\,\mathrm{mrad}$ for $T = 80\,\mathrm{ms}$, $1\,\mu Gal \;\hat{=}\; 265\,\mathrm{mrad}$ for $T = 160\,\mathrm{ms}$. (b) Doppler insensitive configuration. This measurement normally only makes sense in terms of phase, but we can use the same relation as in the Doppler sensitive case to calculate an equivalent gravity shift.
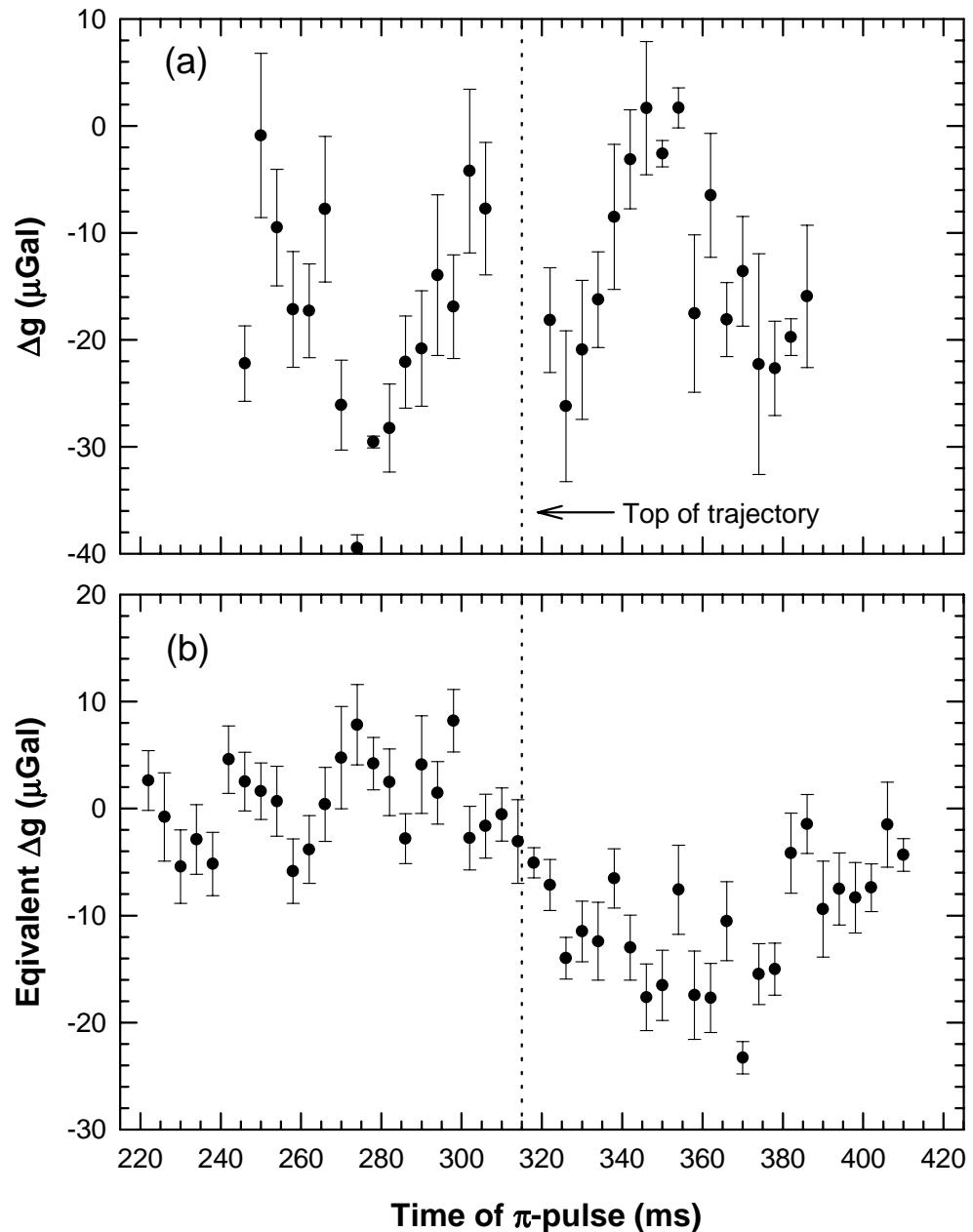
Figure 6.22: Effect of varying the time of the central interferometer pulse. (a) Doppler sensitive configuration. $1\,\mu Gal \,\hat{=}\, 66\,\mathrm{mrad}$ for $T = 80\,\mathrm{ms}$. (b) Doppler insensitive configuration. This measurement normally only makes sense in terms of phase, but we can use the same relation as in the Doppler sensitive case to calculate an equivalent gravity shift.

6.22(a) and 6.22(b), respectively. Theoretically, the Doppler insensitive result should be completely independent of the pulse time, and the Doppler sensitive result should only show a slight parabolic dependence due to gravity gradients and a linear term due to the finite speed of light. That they both show substantial, while markedly different, variations is disturbing. They seem to exhibit a certain degree of antisymmetry and, perhaps, periodicity. So far we have not been able to determine the cause of the problem.

If the magnitude of the variations were the same for 160 ms between pulses, then we would have to include it in our error budget as an possible systematic of approximately $\pm 10\,\mu$Gal. But since it shows up in the Doppler insensitive scan as well, it is probable phase related and its effect on the gravity measurement for $T = 160$ ms should be smaller by a factor of 4. This means a possible systematic error of $\pm 2.5\,\mu$Gal.

6.7.3   Fluctuations during long term measurements

Another cause of concern are the occasional rapid changes in the measured gravity value during long term measurements. Fig. 6.23 shows a few examples of such rapid changes during the comparison measurement with the falling corner–cube gravimeter. It would be interesting to know if the effect is also present in the corner–cube data, but it was completely masked by the higher levels of measurement noise.

The changes have typical rise and fall times of less than an hour, which should be too rapid for most environmental effects like tides or changes in air pressure. On the other hand, the data shows a certain periodicity which suggests that tidal effects, most probably due to ocean loading, might play a role. We have therefore used also used a different ocean loading model (used by NOAA to analyze the falling corner-cube measurements) to analyze our data. While this leads to a somewhat different looking graph (Fig. 6.23c), it does not eliminate the jumps. We can also rule out air pressure changes as the cause, since an independent recording of the pressure during the experiment shows no equivalent jumps.

Without an apparent explanation for the jumps, we have to assume that they are the manifestation of a yet unidentified, time dependent systematic effect of up to 3μGal.

6.8   Summary

Figure 6.24 shows a graphical representation of all the systematic errors discussed in this section. In addition to giving order of magnitude estimates of these effects for the current
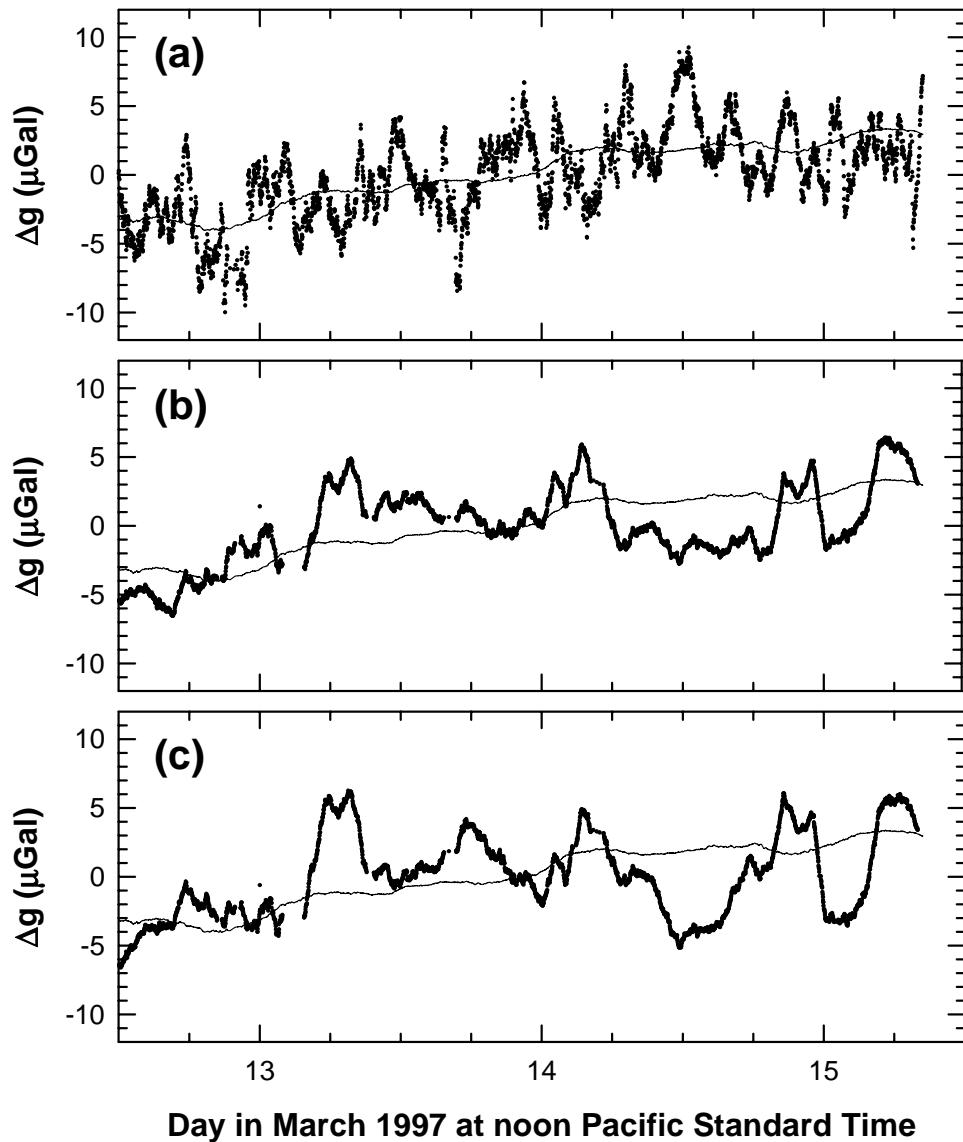
Figure 6.23: Rapid fluctuations in long term gravity records.

instrument, the diagram also points out the improvements achieved since the early days of the project. Furthermore, it indicates potential pitfalls that, luckily, never surfaced in the context of the current experiment — either because they were anticipated and dealt with in advance, or because they would show up only under slightly different conditions.

Recognizing and controlling the Coriolis sensitivity led to biggest improvement of the experimental accuracy, not counting the use of the correct value of the cesium D_2−wavelength. The next biggest improvement can be attributed to enclosing the active vibration isolation system with magnetic shielding.

Currently, instrumental accuracy is limited mostly by the difficulty of minimizing the interferometers sensitivity to Coriolis forces, and by nonlinear phase shifts in the RF electronics controlling the frequency difference of the Raman beams. There are also some additional unidentified problems, most probably are related to noise synchronous with the experiment, and more care has to be taken to account properly for all environmental effects.

| > 100 μGal	10-100 μGal	1 - 10 μGal	0.1 - 1 μGal	< 0.1 μGal	Possible systematic errors
					Cs wavelength
					Laser lock offset
					RF phase shifts
					Timing of pulses
					Chirping of pulses
					Switching of pulses
					Coriolis force
					Gravity gradient
					Zeeman shift
					AC Stark shift
					DC Stark shift
					Cold collisions
					Tilt
					Retro reflection
					Standing waves
					Wavefront curvature
					Speckle
					Leakage light
					Dispersion of Cs vapor
					Dispersion of air
					Dispersion of windows
					Berry phase
					Finite speed of light
					2nd order Doppler shift
					Gravitational Redshift
					Other relativistic effects
					Synchronous vibrations
					Synchronous fields
					Synchronous noise
					Pressure correction
					Tide corrections
					Other environmental effects
					Conventions, definitions

Figure 6.24: Summary of systematic errors.

Chapter 7

Conclusion

7.1   Current status

After implementing the improvements discussed earlier in this thesis we have performed
another atom interferometer measurement of g. The results are shown in Table 7.1, including
some of the corrections that we apply to the raw gravity value. While some of these
corrections (polar motion, transfer to top of fountain) are simply a matter of convention,
others (RF phase shift, cesium lock offset) are necessary to account for known systematic
effects. The table also indicates the most important known measurement uncertainties.

	Value (μGal)	Uncertainty
Measured g value (tide corrected)	$979,933,179$	$\pm\,1$
Polar motion	-4.8	$\pm\,0$
Atmospheric pressure	$+0.7$	$\pm\,0.1$
RF phase shift	-6	$\pm\,2$
Cesium lock offset	-3	$\pm\,1$
AC Stark shift	0	$\pm\,2$
Coriolis effect due to Earth's rotation	0	$\pm\,2$
Tilt and retro-reflection	0	$\pm\,1$
Finite speed of light	$+0.3$	$\pm\,0.1$
Transfer to top of fountain	-6.0	$\pm\,0.2$
Atom interferometer gravity value	$979,933,160$	$\pm\,4$

Table 7.1: Calculation of atom interferometer gravity value.

	Value (μGal)	Uncertainty
Measured g value (tide corrected)	$979,933,304$	± 2
Polar motion	-5.9	± 0
Atmospheric pressure	$+1.7$	± 0.1
Falling corner–cube gravity value	$979,933,300$	± 2

Table 7.2: Calculation of falling corner–cube gravity value.

We can compare this new result to the falling corner–cube measurement taken several months earlier, but we have to consider the possibility that the gravity value could have changed in the meantime. For example, changes in the local mass distribution caused by the major construction work in vicinity of our laboratory (Sec. 6.6.6) or seasonal changes in water table (Sec. 6.6.2) could be responsible for differences up to a few μGal.

Table 7.3 nevertheless shows that after including the measurement height correction (Sec. 6.5.2) our value for g and the one measured by the classical absolute gravimeter now agree within $(7 \pm 7) \times 10^{-9}$ g. This is consistent with the estimated systematic uncertainty and is by far the highest accuracy achieved by any matter wave interferometer measurement so far. It is also in marked contrast to the consistent discrepancies of order $1 - 10\,\%$ between classical and neutron interferometric gravity measurements [69, 70, 71, 72].

7.2   Future prospects

To improve the measurement accuracy even further it will be necessary to improve control of the Raman phase and to address problems due to Coriolis forces and environmental effects. A good way to address these issues would be to build portable versions of the atom

Atom interferometer gravity value		$979,933,160$	$\pm$	4
Falling corner-cube gravity value	$-$	$979,933,300$	$\pm$	2
Measurement height correction	$+$	147	$\pm$	5
Difference		7	$\pm$	7

Table 7.3: Comparison between atom interferometer and falling corner cube gravity measurements. An independent measurement of the gravity gradient (using LaCoste-Romberg spring-type gravimeters) is used to compensate for the difference in measurement height. The atom interferometer gravity value is slightly higher.

interferometer in order to facilitate measurements and comparison studies with different instruments at sites better suited than our current laboratory. Being able to rotate the instruments around the vertical axis would also allow one to identify and eliminate Coriolis effects. There are several other possible improvements: Horizontal velocity selection can reduce Coriolis effects. Additional Raman pulses can increase the separation between interferometer paths and, consequently, the measurement sensitivity. Alternatively, one can use a different intermediate state and shorter wavelength Raman lasers to achieve the same effect. Using a taller fountain and a pulse spacing larger than the current $T = 160\,\text{ms}$ can decrease the relative importance of Raman phase errors. Keeping the atoms in same internal state for both interferometer paths would substantially reduce the sensitivity to magnetic and electric fields.

For practical applications, many of which only require an accuracy of $\Delta g/g \sim 10^{-8}$, one might also try to design a smaller, simplified instrument. In this case, it might be possible to use either continuous atomic beams or high repetition rates ($> 10\,\text{Hz}$) to circumvent aliasing problems to alleviate the need for a complex active vibration isolation system.

Future experiments could use the techniques developed here to perform test of the equivalence principle or to measure Newton's gravitational constant, G. It should also be possible to exploit the wavelength dependence of the interferometer phase shift: Using different intermediate states for the Raman transitions would allow one to compare the wavelengths of all the optical transitions that are accessible in this way, with a precision of 10^{-9} or better.

Bibliography

[1] I. Marson and J. E. Faller, J. Phys. E **19**, 22 (1988).

[2] W. A. Prothero and J. M. Goodkind, J. Sci. Instrum. **39**, 1257 (1968).

[3] J. M. Goodkind, in *Near zero*, edited by J. D. Fairbank (W.H. Freeman, New York, 1988), pp. 784–794.

[4] G. P. Arnautov *et al.*, Metrol. **19**, 49 (1983).

[5] T. M. Niebauer, G. Sasagawa, J. Faller, and R. Hilt, Metrol. **32**, 159 (1995).

[6] V. P. Chebotayev, B. Y. Dubetsky, A. P. Kasantsev, and V. P. Yakovlev, J. Opt. Soc. Am. B **2**, 1791 (1985).

[7] J. F. Clauser, Physica B **151**, 262 (1988).

[8] O. Carnal and J. Mlynek, Phys. Rev. Lett. **66**, 2689 (1991).

[9] D. W. Keith, C. R. Ekstrom, Q. A. Turchette, and D. E. Pritchard, Phys. Rev. Lett. **66**, 2693 (1991).

[10] F. Riehle *et al.*, Phys. Rev. Lett. **67**, 177 (1991).

[11] M. Kasevich and S. Chu, Appl. Phys. B **54**, 321 (1992).

[12] E. M. Rasel *et al.*, Phys. Rev. Lett. **75**, 2633 (1995).

[13] T. L. Gustavson, P. Bouyer, and M. Kasevich, Phys. Rev. Lett. **78**, 2046 (1997).

[14] D. S. Weiss, B. C. Young, and S. Chu, Appl. Phys. B **59**, 217 (1994).

[15] A. Peters *et al.*, Philos. Trans. R. Soc. London, Ser. A **355**, 2223 (1997).

[16] B. Young, Ph.D. thesis, Stanford University, 1997.

[17] K. Moler, D. S. Weiss, M. Kasevich, and S. Chu, Phys. Rev. A **45**, 342 (1992).

[18] R. P. Feynman and A. R. Hibbs, *Quantum Mechanics and Path Integrals* (McGraw-Hill, New York, 1965).

[19] C. Lämmerzahl and Christian J. Bordé, Phys. Lett. A **203**, 59 (1995).

[20] K. P. Marzlin and J. Audretsch, Phys. Rev. A **53**, 312 (1996).

[21] C. J. Bordé, Phys. Lett. A **140**, 10 (1989).

[22] C. J. Bordé, in *Laser Spectroscopy X*, edited by M. Ducloy, E. Giacobino, and G. Camy (World Scientific, Singapore, 1992), pp. 239–245.

[23] P. Storey and C. Cohen-Tannoudji, J. Phys. II France **4**, 1999 (1994).

[24] B. Young, M. Kasevich, and S. Chu, in *Atom Interferometry*, edited by P. R. Berman (Academic Press, Chestnut Hill, 1997), Chap. 9, pp. 363–406.

[25] J. Vanier and C. Audoin, *The quantum physics of atomic frequency standards* (Adam Hilger Ltd, Bristol, 1989).

[26] P. Meystre and M. Sargent III, *Elements of quantum optics* (Springer–Verlag, Berlin, 1990).

[27] E. L. Raab *et al.*, Phys. Rev. Lett. **59**, 2631 (1987).

[28] K. E. Gibble, S. Kasapi, and S. Chu, Opt. Lett. **17**, 526 (1992).

[29] D. S. Weiss *et al.*, in *Light Induced Kinetic Effects on Atoms, Ions and Molecules*, edited by I. Moi *et al.* (ETS Editrice, Pisa, 1991), pp. 35–44.

[30] C. Salomon *et al.*, Europhys. Lett. **12**, 683 (1990).

[31] A. N. Nesmeianov, *Vapor pressure of the chemical elements* (Elsevier Pub. Co., Amsterdam, 1963).

[32] J. L. Hall, L. Hollberg, T. Baer, and H. G. Robinson, Appl. Phys. Lett. **39**, 680 (1981).

[33] J. E. Thomas *et al.*, Phys. Rev. Lett. **48**, 867 (1982).

[34] P. Bouyer, T. Gustavson, K. Haritos, and M. Kasevich, Opt. Lett. **21**, 1502 (1997).

[35] M. Weitz, B. C. Young, and S. Chu, Phys. Rev. Lett. **73**, 2563 (1994).

[36] K. Gibble, S. Chang, and R. Legere, Phys. Rev. Lett. **75**, 2666 (1995).

[37] T. J. Sumner, J. M. Pendlebury, and K. F. Smith, J. Phys. D **20**, 1095 (1987).

[38] J. M. Hensley, A. Peters, and S. Chu, J. Sci. Instrum. (to be published).

[39] C. Shum *et al.*, J. Geophys. Res. **102**, 25173 (1997).

[40] D. McCarthy, IERS technical note 21, U.S. Naval Observatory (unpublished).

[41] H. G. Scherneck, Geophys. J. Int. **106**, 677 (1991).

[42] C. Le Provost *et al.*, J. Geophys. Res. **99**, 24777 (1994).

[43] I. Marson *et al.*, Metrol. **32**, 137 (1995).

[44] D. Greenberger and A. Overhauser, Rev. Mod. Phys. **51**, 43 (1979).

[45] E. Simon, P. Laurent, and A. Clairon, Phys. Rev. A **57**, 436 (1998).

[46] T. Miller and B. Bederson, Adv. At. Mol. Phys. **13**, 1 (1977).

[47] K. Gibble and S. Chu, Phys. Rev. Lett. **70**, 1771 (1993).

[48] S. Ghezali, P. Laurent, S. Lea, and A. Clairon, Europhys. Lett. **36**, 25 (1996).

[49] K. B. Eriksson, I. Johansson, and G. Norlén, Ark. Fys. **28**, 233 (1964).

[50] G. Avila, P. Gain, E. de Clercq, and P. Cerez, Metrol. **22**, 111 (1986).

[51] G. Carlsson, A. Kastberg, and L. R. Pendrill (unpublished).

[52] K.-H. Weber and C. J. Sansonetti, Phys. Rev. A **35**, 4650 (1987).

[53] J. W. Goodman, *Statistical Optics* (Wiley, New York, 1985).

[54] E. L. O'Neill, *Introduction to Statistical Optics* (Addison-Wesley Pub. Co., Reading, 1963).

[55] M. S. Fee, Ph.D. thesis, Stanford University, 1992.

[56] J. Anandan, Phys. Rev. D **30**, 1615 (1984).

[57] J. Audretsch and C. Lammerzahl, Appl. Phys. B **54**, 351 (1992).

[58] S. Wajima, M. Kasai, and T. Futamase, Phys. Rev. D **55**, 1964 (1997).

[59] S. Pancharatnam, Proc. Indian Acad. Sci. A **44**, 247 (1956).

[60] M. Berry, Proc. R. Soc. London, Ser. A **392**, 45 (1984).

[61] M. Reich, U. Sterr, and W. Ertmer, Phys. Rev. A **47**, 2518 (1993).

[62] J. Anandan, J. Christian, and K. Wanelik, Am. J. Phys. **65**, 180 (1997).

[63] P. J. Melchior, *The tides of the planet earth* (Oxford, New York, 1983).

[64] G. Sasagawa, Private communication, 1997.

[65] W. Rabbel and J. Zchau, J. Geophys. **56**, 81 (1985).

[66] *User manual, FG5 absolute gravimeter*, micro–g.

[67] J. Wahr, J. Geophys. Res. **90**, 9363 (1985).

[68] W. Peltier, Science **265**, 195 (1994).

[69] R. Colella, A. Overhauser, and S. Werner, Phys. Rev. Lett. **34**, 1472 (1975).

[70] J. L. Staudenmann, S. Werner, R. Colella, and A. Overhauser, Phys. Rev. A **21**, 1419 (1991).

[71] K. Littrell, B. Allman, and S. Werner, Phys. Rev. A **56**, 1767 (1997).

[72] S. A. Werner, J. Phys. Soc. Jpn. A **65**, 51 (1997).